BOILING IN CAPILLARY-FED POROUS EVAPORATORS SUBJECT TO HIGH HEAT FLUXES

by

Srivathsan Sudhakar

A Dissertation

Submitted to the Faculty of Purdue University
In Partial Fulfillment of the Requirements for the degree of

Doctor of Philosophy

School of Mechanical Engineering
West Lafayette, Indiana
August 2021

THE PURDUE UNIVERSITY GRADUATE SCHOOL
STATEMENT OF COMMITTEE APPROVAL

Dr. Justin A. Weibel, Co-chair
School of Mechanical Engineering

Dr. Suresh V. Garimella, Co-chair
School of Mechanical Engineering

Dr. Jong Hyun Choi
School of Mechanical Engineering

Dr. Shripad Revankar
School of Nuclear Engineering

Approved by:
Dr. Nicole L. Key

To mom and dad,

ACKNOWLEDGMENTS

I would like to express my immense gratitude and thank my advisors Dr. Justin Weibel and Dr. Suresh Garimella. Their mentorship at Purdue has nurtured my critical and creative thinking. The confidence that they exhibit has made me grow professionally and has helped me develop a more fearless mindset towards approaching research, and life in general. I thank Dr. Justin Weibel for cultivating in me the importance of effective communication and meticulous detail in approaching any task at hand.

I thank Dr. Jong Hyun Choi and Dr. Shripad Revankar for serving in my thesis committee. Their feedback has been very valuable to my research.

I take this opportunity to thank Toyota Research Institute of North America for their financial support. Special thanks to Dr. Ercan Dede, Dr. Feng Zhou and Dr. Shailesh Joshi for their constructive feedback and discussion of ideas during my PhD, and for their mentorship during my internship at Toyota.

I am truly grateful for the help and cooperation of each of my colleagues at work, who have shared their time and ideas in addition to their humor and inspiration. I would specially like to thank Dr. Kevin Drummond, Dr. Aakriti Jain, Dr. Carolina Mira Hernandez, Dr. Aditya Chandramohan, Matthew Clark, Kalind Baraya, Rishav Roy and Manohar Bongarala for valuable discussions and ideas for implementing designs into practice.

I am also truly grateful for the help of Steven Titolo of Thermophysical Properties Research Laboratory in West Lafayette, for helping in the fabrication of almost all the designs presented here. Without his help, many of my ideas would not have been brought to fruition.

I am blessed to have friends who provided their support through some tough times. Special thanks to Kaushik Muralidharan, Dr. Swetha Ramadesikan, Aditya Raghunathan, Dr. Aaditya Candadai, Dr. Prabhu Kumar and Rajath Kantharaj. I thank the Purdue Cricket team for their friendship and amusement.

Finally, I thank my parents and family back home, for their love and support.

TABLE OF CONTENTS

LIST OF TABLES 9

LIST OF FIGURES 10

NOMENCLATURE 18

ABSTRACT 22

1. INTRODUCTION 25
   - 1.1 Background 25
   - 1.2 Objectives 26
   - 1.3 Major Contributions 27
   - 1.4 Organization of the Document 29

2. LITERATURE REVIEW 30
   - 2.1 Design Rationale of Hybrid Evaporator Wick Structures 30
   - 2.2 Recent Developments and Limitations in Capillary-fed Boiling 31
   - 2.3 Liquid-Feeding Methods for Experimental Characterization of Wick Structures 32
   - 2.4 Surface Treatments to Maintain Wettability of Copper Wicks 33
   - 2.5 Models for Two-Phase Flow in Heated Porous Media 34
   - 2.6 Models for Vapor Chamber Transport 35
   - 2.7 Air-Cooled Heat Sinks with Embedded Vapor Chambers 36

3. DESIGN OF AN AREA-SCALABLE TWO-LAYER EVAPORATOR WICK FOR HIGH-HEAT-FLUX VAPOR CHAMBERS 40
   - 3.1 Two-layer Evaporator Wick Concept 40
   - 3.2 Reduced-order Model of Two-Layer Wick 41
     - 3.2.1 Fluid Pressure Drops 42
     - 3.2.2 Thermal Resistances 47
   - 3.3 Validation of Reduced-Order Model 48
     - 3.3.1 Numerical Model for Pressure Drop in the Two-Layer Wick 49
     - 3.3.2 Comparison of Reduced-Order and Numerical Models 50
   - 3.4 Two-Layer Wick Performance Prediction 51
     - 3.4.1 Relative Magnitude of Pressure Drops and Temperature Drops 51
     - 3.4.2 Parametric Effects on Performance 53

3.5 Performance Advantages of Proposed Two-layer Wick Over Single-Layer Wicks......... 55
3.6 Conclusions.. 56
4. EXPERIMENTAL INVESTIGATION OF BOILING REGIMES IN A CAPILLARY-FED TWO-LAYER EVAPORATOR WICK 70
4.1 Two-Layer Wick Fabrication.. 70
4.2 Experimental Methods 71
4.2.1 Capillary-fed Boiling Experimental Facility 71
4.2.2 Soldering and Sealing 73
4.2.3 Testing Procedure 75
4.2.4 Data Reduction and Uncertainty Characterization 76
4.3 Results.. 77
4.3.1 Baseline Single-Layer Evaporator Wick 78
4.3.2 Two-Layer Evaporator Wick.. 79
4.4 Conclusions.. 81
5. AREA-SCALABLE HIGH-HEAT-FLUX DISSIPATION AT LOW THERMAL RESISTANCE USING A CAPILLARY-FED TWO-LAYER EVAPORATOR WICK............ 90
5.1 Characterization and Imaging of the Two-Layer Wick Structure 90
5.1.1 SEM Imaging of the Liquid-Feeding Posts and Vapor Vents 91
5.1.2 μ-CT Scans of the Two-Layer Wick.. 92
5.2 Capillary-fed Boiling Experimental Characterization 92
5.2.1 Experimental procedures 92
5.2.2 Single-Layer Wicks Testing: Effect of Sintered Particle Size........................ 93
5.2.3 Two-Layer Wick Testing.. 95
5.3 Discussion 96
5.4 Conclusions.. 98
6. ROLE OF VAPOR-VENTING AND LIQUID-FEEDING ON DRYOUT LIMIT OF TWO-LAYER EVAPORATOR WICKS 108
6.1 Designs of Two-Layer Wicks 108
6.2 Results.. 109
6.2.1 Effect of Vapor-Venting Area 110
6.2.2 Effect of Post Area and Post Spacing 111

6.3 Conclusions 112
7. A SEMI-EMPIRICAL MODEL FOR THERMAL RESISTANCE AND DRYOUT DURING BOILING IN THIN POROUS EVAPORATORS FED BY CAPILLARY ACTION 117
7.1 Model Formulation 117
7.1.1 Heat transfer relations and prediction of thermal resistance 118
7.1.2 Hydrodynamic relations and prediction of dryout 120
7.2 Experimental Measurements of Dryout Heat Flux and Thermal Resistance 124
7.3 Illustration of Model Predictions for an Example Case 125
7.4 Model Calibration 127
7.4.1 Evaluation of effective porous media properties 127
7.4.2 Model calibration against sintered wick experimental results 128
7.4.3 Model calibration against data from the literature 130
7.4.3.1 Thermal resistance calibration 130
7.4.3.2 Dryout heat flux model calibration 131
7.5 Conclusions 132
8. PREDICTION OF DRYOUT LIMITS OF HIGH-HEAT-FLUX VAPOR CHAMBERS CONSIDERING BOILING IN THE EVAPORATOR WICK 147
8.1 Heat Transfer Model Formulation 147
8.1.1 Effective heat flux from substrate conduction 148
8.1.2 Evaluation of vapor chamber temperature fields 149
8.1.2.1 Evaporation based model of the evaporator wick 149
8.1.2.2 Modeling boiling in the evaporator wick 152
8.1.3 Coupling vapor chamber model with substrate conduction 154
8.2 Wick hydrodynamic model formulation 156
8.3 Results 158
8.3.1 Example case study simulation 158
8.3.2 Comparison of evaporation and boiling models 160
8.4 Conclusions 161
9. CONCLUSIONS AND FUTURE WORK 169
9.1 Summary of conclusions 169
9.2 Future Work 171

APPENDIX A. LIST OF EXPERIMENTAL EQUIPMENT 175
APPENDIX B. TECHNICAL DRAWINGS OF CUSTOM FABRICATED COMPONENTS 176
APPENDIX C. REDUCED ORDER MODEL OF HOMOGENEOUS AND GRID-PATTERNED EVAPORATOR WICK STRUCTURES 187
APPENDIX D. SUBSTRATE HEAT SPREADING ANALYSIS 192
APPENDIX E. TRANSIENT ANALYSIS OF NON-UNIFORM HEAT INPUT PROPAGATION THROUGH A HEAT SINK BASE 197
APPENDIX F. PORE-SCALE EVAPORATION MODEL 217
APPENDIX G. BOILING CURVES FOR SINTERED PARTICLE WICKS 220
APPENDIX H. EFFECTIVE THERMAL RESISTANCE OF THE HEAT SINK FIN ARRAY 223
APPENDIX I. EVALUATION OF EVAPORATION AND BOILING HEAT TRANSFER COEFFICIENTS 224
APPENDIX J. ALGORITHM FOR SOVING WICK HYDRODYNAMICS 226
APPENDIX K. MEASUREMENT OF CAPILLARY PRESSURE – SATURATION RELATIONSHIP IN SINTERED POROUS MEDIA 229
REFERENCES 240
VITA 253
PUBLICATIONS 254

LIST OF TABLES

Table 2.1. Recent developments in capillary-fed evaporation/boiling on evaporator wicks for high-heat-flux dissipation. All of the studies included use water as the working fluid. The superheat and thermal resistance correspond to the values as measured at the maximum heat flux/power. 37

Table 2.2. Example of experimental characterization of air-cooled heat sinks with embedded vapor chambers 38

Table 3.1. Pressure drop ratios and temperature drops for the three different evaporator wicks, at a heat input of Q = 1 kW over an area of 1 cm^2........ 58

Table 5.1. Properties of the single-layer sintered porous wicks. 99

Table 6.1. Key dimensions and geometric parameters of the two-layer wick samples tested. The wicks are fabricated using 180 – 212 μm size particles; the dimensions that remain constant across the designs are t_{cap} = 800 μm, t_{post} = 400 μm, and t_{base} = 400 μm. 113

Table 7.1. Properties of the working fluid and porous evaporator wick used in the example case simulation (properties are calculated at saturation temperature of 373 K). 134

Table 7.2. Relations for the intrinsic permeability (K), effective thermal conductivity (k_{eff}), and effective pore radius (r_{eff}) for three commonly used evaporator wick structures. 135

Table 7.3. Measured dryout heat flux and boiling thermal resistance of the wick structures at two different heater sizes. 136

Table 8.1. Properties of the working fluid and porous evaporator wick used in the vapor chamber simulation (properties are calculated at a temperature of 300 K). 162

Table A.1. Equipment used in the capillary-fed boiling test facility 175

Table B.1. Description of components used in the capillary-fed boiling test facility 176

Table D.1. Values of individual resistances in the two test cases, with and without heat spreading. 194

Table E.1. Values of the dimensional parameters chosen for the case studies. 216

Table K.1. The measured diameter, thickness and mass of the three different samples used in the experimental measurements 235

LIST OF FIGURES

Figure 2.1. (a) The two-phase flow configuration (liquid-vapor counterflow) and the associated saturation profiles in a packed bed of porous particles heated from below, as described by Udell [37] and Bau and Torrance [38]... 39

Figure 3.1. (a) A three-dimensional schematic drawing of the proposed two-layer evaporator wick structure is shown with liquid (blue) and vapor (red) flow pathways indicated. The view is cut by planes intersecting the liquid-feeding posts (left) and the vapor vents (right) to reveal the internal structure. Cross-sectional schematic diagrams are shown with the two-layer evaporator wick structure incorporated within a vapor chamber heat spreader (with one half of the geometry shown); (b) the liquid-phase (ΔP_l) and vapor-phase (ΔP_v) pressure drops and (c) thermal resistances (R) are drawn along the primary fluid flow path (not to scale). 59

Figure 3.2. (a) Plan-view diagram of the evaporator footprint area of side length l_{evap}, for an example 5×5 square array of liquid-feeding posts (filled circles) and an offset 4×4 square array of vapor vents (open dots). Square unit cells around one post and one vent are outlined. The square unit cells are approximated by axisymmetric radial unit cells with (b,d) plan and (c,e) side views shown. 60

Figure 3.3. (a) Plan view diagram of the evaporator footprint area of side length $\mathrm{l}_{\mathrm{evap}}$, for an example 5 × 5 array of posts with dashed lines showing one-eighth of the geometry. (b) Three-dimensional view of one-eighth section of the two-layer wick used for the numerical simulations, with the colors distinguishing the porous wick and vapor regions. The meshed (c) porous wick region (wick domain) and the (d) open region (vapor domain) are shown with the boundary conditions labelled, namely, the inlet, outlet, and symmetry, and no-slip boundaries. Insets in (c) and (d) show a close-up view of the mesh. 61

Figure 3.4. Pressure contours predicted by the numerical simulation for the (a) wick and (b) vapor domains of the two-layer wick. Pressure drops are calculated along the cap layer ($\Delta P_{l,cap}$), post ($\Delta P_{l,post}$), and base layer ($\Delta P_{l,base}$) as indicated by the lines in (a); the vapor flow pressure drop (ΔP_v) is calculated along the lines in (b). (c) A bar chart compares the pressure drop values calculated from the reduced-order model and the numerical simulation. (d) The gauge pressure is plotted radially along the base wick layer (*i.e.*, along the line corresponding to the base layer pressure drop) for the reduced-order model and the numerical simulation.. 62

Figure 3.5. (a) Plan and side-view drawings of an example two-layer evaporator wick design case; in the plan view, liquid-feeding posts are filled circles and vents are open dots (dimensions shown in mm, not to scale). Histograms are shown for the different (b) pressure drops and (c) temperature drops for this baseline case at a heat input of Q = 1 kW over 1 cm^2 of heat input area.. 63

Figure 3.6. Effect of post diameter on the total pressure drop and the total temperature drop, for d_{vent} = 1 mm and t_{cap} = 1 mm, with all other wick geometric parameters fixed as in the baseline case. The insets show plan-view drawings (to scale) of the two-layer evaporator wick designs at the extreme post diameters. 64

Figure 3.7. Effect of cap layer thickness on the total pressure drop and the total temperature drop, for d_{post} = 1 mm and d_{vent} = 1 mm, with all other wick geometric parameters fixed as in the baseline case. Insets show side-view drawings of the two-layer wick at the extreme cap layer thicknesses (not to scale, dimensions in mm). 65

Figure 3.8. Effect of vent diameter on the total pressure drop ratio and the total temperature drop, for d_{post} = 1 mm and t_{cap} = 1 mm, with all other wick geometric parameters fixed as in the baseline case. Insets show scaled evaporator areas for extreme cases of vent diameters. 66

Figure 3.9. Effect of increasing post array size on the total pressure drop ratio ($\Delta P_{total}/\Delta P_c$) and the total temperature drop (ΔT_{total}) for d_{vent} = 1 mm, t_{cap} = 1 mm. This is achieved by fixing the footprint area covered by the posts to obtain a target temperature drop, while varying post diameter (d_{post}). Insets show scaled evaporator areas for a 5 × 5 and a 10 × 10 array of posts. 67

Figure 3.10. Schematic drawings of (a) homogeneous and (b) grid-patterned evaporator wicks. Important characteristic dimensions of the two wicks, along with the primary liquid flow pathway (in blue arrows) and vapor flow pathway (in red arrows), are shown. 68

Figure 3.11. Comparison of the pressure drop performance of the two-layer wick and the grid-patterned wick for varying array sizes. The blue line at a pressure drop ratio of 1 signifies the cut-off for operation of the vapor chamber due to the capillary limit. 69

Figure 4.1. Schematic diagrams showing the sequence of process steps in the fabrication of the two-layer wick: (a) copper substrate; (b) first sintering of porous copper layer; (c) laser machining to form liquid-feeding posts; (d) second sintering to add the cap layer; and (e) laser machining to form vapor vents. (f) An SEM image of the sintered copper particle morphology after step (b). (g) A top-down image of the fabricated two-layer wick. 83

Figure 4.2. (a) Schematic diagram of the capillary-fed boiling test facility that consists of a heater assembly inserted into the bottom wall of a saturated test chamber, with important components labeled. (b) Zoomed-in view near the wick fixture showing the liquid flow pathway from the periphery to the evaporator region; the dam prevents flooding over the top of the wick. (c) Exploded three-dimensional drawing of the heater assembly. 84

Figure 4.3 (a) An isometric view of the soldering assembly used to form a thermal connection between the wick substrate and the heater block. The substrate of the wick is held on a graphite base while the heated block is centered on it using a graphite stand. (b) A close-up view of the thermocouple locations (T_1-T_5) and important dimensions of the heater block neck (not-to-scale). 85

Figure 4.4. Plan view and sectioned side view schematic diagrams (dimensions in mm) of the (a) single-layer evaporator wick and the (b) 5 × 5 and (c) 10 × 10 two-layer wick designs.

For the two-layer wicks, the plan view is enlarged near the evaporator region to show the features: solid circles represent the vents in the cap layer, while the dashed circles represent the posts below the cap layer. The plan view diagrams are drawn to scale; the side view sections are not drawn to scale. 86

Figure 4.5. Steady-state (a) capillary-fed boiling curves and (b) wick thermal resistance as a function of input heat flux for the baseline single-layer wick and two-layer wicks. The last point in each curve represents the final steady-state data before the occurrence of complete dryout event. The error bars represent the measurement uncertainties. 87

Figure 4.6. Series of images captured by the high-speed visualization setup, at (a) 45 W/cm^2, (b) 65 W/cm^2 and (c) 98 W/cm^2, showing the 1 cm^2 heated area of the single-layer wick as viewed from the top. Section-view schematic diagrams are shown at each steady heat flux to illustrate the different boiling regimes in the wick. 88

Figure 4.7. Visualization images showing the 1 cm^2 heated area of the two-layer wick as viewed from the top, at (a) 98 W/cm^2, (b) 152 W/cm^2 and (c) 198 W/cm^2. Section-view schematic diagrams are shown to illustrate the different regimes of boiling in the wick. 89

Figure 5.1. (a) Schematic diagram of a two-layer evaporator wick with a 4 × 4 array of liquid-feeding posts and an offset 3 × 3 array of vapor vents. The primary flow pathways for liquid (in blue) and vapor (in red) are indicated. SEM images are taken during the fabrication of the wick to show the structure of (b) a liquid-feeding post before the cap layer is attached and (c) a vapor vent in the cap layer. (d) An SEM image of a cutaway view of the sectioned two-layer wick sample. 100

Figure 5.2. (a) Plan view of the two-layer evaporator wick sample (4 × 4 posts, 3 × 3 vents) used for μ-CT scan imaging. (b) Reconstructed side-view slices from a μ-CT scan of the evaporator wick at different vertical cross-sections across the wick. (c) Schematic diagrams illustrating the different wick features identified in the scan images. 101

Figure 5.3. Plan and section view diagrams of the single-layer wick design. The single-layer wick has a thickness t_{base} over the central evaporator area, supplied by a thicker bulk wick of thickness t_{bulk}. 102

Figure 5.4. SEM images of sintered wicks with different particle size ranges of (a) 45 – 53 μm, (b) 90 – 106 μm, and (c) 180 – 212 μm. 103

Figure 5.5. (a) Capillary-fed boiling curves and (b) wick resistance versus heat fluxes for the three single-layer wick designs, each sintered with a different particle size range. The error bars represent the uncertainty in the measured heat flux and the wick resistance. The legend nomenclature indicates the particle size range and the wick thickness in microns. 104

Figure 5.6. Schematic diagram (plan and side view) of the two-layer evaporator wick tested in this work. This design consists of a 15 × 15 array of vertical liquid feeding posts and an offset 14 × 14 array of vapor vents over a 15 mm × 15 mm area. In the plan view, the open circles are the vents and the filled circles represent the posts below. The evaporator region is the center 10 mm × 10 mm area (d_{post} = 650 µm; d_{vent} = 500 µm; t_{post} = 400 µm; t_{cap} = 700 µm; t_{base} = 400 µm). 105

Figure 5.7. (a) Boiling curves and (b) wick resistance for the two-layer wick comprised of 180-212 µm particles. The two-layer wick has a 15 × 15 array of liquid-feeding posts over a 15 mm × 15 mm area. 106

Figure 5.8. Compilation of capillary-fed boiling performance of different evaporator wicks tested in the literature: (a) Maximum heat flux as a function of heater area and (b) resistance at maximum power as a function of the corresponding power (values above 0.2 K/W are omitted to focus on the low-resistance data; all omitted data fall below a maximum power of 200 W). In comparison to other evaporator wicks, the two-layer wick (star symbol) achieves high-heat-flux dissipation over a large heater area (i.e., higher power) at a lower thermal resistance. 107

Figure 6.1. (a) Schematic diagram (top view) of the two-layer evaporator wick design; the square bulk wick region (side length l_{bulk} = 30 mm) supplies the square heated region (side length l_{evap} = 10 mm) where the two-layer wick features are fabricated. (b-e) Top-view and sectioned side-view schematic diagrams of Wicks 1-4. The top view diagrams are drawn to scale for one symmetric quadrant of the evaporator area; the open circles represent vents in the cap layer, while the filled circles represent the posts below. The side-view diagrams are not to scale in the thickness direction.. 114

Figure 6.2. (a) Boiling curves and (b) wick thermal resistance curves for the four two-layer wick designs. The error bars in (a) and (b) represent the uncertainty in the heat flux and thermal resistance, respectively. 115

Figure 6.3. Plan-view images from high-speed visualization taken during capillary-fed boiling in the two-layer wick, and section-view schematic diagrams depicting the observed boiling behavior, for (a) Wick 1 and (b) Wick 2 at similar heat flux of ~ 240 W/cm^2. Less vapor venting area for Wick 1 causes bubbling through the cap layer, which can disrupt liquid feeding to the substrate. Greater vapor venting area in Wick 2 ensures that vapor exits through the vents. 116

Figure 7.1. A schematic diagram of the two-phase flow configuration of interest in this work, and saturation profiles during boiling in capillary-fed porous evaporators. 137

Figure 7.2. (a) Top-down view and cross-sectional side view schematic diagrams showing the geometry and boundary conditions for the cylindrical porous evaporator solution domain. The heat input is applied over a radius r_e over which boiling occurs. (b) A control volume considered in the thickness direction for the heat transfer model. 138

Figure 7.3. A schematic diagram illustrating the heating and liquid feeding mechanism for the evaporator wick, within the saturated test chamber. The inset image shows a photograph of a sample 90 – 106 µm particle wick structure. 139

Figure 7.4. (a) A plot of the liquid saturation s as a function of the normalized radial coordinate r/r_e for the example case (refer Table 7.1 for properties) at different heat fluxes, calculated using the saturation exponent value n = 3. At q_w = 395 W/cm^2, dryout is indicated by the value of liquid saturation falling to zero at the center of the domain

($s(r = 0)=0$). (b) A plot of the liquid, average vapor, and capillary pressures as a function of the radial coordinate at the dryout heat flux (q_w = 395 W/cm^2)......... 140

Figure 7.5. A plot of the liquid saturation at the center of the wick domain ($s(r = 0)=0$) as a function of the applied heat flux q_w for different values of the saturation exponent n for the example case (refer to Table 7.1 for properties). The values of the dryout heat flux at which ($s(r = 0)=0$) are labelled. 141

Figure 7.6. (a) A plot of the superheat of the solid matrix ($\theta_s = T_s - T_{sat}$) along the z-direction for different values of the film thickness ratio δ/r_{eff} for the example case (refer Table 7.1 for properties)... 142

Figure 7.7. Comparison of the predicted and experimentally measured heat fluxes at a given superheat. 143

Figure 7.8. Comparison of the predicted and experimentally measured dryout heat fluxes (the two different values of dryout heat flux for each particle size correspond to the two different heater sizes). 144

Figure 7.9. Comparison of the predicted and experimentally measured heat fluxes from three different evaporator wick structures in the literature: sintered particle [5] (circles), sintered screen mesh [6] (diamonds) and micro-pillar structures [84] (squares)... 145

Figure 7.10. A comparison of the experimentally measured values of dryout heat flux from the literature and predicted values from the model developed in this study. The comparison includes data on sintered particle wicks from Weibel [98] and Sudhakar *et al.* [73], sintered screen mesh wick structures from Li and Peterson [6,97], and micro-pillar wick structures from Cai and Bhunia [10,84]................................. 146

Figure 8.1. (a) A schematic diagram of the heat transfer solution domain consisting of a solid heat spreader (thickness t_s), vapor chamber (evaporator and condenser wick thicknesses $t_{wick,1}$ and $t_{wick,2}$; vapor core thickness t_{vap}), and an air-cooled fin array (height H_{fin}, thickness t_{fin}, spacing G_{fin}). (b) A diagram illustrating the heat transfer solution method consisting of solving separate conduction and vapor chamber sub-models, and coupling them using an iterative process... 163

Figure 8.2. A schematic diagram of the solution domain (quarter geometry of the evaporator wick) and boundary conditions used in the wick hydrodynamics (numerical) model. The domain consists of a boiling region (shown in red) and an evaporation region outside. Inset diagrams show sketches of a control volume spanning the wick thickness in the boiling and evaporation region. 164

Figure 8.3. (a) Plan view and (b) cross-sectional view schematic diagram of the simulated geometry and boundary conditions for the example case illustration. The plan view is drawn to scale; the cross-sectional view is not-to-scale. The dashed line in the plan view denotes the line across which the temperature profiles are plotted.............. 165

Figure 8.4. (a) Footprint area of the quarter geometry of the wick used in the wick hydrodynamics simulation (200 × 200 cells), that shows the boiling area found from the temperature cutoff (cells in red). A plot of the (b) saturation profiles and (c) pressure profiles along the evaporator wick and the vapor core along the diagonal of the quarter geometry.

The results are shown at four discrete heat fluxes ranging from Q = 25 W (no occurrence of boiling) to Q = 275W (dryout occurs). 166

Figure 8.5. (a) Plots of steady state temperature profiles (along the dashed line in Figure 8.3 (a)) at four different planes (source, wall-wick, vapor core saturation and condenser side) for different input powers ranging from Q = 25 W – 275 W. (b) Evolution of the effective heat transfer coefficient h_w with iteration number, showing convergence of the value, which is used to obtain the steady state temperature profiles. 167

Figure 8.6. A plot of the capillary pressure ratio ($P_c(0,0)/P_{c,max}$) of the vapor chamber as a function of heat input Q for the boiling and evaporation models. The model predicted dryout heat flux values are 275 W for the boiling model and ~1300 W for the evaporation model.. 168

Figure B.1. Technical drawing of the chamber front wall, made from polycarbonate. All the dimensions are in millimeters. 177

Figure B.2. Technical drawing of the chamber bottom wall, made from PEEK. All the dimensions are in millimeters. 178

Figure B.3. Technical drawing of the chamber side wall, made from PEEK. All the dimensions are in millimeters. 179

Figure B.4. Technical drawing of the top wall of the test chamber, made from PEEK. All the dimensions are in millimeters. 180

Figure B.5. Technical drawing of the dam structure used to seal and avoid flooding over the top of the wick. All the dimensions are in millimeters. 181

Figure B.6. Technical drawing of the glass cover on the top chamber wall, made from PEEK. All the dimensions are in millimeters. 182

Figure B.7. Technical drawing of the copper heater block. All dimensions are in millimeters. 183

Figure B.8. Technical drawings of the PEEK insulation used around the copper heater block. All dimensions are in millimeters 184

Figure B.9. Technical drawings of the PEEK insulation used around the copper heater block. All dimensions are in millimeters. 185

Figure B.10. Technical drawings of the fixture that is used to seal the heater block/wick assembly into the test facility. All dimensions are in millimeters. 186

Figure C.1. Schematic drawings of cross-sections of a vapor chamber incorporating a (a) homogeneous and (b) grid-patterned wick. The pressure drops (ΔP) and thermal resistances (R) along the primary fluid flow path are shown for both cases. 190

Figure C.2. Plan view diagram of the grid patterned wick over the evaporator area for an example 5-by-5 grid pattern (filled squares). A square unit cell around a grid is outlined, which is approximated by an axisymmetric radial unit cell with (b) plan and (c) side views shown. 191

Figure D.1. (a) Domain and boundary conditions for calculating the spreading area in the substrate. (b) Temperature map on the wick side from the conduction solution... 195

Figure D.2. Schematic diagram of two configurations (a) with and (b) without heat spreading. 196

Figure E.1. Schematic diagram of the chip-on-substrate domain. 208

Figure E.2. (a) Plan-view locations and (b) transient heat input profiles for multiple heat sources on a single substrate. (c) The nondimensional temperature profile is shown for the coolant side at selected nondimensional time instants (indicated by the dots on the axis in (b)). 209

Figure E.3. (a) Nondimensional temperature-time plot at the center of the coolant-side surface and (b) mean steady temperature profile. 210

Figure E.4. Variation of spatial non-uniformity with non-dimensional thickness d^* for different (a) Bi (at $1/b^* = 0.5$) and (b) $1/b^*$ (at $Bi = 0.1$). 211

Figure E.5. (a) Isolines of spatial non-uniformity map for Bi versus d^* (at $1/b^* = 0.5$); case studies are indicated on the map with a dot. Nondimensional temperature profiles on the coolant side are shown for (b) Case #1 and (c) Case #2. 212

Figure E.6. Schematic drawings of: (a) Case #1 (air-cooled device); (b) Case #2 (embedded microchannel cooling); and (c) Case #3 (low-power device); the solution domain is outlined with a dotted line. 213

Figure E.7. Variation of temporal non-uniformity with Fo for different ω ($d^* = 0.1$, $1/b^* = 0.5$, $Bi = 0.1$). 214

Figure E.8. (a) Isolines of temporal non-uniformity map for ω versus Fo ($d^* = 0.1$, $1/b^* = 0.5$, $Bi = 0.1$); dots on the map indicate representative cases with high (Case A; $\omega = 0.5$ and $Fo = 0.02$) and low (Case B; $\omega = 0.5$ and $Fo = 0.75$) frequency heat inputs. The evolution of the non-dimensional center point temperature over one time period in the steady-periodic regime is shown for (b) Case A and (c) Case B. 215

Figure F.1. A schematic diagram illustrating the pore-scale evaporation model, including the resistances for heat transfer by conduction across a thin liquid film and evaporation from the liquid-vapor interface. 219

Figure G.1. (a) The input heat flux (q_w) plotted against the measured substrate superheat (ΔT_{sub}) and (b) the thermal resistance plotted against the input heat flux, for the three particle size evaporator wicks, for a heater size of 10 mm × 10 mm. Error bars in part (a) and (b) show the uncertainty in the measured heat flux and the thermal resistance, respectively 221

Figure G.2. (a) The input heat flux (q_w) plotted against the measured substrate superheat (ΔT_{sub}) and (b) the thermal resistance plotted against the input heat flux, for the three particle size evaporator wicks, for a heater size of 5 mm × 5 mm. Error bars in part (a) and

(b) show the uncertainty in the measured heat flux and the thermal resistance, respectively 222

Figure K.1. (a) A schematic diagram of the experimental setup used to measure capillary pressure – saturation relationship in porous media. (b) An exploded view of the test section showing internal parts. 236

Figure K.2. A plot of the air pressure against time during the duration of the test. At the start of the test, gas pressure is reduced successively (negative values) to allow imbibition into the sample. To obtain the drainage curve, the gas pressure is increased in steps until the sample is completely drained. 237

Figure K.3. A plot of the imbibed mass plotted against the capillary pressure (at steady state) for the 180 – 212 µm sample. The blue and the red curves are obtained for samples before and after acid cleaning respectively. 238

Figure K.4. The capillary pressure – saturation plot for the three samples (45 – 53 µm, 90 – 106 µm and 180 – 212 µm) 239

NOMENCLATURE

a	heat source length (m)
A	area (m^2)
$\underline{a}_{lk}$	coefficients of 2D Fourier series (K)
$\underline{b}_{lk}$	coefficients of 2D Fourier series (K/s)
b	substrate length (m)
Bi	Biot number (-)
$c_{1\text{-}9}$	constants
C	empirical constant (in equation (3.21))
C_E	Ergun coefficient (-)
d	substrate thickness/diameter (m)
d_{part}/D	mean particle diameter (m)
d_{pore}	mean pore diameter (m)
f	friction factor
Fo	Fourier number (-)
G_{fin}	spacing between fins (m)
h	heat transfer coefficient (W/m^2K)
$\tilde{h}_{evap}$	volumetric evaporation heat transfer coefficient (W/m^3K)
h_{fg}	heat of vaporization (J/kgK)
H_{fin}	fin height (m)
k	thermal conductivity (W/mK)
K	permeability (m^2)
K_{rl}	liquid relative permeability (-)
K_{rv}	vapor relative permeability (-)
l	length (m)
l_x	length of the heat source in x direction (m)
l_y	width of the heat source in y direction (m)
L_x	length of the vapor chamber in x direction (m)
L_y	width of the vapor chamber in y direction (m)

$\dot{m}$	mass flow rate (kg/s)
n	saturation exponent in $K_{rl} = s^n$ (-)
N	number of pores in a control volume (-)
P	pressure (Pa)
P_O	saturation pressure corresponding to the volume average vapor core temperature (Pa)
P_v	vapor pressure (Pa)
q	heat flux (W/m^2)
q_w	computed heat flux at the spreader – wick boundary (W/m^2)
$\tilde{q}$	volumetric heat flux (W/m^3)
Q	heat input (W)
r	radius/radial coordinate (m)
r_{eff}	effective pore radius (m)
R/R_{th}	thermal resistance (K/W)
R	specific gas constant (J/Kg/K)
s	liquid saturation (-)
S	spacing between liquid feeding posts (m)
t	thickness/height (m) (in main document)
t_{fin}	fin thickness (m)
t_s	thickness of heat spreader (m)
t_{vap}	thickness of vapor core (m)
$t_{wick,1}$	thickness of evaporator-side wick (m)
$t_{wick,2}$	thickness of condenser-side wick (m)
T	temperature (K)
$\overline{T}$	z-averaged temperature (K)
T_{air}	ambient temperature (K)
T_{sat}	saturation temperature (K)
u	x-component of velocity (m/s)
v	y-component of velocity (m/s)
$\vec{U}$	velocity vector (m/s)
U	uncertainty (-)
v_{fg}	specific volume change (m^3/kg)

x,y,z	Cartesian coordinate directions (m)

Greek symbols

α	diffusivity (m^2/s)
θ	Temperature rise (K)
λ	constant $\left(\frac{h_{fg}P_O}{R\left(T_{sat}^2\right)_{mean}}\right)$ (Pa/K)
μ	dynamic viscosity (kg/ms)
v	kinematic viscosity (m^2/s)
ρ	density (kg/m^3)
σ	surface tension (N/m); accommodation coefficient (–)
φ	constant $\left(\frac{2\sigma}{2-\sigma}\frac{h_{fg}\rho_{vap}}{\left(T_{vap}^{1.5}\right)_{mean}}\left(\frac{1}{2\pi R}\right)^{0.5}\right)$ (kg m^{-2} s^{-1} K^{-1})
ϕ	porosity (-)
δ	film thickness (m)
θ	evaporator superheat (K)
ω	duty cycle (-)

Subscripts

∞	ambient
1	corresponding to the evaporator side
2	corresponding to the condenser side
air	air flow
avg	average
base	base wick
boil	capillary-fed boiling
bulk	bulk wick
c	capillary
cap	cap layer
cond	condenser
condn	conduction

core	vapor core
Cu	copper
CV	control volume
dry	dryout
D	Duhamel’s solution
eff	effective
e/evap	evaporator/evaporation
grid	grid-patterned wick
h	homogeneous wick/heater
l	liquid
lv	liquid–vapor interface
max	maximum
meas	measured
p	pore
post	liquid-feeding post
rl	relative liquid
rv	relative vapor
s	steady/solder/solid/spreader
sat	saturation
sp	steady periodic
space	space between liquid-feeding posts
sub	substrate
tr	transient
u	unit step solution
v	vapor
vap	vapor core
vent	vapor vent
w	spreader – wick boundary
wall	vapor chamber walls
wick	refers to evaporator wick

ABSTRACT

Thermal management in next generation power electronic devices, radar applications and semiconductor packaging architectures is becoming increasingly challenging due to the need to reject localized high heat fluxes as well as large total powers. Air cooling has been considered as a simple and reliable method for thermal management compared to architectures that incorporate liquid cooling. However, air-cooled heat sinks typically require effective heat spreading to provide the requisite level of area enhancement to dissipate high heat fluxes. Compared to solid metallic heat spreaders, advanced heat sinks that incorporate two-phase heat transfer devices such as vapor chambers can significantly enhance the power dissipation capabilities in such configurations. Vapor chambers are devices that utilize evaporation/boiling processes within a sealed cavity to achieve efficient heat spreading. In high-heat-flux applications, boiling can occur within the internal wick structure of the vapor chamber at the location of the heat input (i.e., the evaporator). The maximum dryout heat flux and thermal resistance of the device is dictated by the resulting two-phase flow and heat transfer in the porous evaporator due to boiling. While various works in the literature have introduced new evaporator wick designs to improve the dryout heat flux during boiling, the enhancement is limited to small, millimeter scale hotspots or at a very high thermal resistance. In additixon, the effective design of such evaporator systems requires mechanistic models that can accurately predict the dryout limit and thermal performance.

This thesis first explores the usage of a novel ‘two-layer’ evaporator wick for passive high heat flux dissipation over large heater areas at a low thermal resistance. Moreover, a new mechanistic (first principles based) model framework is introduced for dryout limit and thermal performance prediction during boiling in capillary fed evaporators, by considering the resulting simultaneous flow of two phases (liquid and vapor) within the microscale porous media.

The novel two-layer wick concept uses a thick ‘cap’ layer of porous material to feed liquid to a thin ‘base’ layer through an array of vertical liquid-feeding ‘posts’. Vapor ‘vents’ in the cap layer allow for vapor formed during the boiling process (which is constrained to the base layer) to escape out of the wick. This two-layer structure decouples the functions of liquid resupply and capillary-fed boiling heat transfer, making the design realize high heat flux dissipation greater than 500 W/cm^2 over large heat input areas of ~1 cm^2. A reduced-order model is first developed to demonstrate the performance of a vapor chamber incorporating such a two-layer evaporator wick

design. The model comprises simplified hydraulic and thermal resistance networks for predicting the capillary-limited maximum heat flux and the overall thermal resistance, respectively. The reduced-order model is validated against a higher fidelity numerical model and then used to analyze the performance of the vapor chamber with varying two-layer wick geometric feature sizes. The fabrication of the proposed two-layer wick is then presented. The thermal performance of the fabricated wicks is characterized using a boiling test facility that utilizes high speed visualization to identify the characteristic regimes of boiling operation in the wicks. The performance is also benchmarked to conventional single-layer wicks.

It is observed that single-layer wicks exhibit an unfavorable boiling regime where the center of the heater area dries out locally, leading to a high value of thermal resistance. The two-layer wicks avoid local dryout due to the distributed feeding provided by the posts and enhance the dryout heat flux significantly compared to single-layer wicks. A two-layer design that consists of a 10 × 10 array of liquid feeding posts provided a 400% improvement in the dryout heat flux. Following a parametric analysis of the effect of particle size, two-layer wicks composed of 180 – 212 μm particles and a 15 × 15 array of liquid feeding posts yielded a maximum heat flux dissipation of 485 W/cm^2 over a 1 cm^2 heat input area while also maintaining a low thermal resistance of only ~0.052 K/W. The effect of vapor venting and liquid-feeding areas is also experimentally studied. By understanding these effects, a parametrically optimized design is fabricated and shown to demonstrate an extremely high dryout limit of 512 W/cm^2. We identify that the unique area-scalability of the two-layer wick design allows it to achieve an unprecedented combination of high total power and low-thermal-resistance heat dissipation over larger areas than was previously possible in the literature.

The results from the characterization of two-layer wicks revealed that the overall performance of the design was limited by the boiling process in the thin base wick layer. A fundamental model-based understanding of the resulting two-phase flow and heat transfer process in such thin capillary-fed porous media was still lacking. This lack of a mechanistic model precluded the accurate prediction of dryout heat flux and thermal performance of the two-layer wick. Moreover, such an understanding is needed for the optimal design of advanced hybrid evaporator wicks that leverage capillary-fed boiling. Despite the existence of various experimental works, there are currently no mechanistic approaches that model this behavior. To fill this unmet need, this thesis presents a new semi-empirical model for prediction of dryout and thermal resistance of capillary-fed evaporator systems. Thermal conduction across the solid and volumetric evaporation within the pores are solved to obtain the temperature distribution in the porous structure. Capillary-driven lateral liquid flow from the outer periphery of the evaporator to its center, with vapor flow across the thickness, is considered to obtain the local liquid and vapor pressures. Experiments are conducted on sintered copper particle evaporators of different particle sizes and heater areas to collect data for model calibration. To demonstrate the wider applicability of the model for other types of porous evaporators, the model is further calibrated against a variety of dryout limit and thermal resistance data collected from the literature. The model is shown to predict the experimentally observed trends in the dryout limit with mean particle/pore size, heater size, and evaporator thicknesses. This physics–based modeling approach is then implemented into a vapor chamber model to predict the thermal performance limits of air-cooled heat sinks with embedded vapor chambers. The governing energy and momentum equations of a low-cost analytical vapor chamber modeling approach is coupled with the evaporator model to capture the effect of boiling in the evaporator wick. An example case study illustrating the usage of the model is demonstrated and compared to a purely evaporation-based modeling approach, for quantifying the differences in dryout limit prediction, signifying the need to account for boiling in the evaporator wick.

The understanding gained from this thesis can be utilized for the prediction of dryout and thermal performance during boiling in capillary limited evaporator systems. The work also suggests the usage of a universal relative permeability correlation for the two-phase flow configuration studied herein for capillary-fed boiling, based on a wide calibration to experimental data. The modeling framework can also be readily leveraged to find novel and unexplored designs of advanced evaporator wicks. From an application standpoint, the new vapor chamber model developed here can be used for the improved estimation of performance limits specifically when high heat fluxes are encountered by the device. This will enable better and informed design of air-cooled heat sink architectures with embedded vapor chambers for high performance applications.

1. INTRODUCTION

1.1 Background

Vapor chambers offer an effective means of spreading heat from a localized source to a larger surface area while incurring a small temperature gradient. The heat input to the evaporator of a vapor chamber is absorbed by a change in phase of a working fluid. Vapor thus formed flows to the condenser section, where heat is rejected and the fluid condenses back to the liquid phase. A porous wick structure lining the inside of the vapor chamber is responsible for passively transporting condensed liquid back to the heat input area by capillary forces. By operating in this two-phase cycle, passive heat spreading may be accomplished at a temperature gradient that can be significantly lesser than in the case of conduction-based solid spreader layers. Thus, vapor chambers find applications within thermal management architectures that rely on heat spreading. In the evaporator region of the device, the lateral feeding of liquid by the porous media is governed only by capillary forces. If the feeding distance is relatively small, the system is independent of orientation with respect to gravity. The gravity independence of such devices (where the evaporator can operate under any orientation without the occurrence of dryout), can be utilized in applications related to microgravity and two-phase heat transport systems in satellites.

The amount of heat input to the vapor chamber dictates the phase-change behavior in the evaporator wick [1]. At low input heat fluxes, the wick operates in a regime wherein evaporation occurs from the liquid menisci sustained at the top of the saturated wick. As heat flux is increased, the menisci recede into the bulk of the wick with increased curvature, providing more capillary pressure for resupply, compensating for the increased liquid flow rate due to evaporation. Depending on the size of the heat input area and the vapor chamber design, further increases in heat flux may cause the menisci to completely recede and dry out (reaching the so-called capillary limit); alternatively, if the surface superheat becomes sufficiently large prior to capillary dryout, vapor bubble nucleation can occur in the wick structure leading to a capillary-fed boiling regime. In some wick structures, incipience of vapor bubbles can completely cut off the capillary resupply pathway, causing immediate dryout via the so-called boiling limit. Early studies that reported *sustained* capillary-fed boiling from porous wick structures [2,3] observed a sharp decrease in the thermal resistance when boiling was initiated. However, sustained boiling in the mesh wick structures [4] reduced the cross-sectional area available for liquid flow, thereby incurring a large pressure drop responsible for premature dryout, at heat fluxes below the notional capillary limit, despite the potential for a reduction in the thermal resistance.

Sintered metal wicks provide relatively higher capillary pressure and effective thermal conductivities in comparison to other conventional wick structures [1]. In addition, the highly tortuous nature of the stochastic network of pores in sintered metal wicks can sustain liquid supply during capillary-fed boiling conditions, making them suitable for high-heat-flux vapor chamber applications in which nucleation is likely to occur. Several studies have evaluated homogeneous sintered metal wicks for dissipating high heat fluxes when operated in the capillary-fed boiling regime [5-8] and identified the critical wick geometric parameters that governed thermal performance and dryout under these conditions. Parametric investigations of wick thickness reported that higher thicknesses yielded higher dryout heat fluxes for homogeneous sintered metal screen wicks [6] and biporous sintered powder wicks [7]. While thicker wicks were capable of providing a larger cross-sectional area for liquid resupply to prevent dryout, thick sintered wicks can result in a large surface superheat during capillary-fed boiling operation [7]. Thin homogeneous sintered metal powder wicks on the order of ~200 μm in thickness can provide a low thermal resistance to boiling [8] but cannot sustain liquid supply at high heat fluxes.

Next-generation high performance electronic systems call for the removal of extreme heat fluxes of about 1 kW/cm^2 [9], while maintaining the surface temperature within specified limits to ensure device reliability. While heat fluxes of ~1 kW/cm^2 have been dissipated by passively-fed wick structures, these demonstrations have been limited by incurring excessive surface temperatures (*e.g.*, 147 K superheat [7]) or being restricted to very small hotspot sizes of 0.04 cm^2 [10,11] or less [12].

1.2 Objectives

The major objectives of this work are to: 1) design, fabricate and experimentally characterize a novel two-layer evaporator wick structure for vapor chambers, that is capable of achieving high-heat-flux dissipation over large heater areas, at a low thermal resistance; 2) experimentally observe and characterize the boiling regimes of operation of the two-layer wick; 3) benchmark the performance of the two-layer wick to conventional wick structures and perform a parametric study of the two-layer wick design. In addition, 4) to develop a mechanistic model for dryout heat flux and thermal resistance prediction during capillary-fed boiling in porous evaporators, and 5) to advance vapor chamber models incorporating nucleate boiling in the evaporator wick.

1.3 Major Contributions

A two-layer evaporator wick is designed to realize on the order of ~1 kW/cm^2 heat dissipation over heat input areas as large as 1 cm^2 and at thermal resistances suitable for electronics cooling applications. A reduced-order model is developed to predict the performance of a vapor chamber incorporating this structure in the evaporator. The reduced-order model is validated against a higher-fidelity numerical model and then used to obtain parametric trends in the total pressure drop and thermal resistance of the vapor chamber. The two-layer wick performance is benchmarked against conventional single-layer wick concepts.

Sintering and laser machining processes are developed to fabricate the proposed two-layer structure. Loose copper particles are sieved to a specific size range using US standard sieves. The particles are held in a graphite mold and sintered onto a copper substrate at high temperature in a vacuum furnace. This step forms a uniform layer of sintered particles, characterized by a mean pore size and porosity. A laser-cutting machine is then used to etch the sintered surface to fabricate posts and retain only a thin base wick layer in the region. A second cap layer is sintered onto the posts and proper contact between these layers is ensured. The vapor vents are formed by laser machining, at locations offset from the posts on the first layer. These processes and the structure of the two-layer wick formed from them are thoroughly investigated using CT scan and SEM imaging.

A novel capillary-fed boiling experimental facility is constructed for thermal characterization of the wick structures. APPENDIX A and APPENDIX B show details of the equipment used, and technical drawings of custom-fabricated components. The test facility is used to measure the dryout heat flux and thermal resistance of the wicks in a saturated environment. A copper heater block is designed to provide uniform heat input to the wick. To provide a low resistance thermal connection between the wick and the heater block, the wick is soldered onto the heater block using a high-temperature lead-tin solder. The soldering methodology, sealing, data reduction and uncertainty propagation analysis is performed for the designed test facility. High-speed visualization is used to observe the boiling behavior during the capillary-fed operation of the single-layer and the two-layer wicks.

To demonstrate the boiling behavior of two-layer wicks, two designs (5 × 5 and 10 × 10 array of feeding posts) are fabricated and tested. Finer post arrays are shown to provide higher dryout heat fluxes due to more distributed liquid feeding pathways. The dryout mechanism of the two-layer wicks are identified using the high-speed visualization images. The effect of sintered particle size on the capillary-fed boiling performance is experimentally characterized. To realize high-heat-flux dissipation, a two-layer wick with a 15 × 15 array of liquid-feeding posts is fabricated using 180 – 212 µm particles. This two-layer wick is shown to dissipate very high heat fluxes of ~ 500 W/cm^2 at a low thermal resistance of 0.052 K/W. The role of vapor venting and liquid feeding areas on the performance of the two-layer wick is studied. Different designs of the two-layer wick are fabricated by individually varying these parameters and their effect on the dryout limit of the wick is observed.

A new thermofluidic model for dryout and thermal resistance prediction of capillary-fed porous evaporators is developed. Conduction and evaporation heat transfer in the porous medium are solved to obtain the boiling thermal resistance. The hydrodynamic model considers lateral liquid flow and vapor flow across the thickness to find the local liquid saturation and liquid/vapor pressures. The input heat flux at which the liquid saturation at the center of the evaporator falls to zero is defined as the dryout limit. The model is calibrated against a wide variety of experimental data on dryout heat flux and thermal resistance collected from the literature, on sintered particles, screen mesh and micropillar structures. For the thermal resistance prediction, the calibrated values of film thickness ratios are found to depend on the specific wick structure, a structure specific calibration with an accuracy of ± 25% is obtained. For the dryout heat flux prediction, the model is universally calibrated to a wide variety of porous evaporators, using a single saturation exponent value of $n = 4$ with a mean absolute percentage error of 29%. The model captures the overall trends in particle/pore size, evaporator wick thickness and heater size.

This new capillary-fed boiling model is implemented into a vapor chamber transport model for dryout limit and thermal performance prediction. The heat transfer model formulation considers 3D conduction in the solid wall and couples it iteratively to the analytical vapor chamber model using an average heat transfer coefficient between the wall–evaporator wick interface. A wall superheat threshold criterion is used to find the region of the wick undergoing boiling. A numerical finite-volume based approach is used to separately solve for the pressure fields with a quarter geometry of the evaporator wick. This modeling framework can be used for thermal performance prediction of high-heat-flux vapor chambers used as embedded heat spreaders in air-cooled heat sinks.

1.4 Organization of the Document

Chapter 1 contained the background information for boiling in vapor chambers. It also presented the objectives and major contributions from this work. Chapter 2 covers a review of the literature on the design of porous wicks for usage in high-heat-flux vapor chambers, fabrication and characterization of hybrid wick structures for high-heat-flux dissipation, and the current limitations in this field. Chapter 3 proposes the design of a novel evaporator wick structure for area-scalable high heat flux dissipation and develops a reduced-order model to predict the performance of the new design in comparison to conventional wick designs. Chapter 4 provides details regarding the fabrication and experimental characterization of the new design in comparison to conventional single-layer wick designs. Chapter 5 demonstrates the usage of the new wick design to dissipate very high heat fluxes of ~ 500 W/cm^2 at a low value of thermal resistance. Chapter 6 studies the parametric effects of vapor venting and liquid feeding areas on the dryout limit of two-layer wick. Chapter 7 presents the semi-empirical model for dryout and thermal resistance prediction in capillary-fed porous media. Chapter 8 introduces the development of the vapor chamber boiling model. Chapter 9 concludes with a summary and proposes avenues for future work in this field.

2. LITERATURE REVIEW

2.1 Design Rationale of Hybrid Evaporator Wick Structures

Homogeneous wicks impose an intrinsic tradeoff between the maximum supported heat flux and thermal resistance during boiling. A number of efforts to fabricate and characterize heterogeneous or hybrid evaporator wick designs have aimed to enhance boiling heat transfer during high heat flux operation, compared to homogeneous wicks. Such heterogeneous wicks may include patterned features to ease vapor removal and provide dedicated liquid-feeding pathways to prevent dryout during capillary-fed boiling operation. Mughal and Plumb [3] concluded that providing a high-permeability pathway for vapor flow, by cutting channels in the evaporator wick, doubled the dryout heat flux. Ju *et al*. [13] developed wick structures that used lateral or columnar wick arteries to supply liquid to a thin wicking layer; these wicks were able to dissipate ~350 W/cm^2 input over a 1 cm^2 evaporator area. Weibel *et al.* [14] evaluated grid-patterned sintered wicks that provided vapor removal pathways during boiling, reducing the evaporator surface superheat by 30% compared to uniform sintered wick layers. Zhao and Chen [15] tested a micro-grooved sintered powder wick that improved the dryout heat flux over a uniform wick by 300%. These studies have demonstrated that providing separate liquid flow and vapor extraction pathways can improve the performance of an evaporator wick operating at high heat fluxes.

Ryu *et al.* [16] used metal foam layers to supply liquid to a thin micro-post wick to achieve high dryout heat fluxes greater than 400 W/cm^2. The high capillary pressure of the micro-post layer helped sustain liquid menisci, while the high-permeability metal foam provided auxiliary liquid supply. Weisenseel *et al.* [17] employed silicon carbide wicks with horizontal vapor removal channels to reduce thermal resistance at the evaporator of loop heat pipes. In addition, lateral or columnar arteries that supply a thin layer of wick [13] as well as grid-patterned wicks [14,18] have all been shown to increase the dryout heat flux while reducing the surface superheat during capillary-fed boiling, as compared to homogeneous wicks. Weibel and Garimella [19] have provided a review of the recent state-of-the-art in the design and characterization of evaporator wicks and vapor chambers.

2.2 Recent Developments and Limitations in Capillary-fed Boiling

Recent developments related to porous evaporator wicks for capillary-fed boiling, all using water as the working fluid, are summarized in Table 2.1. This table chronologically catalogs the evaporator wick types, saturation temperature during testing, heater size, maximum heat flux, maximum total power dissipation, and the superheat and thermal resistance at the maximum power dissipation. Sintered copper porous wicks are most commonly used for capillary-fed boiling due to their high conductivity and because they offer many parallel fluid flow paths for liquid replenishment during boiling. Weibel *et al*. [5] studied evaporation and boiling behaviors from sintered monoporous copper wicks and reported heat flux dissipation greater than 500 W/cm^2. To improve on the thermal performance of monoporous wicks, different surface nanostructuring techniques and chemical modifications have been evaluated in the literature. In the case of copper wicks, growing copper oxide (CuO) nanostructures improves the wettability of the wick [20,21]. In addition to increasing the capillary performance, the roughness of the CuO nanostructures has been shown to provide increased nucleation site densities, which enhances the heat transfer coefficients during boiling. Nam *et al.* [20] showed that nanostructuring copper micro-post wicks enhances the dryout heat flux by 70% compared to bare copper micro-posts, reporting dryout heat fluxes as high as ~800 W/cm^2. Nevertheless, monoporous wicks have one characteristic pore size, which can be tuned to either provide a high capillary pressure or high permeability, but not a combination of both. Biporous wicks overcome this limitation, where the larger pores offer a high permeability for better liquid feeding, while the smaller pores can sustain liquid menisci for capillary feeding during high-heat-flux operation. Biporous wicks composed of patterned carbon nanotube (CNT) forests were investigated by Cai and Chen [72] and shown to dissipate extreme heat fluxes of ~900 W/cm^2; Semenic and Catton [7] used sintered copper biporous wicks to dissipate 990 W/cm^2.

While extremely high heat fluxes have been passively dissipated by capillary-fed boiling, Table 2.1 reveals that these fluxes are either limited to small hotspots (typically less than a few mm^2 and ~10s of W total power) or are attained at a very large surface superheat above the saturation temperature. Multiple studies have clearly demonstrated that there is a very strong inverse relationship between the heat input area and the dryout heat flux that can be supported by capillary-fed boiling. For example, Coso and Srinivasan [11] observed (for their biporous silicon pin fin wicks) that the maximum heat flux decreased from 733 W/cm^2 to 277 W/cm^2 when the heat input area was increased from 6.25 mm^2 (2.5 mm × 2.5 mm) to 100 mm^2 (10 mm × 10 mm). This effect can be primarily attributed to the increased fluid flow length to feed liquid to the center of the larger heated areas. Very thick wicks, on the other hand, can sustain high heat fluxes over somewhat larger areas, but the added impedance, posed by the longer vapor travel paths from the substrate through the thicker wick, induce a high surface superheat in this case. For example, the 990 W/cm^2 of heat flux dissipated using sintered copper biporous wicks over 32 mm^2 [7] was attained at a surface superheat of ~150 K.

Effective fluid delivery throughout the evaporator region and efficient vapor removal from the wick are both necessary to enhance the dryout limits of porous wicks over larger evaporator areas (~1 cm^2). A few different hybrid sintered evaporator wick designs have been proposed to achieve this goal. Dai *et al*. [22] used a combination of sintered screen mesh and rectangular microchannels for the evaporator wick; the microchannels provide high-permeability pathways for liquid feeding, while the smaller pores in the screen mesh provide a high capillary pressure. These wicks demonstrated 150 W/cm^2 dissipated over an area of 1 cm^2. Hwang *et al*. [23] fabricated and tested a sintered copper evaporator wick with lateral converging arteries that feed a thin layer of sintered particles within the heated area. The arteries provide liquid feeding while the small thickness of the sintered layer keeps its thermal resistance to a minimum. Heat fluxes of ~580 W/cm^2 were dissipated over a 1 cm^2 heater area, albeit at a high superheat of ~72 K. The high superheat was attributed to local dryout occurring in the center of the heated area.

2.3 Liquid-Feeding Methods for Experimental Characterization of Wick Structures

Vapor chambers are devices that maintain saturated working conditions; non-condensable gases are purged before charging the porous wick with the working fluid. Hence, to experimentally characterize the dryout heat flux and thermal resistance of standalone wick structures, they are typically sealed in a test chamber and the working fluid is thoroughly degassed to remove any non-condensable gases. The porous wick must not be submerged in the working fluid, and should draw liquid uniformly in all directions, to replicate the feeding conditions inside a vapor chamber. Flooding of the wick can cause a drastic difference in the test conditions and the maximum heat flux sustained by the porous wick. The mechanism of capillary-fed boiling is different from pool boiling, where the heated surface is submerged by the working fluid.

Hence, several studies in the literature [5, 24, 72] have tested evaporator wicks by orienting them vertically and submerging the lower edge into a liquid bath, thus avoiding any flooding over the evaporator area located above the surface of the bath. This method can provide uniform liquid feeding to small evaporator areas (a few mm^2 in size) if they are located far above the liquid bath; however, the height of the evaporator region above the liquid level should be kept small to avoid incurring a large gravitational pressure drop that governs the behavior. In general, these studies note that the height of the evaporator above the liquid level can influence the phase change process and dryout heat flux. Alternatively, several studies [6,25] have characterized horizontally oriented evaporator wicks placed flush with the surface of a liquid bath; in this configuration it is difficult to maintain the liquid level to be even with the height of the thin wicks. For example, Li and Peterson [6] tested sintered screen mesh wicks that were placed horizontally at the surface of a saturated liquid bath and reported that flooding could have occurred in their thinnest wicks (0.2 mm thick). To overcome the difficulty in maintaining the liquid level while taking advantage of horizontal liquid feeding, evaporator wicks have also been tested by placing them on raised pedestals, using a collar wick on the sidewalls of the pedestal for feeding from the bath below [7, 26]. While this approach does not require precise control of the liquid level, it requires a more complicated sample fixture and must account for potential evaporation/boiling from the exposed pedestal sidewalls.

2.4 Surface Treatments to Maintain Wettability of Copper Wicks

Sintered copper wicks, although intrinsically hydrophilic, can become nonwetting on prolonged exposure to air. Shirazy *et al.* [27] studied the effect of different atmospheres (room air, dry air, nitrogen) on the wettability transition (from hydrophilic to hydrophobic) in copper foams. By studying the surface chemistry of the foams using X-ray spectroscopy, they concluded that adsorption of volatile organic compounds (VOCs) in air is the primary reason for the wettability transition. Any degradation in the wettability can drastically affect the maximum heat flux that can be dissipated when a wick operates under capillary action, as shown by Wong and Lin [28]. Previous studies that tested copper wicks typically used chemical or thermal functionalization techniques to grow a stable wetting copper oxide prior to testing. Nam *et al.* [29] used an alkali solution, composed of $NaClO_2$, $NaOH$, $Na_3PO_4 \cdot 12H_2O$, to oxidize their copper micropost samples and form copper (II) oxide. Hwang *et al.* [23] saturated their copper wicks with water and heated to 150 C to dry it. The saturation-drying process is repeated twelve times for thermal oxidation of the samples. In contrast, acid treatment of copper wicks can be used to strip any surface oxidation and reduce the samples to pure copper. Weibel *et al.* [5] and Iverson and Garimella [30] used dilute piranha (mixture of H_2SO_4 and H_2O_2) for reducing their wicks to pure copper before testing.

2.5 Models for Two-Phase Flow in Heated Porous Media

Analytical and empirical models are available for the prediction of critical heat flux (CHF) in pool boiling from porous coated surfaces that are submerged in the working fluid. Liter and Kaviany [31] modeled CHF in saturated pool boiling considering the liquid/vapor counter-current flow hydrodynamics within the porous structure. The length scale of locations for vapor to escape from the surface into the liquid pool was predicted to affect the CHF. The authors therefore concluded that modulating the geometry of the porous coating to alter the length scale of vapor-escape locations can significantly improve CHF compared to pool boiling over plain surfaces. Webb [32] and Rao and Balakrishnan [33] also developed simplified analytical models for pool boiling from porous coated surfaces. Other works (e.g., Chang and You [34]) have experimentally studied the effect of particle size in pool boiling over microporous diamond surfaces and developed an empirical correlation for the CHF as a function of mean particle diameter by fitting to data.

Critical heat flux (CHF) models for pool boiling from submerged porous-coated surfaces are not directly applicable to the prediction of dryout during capillary-fed boiling in porous evaporators. In pool boiling, models posit that CHF is governed by stability of the liquid-vapor counterflow (e.g., Zuber’s limit [35]), in addition to viscous drag resistance imposed by the solid matrix on the liquid-vapor counterflow [31]. In contrast, the liquid flow in capillary-fed evaporators occurs laterally into the heated region, with a limit that is governed by the liquid flow pressure drop from the edge of the evaporator (from where liquid is fed) to the center. Consequently, the heater size, and thus the capillary-feeding length, more dramatically affect the dryout heat flux during capillary-fed boiling [36] than in pool boiling [31].

The maximum heat flux sustained by a thick bed of liquid-saturated porous particles (heated on one end) was modeled by Udell [37] and Bau and Torrance [38]. Considering one-dimensional, steady, two-phase counter-current flow in the bed, these models assumed three separate zones for heat transfer: namely, a vapor zone closest to the heated end, an intermediate two-phase zone, and then a saturated liquid zone, as shown schematically in Figure 2.1.

Temperature gradients were neglected within the two-phase zone (isothermal zone) and the flow of liquid and vapor phases were governed by Darcy's law. While heated from below, downward liquid flow through the bed is driven by capillary action and gravity, while upward vapor flow is driven by buoyancy forces. The local liquid saturation (the fraction of porous volume filled with liquid) is minimum at the bottom of the two-phase zone and increases monotonically along the thickness of the bed (see Figure 2.1 (a)). The saturation profiles exhibit step changes on either end of the two-phase zone (minimum value is higher than zero due to an irreducible saturation, as described by Udell [37]). Counter-current flow models [37,38] are used extensively in applications involving two-phase flows in heated particulate beds to find the length of the two-phase zone and the critical (maximum) heat flux sustained by the bed.

Tung and Dhir [39] developed analytical pressure drop models for two-phase flow (both co-current and counter-current) in porous media. All of these models [37-39] utilize relative permeability (i.e., the permeability of each phase within the porous media in the presence of the other phase), typically modeled as a function of the local liquid saturation. The widely used correlations for relative permeability (most commonly taking the form $K_l = s^n$) are tabulated by Scheidegger [40] and Kaviany [41].

2.6 Models for Vapor Chamber Transport

This section provides a brief review of some of the types of models employed in the literature to describe vapor chamber transport, typically achieving a compromise between computational cost/expense and fidelity. Various works in the past have utilized high fidelity modeling of vapor chambers using finite volume-based approaches to simulate the mass, momentum, and thermal transport within the device [42–44], but they can become computationally expensive and hard to track. Lower cost models for vapor chambers are available in the literature; for example, 1D resistance network-based modeling described in Ref. [45] and [46] but such simplified models may not be applicable to cases where dimensionality is important (for a generalized three-dimensional geometry and boundary conditions). Aghvami and Faghri [47] and Lefevre and Lallemand [48] developed analytical models to evaluate the 3D steady state temperature fields. Recently, Patankar *et al.* [49] developed a low-cost analytical model for transient vapor chamber transport, applicable for any arbitrarily placed, localized transient heat sources.

However, despite the widespread observance of nucleate boiling in vapor chambers as described in, all past modeling efforts cited here typically only consider the single-phase transport of liquid through a fully saturated porous media (on the evaporator and condenser side) and do not account for boiling in the wick. Ranjan *et al.* [43] developed an empirical framework to incorporate the effect of boiling in a vapor chamber; they used a temperature threshold to distinguish a 'boiling region' of the wick and modeled this region with a higher effective thermal conductivity (obtained empirically) compared to the surrounding evaporative region.

2.7 Air-Cooled Heat Sinks with Embedded Vapor Chambers

In the literature, experimental characterization of air-cooled heat sinks with embedded vapor chambers has been studied and compared to solid heat spreaders. Table 2.2 lists a brief summary of the air flow boundary (air temperature, velocity), heat sink height, vapor chamber dimensions and the range of powers that have been experimentally achieved. Li *et al.* [52] characterized the thermal resistance of the heat sink with a vapor chamber and compared its performance to an architecture without a vapor chamber. They also studied the effect of fin dimensions and air flow Reynolds number on the thermal performance. Peng *et al.* [55] studied the effect of air flow rate and working fluid (of the vapor chamber). These studies [51,52,55] used wind tunnels to provide a known velocity/Reynolds number of air flow to the heat sink. Chang *et al.* [53] studied the effect of heater size (5 mm × 5 mm, 10 mm × 10 mm) on the behavior of a vapor chamber attached to a fan cooled heat exchanger. They also used uniform background and hotspot heating (to simulate the boundary conditions in the dies of silicon microprocessor packages) and studied its effect on the behavior of the vapor chamber. However, the references in Table 2.2 have typically tested heat inputs less than 100 W/cm^2, and have not reported the occurrence of boiling within the vapor chamber.

Table 2.1. Recent developments in capillary-fed evaporation/boiling on evaporator wicks for high-heat-flux dissipation. All of the studies included use water as the working fluid. The superheat and thermal resistance correspond to the values as measured at the maximum heat flux/power.

Reference		Evaporator Wick Type	Saturation Temp. (°C)	Heater Size* (mm^2)	Maximum Heat Flux (W/cm^2)	Maximum Power (W)	Superheat (K)	Thermal Resistance (K/W)
Semenic and Catton [7]	2009	Biporous sintered copper particles	40	32 (circular)	990	317	147	0.46
Weibel *et al.* [5]	2010	Sintered copper particles	100	25	596	149	26	0.17
Hwang *et al.* [23]	2011	Lateral converging arteries supplying a monolayer of sintered copper particles	43	100	580	580	72	0.12
Nam *et al.* [20]	2011	Nanostructured copper microposts	44	25	160	40.0	32	0.80
				4	800	32.0	35	1.1
Cai and Chen [72]	2011	Biporous carbon nanotube pillars	100	100	190	190	90	0.47
				4	938	37.5	94	2.5
Weibel *et al.* [18]	2012	Grid-patterned sintered copper particles	100	25	580	145	17	0.12
Coso and Srinivasan [11]	2012	Biporous silicon pin fins	100	100	277	277	14	0.051
				6.25	733	45.8	7	0.15
Cai and Bhunia [10]	2012	Biporous carbon nanotube pillars/stripes	100	4	770	30.8	35	1.1
				100	140	140	25	0.18
Dai *et al.* [22]	2013	Copper screen mesh sintered on microchannels	100	100	153	153	17	0.11
Palko *et al.* [12]	2015	Copper inverse opals	100	0.6 (0.3 mm × 2 mm)	1250	7.5	10	1.3
Ryu *et al.* [16]	2017	Copper metal foam supplying a copper micro-post layer	30	16	429	68.6	79	1.2
Lv and Li [50]	2017	Sintered copper mesh	-	10 (5 mm × 2 mm)	490	49	-	1.1

Table 2.2. Example of experimental characterization of air-cooled heat sinks with embedded vapor chambers

Reference	**Air Flow Boundary**	**Heat Sink Height, t_{fin} (mm)**	**Vapor chamber dimensions (mm×mm×mm)**	**Range of powers, Q (W)**	**Heater size, (mm×mm)**
Koito et al. [51]	T_{air}= 20-30 C V_{air}= 1.5 m/s		76.2 × 88.9 × 4.6	16-32	24.5 × 24.5
Li et al. [52]	Re = 10000-60000	10-30	87.6 × 92 × 4	~ 30	
Chang et al. [53]	T_{air} = 45 C		130 × 20 × 3.3	30-70	5 × 5, 10 × 10
Wong et al. [54]	T_{air} = 25-30 C	35	100 × 80 × H	40-220	11 × 11
Peng et al. [55]	T_{air}= 15 C V_{air}= 4.5 m/s	60	80 × 75 × 15	0-100	Diameter: 30 mm
Prasher [56]	-		89 × 30 × 3	30	10 × 10

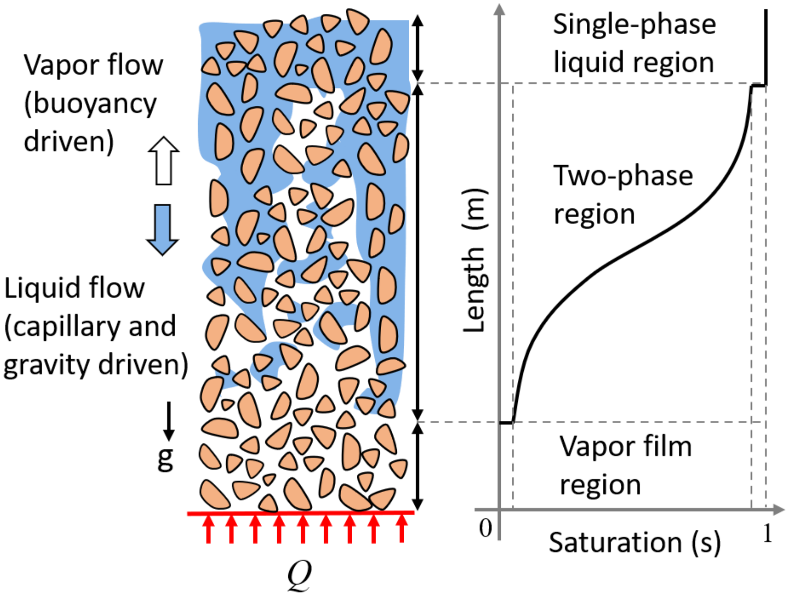
Vapor flow
(buoyancy
driven)
Liquid flow
(capillary and
gravity driven)
g
Q
Single-phase
liquid region
Two-phase
region
Vapor film
region
Length (m)
0
Saturation (s)
1

Figure 2.1. (a) The two-phase flow configuration (liquid-vapor counterflow) and the associated saturation profiles in a packed bed of porous particles heated from below, as described by Udell [37] and Bau and Torrance [38].

3. DESIGN OF AN AREA-SCALABLE TWO-LAYER EVAPORATOR WICK FOR HIGH-HEAT-FLUX VAPOR CHAMBERS

This chapter proposes and designs the two-layer evaporator wick. A reduced-order model is developed to predict the performance of a vapor chamber incorporating this structure in the evaporator. The reduced-order model is validated against a higher-fidelity numerical model, and used to obtain parametric trends in the wick pressure drop and evaporator thermal resistance. The material in this chapter was published in *IEEE Transactions on Components, Packaging and Manufacturing Technology (CPMT)* [57].

3.1 Two-layer Evaporator Wick Concept

Figure 3.1 (a) shows a three-dimensional drawing of the proposed two-layer wick structure, as well as a cross-sectional schematic diagram of this two-layer structure incorporated as the evaporator inside a vapor chamber heat spreader. The condensed working fluid returns to the evaporator section from the periphery of the vapor chamber through a conventional bulk wick (thickness t_{bulk}). Liquid is routed from the bulk wick surrounding the evaporator section into a relatively thick wick cap layer (thickness t_{cap}) into an array of vertical liquid-feeding posts (diameter d_{post}). These posts uniformly distribute the liquid to a thin base wick (thickness t_{base}). Vapor generated by capillary-fed boiling in the base wick escapes through gaps between the posts (spacing S) and on through vapor vents in the cap wick layer (diameter d_{vent}) into the vapor core.
Although thinner wicks provide lower thermal resistance during capillary-fed boiling compared to thicker wicks, they cannot sustain liquid resupply at high heat fluxes. In order to leverage the low thermal resistance offered by a thin evaporator wick, the two-layer structure uses the thick layer as a means to adequately feed liquid from the top. Alternative strategies have explored *lateral* feeding using wedge-shaped wick geometries [58] and converging arteries [23] that supply liquid within a central evaporator. However, the liquid-feeding structures in these approaches occupy a part of the base area, inherently reducing the available evaporator area for the phase change process. The proposed top-down feeding approach decouples the liquid-feeding structure (*i.e.*, the wick cap layer) from the capillary-fed boiling region in the evaporator; the complete evaporator footprint area is made available to the wick cap layer for capillary supply. Prior top-down feeding

approaches [59] consisted of vertical posts covered by a uniform porous wick, directly connected from the condenser side to the evaporator. These long arteries spanning the entire thickness of a vapor chamber incur an increased pressure drop that negates any improvement over lateral feeding [59]. Regardless of the vapor chamber design, the two-layer evaporator structure allows for different designs of the thickness and length of the liquid-feeding posts.

Under steady operation of a vapor chamber, the vapor core is at saturated condition, and the local vapor pressure and temperature are related via the saturation curve. There can be a large pressure gradient in the vapor exiting a wick through tortuous pathways during capillary-fed boiling, resulting in a high evaporator temperature. High-permeability vapor venting with grooved-wick [58] and patterned-wick [18] structures has been shown to decrease the surface superheat significantly and extend the dryout heat flux. The vapor vents in the proposed two-layer evaporator wick structure provide a relatively unimpeded pathway for vapor to exit through the cap wick layer via the gaps between the liquid-feeding posts.

3.2 Reduced-order Model of Two-Layer Wick

A reduced-order model is developed to estimate the internal pressure drops and thermal resistances in a vapor chamber incorporating the two-layer evaporator wick design. This model is used to find the overall thermal resistance of the vapor chamber and to predict if the capillary pressure of the porous wick structure is sufficient to maintain operation at a given heat flux for various two-layer wick designs.

A schematic diagram showing the predominant pressure drops and thermal resistances considered in the model is shown in Figure 3.1 (b) and (c), respectively. The diagrams show one half of the geometry of a square vapor chamber, with evaporator and condenser square edge lengths l_{evap} and l_{cond}, respectively. A constant heat input Q at the evaporator is rejected from the condenser side of the vapor chamber. There is a viscous liquid-phase pressure drop in the bulk wick structure from the periphery to the evaporator ($\Delta P_{l,bulk}$), along the cap wick layer ($\Delta P_{l,cap}$), through the liquid-feeding posts ($\Delta P_{l,post}$), and to the furthest extent in the thin base wick layer ($\Delta P_{l,base}$). Vapor flow incurs a pressure drop as it passes through the space between the posts ($\Delta P_{v,space}$), across the vapor vents ($\Delta P_{v,vent}$), and outward in the vapor core ($\Delta P_{v,core}$). The pressure drop for the wick along the side wall of the vapor chamber is assumed to be negligible compared to the bulk liquid pressure due to the small thickness of the vapor chamber relative to the lateral dimensions. The evaporator temperature rise above saturation is governed by conduction resistances across the evaporator and condenser walls (R_{wall}) and condenser-side wick ($R_{wick,cond}$), the capillary-fed boiling resistance in the base wick (R_{boil}), and the thermal resistance associated with the total differential in the saturation pressure of the vapor (R_{sat}). Note that the conduction resistance through the wick on the evaporator side is effectively bypassed during boiling because nucleation occurs from the substrate-wick interface. Moreover, the condensation resistance across the liquid-vapor interface (on the condenser side) is assumed to be negligible compared to the conduction resistances [60]. The model assumes that the porous wick is composed of sintered particles of mean diameter d_{part}; the effective pore radius is taken as $r_{pore} = 0.21\ d_{part}$ [1]. The capillary pressure of the wick is calculated directly from the pore radius, assuming a highly wetting fluid, as

$$P_c = \frac{2\sigma}{r_{pore}} \tag{3.1}$$

For a wick porosity of ϕ, the liquid permeability is calculated as [1]

$$K = \frac{d_{part}{}^2 \phi^3}{150\left(1-\phi\right)^2} \tag{3.2}$$

To simplify the problem, the rectangular vapor chamber is modeled as a cylindrical disk, with effective evaporator (r_{evap}) and condenser (r_{cond}) radii calculated such that the footprint area is equivalent to the square edge lengths l_{evap} and l_{cond}.

3.2.1 Fluid Pressure Drops

The liquid-phase pressure drops are calculated using the one-dimensional governing momentum equation for radial flow in porous media given by

$$\frac{1}{\phi^2}\left(u_l \frac{\partial u_l}{\partial r}\right) = -\frac{1}{\rho_l}\frac{\partial P}{\partial r} - \frac{\nu_l u_l}{K} + \frac{\nu_l}{\phi}\left[\frac{1}{r}\frac{\partial}{\partial r}\left(r\frac{\partial u_l}{\partial r}\right) - \frac{u_l}{r^2}\right] \tag{3.3}$$

where u_l is the liquid flow velocity in the radial direction. A total mass flow rate is calculated from the heat input,

$$\dot{m}_{total} = Q/h_{fg} \tag{3.4}$$

To calculate the bulk liquid pressure drop ($\Delta P_{l,bulk}$), a bulk velocity is calculated from the total mass flow rate as

$$u_{l,bulk}\left(r\right)=\dot{m}_{total}/\left(\rho_l 2\pi r t_{bulk}\right) \tag{3.5}$$

Integrating equation (3.3) from the condenser radius to the evaporator radius gives the value of the pressure drop as

$$\Delta P_{l,bulk}=\frac{-\rho_l {c_1}^2}{2\phi^2}\left(\frac{1}{{r_{evap}}^2}-\frac{1}{{r_{cond}}^2}\right)+\frac{\mu_l c_1}{K}\ln\left(\frac{r_{cond}}{r_{evap}}\right);$$

$$c_1=\frac{\dot{m}_{total}}{2\pi\rho_l t_{bulk}} \tag{3.6}$$

Liquid pressure drop along the cap layer is calculated assuming a uniform extraction of liquid from the cap underside area to the posts below. The mass flow rate of liquid in the cap layer is thereby a function of radial position and decreases from $\dot{m}_{total}$ at the evaporator periphery (r_{evap}) to zero at the center:

$$\dot{m}_{l,cap}\left(r\right)=\dot{m}_{total}\left(r^2/r^2{}_{evap}\right) \tag{3.7}$$

A cap-layer liquid flow velocity is calculated as

$$u_{l,cap}\left(r\right)=\dot{m}_{l,cap}/\left(\rho_l 2\pi r t_{cap,eff}\right) \tag{3.8}$$

where, to account for the reduced area available for flow due to the vapor vents, a reduced effective thickness of the cap layer $t_{cap,eff}$ is calculated based on the equivalent porous volume of the cap layer. Integrating equation (3.3) from $r = r_{evap}$ to $r = 0$, the cap-layer pressure drop is,

$$\Delta P_{l,cap}=\rho_l\left[\frac{{c_2}^2}{\phi^2}+\frac{\nu_l c_2}{K}\right]\frac{{r_{evap}}^2}{2};\; c_2=\frac{\dot{m}_{total}}{2\pi\rho_l {r_{evap}}^2\, t_{cap,eff}} \tag{3.9}$$

Liquid pressure drop through each liquid-feeding post is calculated assuming uniform axial flow in a cylindrical porous medium:

$$\Delta P_{l,post}=\frac{\nu_l \dot{m}_{post}}{\pi {r_{post}}^2 K}t_{post} \tag{3.10}$$

where t_{post} is the post height. The total mass flow rate is divided equally through all posts, *i.e.*, $\dot{m}_{post} = \dot{m}_{total}/N_{post}$, where N_{post} is the number of posts.

For calculation of the liquid pressure drop through the base wick layer ($\Delta P_{l,base}$), a unit cell around each post in the evaporator footprint area is considered. Figure 3.2 (a) shows a plan view of the two-layer wick evaporator footprint area; a square unit cell geometry around a post is outlined. This square unit cell is approximated as an axisymmetric radial geometry (Figure 3.2 (b-c)) centered at the post (r_{post}) and extended outward to an effective radius ($r_{eff,post}$). The value of this effective radius is calculated by equating the circular and square areas,

$$\pi r_{eff,post}^{2} = \frac{l_{evap}^{2}}{N_{post}} \tag{3.11}$$

The base layer liquid pressure drop is calculated considering radially outward flow from the center of each post to the effective radius ($r_{eff,post}$) where the liquid evaporates completely. It is assumed that capillary-fed boiling only occurs in the footprint area *not* covered by the posts, *i.e.*, the heat flux becomes

$$q = \frac{Q}{\pi\left(r_{evap}^{2} - N_{post} r_{post}^{2}\right)} \tag{3.12}$$

The mass flow rate of liquid flowing radially outward in the base wick increases from $r = 0$ up to the post radius ($r = r_{post}$) as liquid is fed from the post uniformly and decreases outside the post radius due to vaporization until complete evaporation at $r = r_{eff,post}$:

$$\dot{m}_{l,base}\left(r\right) = \begin{cases} \dot{m}_{post}\left[\dfrac{r^{2}}{r_{post}^{2}}\right] & 0 \le r \le r_{post} \\ \dot{m}_{post}\left[\dfrac{r_{eff,post}^{2} - r^{2}}{r_{eff,post}^{2} - r_{post}^{2}}\right] & r_{post} \le r \le r_{eff,post} \end{cases} \tag{3.13}$$

Equation (3.3) is integrated from $r = 0$ to $r = r_{eff,post}$ with an associated liquid flow velocity, $u_{l,base} = \dot{m}_{l,base}/(2\pi\rho_l r t_{base})$, to give

$$\Delta P_{l,base} = \left(\frac{\rho_l c_3^{2}}{\phi^{2}} + \frac{\mu_l c_3}{K}\right)\frac{r_{post}^{2}}{2} + \\ \frac{\mu_l c_4}{K_{eff}}\left(\ln\left(\frac{r_{eff,post}}{r_{post}}\right) - \frac{r_{eff,post}^{2} - r_{post}^{2}}{2 r_{eff,post}^{2}}\right) + \\ \frac{\rho_l c_4^{2}}{\phi_{eff}^{2}}\left(\frac{1}{r_{eff,post}^{2}} - \frac{1}{2 r_{post}^{2}} - \frac{r_{post}^{2}}{2 r_{eff,post}^{4}}\right)$$

where,

$$c_3 = \frac{\dot{m}_{post}}{2\pi\rho_l t_{base}\, r_{post}^{2}};\ c_4 = \frac{\dot{m}_{post}}{2\pi\rho_l t_{base}\left(1 - r_{post}^{2}/r_{eff,post}^{2}\right)} \tag{3.14}$$

In the above equation, values for the effective porosity ϕ_{eff} and effective permeability K_{eff} are altered accounting for a reduced area available for liquid flow due to vapor formation in the wick. This change is confined to the region where boiling occurs, *i.e.*, from $r = r_{post}$ to $r = r_{eff,post}$. To calculate the area reduction during boiling, the wick is assumed to be composed of spherical particles in a cubic packing. Following Ref. [61], pseudo-vapor columns are assumed to be sustained in pore spaces during capillary-fed boiling, and the porous structure is represented as a series of vapor columns in between an extended surface of copper particles. Based on the expressions for the dimensions of these vapor columns, the area reduction for liquid flow is found based on the geometry of the cubic-packed spheres. This area reduction is equated to a porosity reduction and a new value of porosity ϕ_{eff} is found. The reduced permeability K_{eff} is found using equation (3.2) with this new porosity value.

Depending on the specific geometry chosen for the two-layer wick structure, vapor flow through the spaces between the posts is better represented using either one-dimensional upward flow (if the posts are relatively long and closely spaced) or radial flow (if the posts are relatively short and widely spaced). The current model calculates both one-dimensional approximations and the highest value is taken as a conservative estimate of this pressure drop ($\Delta P_{v,space}$). For both cases, vapor is assumed to be formed directly above the base wick, where boiling occurs, in a region from $r = r_{vent}$ to $r = r_{eff,vent}$ within a unit cell around each vent, as shown in Figure 3.2 (d-e). Because the number of vents is smaller than the number of liquid-feeding posts, the mass flow rate of vapor in a vent unit cell is calculated as $\dot{m}_v = \dot{m}_{post}\,(N_{post}/N_{vent})$. For the upward flow case, the vapor flows upward in the cylindrical area of radius $r_{eff,vent}$; a Hagen-Poiseuille velocity profile and a corresponding pressure drop are calculated. For the radial flow case, vapor is assumed to flow radially inward from $r = r_{eff,vent}$ to $r = r_{vent}$, where it escapes into the vents above. (see the side view of the vapor vent unit cell in Figure 3.2 (e)). In the radial flow case, the mass flow rate is a function of the radial position as vapor mass is being accumulated during the inward flow over the boiling area; the mass flow rate increases from a value of zero at $r=r_{eff,vent}$ to $\dot{m}_v$ at $r=r_{vent}$,

$$\dot{m}_{v,space}\left(r\right)=\dot{m}_v\left[\frac{r_{eff,vent}{}^2-r^2}{r_{eff,vent}{}^2-r_{vent}{}^2}\right] \tag{3.15}$$

The corresponding pressure drop is calculated by integrating the one-dimensional governing momentum equation for radial flow given by

$$u_v \frac{\partial u_v}{\partial r} = -\frac{1}{\rho_v}\frac{\partial P}{\partial r} + \nu_v \left[\frac{\partial}{\partial r}\left(\frac{1}{r}\frac{\partial\left(r u_v\right)}{\partial r}\right)\right] \tag{3.16}$$

where $u_v = \dot{m}_{v,space}(r)/(2\pi\rho_v r t_{post})$ is the vapor flow velocity in the radial direction, to obtain

$$\Delta P_{v,space} = \begin{cases} \dfrac{8\nu_v \dot{m}_v}{\pi\left(r_{eff,vent}\right)^4} t_{post} & \text{if upward flow} \\ \rho_v \left[\begin{matrix}\dfrac{1}{r_{vent}^2} - \dfrac{1}{r_{eff,vent}^2} + \\ \dfrac{r_{vent}^2 - r_{eff,vent}^2}{\left(r_{eff,vent}\right)^4}\end{matrix}\right]\dfrac{c_5^2}{2} & \text{if radial flow} \end{cases}$$

where,

$$c_5 = \frac{\dot{m}_v}{2\pi\rho_v t_{post}\left(1 - \dfrac{r_{vent}^2}{r_{eff,vent}^2}\right)} \tag{3.17}$$

Minor losses are included to account for the sudden contraction into the vapor vents from the space below, based on an empirical correlation for abrupt contractions in cylindrical pipes [62],

$$\Delta P_{v,contraction} = \left[1 - \left(\frac{r_{vent}}{r_{eff,vent}}\right)^4 + K_m\right]\frac{1}{2}\rho_v v_{vent}^2$$

where

$$K_m = \begin{cases} 1.2 + \dfrac{38}{\mathrm{Re}_{vent}} & \mathrm{Re}_{vent} < 2000 \\ \dfrac{1}{2}\left(1 - \dfrac{r_{vent}}{r_{eff,vent}}\right)^2 & \mathrm{Re}_{vent} > 2000 \end{cases} \tag{3.18}$$

where K_m is the minor loss coefficient, which depends on the Reynolds number of flow through the vent, $\mathrm{Re}_{vent} = 2\rho_v v_{vent} r_{vent}/\mu_v$. Pressure drop through the cylindrical vapor vents is calculated using a Hagen-Poiseuille flow approximation, with a fully developed friction factor used based on the flow Reynolds number [62],

$$\Delta P_{v,vent} = \left[\frac{f\,t_{cap}}{2r_{vent}}\right]\frac{1}{2}\rho_v v_{vent}^{\;2}$$

where

$$f = \begin{cases} \dfrac{64}{\mathrm{Re}_{vent}} & \mathrm{Re}_{vent} < 2000 \\ \left[1.14 - 2\log\left(\dfrac{21.25}{\mathrm{Re}_{vent}^{\;0.9}}\right)\right]^{-2} & \mathrm{Re}_{vent} > 2000 \end{cases} \tag{3.19}$$

The minor losses due to the expansion from the vapor vents to the vapor core, estimated assuming flow through an abrupt expansion in cylindrical pipes, are negligible for the area ratios considered in this study.

The viscous vapor flow through the vapor core is assumed to incur a negligible pressure drop, due to the comparatively large cross-sectional area and expanding radius of the vapor core in the flow direction. The sum of liquid and vapor pressure drops gives the total pressure drop in the vapor chamber,

$$\begin{gathered} \Delta P_{total} = \Delta P_{l,bulk} + \Delta P_{l,cap} + \Delta P_{l,post} + \Delta P_{l,base} + \\ \Delta P_{v,space} + \Delta P_{v,vent} + \Delta P_{v,contraction} \end{gathered} \tag{3.20}$$

For the chamber to operate at a given heat input, the total pressure drop should be less than the capillary pressure supported by the sintered wick, *i.e.*, $\Delta P_{total}/\Delta P_c \le 1$ is a required condition for continued operation of the vapor chamber.

3.2.2 Thermal Resistances

To calculate the temperature drop across the base wick due to capillary-fed boiling (ΔT_{boil}), the empirical correlation proposed by Smirnov [61] is used:

$$C\left(\frac{\Delta T_{boil} - \Delta T^*}{d_{pore}}\right)^{5/6} = q\left(\frac{h_{fg}\sigma k_l^{\;3}}{\nu_l}\right)^{-1/6}\left(1-\phi_{eff}\right)^{-1/6} k_{eff}^{\;-1/3}$$

where

$$\Delta T^* = \frac{4\sigma T_{sat}}{\rho_v h_{fg} d_{pore}};\; k_{eff} = k_{Cu}\frac{(1-\phi)}{(1+\phi/2)}; C = 0.32 \tag{3.21}$$

This model assumes the capillary-fed boiling phenomenon can be represented by evaporation from a thin-liquid film coated over extended surfaces formed by the porous structure. The empirical constant *C* is taken from a previous curve fit to a set of experimental capillary-fed boiling performance data [19]. In equation (3.21), ΔT^* is the nucleation superheat and k_{eff} is the effective thermal conductivity of the wick. The saturation temperature change in the vapor phase is calculated from the associated vapor pressure drops using the Clausius-Clapeyron relation

$$\Delta T_{sat} = \frac{T_{sat} v_{fg}}{h_{fg}} \Delta P_v \tag{3.22}$$

The temperature drops in the walls and the condenser wick are calculated assuming one-dimensional conduction as

$$\begin{aligned} \Delta T_{condn} &= \Delta T_{walls} + \Delta T_{wick,cond} \\ &= Q\left(\frac{t_{wall}}{A_{evap} k_{Cu}} + \frac{t_{wall}}{A_{cond} k_{Cu}} + \frac{t_{wick,cond}}{A_{cond} k_{eff}} \right) \end{aligned} \tag{3.23}$$

The total temperature drop is calculated by summing the individual temperature differentials:

$$\Delta T_{total} = \Delta T_{boil} + \Delta T_{sat} + \Delta T_{condn} \tag{3.24}$$

3.3 Validation of Reduced-Order Model

The one-dimensional model description of the two-layer wick is validated by comparing to a numerical model that solves for the multi-dimensional fluid flow behavior. A fixed baseline two-layer wick geometry is used for this comparison. The porous wick is taken to be composed of cubic-packed (ϕ = 0.48) sintered copper particles of mean diameter d_{part} = 100 µm. The working fluid considered is water. The thickness of the base wick layer (t_{base}) is taken to be 200 µm. (a) shows the plan view of the evaporator footprint area for the example case consisting of a uniform 5 × 5 array of posts and an offset 4 × 4 array of vents. The following additional dimensions of the two-layer wick and vapor core are chosen for the baseline: d_{post} = 1 mm, d_{vent} = 1 mm, t_{base} = 0.2 mm, t_{core} = 0.9 mm.

3.3.1 Numerical Model for Pressure Drop in the Two-Layer Wick

In the numerical model, the two-layer wick structure is separated into a liquid flow domain consisting of the porous wick regions and a vapor flow domain consisting of the open spaces within the wick and in the vapor core. The three-dimensional continuity and momentum equations are solved in one-eighth symmetric sections of these domains in ANSYS Fluent [63] to obtain the pressure drop values. A three-dimensional view of the wick and vapor domains of the two-layer wick section is shown in Figure 3.3(b).

Figure 3.3 (c) shows the meshed wick domain along with the boundary conditions imposed. The inlet to the domain is the outer face of the cap layer at the edge of the evaporator region. A pressure inlet boundary condition is specified on the inlet face with a constant (zero) value of gauge pressure. The domain outlet is the exposed top surface of the base wick layer where evaporation occurs. A mass outlet boundary condition is specified on the outlet face with a known evaporative mass flux based on the heat input, as calculated from the mass flow rate in equation (3.4). There are two symmetry boundaries, and the rest of the wick boundaries that interface with the vapor domain are modeled as no-slip walls. A porous-flow formulation of the governing equations that considers viscous and inertial dissipation accounting for the wick porosity (ϕ) and the permeability (K) is used for the wick domain as seen in Ref. [64]. Note that the evaporating portion of the base wick layer (*i.e.*, not covered by liquid-feeding posts) is modeled with reduced values of porosity (ϕ_e) and permeability (K_e) to simulate the capillary-boiling conditions, as in the reduced-order model (see section 3.2.1). Other inputs to the numerical solver include the thermophysical properties of the working fluid.

Figure 3.3 (d) shows the vapor flow domain and the boundary conditions. The mass inlet boundary condition on the vapor domain is the top surface of the base wick layer, which mirrors the outlet face of the wick domain. Vapor flows through the space between liquid feeding posts, up the vapor vents, and expands into the large vapor core, ultimately flowing outward to the outlet face. A pressure outlet boundary condition is specified on the outlet face, with a constant (zero) value of gauge pressure. There are two symmetry faces while the remaining boundaries that interface with the wick domain are modeled as no-slip walls.

3.3.2 Comparison of Reduced-Order and Numerical Models

The two-layer wick geometry described in sub-section 3.3.1 is simulated for a heat input of $Q = 100$ W. Figure 3.4 (a) and (b) respectively show the liquid and vapor pressure contours predicted by the numerical model. A gradient-based mesh refinement was performed, wherein cells in regions of high pressure gradient were refined, to arrive at the results reported here, for meshes containing 160,000 cells in the wick domain and 425,000 cells in the vapor domain; further refinement in each case provided negligible change in the total pressure drop. In the wick domain (Figure 3.4 (a)), the highest pressure gradient is along the thin base wick. Pressure contours in the base wick layer can be seen as rings around each post, indicating that the liquid flows radially around each post. In the vapor domain (Figure 3.4 (b)), the pressure in the vapor core remains largely uniform, except for localized higher pressure regions above each vent. The highest pressure regions are near the outer edge of the evaporator region within the vapor spaces between the liquid-feeding posts; because there is no vent directly above these regions, vapor originating at the inlet face close to the edge must flow a relatively longer distance to reach the nearest vent, resulting in a larger pressure drop. The minimum pressure in the domain is at the start of each vent because the flow encounters a sudden contraction and turns into the narrow vapor vents from the wider vapor space between the posts.

The pressure drops across different regions in the wick and vapor domain predicted by the numerical simulation are compared with corresponding values from the reduced-order model predictions. As shown in Figure 3.4 (a), the pressure drop in the cap layer of the wick domain ($\Delta P_{l,cap}$) is calculated across a line along the middle of the cap layer from the inlet to the center of the domain. The pressure drop along the post ($\Delta P_{l,post}$) is calculated along the centerline of the centermost post in the array; the pressure drop and the mass flow rate are nearly the same across all the posts. The base layer pressure drop ($\Delta P_{l,base}$) is calculated along a line from the middle post outward to the point of minimum pressure in the domain, diagonally between the posts. In the vapor domain, the total vapor pressure drop (ΔP_v) is calculated along the centerline of a vent starting from the inlet face, and then along the vapor core leading to the outlet face. However, the pressure drop differs for each vent because the pressure over the inlet face is non-uniform; an average value of pressure drop is calculated by averaging the total vapor pressure drop calculated along the centerlines of the three vents. This average value of vapor pressure drop is used in the comparison to the reduced-order model prediction.

Figure 3.4 (c) shows a bar chart of the different pressure drops in the numerical simulation compared to the corresponding values from the reduced-order model. It is noted that the largest difference is in the base wick layer (17%), while the other pressure drop values match within 5%. The difference observed in the base wick layer pressure drop is explained with Figure 3.4 (d), which shows the gauge pressure along the base layer in the numerical simulation compared to the radial flow approximation from the reduced-order model. Pressure remains almost constant under the post (where boiling does not occur), and drops rapidly outside the post due to the reduced porosity and permeability in the boiling wick. While the pressure gradient matches between the simulation approaches, the flow length in the base wick layer is shorter in the reduced-order model due to the simplified one-dimensional assumption that calculates the flow length based on the area of the unit cell given by equation (3.11). In the numerical simulation, the flow length is slightly larger and there is a minimum pressure region in the base layer diagonally between the posts. Overall, it is concluded that the reduced-order model adequately represents the nature of the fluid flow in the two-layer wick and provides a satisfactory prediction of the total pressure drop.

3.4 Two-Layer Wick Performance Prediction

The reduced-order model developed in Section 3.2 can be used to find two-layer evaporator wick designs that are capable of sustaining liquid supply at a given heat input while maintaining a target evaporator temperature. Various vapor chamber dimensions are held constant for the analysis. The thicknesses of the vapor chamber walls (t_{wall}) and the condenser-side wick ($t_{wick,cond}$) are each set to 200 µm. The condenser and the evaporator square edge lengths are l_{cond} = 100 mm and l_{evap} = 10 mm, respectively. The bulk wick thickness t_{bulk} is chosen to be 1.5 mm with a total vapor chamber thickness of 3 mm.

3.4.1 Relative Magnitude of Pressure Drops and Temperature Drops

A baseline two-layer evaporator wick design is analyzed first in order to assess the relative magnitude of the different pressure and temperature drops at a heat input of Q = 1 kW (*i.e.*, flux of 1 kW/cm^2). The baseline case is the same as specified in Section 3.3. Figure 3.5 (a) shows drawings of the baseline design, which has a uniform 5×5 square array of liquid feeding posts and an offset 4×4 square array of vapor vents, with the following geometrical parameters: d_{post} = 1 mm, d_{vent} = 1 mm, and t_{cap} = 1 mm.

Figure 3.5 (b) provides a histogram of the different liquid pressure drops and the total vapor pressure drop. The maximum pressure drop is incurred in the thin base wick ($\Delta P_{l,base}$); this large pressure drop is due to the small cross section for flow that is further reduced by vapor formation, even over the short flow length. The bulk wick and cap wick layer liquid pressure drops are higher than that in the liquid feeding posts, as a result of this specific design case having relatively thick posts; generally, these pressure drops are of a similar magnitude, depending on the design. The vapor pressure drop also contributes a significant portion to the total pressure drop for this particular design, but can be significantly reduced for wider vents. To a large extent, $\Delta P_{l,base}$ governs the overall pressure drop in the vapor chamber. A sufficiently dense array of liquid-feeding posts (*i.e.*, more unit cells with a decreased flow length in the base wick layer) would be necessary to reduce this pressure drop such that a capillary limit is not encountered. This highlights the need for distributed liquid feeding with an array of posts to enable use of the thin base wick over the entire 1 cm^2 evaporator area.

A histogram of the different temperature drops for the example design is shown in Figure 3.5 (c). The boiling resistance induces the highest temperature drop and represents the limiting factor on the thermal performance of a vapor chamber incorporating the two-layer wick design. This temperature drop is amplified by the reduction in footprint area for capillary-fed boiling due to the presence of posts (from which boiling is assumed not to occur). Therefore, the thermal performance of the vapor chamber is expected to be sensitive to the diameter of the liquid-feeding posts, which determine the amplification of the heat flux. While the conduction temperature drops are not negligible, they are a part of the vapor chamber design and not of the two-layer wick proposed in this work, and hence not a primary focus here. The saturation temperature change in the vapor phase is negligible. Considering that the base layer pressure and temperature drops largely govern the performance, note that the model predictions are reliant on the accuracy of the correlations used to predict these terms; given the sensitivity of the performance predictions to the base wick thickness, the value in this study was chosen to match the thickness and particulate composition of a wick investigated in prior experiments from which the capillary-fed boiling empirical correlation parameters adopted in this study were developed [18]. In addition, keeping this wick thickness small is central to the design concept and helps achieve the low evaporator temperatures desired.

3.4.2 Parametric Effects on Performance

The effects of the two-layer wick post diameter, cap layer thickness, and the vent diameter on the pressure drop and thermal performance are investigated for a 5 × 5 post array design. As any one of these parameters is varied individually, the other two parameters remain fixed at the baseline values of $d_{post} = 1$ mm, $d_{vent} = 0.5$ mm, and $t_{cap} = 1$ mm; all other wick geometric parameters are the same as the baseline case and the heat input remains $Q = 1$ kW.

Figure 3.6 shows the total pressure drop, ΔP_{total} (left vertical axis; blue line) and the total temperature drop, ΔT_{total} (right vertical axis; red line) plotted against the post diameter, keeping all other wick geometric parameters fixed. For a fixed array size, increasing the post diameter reduces the total pressure drop. Thicker posts reduce the pressure drop contribution from the posts; more importantly, the flow length in the thin base wick layer is shortened, thereby decreasing the total pressure drop. Conversely, the temperature difference across the vapor chamber increases with post diameter; thicker posts occupy a large area of the evaporator footprint, reducing the area available for boiling.

Figure 3.7 plots ΔP_{total} and ΔT_{total} against the cap layer thickness, while keeping other wick geometric parameters fixed. Note that for constant bulk wick and base wick layer thicknesses, a change in the cap layer thickness implies a concomitant elongation or shortening of the liquid feeding posts. Therefore, when the cap layer thickness is reduced, the liquid pressure in the thinner cap ($\Delta P_{l,cap}$) and longer posts ($\Delta P_{l,post}$) both increase. Conversely, increasing cap layer thickness yields shorter posts with narrower spaces between them, which increases the vapor pressure drop ($\Delta P_{v,space}$ and $\Delta P_{v,vent}$). This tradeoff gives rise to an optimum cap thickness at which the total pressure drop is minimized (~0.8 mm in Figure 3.7), for all other parameters fixed. The temperature drops remain almost constant with cap thickness, with the only effect being a small increase in the saturation temperature change in the vapor phase at larger cap thicknesses for which vapor flow is restricted in the narrow spaces between posts.

The effect of vent diameter on ΔP_{total} and ΔT_{total} is shown in Figure 3.8. In general, wider vapor vents increase the pressure drop through the cap layer ($\Delta P_{l,cap}$) because the effective liquid flow area is reduced, while narrower vents increase the vapor pressure drop through the vent itself

($\Delta P_{v,vent}$). Despite this apparent tradeoff, the pressure drop increase due to narrowed vents outweighs any decrease in the cap layer pressure drop. This analysis indicates that the vent diameters should be made as large as possible, up to the physical limit of overlapping with the liquid-feeding posts, to minimize the total pressure drop for a given array size. The thermal performance is largely unchanged within the range of vent diameters tested, as a result of the negligible contribution of the vapor vents to the saturation pressure change.

A comparative interrogation of Figure 3.6 to Figure 3.8 reveals that the pressure drop and the thermal resistance of the two-layer wick structure are predominantly affected by the post and vent diameters at a given array size; the cap layer thickness has a significantly smaller effect. This is because the post diameter directly influences the largest contributing pressure drop ($\Delta P_{l,base}$) and temperature drop (ΔT_{boil}), and the vent diameter affects the non-negligible vapor pressure drop (ΔP_v). In addition, note that the total pressure drop for the baseline case, and parametric variations thereof, were always greater than the available capillary pressure of the wick structure (P_c = 5891 Pa).

The number of liquid feeding posts in the array can be varied to design a two-layer evaporator wick structure with reduced pressure drop. Plotted in Figure 3.9 are the pressure drop ratio ($\Delta P_{total}/\Delta P_c$), left vertical axis; blue line) and the total temperature drop (ΔT_{total}, right vertical axis; red line) with varying array sizes, from a sparse 5 × 5 array to a densely packed 10 × 10 array of posts. A pressure drop ratio ($\Delta P_{total}/\Delta P_c$) value of less than unity (a solid blue cut-off line at unity is shown in the figure) signifies that the vapor chamber can operate without reaching a capillary limit at the given heat flux. To design for a nearly fixed total temperature differential, the post diameter can be reduced as the array size increases, to maintain the associated footprint area covered by the posts. In Figure 3.9, the footprint area is chosen such that the total temperature drop is ~40 K across the different array sizes; the corresponding post diameter is shown on the abscissa. It is noted that increasing array sizes yield reduced total pressure drop due to the reduced flow length around each post in the base layer, thereby reducing the predominant $\Delta P_{l,base}$. Arrays of size 9 × 9 and larger yield a pressure drop below the critical limit in this case.

As demonstrated in this section, the reduced-order model developed in this study allows for study of the design trade-offs resulting from changes to the two-layer wick geometry. These trade-offs must be considered so that an evaporator design avoids the capillary limit while achieving some target vapor chamber thermal resistance at a given heat input. The model can be exploited to generate two-layer wick designs for various device heat input and thermal resistance needs.

3.5 Performance Advantages of Proposed Two-layer Wick Over Single-Layer Wicks

The reduced-order model developed in this work helped estimate the performance of the two-layer wick design. In this section, similar reduced-order models for conventional single-layer wick designs are used to assess the relative performance advantages of the two-layer wick. Specifically, homogeneous and grid-patterned evaporator wick designs (schematic diagrams in Figure 3.10) are compared to the two-layer wick. The homogeneous wick has a uniform-thickness (t_{base}) wick layer over the evaporator region to which liquid is supplied by a thick bulk wick (t_{bulk}) around the periphery. The grid-patterned evaporator wick structure has square grids (length l_{grid}) running across the evaporator region to enhance liquid feeding of the thin wick base layer (thickness t_{base}) during high-heat-flux capillary-fed boiling operation [13,15,18]. In order to maintain a constant thermal resistance for each of the different evaporator wicks while assessing the pressure drop imposed, the same value of t_{base} = 200 µm is used for all the wicks. All the wick and working fluid properties, including the particle, pore diameter and porosity of the wick, are kept the same as in the two-layer wick model (Sections 3.2 and 3.3). The dimensions of the vapor chamber, including the evaporator area of 1 cm^2 used in Section 3.4, also remain the same. The reduced-order models developed for the homogeneous and grid-patterned evaporator wick designs are summarized in APPENDIX C. The remainder of this section compares their performance against the two-layer wick design proposed in this work.

The total pressure drop and thermal resistance of the homogeneous and grid-patterned evaporator wicks are calculated at a heat input of Q = 1 kW. For the homogeneous evaporator wick, the total pressure drop is very high due to the small cross-sectional area available for liquid flow in the thin base layer without any additional feeding pathways. The pressure drop ratio (ratio of total fluid pressure drop to the capillary pressure) for the homogeneous evaporator wick is ~17 at a heat input of Q = 1 kW. This ratio is very high compared to any of the two-layer wick designs assessed in Section 3.4 and indicates that the homogeneous evaporator wick would dry out at a very low heat flux.

The pressure drop ratio of the grid-patterned evaporator wick is compared to the two-layer wick in Figure 3.11. The results are obtained at a constant temperature drop of ~40 K over all the cases, to compare the pressure drop performance of the wicks. The array size for the grid-patterned wick refers to the number of grids, while the array size for the two-layer wick refers to the number of posts in each direction of the square array. The two-layer wick outperforms (*i.e.*, has a lower pressure drop ratio than) the grid-patterned wick as the array size increases. It is noted that for the grid-patterned wick, increasing array size does not produce a sufficient reduction in the pressure drop ratio, and thus a viable geometry for operation of the vapor chamber without a capillary limit is not reached. In contrast, the two-layer wick exhibits a significant reduction in the pressure drop ratio with increasing array size. This behavior can be explained by the design constraints that apply to each wick type. The same amount of evaporator footprint must be made available for capillary-fed boiling to keep the temperature drop at ~40 K, irrespective of the array size. For the grid-patterned wick, this necessitates a decrease in the width of the liquid-feeding pathways, and hence an increase in the pressure drop. For the two-layer wick, increasing the array sizes requires a larger number of thinner posts, which does not incur a large pressure drop penalty because they are all drawing from the same, thick cap layer. A summary of the comparison of the performance of the different evaporator wicks is tabulated in Table 3.1. The reduced pressure drop offered by the two-layer wick design, at the same thermal resistance, indicates that this design offers the potential to dissipate higher heat fluxes than the other two wick structures before the capillary limit would be reached.

3.6 Conclusions

A two-layer vapor chamber evaporator wick structure is evaluated. To support high-heat-flux operation during capillary-fed boiling, evaporator wicks must be adequately fed with working fluid over their entire area while imposing a low thermal resistance. The two-layer evaporator design has a thin base wick layer supplied by an array of liquid-feeding posts from a thicker cap wick layer above. Vapor formed by boiling in the wick base layer passes out of the evaporator through the spaces between the posts and vapor vents in the cap layer. The base wick imposes a low thermal resistance during capillary-fed boiling, while the cap layer and liquid-feeding posts are responsible for providing uniform liquid supply over the entire evaporator area.

A reduced-order model is developed to predict the hydraulic and the thermal performance of the two-layer wick incorporated within a vapor chamber heat spreader. Comparing against a higher-fidelity numerical model, it is found that the reduced-order, one-dimensional model adequately represents the fluid flow behavior and the pressure drop in the two-layer wick. Parametric studies identified that the number and size of liquid-feeding posts critically affects both the pressure drop and thermal performance. Large arrays with smaller diameter posts can reduce the total pressure drop while maintaining the same area available for capillary-fed boiling in the base wick (*i.e.*, maintaining constant thermal resistance). The reduced-order model predicts that heat fluxes on the order of ~1 kW/cm^2 can be dissipated over areas as large as 1 cm^2 without suffering from dryout by utilizing a sufficiently large number of liquid-feeding posts. The reduced-order model uses first-order approximations to provide useful insights into the design of the proposed two-layer evaporator wick structure. Comparison to other single-layer wick structures (homogeneous and grid-patterned wicks) shows that the two-layer wick has a lower pressure drop at the target heat fluxes, such that the capillary limit (dryout) would not be reached.

Table 3.1. Pressure drop ratios and temperature drops for the three different evaporator wicks, at a heat input of Q = 1 kW over an area of 1 cm^2

Wick structure	**Feature array size**	**Pressure drop ratio ($\Delta P_{total}/ \Delta P_c$)**
Homogeneous wick		17
Grid-patterned wick	6×6	1.8
	8×8	1.5
	10×10	1.4
Two-layer wick	6×6	1.7
	8×8	1.1
	10×10	0.8

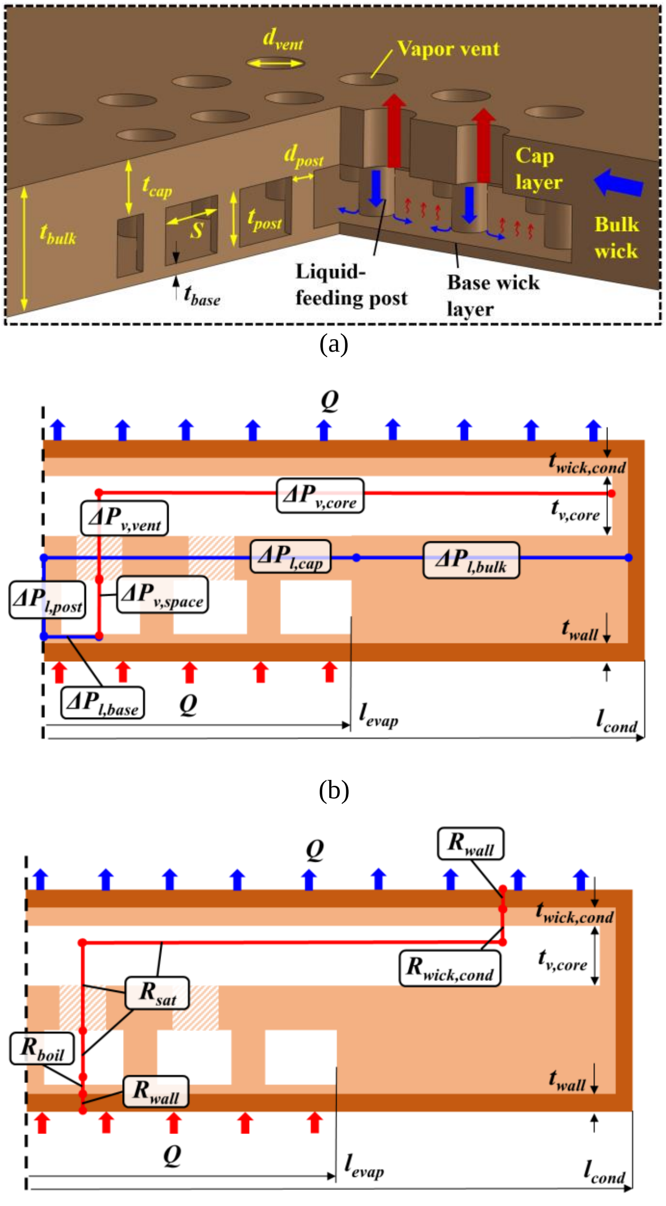
d_{vent}
Vapor vent
d_{post}
Cap layer
Bulk wick
t_{cap}
t_{bulk}
S
t_{post}
t_{base}
Liquid-feeding post
Base wick layer
Q
$t_{wick,cond}$
$\Delta P_{v,core}$
$\Delta P_{v,vent}$
$t_{v,core}$
$\Delta P_{l,cap}$
$\Delta P_{l,bulk}$
$\Delta P_{l,post}$
$\Delta P_{v,space}$
t_{wall}
$\Delta P_{l,base}$
l_{evap}
l_{cond}
R_{wall}
$R_{wick,cond}$
R_{sat}
R_{boil}

(a)

(b)

(c)

Figure 3.1. (a) A three-dimensional schematic drawing of the proposed two-layer evaporator wick structure is shown with liquid (blue) and vapor (red) flow pathways indicated. The view is cut by planes intersecting the liquid-feeding posts (left) and the vapor vents (right) to reveal the internal structure. Cross-sectional schematic diagrams are shown with the two-layer evaporator wick structure incorporated within a vapor chamber heat spreader (with one half of the geometry shown); (b) the liquid-phase (ΔP_l) and vapor-phase (ΔP_v) pressure drops and (c) thermal resistances (R) are drawn along the primary fluid flow path (not to scale).

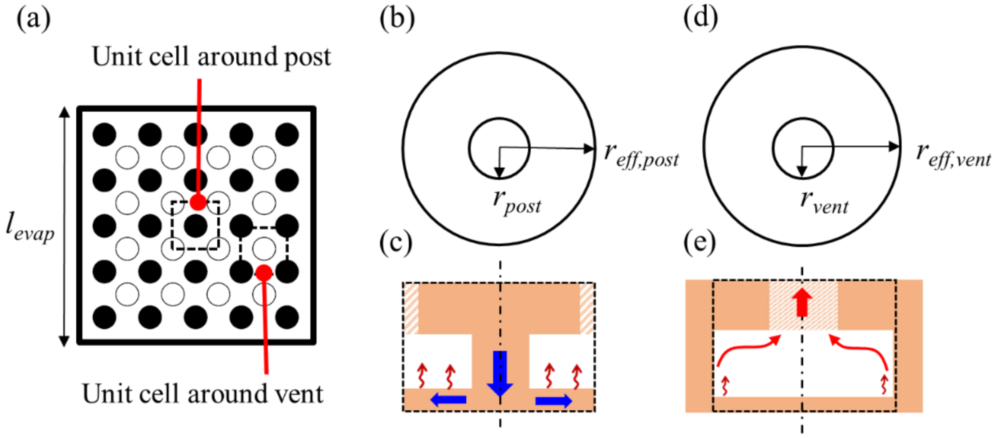
(a)
Unit cell around post
l_{evap}
Unit cell around vent
(b)
$r_{eff,post}$
r_{post}
(c)
(d)
$r_{eff,vent}$
r_{vent}
(e)

Figure 3.2. (a) Plan-view diagram of the evaporator footprint area of side length l_{evap}, for an example 5×5 square array of liquid-feeding posts (filled circles) and an offset 4×4 square array of vapor vents (open dots). Square unit cells around one post and one vent are outlined. The square unit cells are approximated by axisymmetric radial unit cells with (b,d) plan and (c,e) side views shown.

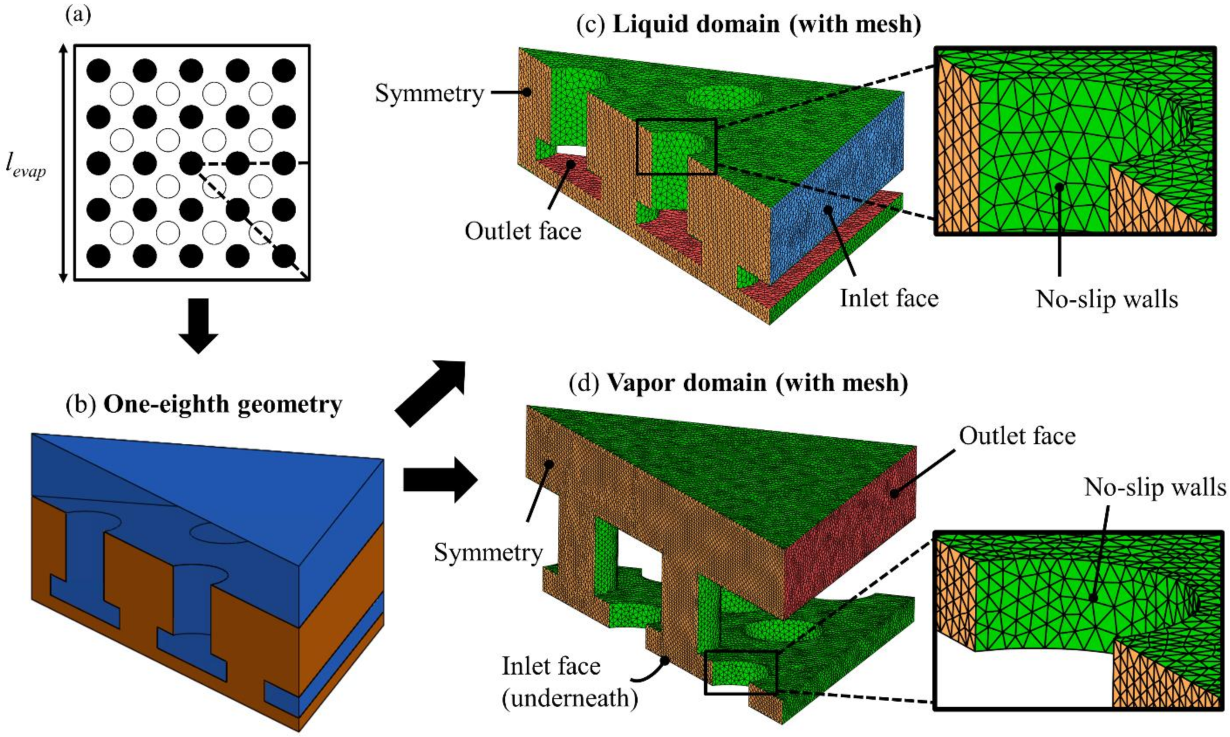
(a)
l_{evap}
(b) **One-eighth geometry**
(c) **Liquid domain (with mesh)**
Symmetry
Outlet face
Inlet face
No-slip walls
(d) **Vapor domain (with mesh)**
Outlet face
No-slip walls
Symmetry
Inlet face
(underneath)

Figure 3.3. (a) Plan view diagram of the evaporator footprint area of side length l_{evap}, for an example 5 × 5 array of posts with dashed lines showing one-eighth of the geometry. (b) Three-dimensional view of one-eighth section of the two-layer wick used for the numerical simulations, with the colors distinguishing the porous wick and vapor regions. The meshed (c) porous wick region (wick domain) and the (d) open region (vapor domain) are shown with the boundary conditions labelled, namely, the inlet, outlet, and symmetry, and no-slip boundaries. Insets in (c) and (d) show a close-up view of the mesh.

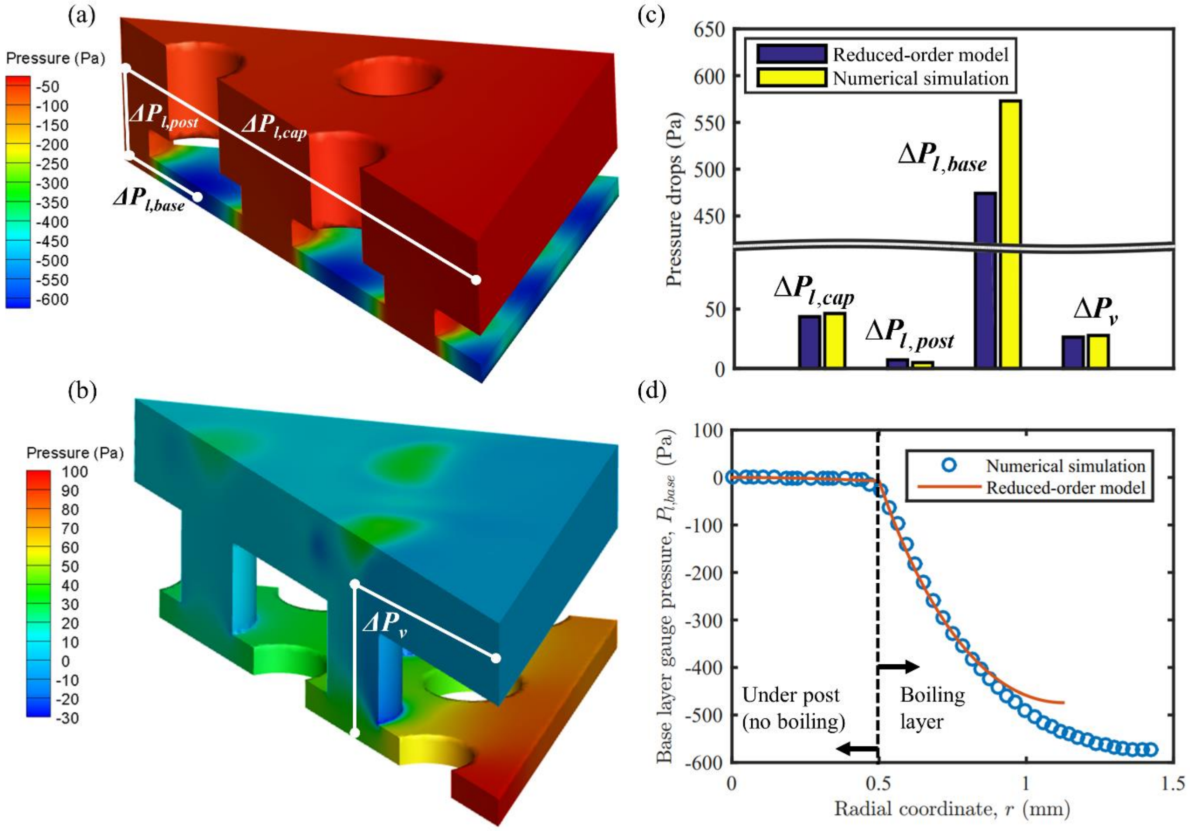

Figure 3.4. Pressure contours predicted by the numerical simulation for the (a) wick and (b) vapor domains of the two-layer wick. Pressure drops are calculated along the cap layer ($\Delta P_{l,cap}$), post ($\Delta P_{l,post}$), and base layer ($\Delta P_{l,base}$) as indicated by the lines in (a); the vapor flow pressure drop (ΔP_v) is calculated along the lines in (b). (c) A bar chart compares the pressure drop values calculated from the reduced-order model and the numerical simulation. (d) The gauge pressure is plotted radially along the base wick layer (*i.e.*, along the line corresponding to the base layer pressure drop) for the reduced-order model and the numerical simulation.

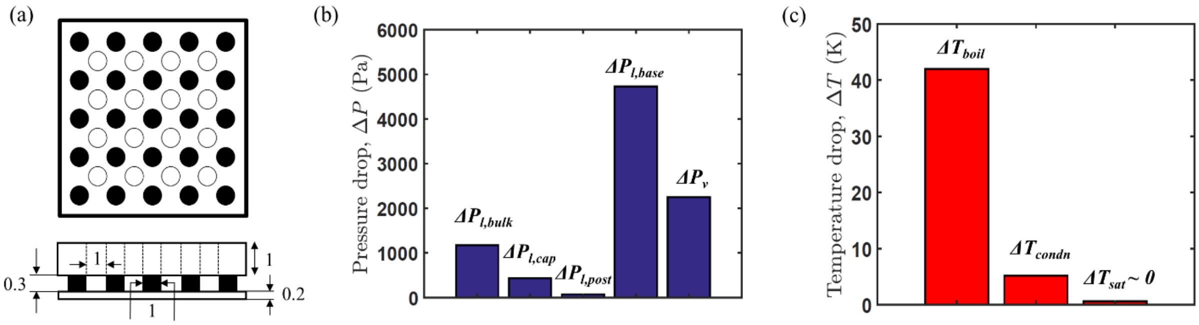

Figure 3.5. (a) Plan and side-view drawings of an example two-layer evaporator wick design case; in the plan view, liquid-feeding posts are filled circles and vents are open dots (dimensions shown in mm, not to scale). Histograms are shown for the different (b) pressure drops and (c) temperature drops for this baseline case at a heat input of Q = 1 kW over 1 cm^2 of heat input area.

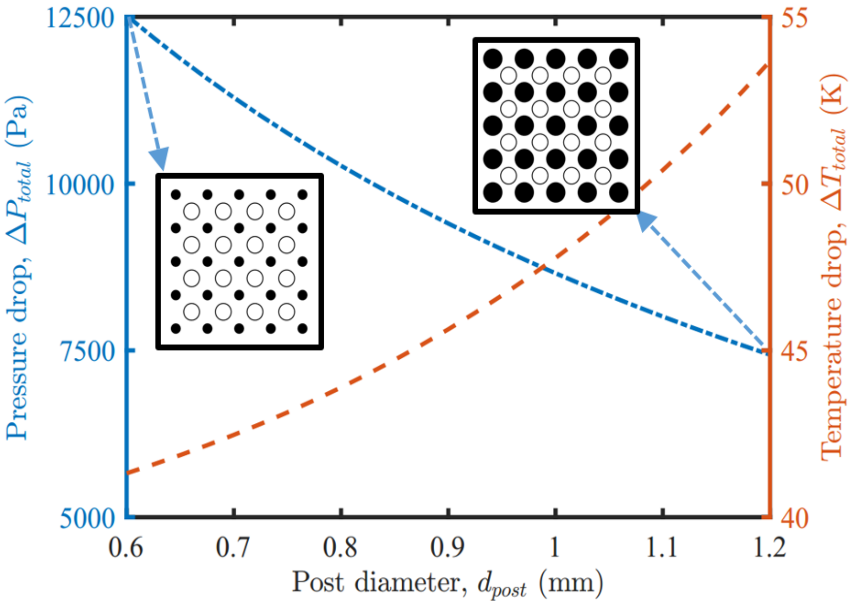

Figure 3.6. Effect of post diameter on the total pressure drop and the total temperature drop, for d_{vent} = 1 mm and t_{cap} = 1 mm, with all other wick geometric parameters fixed as in the baseline case. The insets show plan-view drawings (to scale) of the two-layer evaporator wick designs at the extreme post diameters.

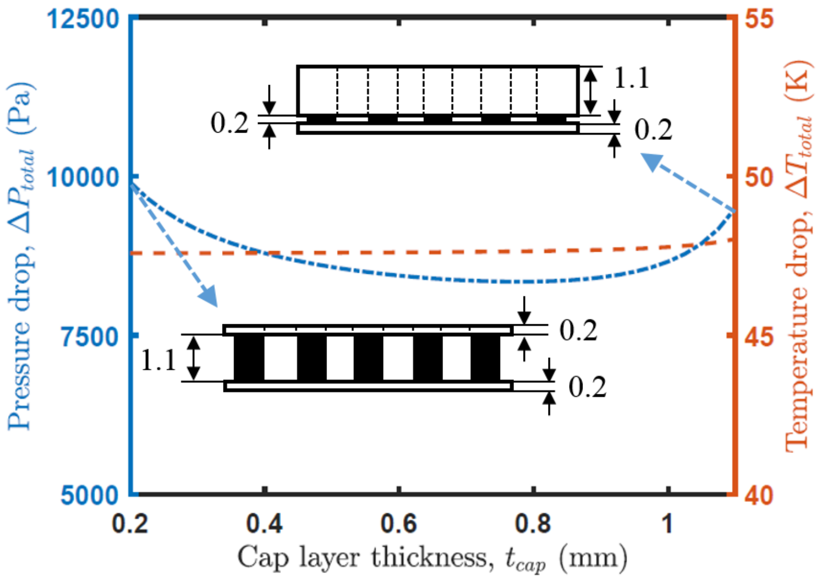

Figure 3.7. Effect of cap layer thickness on the total pressure drop and the total temperature drop, for d_{post} = 1 mm and d_{vent} = 1 mm, with all other wick geometric parameters fixed as in the baseline case. Insets show side-view drawings of the two-layer wick at the extreme cap layer thicknesses (not to scale, dimensions in mm).

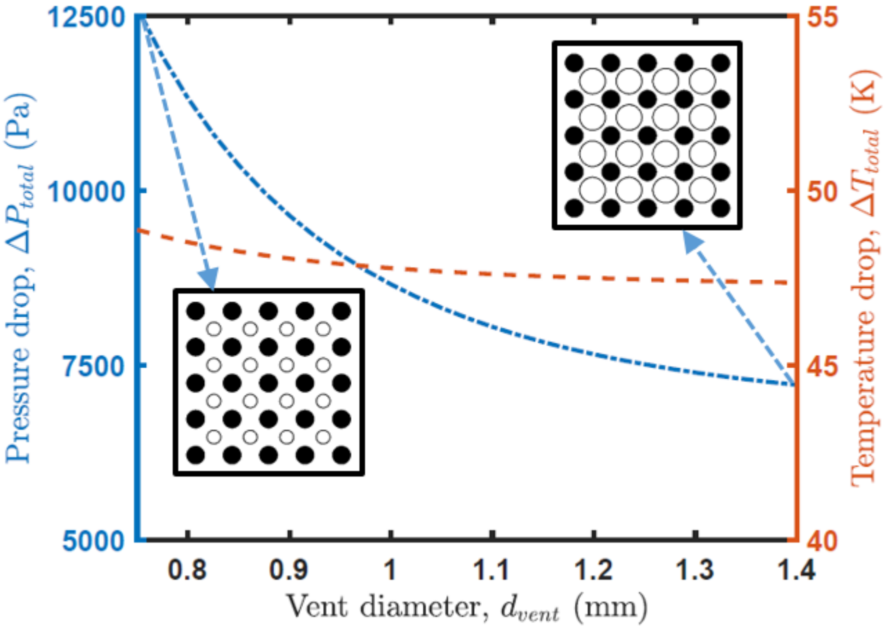

Figure 3.8. Effect of vent diameter on the total pressure drop ratio and the total temperature drop, for d_{post} = 1 mm and t_{cap} = 1 mm, with all other wick geometric parameters fixed as in the baseline case. Insets show scaled evaporator areas for extreme cases of vent diameters.

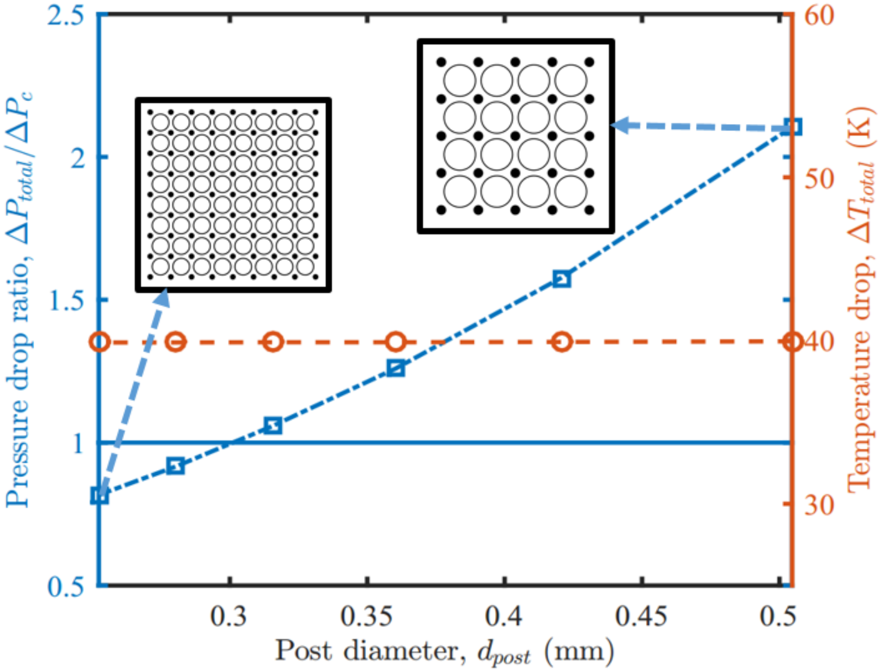

Figure 3.9. Effect of increasing post array size on the total pressure drop ratio ($\Delta P_{total}/\ \Delta P_c$) and the total temperature drop (ΔT_{total}) for d_{vent} = 1 mm, t_{cap} = 1 mm. This is achieved by fixing the footprint area covered by the posts to obtain a target temperature drop, while varying post diameter (d_{post}). Insets show scaled evaporator areas for a 5 × 5 and a 10 × 10 array of posts.

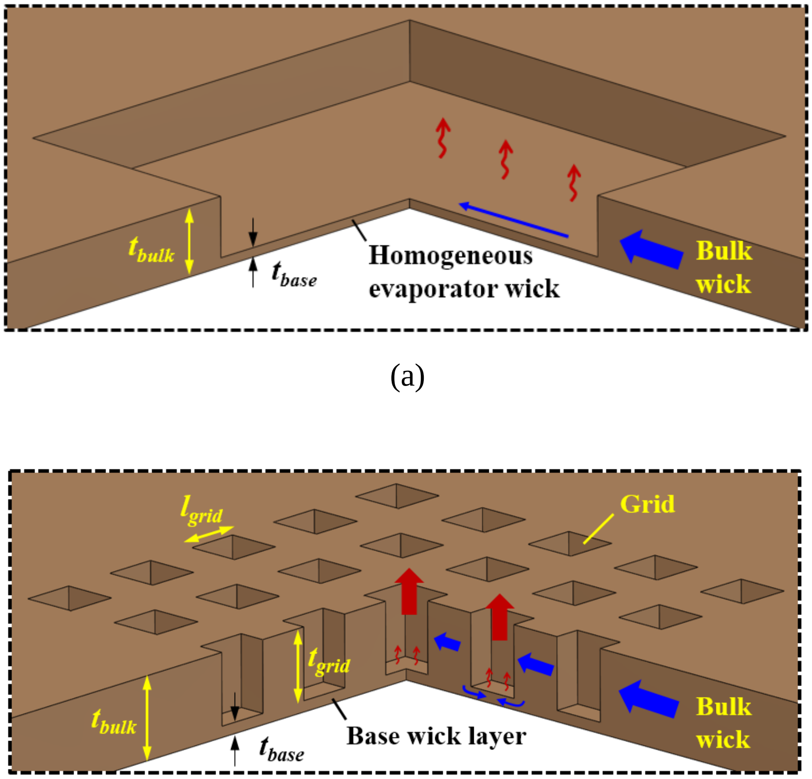
t_{bulk}
t_{base}
Homogeneous evaporator wick
Bulk wick
l_{grid}
Grid
t_{grid}
t_{bulk}
t_{base}
Base wick layer
Bulk wick

(a)

(b)

Figure 3.10. Schematic drawings of (a) homogeneous and (b) grid-patterned evaporator wicks. Important characteristic dimensions of the two wicks, along with the primary liquid flow pathway (in blue arrows) and vapor flow pathway (in red arrows), are shown.

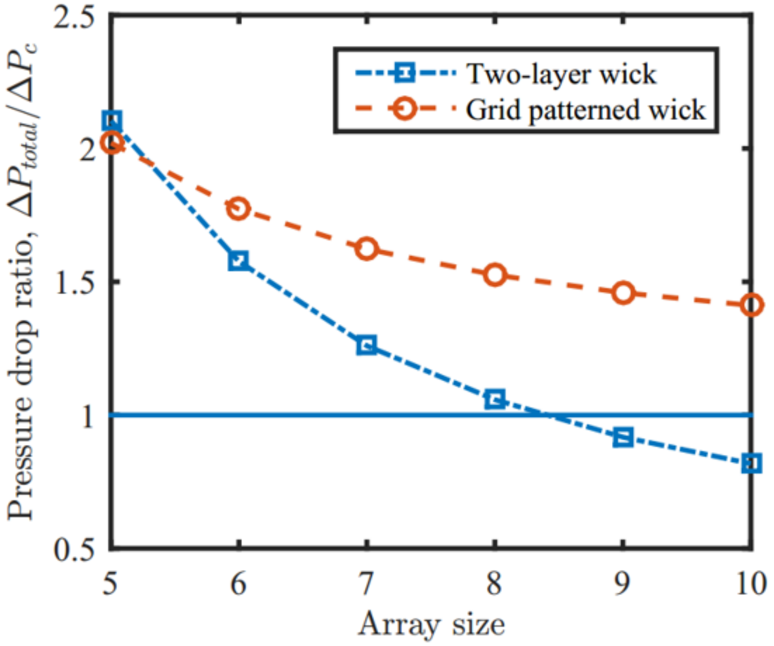

Figure 3.11. Comparison of the pressure drop performance of the two-layer wick and the grid-patterned wick for varying array sizes. The blue line at a pressure drop ratio of 1 signifies the cut-off for operation of the vapor chamber due to the capillary limit.

4. EXPERIMENTAL INVESTIGATION OF BOILING REGIMES IN A CAPILLARY-FED TWO-LAYER EVAPORATOR WICK

The current chapter experimentally investigates boiling behavior in a capillary-fed two-layer evaporator wick design. A novel experimental facility is developed for testing wicks in a capillary-fed situation that replicates the conditions near the evaporator region of a vapor chamber. Two designs of the two-layer wick are tested and compared to a homogeneous (single-layer) evaporator wick. The two-layer wicks provide a significant enhancement in the dryout heat flux while maintaining a low thermal resistance, as anticipated by the design rationale. High-speed visualizations are acquired in order to map these results to the different boiling behaviors exhibited by the single- and two-layer wicks. The material from this chapter was published in the *International Journal of Heat and Mass Transfer* [65].

4.1 Two-Layer Wick Fabrication

The two-layer wick is fabricated using a combination of sintering and laser machining steps as shown in Figure 4.1. The goal of the present study is to demonstrate and characterize the behavior of the novel two-layer wick during capillary-fed boiling; an extensive parametric analysis of the effects of particle size or other wick properties is not part of the scope. The choice of particle size and sintering conditions were informed by our previous work on pool boiling from sintered particulate surfaces [66]. Irregular copper particles manufactured by water atomization (ACu Powder International) are sieved to obtain the desired range of 90-106 µm diameter particles (USA standard sieve numbers. 140 and 170). A copper substrate is sanded using 220 grit sandpaper and then inverted onto a graphite mold with a recess of the desired depth containing loose copper particles. The mold and substrate are placed inside a bell-jar vacuum furnace. The furnace is evacuated using a vacuum pump to ~ 1.33 Pa over a period of 2 hr, after which a diffusion pump runs for ~ 12 hr to reach a high vacuum of 0.00133 Pa. To sinter the particles, the furnace temperature is ramped over 2.5 hr from room temperature to 950 °C, and then held constant for a period of 0.5 hr. The furnace is allowed to cool down to room temperature overnight; high vacuum is held throughout cooling to avoid oxidation of the wick. Figure 4.1 (f) shows a scanning electron microscopy (SEM) image of the sintered wick; the irregular particles and highly tortuous nature of the pores are apparent.

A homogeneous sintered layer is fabricated in the first sintering step (Figure 4.1 (b)). Next, a laser-cutting machine in the Birck Nanotechnology Center at Purdue University (Universal Laser Systems PLS6MW) is used to etch the sintered surface over the central area to fabricate posts and retain only a thin base wick layer in the region without posts (Figure 4.1 (c)). This non-contact machining avoids fragmentation of the sintered porous wick while fabricating the posts. Compared to using molding processes [13] to form these post-array wick structures, for which removal of the sintered sample is difficult and requires special design considerations (e.g., see Ref. [67]), laser etching allows for fabrication of comparatively smaller and denser microscale post arrays. To test the effect of the laser machining process on the wetting nature of the wick, a micro-syringe was used to deposit a 3 µl deionized water droplet onto multiple locations of the native sintered wick and the laser-etched regions. High-magnification videos were recorded using a Nikor D5200 DSLR camera fitted with a Keyence VH-Z50L high-magnification zoom lens. It was observed that the laser-treated regions absorbed the liquid at a similar rate as the native regions of the wick, indicating that the laser machining process did not affect the wetting characteristics.

The wick configuration shown in Figure 4.1 (c) is then inverted onto a graphite mold containing loose copper particles to sinter the second cap layer shown in Figure 4.1 (d). Once the cap layer is sintered, the vents are fabricated by laser etching through the cap layer in the gaps between the posts (Figure 4.1 (e)). Special care was taken, by controlling the number of laser passes, to prevent over-etching through to the exposed base wick layer. A photograph of the as-fabricated two-layer wick is shown in Figure 4.1 (g) for a design having a 5×5 array of liquid-feeding posts and a 4×4 array of vapor vents; the complete dimensions of the fabricated wick samples are detailed in Section 4.3.

4.2 Experimental Methods

4.2.1 Capillary-fed Boiling Experimental Facility

A capillary-fed boiling test facility is constructed to characterize the two-layer wick design. In order to mimic the conditions in the evaporator region of a vapor chamber, the wick must be uniformly fed with liquid from the periphery, purely via capillary action (*i.e.*, the wick in the evaporator region should not be submerged or flooded with liquid). In addition, the wick should be placed in a saturated vapor environment. We develop a novel capillary-fed boiling test facility, which uses a physical restriction (*i.e.*, a dam) to prevent flooding over the top of the horizontal wick. This approach allows the surrounding liquid level to be maintained slightly higher than the wick, to ensure continuous feeding from the sides while avoiding any risk of flooding. The need for active liquid-level control to match the height of the wick is thereby eliminated. Note that the dam design inherently allows for some gravitational assistance to liquid-feeding because the liquid level is higher than the wick level. However, this assistance due to gravitational pressure head is negligible compared to the capillary pressure generated by the wick when operating in a capillary-fed mode (see Section 4.2.3).

The test facility, shown schematically in Figure 4.2 (a), primarily consists of a test chamber, a heater block and insulation assembly, and a condenser loop. The PEEK and polycarbonate chamber side walls are sealed together using a silicone adhesive (RTV 118, McMaster Carr) and stainless-steel screws, while the top wall is sealed with a compressed high-temperature rubber gasket. Deionized (DI) water is used as the working fluid; there are two T-type thermocouples each in the liquid pool and the vapor space above, and two immersion cartridge heaters (120 V, 300 W each) submerged in the liquid pool. The condenser loop consists of a temperature-controlled chiller (not shown in Figure 4.2 (a)) that is connected to a Graham condenser, attached to the top chamber wall, for degassing the liquid. The coolant (water) also routes through a copper condenser coil within the chamber to condense the vapor back to liquid to control the chamber pressure during boiling. Figure 4.2 (b) shows a close-up view of the test facility schematic diagram near the evaporator wick and Figure 4.2 (c) shows an exploded view of the heater assembly. A high-temperature rubber gasket is sealed against the top of the wick and held in place using a PEEK dam that prevents flooding over the wick during test. The dam has openings (seen in Figure 4.2 (c)) to feed the wick from the sides. Thus, the dam allows the surrounding liquid to be at a higher level than the wick and allows for a large tolerance in the height at which this level should be maintained while avoiding flooding. The dam and the gasket both have openings in the middle to allow evaporation from the wick into the vapor space above through a 1 cm^2 square area.

The heater block assembly consists of a copper heater block, a ceramic insulation plate, mineral wool filler insulation, a PEEK outer casing, and a PEEK fixture that is fabricated in two pieces. The copper heater block has a stepped design that has a larger base cross section area (45 mm × 45 mm) that houses nine cartridge heaters (150 W each). Along the top 15 mm, the heater block cross-section is smaller at 10 mm × 10 mm. This neck concentrates the heat input to a smaller area and interfaces directly with the wick substrate, which is soldered onto the top of the heater block (details in 4.2.2). Thermocouples are inserted into three locations along the length of the neck and in two additional lateral locations (data reduction details in Section 4.2.4). The thermocouples along the neck length are used to measure the heat flux and substrate temperature by extrapolation of the temperature gradient, while the lateral thermocouples are used to check if the temperature is uniform over the neck cross-section. The heater block was designed to provide a uniform one-dimensional heat input to the wick. The length of the neck is chosen to be long enough to allow for enough thermocouples to be placed to predict the heat input with good accuracy (uncertainty analysis in Section 4.2.4), but not so long that the gradient would incur very high temperatures at the heater base at the maximum heat flux. Conduction heat transfer simulations were performed using ANSYS Fluent [68] to confirm that the heat flow upon area reduction again became uniform across the neck cross-section at the position of the bottom-most thermocouple. The base of the heater block, which can reach temperatures exceeding the safe operating temperature of PEEK (250 °C), is placed on a ceramic base for insulation, which is supported by springs to accommodate thermal expansion. Immediately surrounding the sides of the copper block is a layer of mineral wool that can withstand temperatures up to 1100 °C.

The test chamber has a window in the top wall for visualization (Figure 4.2 (a)) normal to the 1 cm^2 evaporating area of the wicks. To avoid condensation on the glass windows during visualization, two patch heaters are attached to the window using high-temperature Kapton tape. The high-speed videos are taken using a Phantom VEO 710L high-speed camera, fitted with Nikon Micro-Nikkor 200 mm lens, at a resolution of 640 × 600 pixels and a frame rate of 2000 fps. The visualization is aided by front lighting, using a Titan 300 fiber-optic light source, placed over the window.

4.2.2 Soldering and Sealing

To achieve a low-thermal-resistance connection between the heater block and the wick substrate, they are soldered together. The heater block is fixed upright and solder flux is applied to the top surface. The block is heated to ~ 250 °C using the cartridge heaters and a known quantity of lead-tin solder (Pb30-Sn70; melting point of 249 °C; thermal conductivity, k_s of 41 W/mK) is then deposited on the surface. The solder melts while the flux allows it to wet the copper and spread uniformly over the 1 cm^2 surface. The heater block is then cooled down to room temperature and placed inverted onto the wick substrate, using a graphite fixture to center the heater block with respect to the substrate (as shown in the assembly in Figure 4.3 (a)). The heater block is again heated to 250 °C to melt the solder and form a joint between the heater block and substrate.

To characterize the thickness and uniformity of the soldered joint, a non-destructive µ-CT scan (Bruker Skyscan 1272) of the soldered joint was performed in the Center for Particulate and Powder Processing at Purdue University, with a 2452 × 1640 pixel detector resolution and a reconstructed voxel size of 3.5 µm. The soldered joint thickness is measured to be $t_s = 150$ µm from the µ-CT scan images. A cross section through the center of the joint reveals some voids scattered throughout; a void fraction of 15% was calculated from the scan images. Due to the high conductivity and small thickness of the solder joint, the effect of this porosity on the extrapolated substrate temperature is less than the uncertainty in its calculation (see Section 4.2.4). To obtain a conservative (highest) estimate of the substrate temperature, the uncertainty caused by the porosity of the solder joint is omitted. After each test, the substrate/wick is detached from the heater block by reheating it to the melting point of the solder. The top surface of the heater block is then sanded using 320 grit sandpaper to remove any residual solder before the next sample is attached.

In this study, prior to sealing the heater block and wick into the test facility, the wick is dipped in a solution of 2 M NaOH and 0.1 M $(NH_4)_2S_2O_8$ for 30 min to form Cu(II) oxide, following the procedure of Chen *et al.* [69], which maintains the wettability of the wick throughout the duration of a test.

There are multiple seals in the heater block and insulation assembly (see Figure 4.2 (c)) to avoid leaks in the test chamber. The heater assembly is interfaced with the test chamber using a PEEK fixture that is fabricated in two pieces. After the solder joint is formed, the mineral wool insulation is stuffed between the heater block and the surrounding PEEK assembly. The two pieces of the fixture are then sealed together with silicone adhesive (RTV 118, McMaster Carr). The heater block assembly is then sealed against the bottom wall of the test chamber using an o-ring placed in a groove on the fixture. The rubber gasket on the underside of the wick substrate provides a seal to the fixture below; the rubber gasket on top of the wick seals against the dam to prevent flooding. The dam is pressed on top of the wick using four screws that compress these gaskets.

4.2.3 Testing Procedure

After sealing, deionized water is manually added to the chamber to a level above the wick height, but lower than the dam height (as shown in Figure 4.2 (b)). The total volume of liquid inside the chamber reduces slightly during degassing and otherwise remains constant through the duration of the test. Before running the test, the top of the chamber is sealed and the heat input to the immersion heaters is turned on to vigorously boil and degas the liquid inside the chamber while keeping the valve to the Graham condenser open to atmosphere. The Graham condenser allows pure vapor to condense back to the chamber while purging non-condensable gases. Towards the end of the degassing process, small air bubbles no longer appear in the chamber, and only larger vapor bubbles that nucleate off the immersion heaters remain. After degassing, the valve to the Graham condenser is closed, sealing the test chamber from the surrounding ambient. The metering valve is opened to adjust the flow rate of the coolant into the condenser coil within the chamber; this controls the pressure within the chamber. The pressure inside the chamber is actively adjusted to be slightly above ambient throughout the duration of the test. In this manner, a saturated environment is maintained within the chamber.

To acquire a boiling curve, the power input to the cartridge heaters within the heater block is increased in steps. At each input power level, the system is allowed to reach a steady state, which is defined to have been achieved when the rate of change of the temperatures in the heater block are within 0.1 C/min, measured over a period of 10 min. The temperatures and pressures are recorded at steady state. The power input level is increased till a dryout heat flux is reached. Dryout is characterized by a sudden overshoot in surface temperature, which happens when the wick is no longer capable of feeding liquid to the heat input area.

When water is initially filled to a level above the wick and no evaporation is occurring, the wick becomes flooded as the small gravitational pressure head drives the fluid through the pores of the wick. After the heat input to the heater block is turned on, a certain minimum value of heat flux is required for the rate of evaporation from the wick to match the rate of gravitational liquid feeding from the surrounding reservoir. Above this heat flux, the liquid completely recedes into the evaporator wick, forming menisci on the wick surface that drive operation in a capillary-fed regime. The influence of gravitational liquid feeding on the maximum dryout heat flux can be confirmed to be negligible based on a simple comparison of the gravitational pressure head to the capillary pressure ($P_c = 2\sigma/r_p$, where r_p is the pore radius calculated based on the average particle diameter). This calculation confirms that the capillary pressure is ~60 times higher than the gravitational pressure head, based on the liquid level being maintained at ~ 1 cm above the wick for the duration of the test.

4.2.4 Data Reduction and Uncertainty Characterization

The heater block (Figure 4.3 (b)) has three thermocouples along the neck to measure the heat flux using a linear fit

$$q^{"} = -k_{Cu} \left. \frac{\partial T}{\partial x} \right|_{linear} \tag{4.1}$$

The substrate temperature is then calculated using an extrapolation of the thermocouple reading closest to the substrate (T_1) as,

$$T_{sub} = T_1 - q^{"} \left(\frac{x_1}{k_{Cu}} + \frac{t_s}{k_s} \right) \tag{4.2}$$

where x_1 is the distance from the solder joint to thermocouple location T_1,

The thermal resistance of the wick is characterized based on the difference in temperatures of the substrate and the vapor space,

$$R_{wick} = \frac{T_{sub} - T_{vap}}{q^{"} A_h} \tag{4.3}$$

where the temperature of the vapor space is taken as the average of the two thermocouple readings, which is confirmed to be equal to the saturation temperature calculated based on the measured vapor pressure inside the chamber.

A comprehensive uncertainty analysis is carried out to calculate the uncertainty propagation from the sensor measurements to the heat flux, substrate temperature, and resistance calculations, following Brown *et al.* [70]:

$$U_{R_{wick}} = \left(\frac{{U_{T_{sub}}}^2}{\left(T_{sub} - T_{vap}\right)^2} + \frac{{U_T}^2}{\left(T_{sub} - T_{vap}\right)^2} + \frac{{U_{q^{"}}}^2}{q^{"2}} \right)^{1/2} R_{wick} \tag{4.4}$$

where,

$$U_{q^{"}} = \left[\sum_{i=1}^{3} \left(\frac{\partial q^{"}}{\partial T_i} \right)^2 {U_T}^2 + \sum_{i=1}^{3} \left(\frac{\partial q^{"}}{\partial x_i} \right)^2 {U_x}^2 \right]^{1/2} \tag{4.5}$$

$$U_{T_{sub}} = \left[{U_T}^2 + \left(\frac{x_1}{k_{Cu}} + \frac{t_s}{k_s} \right)^2 {U_{q''}}^2 + \left(\frac{q''}{k_{Cu}} \right)^2 {U_x}^2 \right]^{1/2} \tag{4.6}$$

Equations (4.5) and (4.6) respectively show the uncertainties in the heat flux (slope of the linear fit) and substrate temperature (extrapolated from intercept); the complete expressions for the derivatives in equation (4.5) can be found in Ref. [70]. The thermocouples are calibrated using a Jupiter 4852 dry block calibrator for a wide range of temperatures from 50 – 200 °C. For each set value in the calibrator, the thermocouples are allowed to reach steady state and the voltage readings are recorded. The voltage readings are converted to temperature values using the ITS-90 standard polynomial curve for T-type thermocouples. Based on the difference between the set values and the measured thermocouple values, the uncertainty in the thermocouple measurements, U_T, is taken as ± 0.3 K. The uncertainty in the position of the thermocouple, U_x, is taken as ± 0.2 mm, based on the clearance between the thermocouple probes and machined insertion holes.

4.3 Results

Thermal test results for three different cases are reported: a baseline wick with a homogeneous, single layer of sintered particles over the evaporator area, and two-layer evaporator wicks with two different liquid-feeding post array designs. Figure 4.4 shows a plan view of these wicks. All the wicks are sintered on 38.1 mm × 38.1 mm square copper substrates and cover the central 30 mm × 30 mm area. The evaporator wick covers the central 10 mm × 10 mm heated area, while the 1500 μm thick surrounding feeding wick is the same across all the designs. The baseline homogeneous wick shown in Figure 4.4 (a) has a thin layer of sintered particles in the evaporator area, with a thickness equal to the base wick thickness (200 μm) in the two-layer designs. This wick is fabricated by first using sintering to make the 1500 μm thick wick (Figure 4.1 (b)), followed by laser machining the middle 1 cm^2 area to leave the 200 μm thick layer behind. The choice of dimensions across the three wicks tested allows direct evaluation of the efficacy of the additional liquid-feeding and vapor venting features included in the two-layer designs. Two designs of the two-layer wick (shown in Figure 4.4 (b) and (c)) are tested: a 5 × 5 post array design (d_{post} = 1 mm, d_{vent} = 1 mm) and a 10 × 10 post array design (d_{post} = 0.5 mm, d_{vent} = 0.5 mm). The posts are uniformly arranged in a square array over the 1 cm^2 evaporator area and the vents are offset from the posts. Other dimensions of the two-layer wicks that are kept the same in these two designs are:

t_{base} = 200 μm, t_{cap} = 800 μm, t_{bulk} = 1500 μm, and t_{post} = 500 μm. The choice of two-layer wick designs is informed by the reduced-order thermal-fluid transport model that was developed previously. This model revealed that the maximum pressure drop is incurred by fluid flow through the thin base layer and the formulation of this base layer can significantly affect the dryout heat flux. Moreover, increasing the liquid-feeding post array size from 5 × 5 to 10 × 10 was shown to support an increase in the dryout heat flux, because denser post arrays reduce the size of the evaporator area that each post must feed.

4.3.1 Baseline Single-Layer Evaporator Wick

The homogeneous evaporator wick, with no liquid feeding or vapor venting features, is first tested to serve as a benchmark against which to compare the two-layer wicks. Thin single-layer evaporator wicks can provide a low thermal resistance, but cannot sustain capillary-fed boiling over large heat input areas at high heat fluxes due to restricted liquid feeding from the periphery.

The black curves in Figure 4.5 (a) and (b) respectively show the boiling curve (measured heat flux versus substrate superheat) and the thermal resistance data for the homogeneous wick. With increasing heat flux, the substrate temperature increases monotonically. Nucleate boiling was visually observed within the capillary-fed wick at the first steady heat flux of ~ 24 W/cm^2 (at a substrate superheat of 3.1 K), and for all subsequent steady-state data during the test. At low heat fluxes (< 45 W/cm^2), the slope in the boiling curve is linear and the thermal resistance remains almost constant at ~0.118 K/W. After this initial linear rise in superheat with heat flux, a distinct reduction in the slope of the boiling curve is observed at heat fluxes great than > 45 W/cm^2, which corresponds to an increase in the wick resistance, as seen in Figure 4.5 (b).

Visualizations from high-speed videos are used to identify and explain the mechanism that causes this increase in thermal resistance when the homogeneous wick is in the capillary-fed boiling regime. Figure 4.6 shows top-down images of the wick extracted from the high-speed videos at different steady values of heat fluxes for the homogeneous wick, along with representative cross-sectional schematic diagrams explaining the associated boiling regimes observed in the evaporator wicks. At 45 W/cm^2 and below, the entire 1 cm^2 heated area of the wick undergoes boiling while being fed by the surrounding bulk wick. This is seen in the image taken at 45 W/cm^2 in Figure 4.6 (a); the apparent shiny surface of the wick here indicates that liquid menisci are sustained near the top of the saturated wick surface during capillary feeding. This mode of operation, described by the corresponding diagram in Figure 4.6 (a) and characterized by boiling occurring over the entire heated area, maintains a constant and low value of thermal resistance. As the heat flux increases, a dry spot forms in the middle of the heated area, as shown in the image at 65 W/cm^2 (Figure 4.6 (b)). The wick is not able to sustain this heat flux over the large heat input area and hence starts to dry out in the region farthest from the edge of the wick. This partial dryout phenomenon causes a rise in thermal resistance. With further increases in heat flux, the dry spot grows to nearly the size of the entire heated area. The image taken at the last steady data point, 98 W/cm^2 (Figure 4.6 (c)), shows that the heated area is almost completely dry, with boiling observed only at the edges. A small increase in heat input above this last steady heat flux causes the surface temperature to rise dramatically due to complete dryout of the wick. The test is stopped after the wick appears completely dry in the visualization.

This phenomenon of local or partial dryout has been previously observed during capillary-fed boiling in single-layer porous wicks over relatively large heat input areas. Nam *et al.* [71] reported partial dryout in micro-post wicks and observed that nano-structuring the posts helped to delay the onset of partial dryout owing to enhanced capillary performance. Cai and Chen [72] observed local dryout in carbon nanotube biporous wick structures for larger input areas (1 cm^2) but did not observe it for smaller hotspots (0.04 cm^2). When boiling occurs in a capillary-fed wick, the area furthest from the edge of the heated area (from where it is drawing liquid) dries out first. This is due to the larger pressure drop that is incurred to feed liquid over the longer distance to the center of the heated area.

4.3.2 Two-Layer Evaporator Wick

Figure 4.5 shows the boiling curves and the wick thermal resistance for the 5 × 5 and 10 × 10 post array designs. Unlike the single-layer wick that dries out partially at low heat fluxes, causing an unfavorable increase in thermal resistance, both these two-layer wick designs exhibit a low resistance for the entirety of the boiling curve. It can be seen that there is a small reduction in the thermal resistance with increasing heat flux up to ~100 W/cm^2, after which it remains nearly constant (at a low value of 0.1 K/W) for both two-layer wicks. The thermal resistance curves confirm that partial dryout does not occur in the two-layer wick. This favorable suppression of partial dryout over the heated area is due to liquid feeding from the cap layer through the vertical posts that uniformly distribute liquid to the thin base layer below. In addition, the thermal resistance (~0.1 K/W) of the two-layer wicks is similar to that value for the thin single-layer wick prior to partial dryout when the entire heater area was boiling (as shown and represented in Figure 4.7 (a)). Hence, it can be inferred that there is no adverse effect due to the additional feeding features in the two-layer wick, including the posts and cap layer, because they are designed to minimizing the impedance to vapor outflow while providing top-down liquid supply. A small increase in the heat flux above the highest steady-state result for the two-layer wicks results in a sudden overshoot in the substrate temperature. For the 5 × 5 wick, dryout caused the substrate temperature to increase from ~115 °C to ~135 °C without reaching a steady state. The test was stopped due to this observation of a sudden temperature overshoot. The dryout heat flux of the two-layer wicks is compared against the homogeneous wick at the onset of partial dryout: the 5 × 5 design has a dryout heat flux of 151 W/cm^2 at 0.095 K/W, which is ~3.4 times larger than the onset of partial dryout in the single-layer wick (45 W/cm^2 at 0.113 K/W); the 10 × 10 design has an even higher dryout heat flux of 198 W/cm^2 at 0.105 K/W, a ~ 4.4 times enhancement over the baseline.

High-speed visualizations and the corresponding images shown in Figure 4.7 reveal the capillary-fed boiling behavior and confirm that the liquid and vapor phase are separated during high-heat-flux operation with this two-layer design, thus providing an unimpeded pathway for vapor to escape through the vents without disrupting the liquid feeding. The two-layer evaporator wick designs exhibit notably different boiling mechanisms compared to the homogeneous wick. At low heat fluxes, active bubbling can be seen to occur up through the vents of the wick, as shown in the image at 98 W/cm^2 in Figure 4.7 (a). The surrounding cap layer appears shiny, indicating that it is saturated with liquid. It can be inferred that the spaces between the posts within the two-layer wick remain filled with liquid during this initial stage, causing bubbling through the vents as drawn in the schematic diagram in Figure 4.7 (a). The measured resistance in this regime, where saturated liquid is present within the spaces of the wick, is ~ 0.115 K/W. As the heat flux is increased, a fraction of the vents stop bubbling, as seen in the image at 152 W/cm^2 (Figure 4.7(b)). This indicates that the liquid inside the open spaces of the two-layer wick has started to recede into the surrounding wick, thus leading to a regime where jets of vapor are ejected out of the vents, as drawn in the corresponding schematic diagram. This causes a slight decrease in thermal resistance in this regime, due to the reduced impedance to vapor flow. With further increases in heat flux, bubbling is not seen in the vents (see the image at 198 W/cm^2 in Figure 4.7 (c)), indicating that vapor fills the spaces within the wick. In this separated flow regime, the vapor has an unimpeded flow pathway through the gaps between the posts and out through the vents; the wick resistance is a minimum. It is important to note that the base layer of the wick is still boiling in this regime, as inferred from the low value of wick resistance and observation of bubbling in the base layer seen though the vents. There is no occurrence of a local or partial dryout in the two-layer wick, which would otherwise have caused an increase in thermal resistance, and the posts are able to continually feed the entire base layer during high-heat-flux boiling operation. After the last steady data point at 198 W/cm^2, there is a sudden rise in substrate temperature due to a complete dryout of the base wick layer.

The two-layer wick investigated here has a different behavior compared to other hybrid wicks with enhanced lateral liquid-feeding features that have been previously reported in the literature. Hwang *et al.* [23] evaluated wicks having lateral converging arteries that supply a thin base wick layer. They reported an increase in thermal resistance with increasing heat fluxes, signifying partial dryout of the thin layer. In this design, the lateral direction of feeding to the center of the evaporator area allows for starvation of the base wick at high-heat-fluxes, causing partial dryout. In contrast, the current two-layer wick design has a top-down feeding approach where the posts are evenly distributed over the base layer, providing uniform liquid supply to the entire base layer from the thick cap layer. This top-down feeding approach avoids local/partial dryout and the associated thermal resistance penalty.

4.4 Conclusions

Capillary-fed boiling heat transfer in a novel, two-layer evaporator wick structure proposed by the authors is experimentally studied. A novel capillary-fed boiling experimental setup is developed that simulates the conditions near the evaporator region within a vapor chamber. Three designs of evaporator wicks are tested: a single-layer wick and two designs of the two-layer evaporator wick. The experiments are aided by high-speed visualization to image the evaporator area. The major findings from this study are listed below:

1. The single-layer wick exhibits partial dryout; *i.e.*, dryout in the center of the wick causes an increase in the measured thermal resistance. The dry region expands as the heat flux increases, and ultimately leads to a complete dryout event. The two-layer wicks avoid the

occurrence of partial dryout owing to distributed flow to the entire heated region; a single complete dryout event is observed at much higher heat fluxes.

2. The two-layer wicks extend the dryout heat flux of the single-layer wick while maintaining the same value of boiling thermal resistance as the single-layer wick. This indicates that the feeding structures (*viz*., the posts and cap layer) impose no additional resistance over the boiling resistance of the thin base layer.
3. Denser arrays of liquid feeding posts in the two-layer wick provide an improvement in the dryout heat flux, due to more distributed liquid feeding to the base layer. The 5 × 5 two-layer wick dried out completely beyond 151 W/cm^2 while dryout was extended in the 10 × 10 two-layer wick up to 198 W/cm^2.
4. High-speed visualization images helped identify different boiling regimes during the capillary-fed operation of the single- and two-layer wicks. While partial dryout was observed for the single-layer wick, the two-layer wick operates in a separated-flow regime during high-heat-flux operation. In this mode, the liquid-feeding and vapor removal mechanisms are separated, offering unimpeded flow pathways for liquid and vapor.

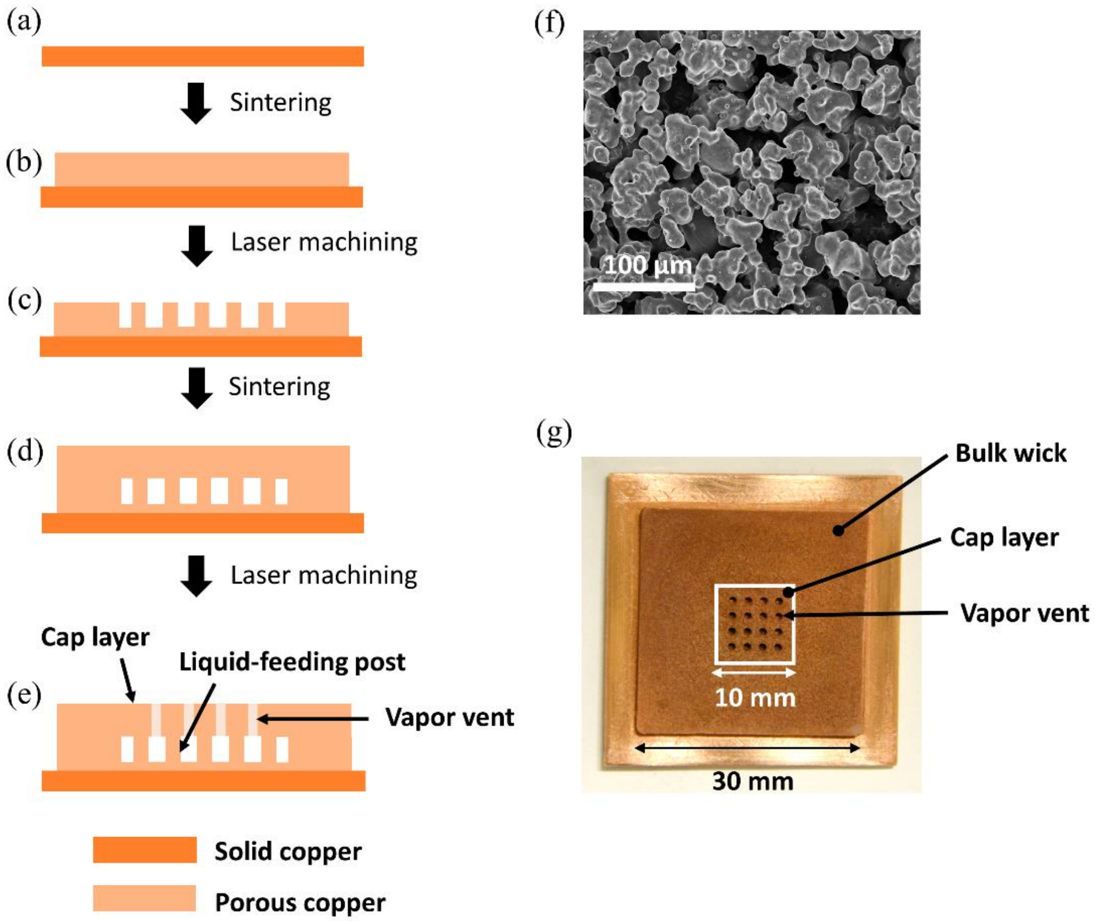
(a)
Sintering
(b)
Laser machining
(c)
Sintering
(d)
Laser machining
Cap layer
Liquid-feeding post
(e)
Vapor vent
Solid copper
Porous copper
(f)
100 µm
(g)
Bulk wick
Cap layer
Vapor vent
10 mm
30 mm

Figure 4.1. Schematic diagrams showing the sequence of process steps in the fabrication of the two-layer wick: (a) copper substrate; (b) first sintering of porous copper layer; (c) laser machining to form liquid-feeding posts; (d) second sintering to add the cap layer; and (e) laser machining to form vapor vents. (f) An SEM image of the sintered copper particle morphology after step (b). (g) A top-down image of the fabricated two-layer wick.

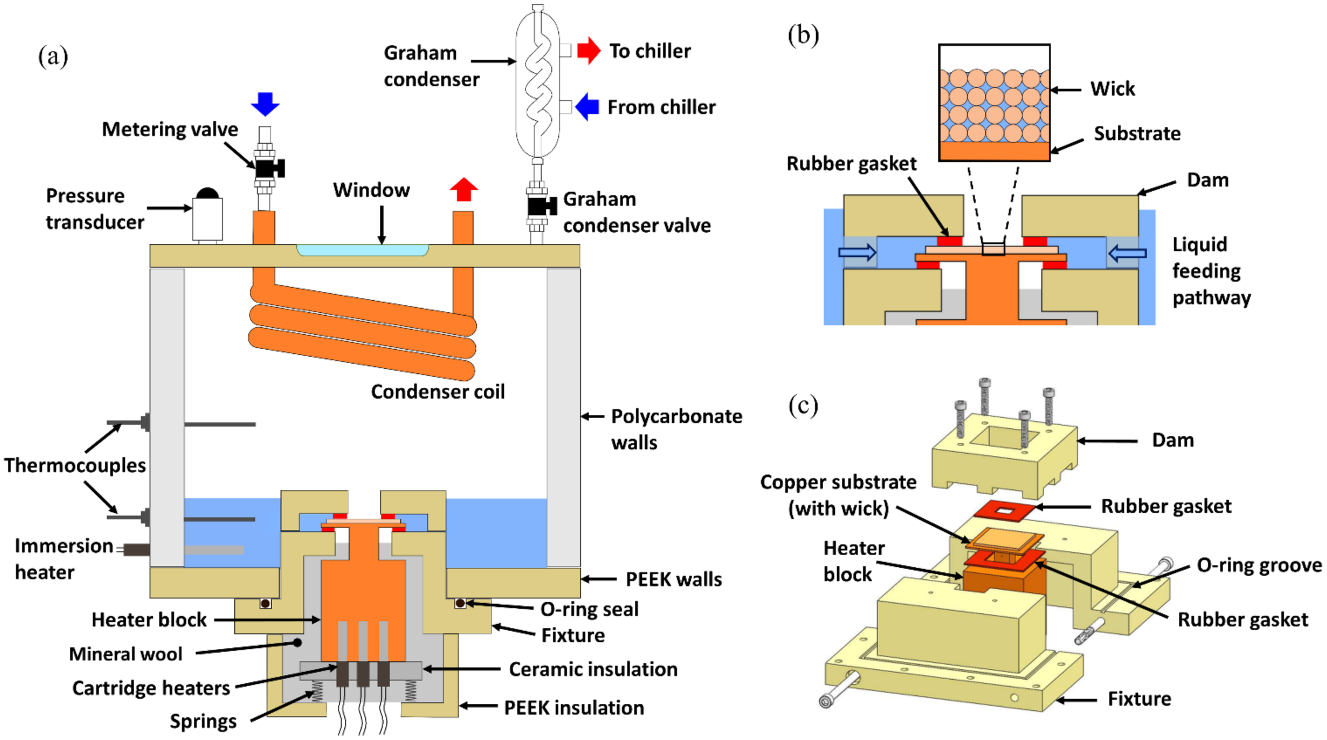
(a)
Graham condenser
To chiller
From chiller
Metering valve
Pressure transducer
Window
Graham condenser valve
Condenser coil
Polycarbonate walls
Thermocouples
Immersion heater
PEEK walls
O-ring seal
Fixture
Heater block
Mineral wool
Cartridge heaters
Springs
Ceramic insulation
PEEK insulation
(b)
Wick
Substrate
Rubber gasket
Dam
Liquid feeding pathway
(c)
Dam
Copper substrate (with wick)
Rubber gasket
Heater block
O-ring groove
Rubber gasket
Fixture

Figure 4.2. (a) Schematic diagram of the capillary-fed boiling test facility that consists of a heater assembly inserted into the bottom wall of a saturated test chamber, with important components labeled. (b) Zoomed-in view near the wick fixture showing the liquid flow pathway from the periphery to the evaporator region; the dam prevents flooding over the top of the wick. (c) Exploded three-dimensional drawing of the heater assembly.

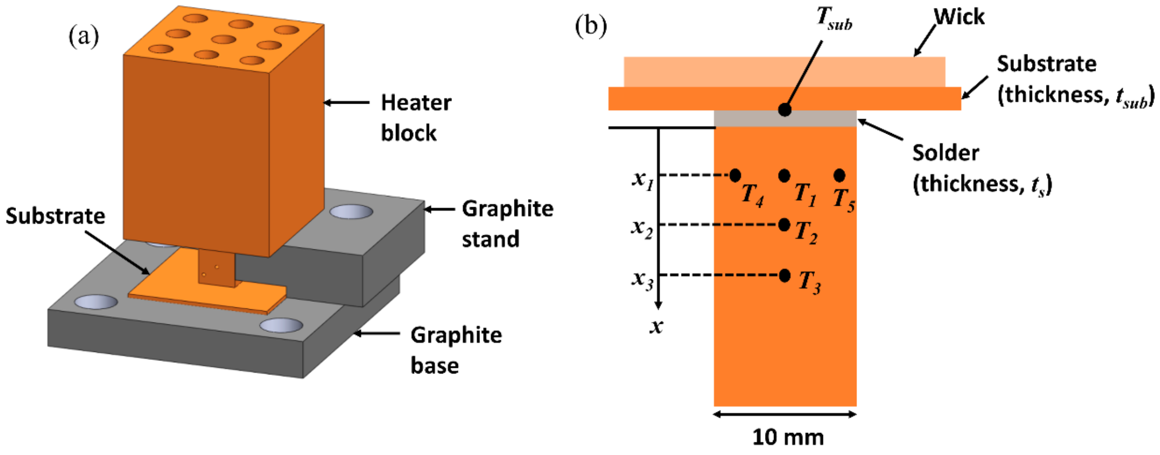
(a)
Heater block
Substrate
Graphite stand
Graphite base
(b)
T_{sub}
Wick
Substrate (thickness, t_{sub})
Solder (thickness, t_s)
x_1
x_2
x_3
x
T_4
T_1
T_5
T_2
T_3
10 mm

Figure 4.3 (a) An isometric view of the soldering assembly used to form a thermal connection between the wick substrate and the heater block. The substrate of the wick is held on a graphite base while the heated block is centered on it using a graphite stand. (b) A close-up view of the thermocouple locations (T_1-T_5) and important dimensions of the heater block neck (not-to-scale).

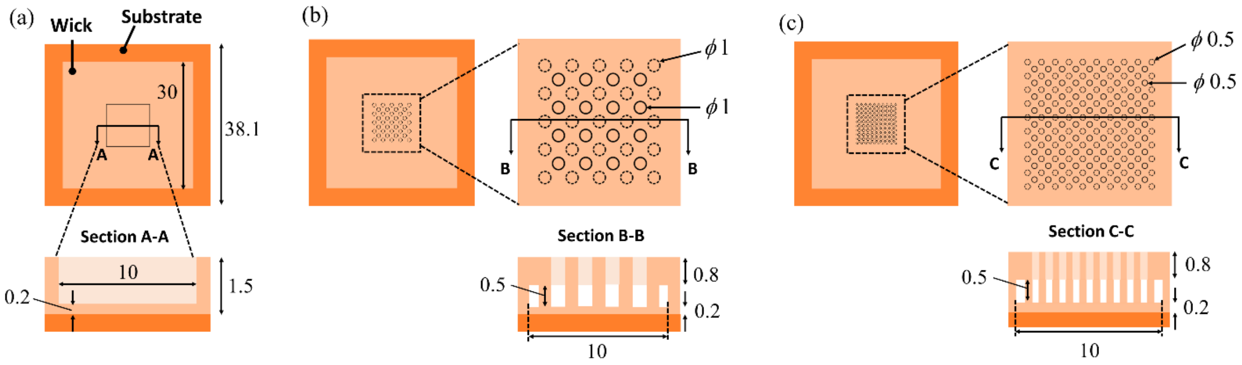
(a)
Wick
Substrate
30
38.1
A
A
Section A-A
10
0.2
1.5
(b)
ϕ 1
ϕ 1
B
B
Section B-B
0.5
0.8
0.2
10
(c)
ϕ 0.5
ϕ 0.5
C
C
Section C-C
0.5
0.8
0.2
10

Figure 4.4. Plan view and sectioned side view schematic diagrams (dimensions in mm) of the (a) single-layer evaporator wick and the (b) 5 × 5 and (c) 10 × 10 two-layer wick designs. For the two-layer wicks, the plan view is enlarged near the evaporator region to show the features: solid circles represent the vents in the cap layer, while the dashed circles represent the posts below the cap layer. The plan view diagrams are drawn to scale; the side view sections are not drawn to scale.

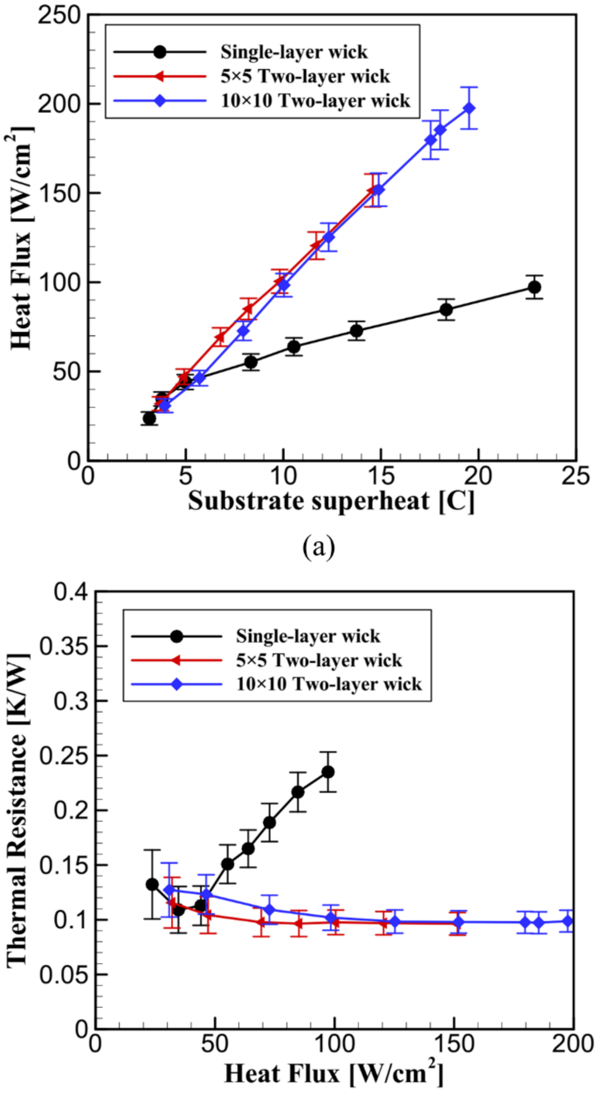

(a)

(b)

Figure 4.5. Steady-state (a) capillary-fed boiling curves and (b) wick thermal resistance as a function of input heat flux for the baseline single-layer wick and two-layer wicks. The last point in each curve represents the final steady-state data before the occurrence of complete dryout event. The error bars represent the measurement uncertainties.

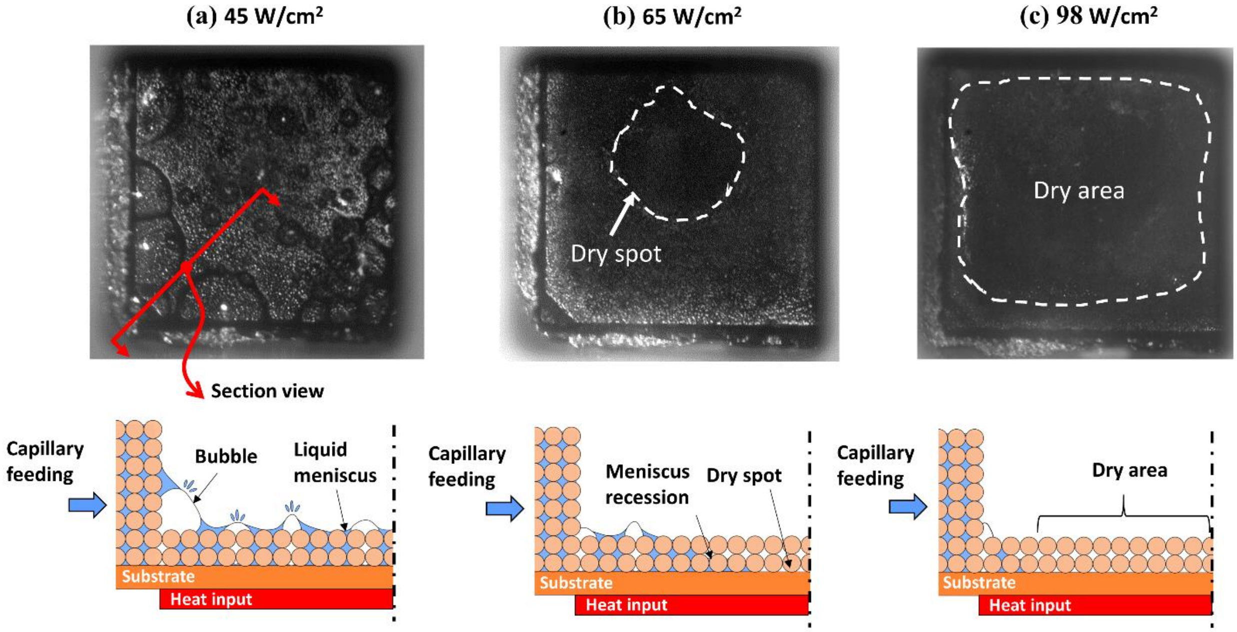
(a) 45 W/cm²
(b) 65 W/cm²
(c) 98 W/cm²
Dry spot
Dry area
Section view
Capillary feeding
Bubble
Liquid meniscus
Substrate
Heat input
Capillary feeding
Meniscus recession
Dry spot
Substrate
Heat input
Capillary feeding
Dry area
Substrate
Heat input

Figure 4.6. Series of images captured by the high-speed visualization setup, at (a) 45 W/cm^2, (b) 65 W/cm^2 and (c) 98 W/cm^2, showing the 1 cm^2 heated area of the single-layer wick as viewed from the top. Section-view schematic diagrams are shown at each steady heat flux to illustrate the different boiling regimes in the wick.

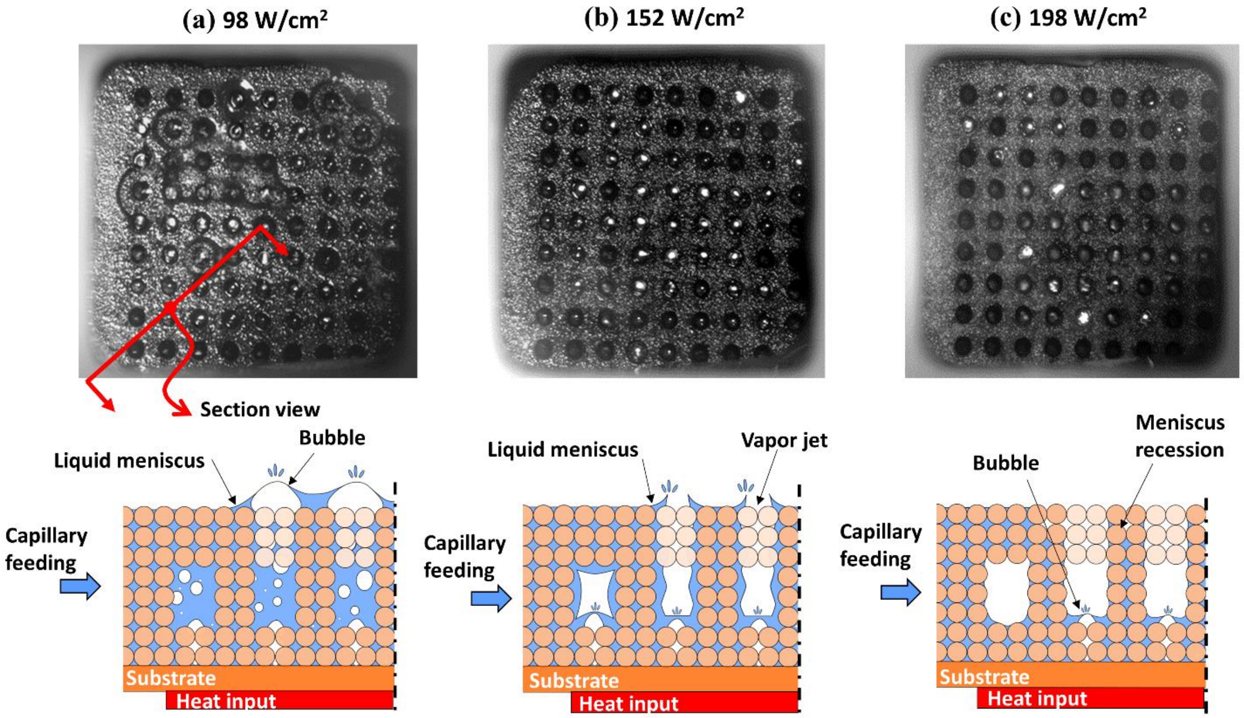
(a) 98 W/cm²
(b) 152 W/cm²
(c) 198 W/cm²
Section view
Liquid meniscus
Bubble
Capillary feeding
Substrate
Heat input
Liquid meniscus
Vapor jet
Capillary feeding
Substrate
Heat input
Meniscus recession
Bubble
Capillary feeding
Substrate
Heat input

Figure 4.7. Visualization images showing the 1 cm^2 heated area of the two-layer wick as viewed from the top, at (a) 98 W/cm^2, (b) 152 W/cm^2 and (c) 198 W/cm^2. Section-view schematic diagrams are shown to illustrate the different regimes of boiling in the wick.

5. AREA-SCALABLE HIGH-HEAT-FLUX DISSIPATION AT LOW THERMAL RESISTANCE USING A CAPILLARY-FED TWO-LAYER EVAPORATOR WICK

The current chapter demonstrates high-heat-flux dissipation using the two-layer evaporator wick previously introduced. The fabrication steps and the internal structure of the two-layer wick are first described, and the effect of sintered particle size on the capillary-fed boiling behavior is then studied for a benchmark single-layer wick. Subsequently, a two-layer wick composed of the best-performing particle size is characterized and its performance compared to the literature. The material is this chapter is published in the *International Journal of Heat and Mass Transfer* [73].

5.1 Characterization and Imaging of the Two-Layer Wick Structure

While most of the prior hybrid evaporator wicks have been fabricated using copper particles sintered in a single step [13,23], the two-layer wick required two separate sintering processes. It is thus critical to confirm that sintering yielded connectivity between the layers of the wick, as required for the desired top-down liquid-feeding to function. In addition, it is important to ensure proper alignment between the layers and confirm that the vapor vents were offset from the posts. Furthermore, the effect of laser ablation on the morphology of the sintered copper wick is characterized to confirm that the primary liquid-feeding path was not impeded. Hence, this section briefly describes the laser machining parameters that were used for fabrication and investigates the internal structure of an as-fabricated two-layer wick through scanning electron microscopy (SEM) and micro-computed tomography (μ-CT) scanning. To destructively investigate the internal structure and surface characteristics resulting from this fabrication approach, an additional two-layer wick sample was fabricated with a 4 × 4 array of liquid feeding posts and an offset 3 × 3 array of vents.

The laser machining process is briefly described here and the laser parameters specified. A multi-wavelength fiber laser (Universal Laser Systems PLS6MW, Birck Nanotechnology Center, Purdue University) is used to ablate the sintered wick to form the features. In each pass across the surface, the laser ablates a portion of the material and achieves a depth on the order of tens of microns. Multiple passes of the laser are required to fabricate the posts and the vents in the two-layer wick having heights on the order of hundreds of microns. The laser power and raster speed can be controlled to affect the ablation depth during each pass. A fabrication recipe was developed by varying the laser power and speeds to identify a combination that gave a near-linear relationship between the ablation depth and number of passes. This recipe was tuned specifically to each sintered particle size and then employed to control the depth. The structure of a two-layer wick fabricated with 90-106 μm particles and a combination of 70% laser power and 10% raster speed is presented below.

5.1.1 SEM Imaging of the Liquid-Feeding Posts and Vapor Vents

The structure of the liquid-feeding posts and the vapor vents is revealed from SEM images. Figure 5.1 (b) shows a perspective view of a liquid-feeding post (d_{post} = 1 mm) fabricated by ablating away the material surrounding the post; this SEM was taken before the cap layer was attached. In the ablated region surrounding the post, the remaining sintered base wick layer remains porous, with only a slight morphology change compared to the as-sintered surface seen at the top of the post. The image in Figure 5.1 (b) also reveals that the laser ablation fuses a thin ring of particles around the sidewalls of the post, perpendicular to the direction of laser movement, but the native sintered wick morphology and porosity within the post is preserved. While the sides of the posts are nearly fused shut and have only a few open pores, this would not impede the primary liquid flow path through the porous core of each post. Figure 5.1 (c) shows a perspective view of a vapor vent (d_{vent} = 1 mm). The sidewall of the vent is fused, as in the case of the posts, while the surrounding bulk wick in the cap layer is unaffected. Despite the side walls being fused, evaporation is not required from the side surfaces of the posts or vents, and therefore, the lack of open pores on these surfaces is not expected to affect the thermal performance (and may even assist in preventing liquid entrainment into the vapor flow pathways). We have thus confirmed that the laser machining process successfully achieves the necessary features for top-down liquid feeding and vapor venting.

To check the alignment between the posts and the vents after fabrication, a quarter section was cut out from the full two-layer wick sample and imaged. To prevent abrasion damage to the sintered particles, this sectioning was achieved using the laser to cut through the entire two-layer wick thickness and solid copper substrate. Figure 5.1 (d) shows a perspective cutaway view of the sectioned two-layer wick. The liquid-feeding posts are seen to be present underneath the cap layer and offset from the vents. The base wick layer thickness above the substrate is also visible.

5.1.2 μ-CT Scans of the Two-Layer Wick

The internal structure of the evaporator wick was investigated by μ-CT scanning (Bruker Skyscan 1272) in the Center for Particulate and Powder Processing at Purdue University. A low-resolution scan (1632 × 1092 pixels; 16.4 μm voxels) was performed to check the alignment and connectivity of the posts and vents, as well as the presence of the thin base layer. Figure 5.2 (a) shows a schematic diagram of a plan view of the two-layer wick sample fabricated for μ-CT scanning. Figure 5.2 (b) shows a series of slices obtained from the reconstruction at different locations along the two-layer wick. Figure 5.2 (c) shows representative schematic diagrams of the two-layer wick cross section at the same locations as the slices in Figure 5.2 (b), to help identify the critical features in each of the scan images. Slice 1 is through the bulk wick in a region outside of the 1 cm^2 two-layer evaporator wick area. A monolithic layer of porous particles is seen, with a well-connected seam formed when sintering the cap layer onto the layer below. Slice 2 is taken though the two-layer wick at a section where there are no post or vent features. The thin base layer is sintered to the substrate underneath the cap layer, with these layers separated by an internal gap equal to the height of the liquid-feeding posts. The μ-CT scan has some artificial noise within this gap above the base layer due to the difficulty for X-rays to penetrate through the solid copper. The vapor vents and the liquid-feeding posts are visible in slices 3 and 4, respectively. There is some tapering of the post and vent sidewalls that results from the laser machining process, which is not material to their intended functioning. Importantly, the posts are seen to be well-sintered to the cap layer, providing a continuous pathway for top-down liquid feeding to the thin base layer. Overall, the μ-CT scan images reveal that the sintering and laser machining processes are successful in ensuring the connectivity of the liquid-feeding features to the base wick layer. In addition, the features of the two-layer wick are confirmed to remain intact after fabrication.

5.2 Capillary-fed Boiling Experimental Characterization

5.2.1 Experimental procedures

The experimental facility, methods for soldering and sealing the wick into the facility, data reduction and uncertainty analysis was described comprehensively in Section 4.2. Prior to testing, the wicks are treated in a dilute piranha solution to strip the surface of any oxides and organic contaminants. The piranha solution is prepared by diluting 15 ml of 96% sulphuric acid (H_2SO_4)

and 5 ml of 30% hydrogen peroxide (H_2O_2) into 100 ml (total volume) aqueous solution. The wicks are soaked in the solution for 60 sec. The copper wicks are then rinsed in DI water and dried thoroughly with a compressed nitrogen gun. The wicks are then immediately sealed into the chamber. For each wick sample, the relationship between imposed heat flux and substrate temperature (boiling curve) is established, and the thermal resistance is determined at each heat flux. Each test is carried out by increasing the heat input in steps and allowing the system to reach steady state at each heat input value. The test is terminated when dryout is reached; dryout is characterized by a sudden rise in the substrate temperature that does not settle to a steady value. In this work, the substrate superheat at the first steady heat input value was high enough to initiate nucleate boiling in the wick; capillary-fed boiling occurs in all of the steady data points reported.

5.2.2 Single-Layer Wicks Testing: Effect of Sintered Particle Size

The reduced-order model for thermal-fluid performance of the two-layer wick, developed in Section 3.2 revealed that the maximum pressure drop occurs in the base wick layer, because of the small cross-sectional area available for fluid flow. Therefore, any change in the particle formulation of this thin porous base wick layer may result in significant changes in performance of the two-layer wick. We evaluate the effect of sintered particle size on capillary-fed boiling by fabricating three different single-layer wicks. Figure 5.3 shows plan and section views of the single-layer wick design. The wick has a thin, uniform layer of sintered particles over the central 1 cm^2 evaporator area; the thickness, t_{base}, is identical to the base layer thickness of the two-layer wick. This thin layer is supplied with liquid from the periphery by a thicker bulk wick (thickness t_{bulk}).

The wicks are fabricated by sintering a wick of thickness t_{bulk} over a square area with edge length l_{bulk}, followed by laser machining the middle 1 cm^2 region down to a thickness, t_{base}. Details of the three wicks tested are given in Table 5.1, fabricated from three different particle size ranges: 45-53 μm, 90-106 μm and 180-212 μm. Each single-layer wick in the table is denoted by a sample ID, which contains the particle size range followed by the thickness (t_{base}) of the evaporator region. The 90-106 μm and 180-212 μm single-layer wicks have two particle diameters across their thickness, while the 45-53 μm wick has four particle diameters across its thickness. Figure 5.4 shows SEM images of the sintered wicks for each different particle size range. The two smaller particle size ranges have irregular-shaped particles manufactured by water atomization, while the larger 180-212 μm particles contain a mix of spherical and irregular particle geometries. Table 5.1 also lists the porosity and a calculated value of permeability for the samples. The porosity is calculated by measuring the weight and volume of the sintered porous layer after sintering. The Carman-Kozeny equation ($K = D^2\varphi^3/(1-\varphi)^2$) is used to estimate the permeability, where D is the mean particle size and φ is the porosity of the wick.

Figure 5.5 (a) and (b) respectively show the boiling curve and wick thermal resistance for the three single-layer wicks. Each boiling curve is characterized by an initial near-linear slope, indicative of a constant thermal resistance and uniform capillary-fed boiling over the entire heat input area. For the two samples with smaller particle sizes, 45-53:200 and 90-106:400, at some heat flux, there is a reduction in slope of the boiling curve and increase in thermal resistance associated with partial dryout in the center of the wick. The trends in the thermal resistance before partial dryout, as well as the heat flux at which partial dryout occurs, are both monotonic with particle size. The wick with the smallest particle sizes, 45-53:200, has the highest resistance that is constant at ~0.27 K/W till dryout begins at ~ 54 W/cm^2, above which the thermal resistance increases with heat flux; complete dryout occurs at 115 W/cm^2. Wick 90-106:400 exhibits a lower constant thermal resistance of ~ 0.15 K/W up to 122 W/cm^2, after which partial dryout begins; complete dryout occurs at 175 W/cm^2. In contrast, partial dryout is not observed in wick 180-212:400 and the resistance is nearly constant (decreases slightly with increasing heat flux) throughout the test. After the last steady data point at 193 W/cm^2, at a wick resistance of 0.075 K/W, complete dryout is triggered.

The trend in wick resistance with particle size, over the range of heat fluxes before partial dryout, can be attributed to the impedance to vapor removal from the wick during boiling. Considering the low permeability of the smaller 45-53 μm particles, vapor escaping the wick incurs a large pressure drop as it flows up through the pore paths. Any pressure drop in the vapor corresponds to an increased saturation temperature drop across the wick thickness. Sample 180-212:400 has the highest permeability and therefore imposes the lowest hydraulic, and hence thermal, resistance. The increase in thermal resistance after the onset of partial dryout in each case is trivially explained from the visualizations; during the partial dryout regime, the center of the heated area is devoid of all liquid and capillary-fed boiling cannot occur in this region, resulting in an increased thermal resistance.

The effect of particle size in sintered coatings on pool boiling behavior has been extensively studied in the literature [74,66]. In addition, there have been detailed characterizations and statistical descriptions of sintered wick structures [75], and their effects on pool boiling [76]. However, few studies have addressed the effect of particle size during capillary-fed boiling; moreover, the wick types, heating area, and wick thicknesses differ between each of these studies. Weibel *et al.* [5] tested the thermal resistance of ~1 mm-thick sintered wicks with three different particle sizes and observed a minimum thermal resistance at an intermediate optimum particle size. Investigations on monolayer sintered porous wicks with different particle sizes performed by Ju *et al.* [13] revealed a higher wick resistance for lower particle sizes. Li *et al.* [6] considered sintered screen mesh wicks and reported that the dryout limit was higher for wicks with larger pore sizes. This was attributed to the decreased flow resistance to capillary flow if the wicks possessed larger pore sizes. In the present work, wick 180-212:400 gave the best boiling performance, providing the highest complete dryout limit along with a low value of thermal resistance. This is attributed to the high permeability of the wick, which allows for ease of liquid feeding. Although the capillary pressure is lower for larger particle sizes ($P_c \sim 1/D$), the effect of the larger wick permeability ($K \sim D^2$), outweighs the effect of the reduced capillary pressure for this evaporator design.

5.2.3 Two-Layer Wick Testing

A two-layer evaporator wick was fabricated with the 180-212 μm particle size range that provided the highest dryout heat flux among the single-layer wicks. It was shown in Section 4.3.2 that denser liquid-feeding post arrays provided a significant improvement in the dryout heat flux without a penalty in the wick resistance. Following this design rule, a two-layer wick with a 15 × 15 array of posts is fabricated to demonstrate high-heat-flux dissipation. Figure 5.6 shows a plan and sectioned side view of the two-layer wick design (identified as 180-212:15×15). The two-layer region is fabricated over a larger 15 mm × 15 mm area (denoted by $l_{two\text{-}layer}$ = 15 mm), while the heat input is the same 10 mm × 10 mm area in the center of the wick (denoted by l_{evap} = 10 mm). This larger two-layer region was used to take advantage of heat spreading in the substrate underneath the wick. A 3D conduction simulation was performed to select the larger two-layer wick region. This heat spreading analysis assumed a uniform heat flux over a 10 mm × 10 mm region on the underside of the substrate, and a uniform heat transfer coefficient on the top side (treating all other boundaries as insulated). The values of the heat transfer coefficient as a function of heat flux were specified based on the results in Section 4.3.2. A 15 mm × 15 mm region was identified as the optimal size for the two-layer wick region; further increases in this area would not further reduce the effective total thermal resistance via heat spreading, but would unfavorably increase the length over which capillary feeding would need to occur within the two-layer wick (likely reducing the maximum heat flux that could be dissipated). APPENDIX D includes the analysis performed to calculate the heat spreading area, and the effect of heat spreading on the total thermal resistance of the two-layer wick. In the facility, the dam that seals this wick has an enlarged 15 mm × 15 mm opening to allow unrestricted release of vapor. The important dimensions of the wick are as follows: d_{post} = 650 μm, d_{vent} = 500 μm, t_{post} = 400 μm, t_{cap} = 700 μm, and t_{base} = 400 μm (see Figure 5.6 for symbol definitions). The base wick thickness and particle composition are the same as in the 180-212:400 single-layer wick.

Figure 5.7 shows the boiling curve and the wick resistance for the two-layer wick (180-212:15×15). In Figure 5.7 (a), the two-layer wick shows a near-linear increase in wick superheat as the heat flux increases till ~130 W/cm^2, after which a change in slope is observed. At low heat fluxes, only the center heated area (10 mm × 10 mm) boils; once the heat flux exceeds ~130 W/cm^2, a larger area undergoes boiling, causing a reduction in the measured thermal resistance thereafter. Above a heat flux of ~240 W/cm^2, the two-layer wick maintains a near constant resistance; once the heat flux exceeds this value, the liquid recedes from the empty spaces between the posts in the wick into the cap layer and within the posts, providing separated pathways for liquid and vapor flow. In this desired mode of operation, the post and cap layers do not impose any additional thermal resistance. Ultimately, the two-layer wick achieves a dryout limit of 485 W/cm^2 at a low thermal resistance of 0.052 K/W. Sudden dryout is triggered beyond 485 W/cm^2 when the menisci in the liquid-feeding cap layer recede completely. It can be noted that partial dryout is not seen in the two-layer wick due to the uniform liquid supply over the entire heated area from the cap layer.

5.3 Discussion

The two-layer wick provides a combination of high-heat-flux dissipation from large heated areas along with a low thermal resistance. In this section, the thermal test results from the two-layer wick in this work are compared against various prior investigations reported in the literature on capillary-fed boiling in porous wicks. Figure 5.8 (a) shows a plot of the maximum heat flux dissipated as a function of heated area, from among the references listed in Table 2.1. This plot reinforces the inverse relationship between heater size and the dryout heat flux described in the introduction. Extremely high heat fluxes of ~700 W/cm^2 and higher have only been dissipated over very small hotspots of less than 10 mm^2. For example, the highest reported heat flux of ~1250 W/cm2 [77] was attained over a very small hotspot of 0.6 mm^2. As the heater sizes increase, the dryout heat fluxes are reduced. Cai and Bhunia [78] noted a decrease in dryout heat flux for carbon nanotube biporous wicks from 770 to 140 W/cm^2 for an increase in heater area from 4 mm^2 to 100 mm^2. Similarly, Nam *et al.* [20] reported that the dryout limit of nanostructured micro-post wicks decreased from ~800 W/cm^2 to 200 W/cm^2 when the heater size was increased from 4 mm^2 to 25 mm^2. In the case of a small hotspot (as opposed to a larger heating area), the liquid must be fed only over a small area of wick to avoid dryout. This reduced flow length significantly reduces the pressure drop in the wick. In addition, for a small hotspot, heat spreading in the underlying substrate plays a stronger role in effectively increasing the area available for phase change. For these reasons, the dryout limits are always lower for larger heater sizes. Consequently, there are only two reports of ~500 W/cm^2 heat dissipation over a relatively large, 1 cm^2 area. Hwang *et al.* [23] developed a sintered evaporator wick with lateral feeding arteries that supply liquid to a thin monolayer of sintered particles. They reported a maximum heat flux dissipation of 580 W/cm^2 over 1 cm^2, albeit at a high surface superheat temperature of 72 K due to the occurrence of partial dryout. The two-layer wick reported here provides a maximum heat flux dissipation of 485 W/cm^2 (star symbol in Figure 5.8 (a)) over 1 cm^2 heat input area, at a significantly lower superheat of only 25 K due to avoidance of partial dryout by the top-down liquid feeding approach.

A new capillary-fed boiling performance map is developed and shown in Figure 5.8 (b) to identify wick types that can simultaneously provide *high power* and *low thermal resistance* operation. This figure plots the thermal resistance at the maximum power level against the maximum total power dissipated. Data points in the region of the plot towards the bottom right indicate superior performance. Although various studies have shown high-heat-flux values, the total power dissipated has been low, owing to the smaller heater areas. In general, thick wicks with multiple layers of sintered particles can dissipate high powers but exhibit large thermal resistances, due to vapor clogging in the pore spaces of the wick during boiling [7]. Reductions in thermal resistance are achieved by providing separate, high-permeability pathways for vapor flow out of the wick, such as with grooved channels [22], grid-patterns [18] or high-permeability foams [16]. In comparison to all previous wicks tested in the literature, the two-layer wick (star symbol in

Figure 5.8 (b)) achieves a unique combination of high power dissipation (485 ± 27 W) combined with a low thermal resistance (0.052 ± 0.008 K/W).

5.4 Conclusions

This study demonstrated high-heat-flux passive dissipation using capillary-fed boiling in a two-layer sintered evaporator wick. The two-layer wick concept uses a thin base-wick layer combined with additional dedicated liquid-feeding and vapor-removal structures to separate the liquid feeding and vapor removal pathways in the porous wick during boiling. The two-layer wick was fabricated using a combination of sintering and laser machining process steps; SEM images and μ-CT scans were analyzed to characterize the as-fabricated internal structures of the two-layer wick. Three single-layer wicks having different particle sizes were fabricated and tested to determine the optimal size range given the strong influence of wick formulation on capillary-fed boiling performance. Increasing the particle size led to an increase in the dryout limit as well as a decrease in the thermal resistance during capillary-fed boiling. This was attributed to an increased permeability provided by larger particle sizes that offered a reduction in the flow impedance to both liquid feeding and vapor removal. To realize high-heat-flux dissipation, a two-layer wick with a 15 × 15 array of liquid-feeding posts was sintered using the largest (180-212 μm) particles. This two-layer wick dissipated a maximum of 485 W/cm^2 over 1 cm^2 at a thermal resistance of 0.052 K/W. Comparing this thermal performance to prior work reported in the literature on capillary-fed boiling reveals that the two-layer wick is able to provide an unprecedented combination of high total power heat dissipation at low thermal resistance.

Table 5.1. Properties of the single-layer sintered porous wicks.

Sample ID	**Particle sizes (μm)**	**Thickness, t_{base} (μm)**	**Measured porosity, φ**	**Calculated permeability, K (m^2)**
45-53:200	45-53	200	0.61	3.730×10^{-9}
90-106:400	90-106	400	0.61	1.433×10^{-8}
180-212:400	180-212	400	0.63	6.334×10^{-8}

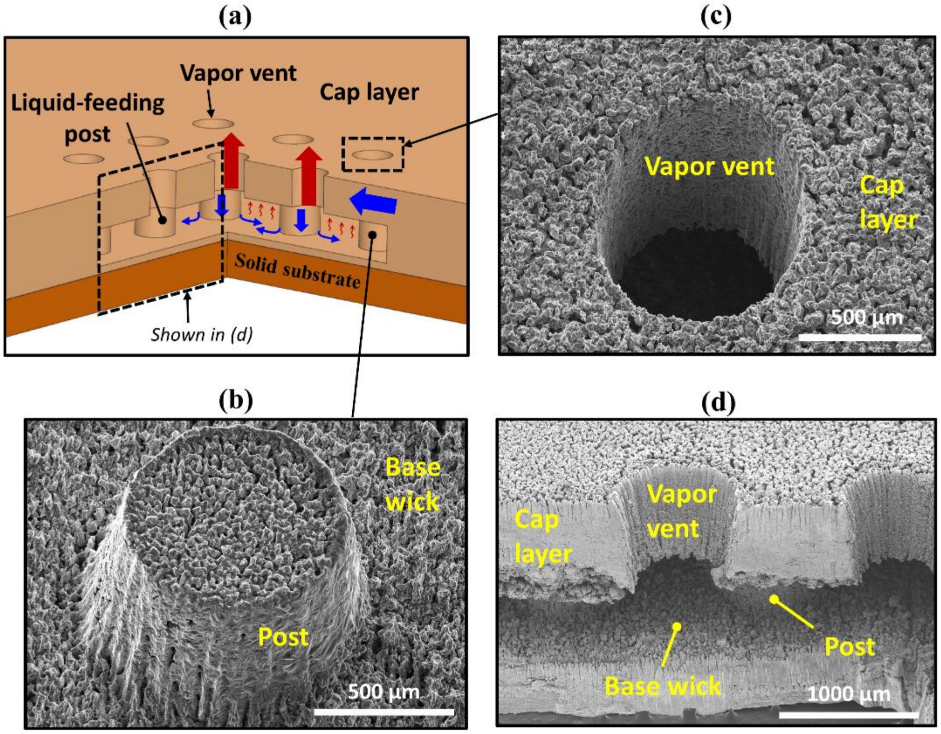
(a)
Vapor vent
Cap layer
Liquid-feeding post
Solid substrate
Shown in (d)
(c)
Vapor vent
Cap layer
500 µm
(b)
Base wick
Post
500 µm
(d)
Vapor vent
Cap layer
Post
Base wick
1000 µm

Figure 5.1. (a) Schematic diagram of a two-layer evaporator wick with a 4 × 4 array of liquid-feeding posts and an offset 3 × 3 array of vapor vents. The primary flow pathways for liquid (in blue) and vapor (in red) are indicated. SEM images are taken during the fabrication of the wick to show the structure of (b) a liquid-feeding post before the cap layer is attached and (c) a vapor vent in the cap layer. (d) An SEM image of a cutaway view of the sectioned two-layer wick sample.

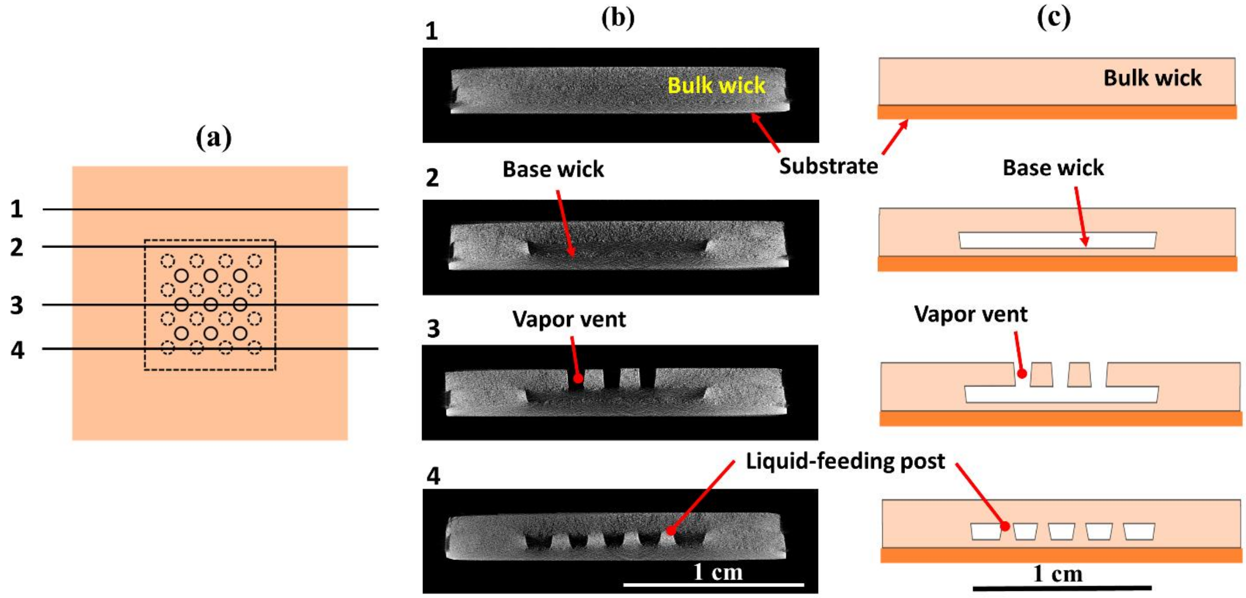
(a)
1
2
3
4
(b)
1
Bulk wick
Substrate
2
Base wick
3
Vapor vent
4
Liquid-feeding post
1 cm
(c)
Bulk wick
Base wick
Vapor vent
1 cm

Figure 5.2. (a) Plan view of the two-layer evaporator wick sample (4 × 4 posts, 3 × 3 vents) used for μ-CT scan imaging. (b) Reconstructed side-view slices from a μ-CT scan of the evaporator wick at different vertical cross-sections across the wick. (c) Schematic diagrams illustrating the different wick features identified in the scan images.

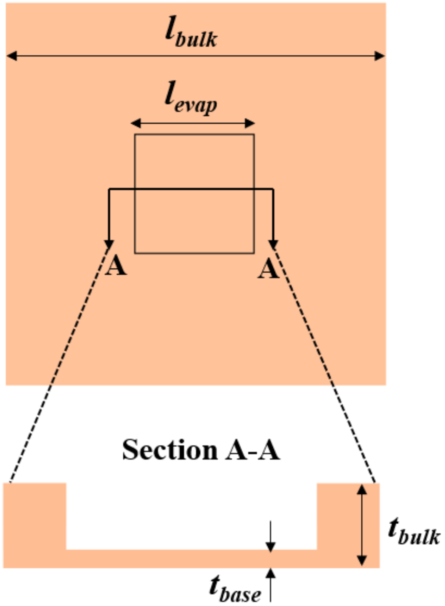
l_{bulk}
l_{evap}
A
A
Section A-A
t_{bulk}
t_{base}

Figure 5.3. Plan and section view diagrams of the single-layer wick design. The single-layer wick has a thickness t_{base} over the central evaporator area, supplied by a thicker bulk wick of thickness t_{bulk}.

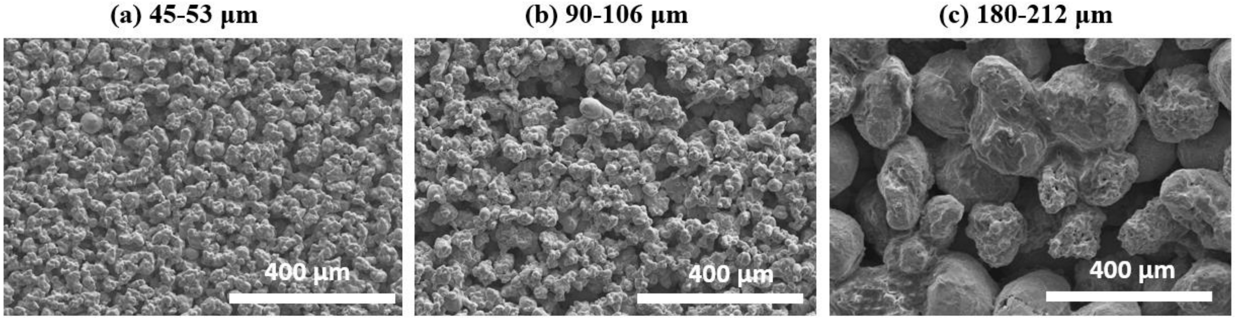
(a) 45-53 µm
(b) 90-106 µm
(c) 180-212 µm
400 µm
400 µm
400 µm

Figure 5.4. SEM images of sintered wicks with different particle size ranges of (a) 45 – 53 μm, (b) 90 – 106 μm, and (c) 180 – 212 μm.

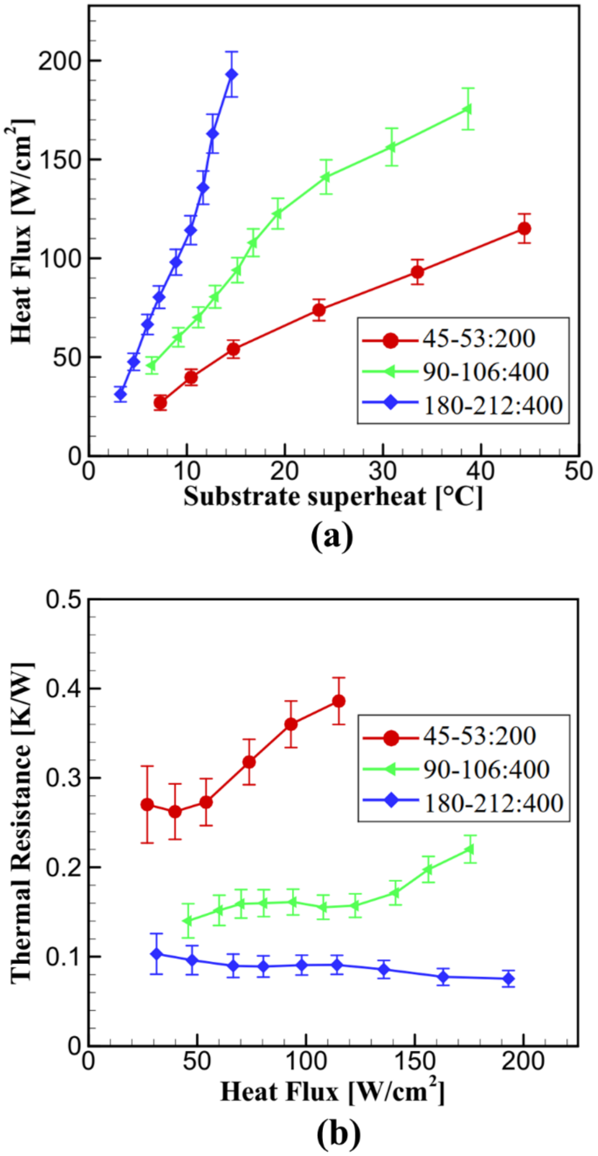

Figure 5.5. (a) Capillary-fed boiling curves and (b) wick resistance versus heat fluxes for the three single-layer wick designs, each sintered with a different particle size range. The error bars represent the uncertainty in the measured heat flux and the wick resistance. The legend nomenclature indicates the particle size range and the wick thickness in microns.

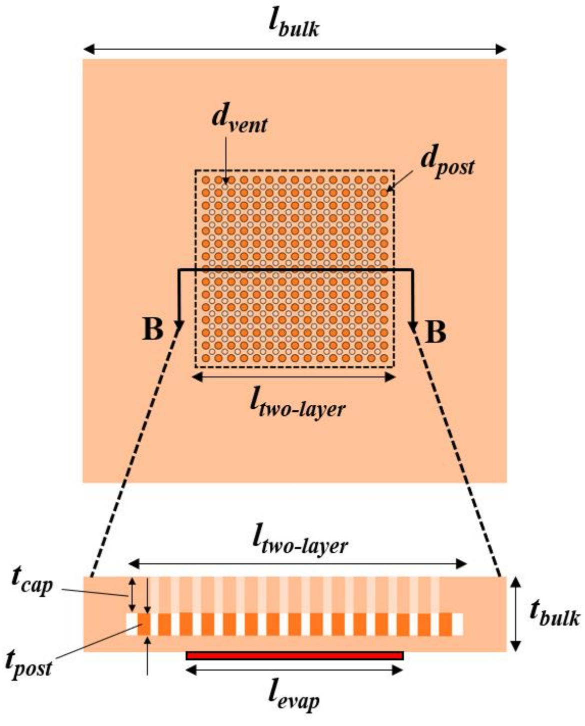
l_{bulk}
d_{vent}
d_{post}
B
B
$l_{two\text{-}layer}$
$l_{two\text{-}layer}$
t_{cap}
t_{bulk}
t_{post}
l_{evap}

Section B-B

Figure 5.6. Schematic diagram (plan and side view) of the two-layer evaporator wick tested in this work. This design consists of a 15 × 15 array of vertical liquid feeding posts and an offset 14 × 14 array of vapor vents over a 15 mm × 15 mm area. In the plan view, the open circles are the vents and the filled circles represent the posts below. The evaporator region is the center 10 mm × 10 mm area (d_{post} = 650 μm; d_{vent} = 500 μm; t_{post} = 400 μm; t_{cap} = 700 μm; t_{base} = 400 μm).

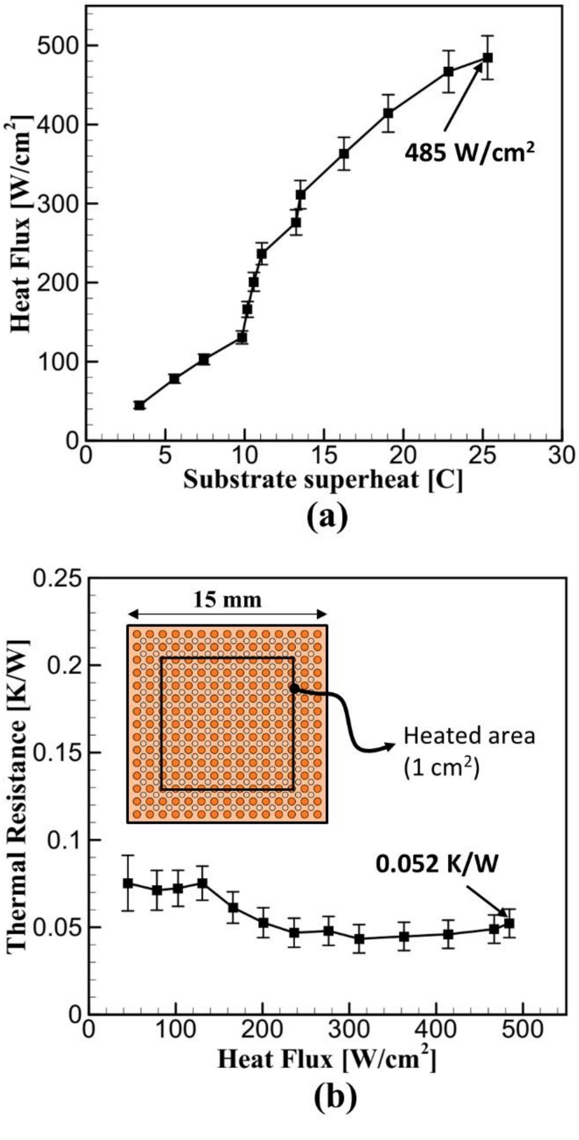

Figure 5.7. (a) Boiling curves and (b) wick resistance for the two-layer wick comprised of 180-212 μm particles. The two-layer wick has a 15 × 15 array of liquid-feeding posts over a 15 mm × 15 mm area.

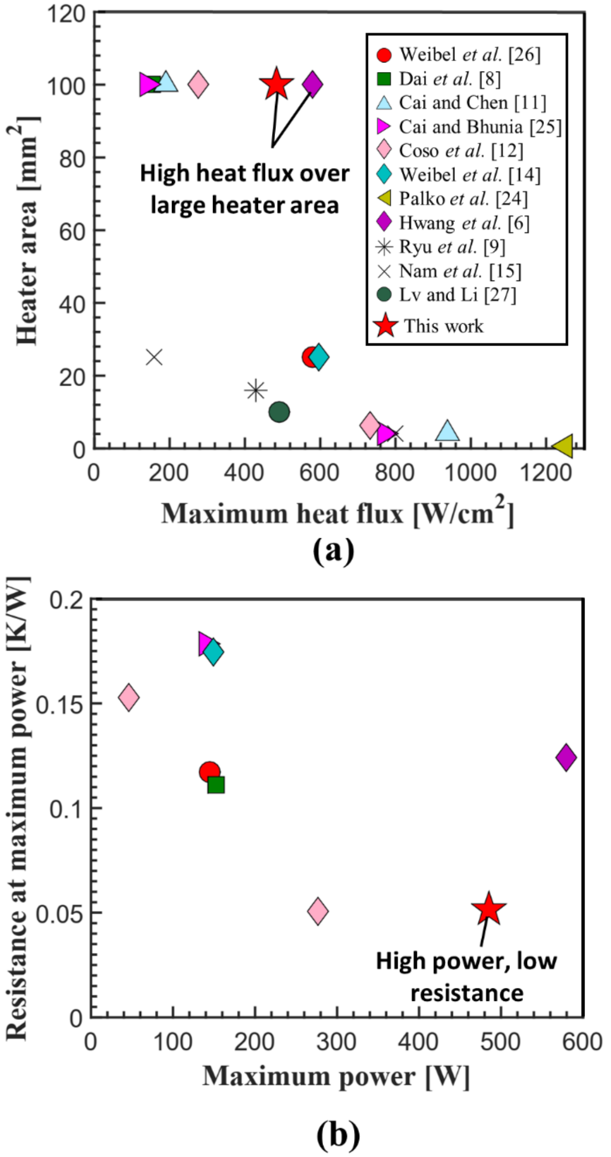

Figure 5.8. Compilation of capillary-fed boiling performance of different evaporator wicks tested in the literature: (a) Maximum heat flux as a function of heater area and (b) resistance at maximum power as a function of the corresponding power (values above 0.2 K/W are omitted to focus on the low-resistance data; all omitted data fall below a maximum power of 200 W). In comparison to other evaporator wicks, the two-layer wick (star symbol) achieves high-heat-flux dissipation over a large heater area (i.e., higher power) at a lower thermal resistance.

6. ROLE OF VAPOR-VENTING AND LIQUID-FEEDING ON THE DRYOUT LIMIT OF TWO-LAYER EVAPORATOR WICKS

The current chapter presents a targeted parametric study of the role of vapor-venting and liquid-feeding on the dryout limit and thermal performance of the two-layer wick. By understanding these effects and appropriately optimizing these parameters of the two-layer wick, we demonstrate high-heat-flux dissipation exceeding 500 W/cm^2 using capillary-fed boiling over large heater areas (1 cm^2). The material in this chapter has been published in the *International Journal of Heat and Mass Transfer* [79].

6.1 Designs of Two-Layer Wicks

A reduced-order analytical model was developed in Section 3.2 for flow and heat transfer in the two-layer wick. The model predicted that denser post arrays over the evaporator area, which reduce the flow length and thereby pressure drop within the thin boiling wick layer, enhance the dryout limit of the wick. In addition, the vapor flow pressure drop was predicted to be significantly affected by the vapor venting area. At a given post array size, the analysis concluded that the vapor vents must be made as large as possible, up to the physical limit of overlapping with the posts, to minimize the total pressure drop. In the current work, geometric design parameters that affect the cross-sectional areas available for vapor venting and liquid feeding are experimentally studied. Different two-layer evaporator wicks were fabricated by independently varying the vent diameter, post diameter, and array pitch. All the designs use sintered copper particles in the size range of 180 – 212 µm. Figure 6.1 (a) shows a top view of the footprint area that is the same for all evaporator wicks tested in this work. A 30 mm × 30 mm bulk feeding wick (side length, l_{bulk}) supplies a central 10 mm × 10 mm heated evaporator area (side length, l_{evap}). The wick is fabricated on a 1 mm-thick copper substrate of dimensions 38.1 mm × 38.1 mm, per the fabrication procedure outlined in Section 4.1. The two-layer wick features are fabricated over the 10 mm × 10 mm evaporator area. Figure 6.1 (b – e) show schematic diagrams of the top views and side views of the different two-layer wick designs (Wicks 1 – 4) for a symmetric quadrant of the evaporator area. The darker filled circles in the top view represent the posts below the cap layer while the open circles represent the vents in the cap layer. The dimensions of the wick features (array sizes, post diameter, d_{post}, vent diameter, d_{vent}) are tabulated in Table 6.1. The dimensions that remain constant across the designs are the cap layer thickness, t_{cap} = 800 μm, post thickness, t_{post} = 400 μm, and base layer thickness, t_{base} = 400 μm.

To analyze the effect of vapor venting area on the performance, Wicks 1 and 2 were fabricated with the same 12 × 12 post array and a fixed post diameter, d_{post} = 500 μm. Wick 1 has a sparse 6 × 6 array of vents of diameter d_{vent} = 500 μm, providing a total vapor venting area of ~ 7% of the total cap layer area (A_{vent}/A_{evap}). For Wick 2, additional vapor vents of diameter 500 μm and 300 μm are laser-machined through the cap layer in a different pattern that yields a significantly larger percentage area for venting (A_{vent}/A_{evap} ~ 16%). The post diameters in Wicks 1 and 2 are fixed at 500 μm, which results in only 2.5 sintered particles on average across the cross-section of each post. To increase the feeding area through each post and study its effect on the thermal performance, the post diameter was enlarged to 650 μm in Wick 3, while keeping the same 12 × 12 post array size and venting area compared to Wick 2 (A_{vent}/A_{evap} ~15%). This results in a much denser array of posts than the previous designs, which consequently leads to a complementary reduction in the vapor flow area in the interstices between the posts. Wick 4 is fabricated with the same total venting area (A_{vent}/A_{evap} ~16%) and post diameter (d_{post} = 650 μm) as Wick 3, but the spacing between the posts is increased to allow more vapor flow area between posts, resulting in a 10 × 10 array of posts.

6.2 Results

The results reported here show boiling curves (heat flux plotted against substrate superheat) in Figure 6.2 (a) and thermal resistance curves (wick resistance plotted against heat flux) in Figure 6.2 (b) for each wick tested. Several general trends in these curves are common to all the two-layer wicks. At low fluxes, the space between the posts of the two-layer wick is filled with liquid and active bubbling occurs through the vents. When the heat flux is increased, the liquid recedes and is only present in the wick regions (base layer, cap layer, and the posts), forming a separated pathway for vapor to escape from the wick base layer through these spaces and out of the vents. This mode of operation leads to a reduced thermal resistance at higher heat fluxes because the vapor flow impedance out of the wick is minimized. Due to the distributed liquid feeding across the base layer, the two-layer wicks do not exhibit partial dryout, which would be observed as a gradual increase in thermal resistance leading to complete dryout. Rather, the test is stopped in the present work when a sudden increase in the substrate temperature is triggered by a complete dryout event. The last steady value of the measured heat flux is reported as the dryout heat flux of the wick, and the corresponding thermal resistance is taken as the dryout thermal resistance.

6.2.1 Effect of Vapor-Venting Area

The area available for vapor venting is observed to significantly affect the dryout limit of the two-layer wick. Comparing the green and blue curves in Figure 6.2 (a), it is noted that Wick 1 (green curve) dries out at a heat flux of 315 W/cm^2. Increasing the fraction of the cap layer for vapor venting from 7% to 16% in Wick 2 (blue curve) yields an increase in the dryout limit to 405 W/cm^2. We attribute this enhancement to a decrease in the vapor pressure drop through the vents. The thermal resistance curves for Wicks 1 and 2 also exhibit an interesting difference in Figure 6.2 (b). At low fluxes, the resistance of Wick 2 is greater than the corresponding values of Wick 1. This is because of the greater open volume in the design of Wick 2 compared to Wick 1, such that a larger portion of Wick 2 is flooded with liquid (having lower thermal conductivity than copper) at low fluxes. This causes the measured thermal resistance to be higher in Wick 2 at low fluxes.

Figure 6.3 shows the top-view visualization images taken during the boiling process over the evaporator region for Wicks 1 and 2 at a similar heat flux of ~240 W/cm^2. A critical difference is observed between the vapor venting processes in the two wicks. Wick 1 restricts the pathway for vapor flow out of the wick due to a smaller venting area. Vapor bubbles through the cap layer instead of exiting through the designated vents, which impedes liquid replenishment by the thick cap layer, as shown in the schematic diagram in Figure 6.3 (a). A transition to this mode of operation causes the measured thermal resistance to increase sharply for heat fluxes greater than 240 W/cm^2 for Wick 1 (as seen in Figure 6.3). In addition, the maximum heat flux that can be dissipated by Wick 1, which is the lowest of all tested, is limited due to this blockage of liquid supply through the cap layer. In comparison, Wick 2 has a greater vent area for vapor to escape, leading to separated flow pathways where the exiting vapor does not obstruct liquid feeding, as illustrated in the schematic diagram in Figure 6.3 (b). There is a notable improvement in the maximum dryout heat flux from 315 W/cm^2 for Wick 1 to 405 W/cm^2 for Wick 2. We conclude that the vapor venting area plays a major role in determining the dryout limit and make the general recommendation that vents should be made as large as possible to minimize the vapor flow pressure drop.

6.2.2 Effect of Post Area and Post Spacing

Dryout can be triggered in the two-layer wick if the posts are not capable of sufficiently feeding the thin base layer. Our prior visualization images of the two-layer wick operation showed that the liquid meniscus recedes into the cap layer and posts as the heat flux increases to high levels. Hence, including more particles across the cross-section of each post can provide a greater area for liquid flow and reduce the chance of the capillary flow path through the post being cut off as the meniscus recedes. All geometric parameters are held constant across Wicks 2 and 3, except that the post diameters are enlarged from 500 μm to 650 μm in Wick 3. From the boiling curves plotted in Figure 6.2 (a), it is observed that Wick 3 (magenta curve) dries out at a maximum heat flux of 457 W/cm^2, which is a 13% increase over Wick 2 (blue curve). This increase is attributed to the additional liquid feeding area. The thermal resistance curves for these two wicks are very similar; the resistance decreases during the part of the boiling curve at lower heat fluxes and reaches a nearly constant value at higher fluxes. While the dryout limit is enhanced due to the greater cross-sectional area of the posts, this also causes a reduction in the vapor flow area between the spaces of the two-layer wick.

To enhance the dryout limit further, the vapor flow area in the interstices between the posts was increased in Wick 4. This wick was fabricated with the same post diameter (d_{post} = 650 μm) as Wick 3, but the posts were spaced further apart, resulting in a slightly sparser 10 × 10 array of posts as shown in Figure 6.1 (e). An offset 9 × 9 array of vents of diameter d_{vent} = 500 μm is fabricated to maintain a constant vapor venting area across Wicks 2, 3 and 4. In Figure 6.2 (a), Wick 4 (red curve) reaches the highest dryout heat flux of ~ 512 (±29) W/cm^2 among the wicks tested. The dryout heat flux is improved from the previous designs due to an effective balance between the liquid feeding cross-sectional area of the posts and the vapor venting areas. The design provides a near-linear increase in the wick superheat with increasing heat fluxes up to complete dryout. The trends in the wick thermal resistance are similar to the previous designs. At lower heat fluxes, the spaces between the posts are flooded with liquid, causing the measured thermal resistance to be higher. With increasing heat flux, the wick provides separated flow pathways for liquid and vapor that causes a reduction in the thermal resistance compared to the values at low heat fluxes. Wick 4 yields a thermal resistance of 0.08 (±0.01) K/W at dryout, the lowest among the wick designs tested.

6.3 Conclusions

A two-layer evaporator wick for use in high-heat-flux vapor chambers is designed to effectively supply liquid by capillary action to a thin base layer that is boiling. Liquid is fed to the base layer using an array of posts that are connected to a thick porous cap layer. Vapor vents in the cap layer allow the vapor to easily escape the wick during capillary-fed boiling. In this study, the effects of the vapor-venting and liquid-feeding areas on the dryout heat flux of two-layer wicks were experimentally investigated. Two-layer wicks with different geometric parameters were fabricated and tested. The total vapor venting area was found to significantly influence the dryout limit of the wick. Increasing the fraction of vapor venting area relative to the heated footprint area from 7% to 16% improved the dryout limit of the wick from 315 W/cm^2 to 405 W/cm^2. It was observed from high-speed visualizations that the lower vapor venting area caused vapor to bubble through the cap layer, obstructing the liquid replenishment pathway and reducing the maximum heat flux. In addition, it was shown that increasing the liquid-feeding area by increasing the cross-sectional area of each post improved the dryout heat flux. Among the tests, a tradeoff was identified: the advantage of increased liquid-feeding area competes with the disadvantage of reducing the area for vapor flow between the posts of the wick. An optimized performance was measured for a 10 × 10 array of 650 μm diameter posts with an offset 9 × 9 array of 500 μm vents. Among all the designs, this wick reached the highest dryout limit of ~ 512 W/cm^2 over a 1 cm^2 heated area at the lowest thermal resistance of 0.08 K/W.

The results of this study offer general guidance on the design of two-layer evaporator wicks. Optimal designs should feature the maximum possible vapor venting area in the cap layer within the limits achievable by the fabrication process. In addition, the post and vent arrays must be designed with care to achieve a balance between the liquid feeding and vapor venting areas. Further performance improvements may be possible by exploring alternative wick compositions, aside from monoporous sintered copper particles, to be used as the thin base layer for increasing the dryout limit during capillary-fed boiling.

Table 6.1. Key dimensions and geometric parameters of the two-layer wick samples tested. The wicks are fabricated using 180 – 212 µm size particles; the dimensions that remain constant across the designs are t_{cap} = 800 µm, t_{post} = 400 µm, and t_{base} = 400 µm.

Sample ID	**Post Array**	**Vent array**	**Post diameter d_{post} (µm)**	**Vent diameter d_{vent} (µm)**	**Fraction of vent area (A_{vent}/A_{evap})**	**Fraction of post area (A_{post}/A_{evap})**	**Dryout heat flux (W/cm^2)**
Wick 1	12 × 12	6 × 6	500	500	0.07	0.28	315
Wick 2	12 × 12	11 × 11	500	500/300	0.16	0.28	405
Wick 3	12 × 12	11 × 11	650	400	0.15	0.48	457
Wick 4	10 × 10	9 × 9	650	500	0.16	0.33	512

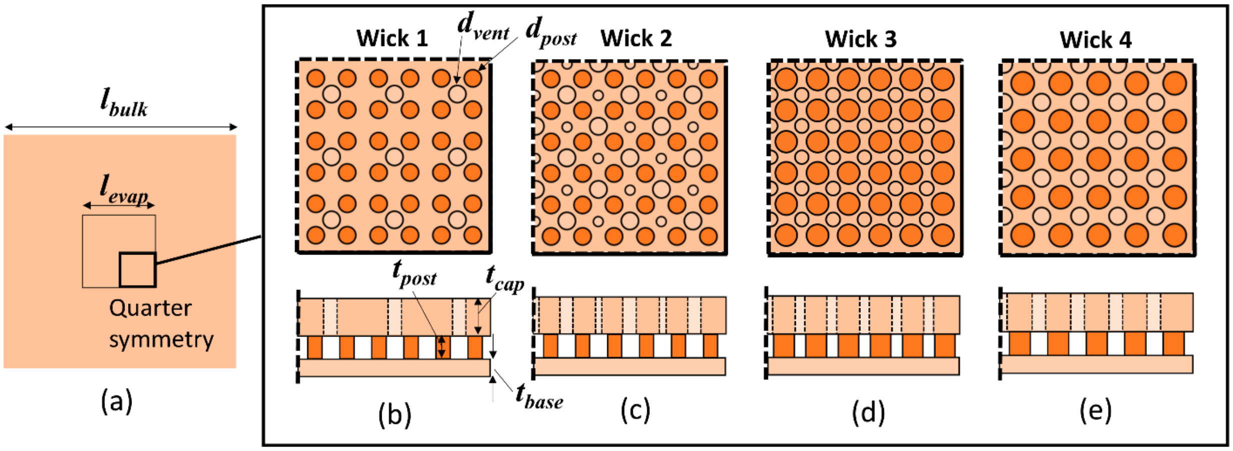

l_{bulk}
l_{evap}
Quarter symmetry
(a)
Wick 1
d_{vent}
d_{post}
Wick 2
Wick 3
Wick 4
t_{post}
t_{cap}
t_{base}
(b)
(c)
(d)
(e)

Figure 6.1. (a) Schematic diagram (top view) of the two-layer evaporator wick design; the square bulk wick region (side length l_{bulk} = 30 mm) supplies the square heated region (side length l_{evap} = 10 mm) where the two-layer wick features are fabricated. (b-e) Top-view and sectioned side-view schematic diagrams of Wicks 1-4. The top view diagrams are drawn to scale for one symmetric quadrant of the evaporator area; the open circles represent vents in the cap layer, while the filled circles represent the posts below. The side-view diagrams are not to scale in the thickness direction.

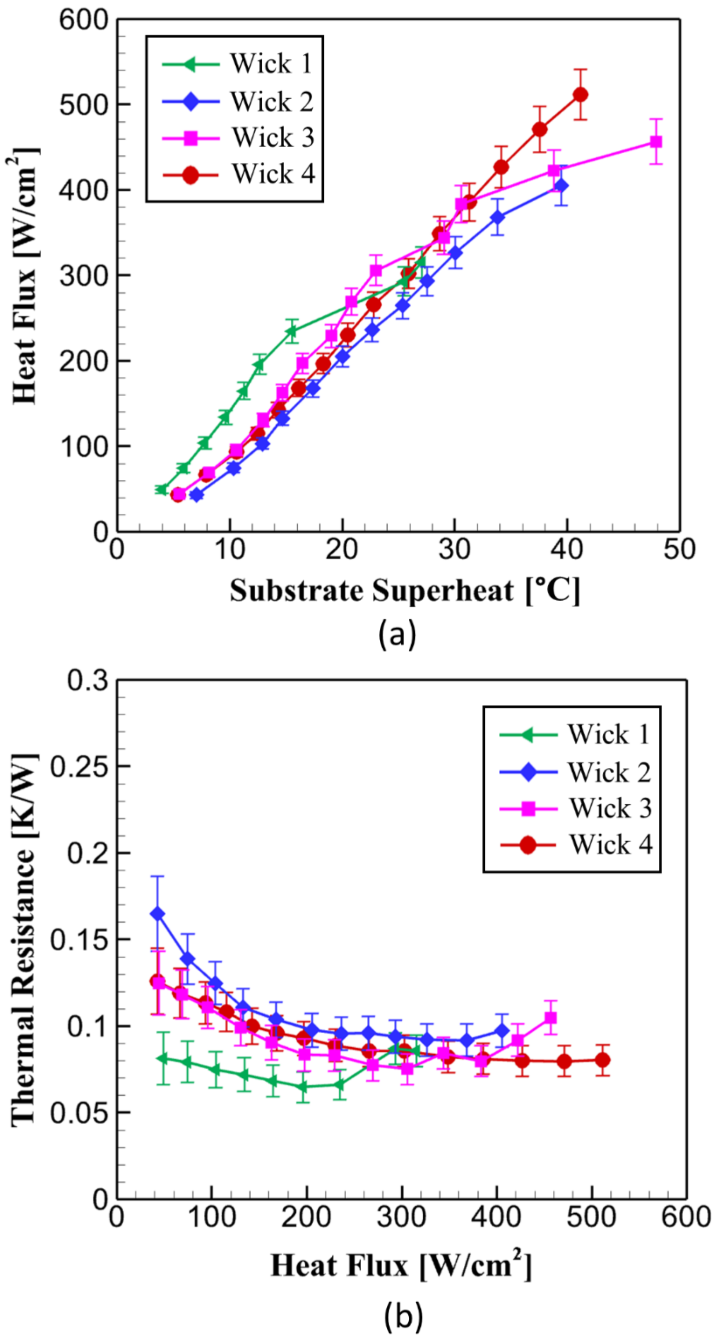

Figure 6.2. (a) Boiling curves and (b) wick thermal resistance curves for the four two-layer wick designs. The error bars in (a) and (b) represent the uncertainty in the heat flux and thermal resistance, respectively.

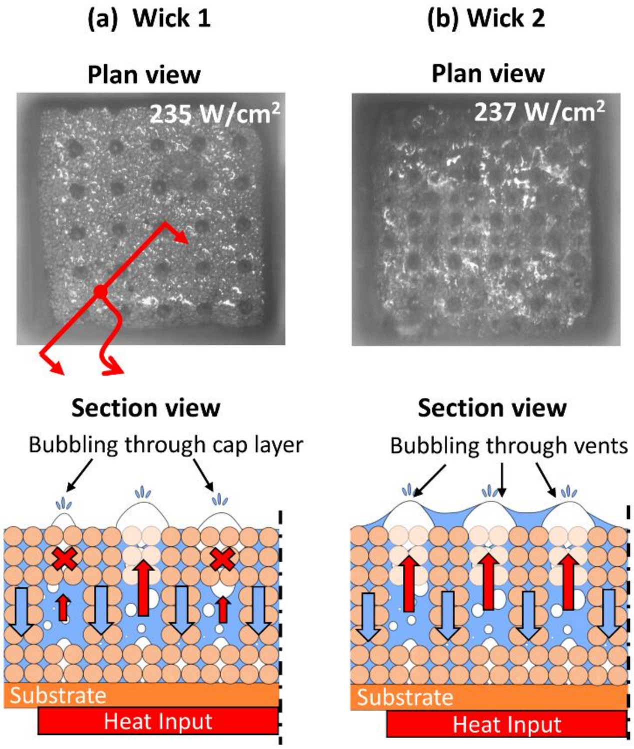
(a) Wick 1
(b) Wick 2
Plan view
Plan view
235 W/cm²
237 W/cm²
Section view
Section view
Bubbling through cap layer
Bubbling through vents
Substrate
Heat Input
Substrate
Heat Input

Figure 6.3. Plan-view images from high-speed visualization taken during capillary-fed boiling in the two-layer wick, and section-view schematic diagrams depicting the observed boiling behavior, for (a) Wick 1 and (b) Wick 2 at similar heat flux of ~ 240 W/cm^2. Less vapor venting area for Wick 1 causes bubbling through the cap layer, which can disrupt liquid feeding to the substrate. Greater vapor venting area in Wick 2 ensures that vapor exits through the vents.

7. A SEMI-EMPIRICAL MODEL FOR THERMAL RESISTANCE AND DRYOUT DURING BOILING IN THIN POROUS EVAPORATORS FED BY CAPILLARY ACTION

This chapter presents a new semi-empirical approach to calculating the dryout limit and thermal resistance during capillary-fed boiling, specifically in thin-porous evaporators commonly used in vapor chambers. Figure 7.1 schematically shows the flow configuration of interest in such porous evaporators. Lateral liquid flow is driven by capillary action from a single-phase region to the center of the two-phase region (the heated zone); vapor flow occurs through the thickness of the porous media. The liquid saturation profile decreases from its maximum value at the edge of the two-phase region to a minimum value at the center. Thermal conduction in the solid structure in the thickness direction, and volumetric pore-scale evaporation within the porous structure, are modeled to obtain the temperature distribution and the thermal resistance. The governing Darcy-Ergun equation (in radial coordinates), corrected for the relative permeability for two-phase flow, is used to solve the hydrodynamics within the evaporator domain. The dryout limit of the evaporator is defined as the input heat flux at which the liquid saturation at the center of the domain reduces to zero. Experiments are conducted using sintered copper particle wicks of different particle sizes and heater areas; the literature is also surveyed for additional experiments, to collect data for broad calibration of the model across a variety of porous evaporators.

7.1 Model Formulation

A cylindrical domain of radius r_e and thickness t as shown in Figure 7.2 (a) is considered as the porous evaporator. A heat input Q_w is supplied at the base wall (at $z = 0$) and the evaporator transports saturated liquid in by wicking action from the periphery at a constant rate ($\dot{m}_l = Q_w/h_{fg}$). Phase change occurs within the region and the vapor thus formed is assumed to flow out through the thickness (in the z direction). The vapor pressure is highest at the base of the evaporator ($z = 0$) and decreases to the saturation vapor pressure at the top (i.e., $P_v = P_{sat}$ at $z = t$, where P_{sat} is the saturation pressure). The following assumptions are made regarding the flow and heat transfer in this modeling framework:

1. At a given heat input Q_w, boiling is assumed to be occurring uniformly over the entire evaporator area.

2. The liquid flows one-dimensionally in the radial direction, from the outer periphery where it is fed ($r = r_e$) to the center of the domain ($r = 0$), evaporating completely. Thus, the liquid pressure is a function of the radial coordinate r only.
3. The vapor formed flows one-dimensionally in the axial direction from the wall ($z = 0$) through the porous evaporator thickness (to $z = t$).
4. Heat transfer occurs by one-dimensional conduction (in the z direction) from the heated wall through the solid porous matrix, by evaporation into the open pores within the porous medium, and ultimately to the saturated vapor above. Radial conduction in the porous evaporator structure is neglected.
5. The temperature of the saturated vapor within the pore spaces along the thickness of the evaporator is uniform and equal to the saturation temperature T_{sat} (*i.e.,* the saturation temperature change, due to the viscous vapor flow pressure drop through the thickness direction is very small and therefore neglected).

In the following subsections, the heat transfer relations are first presented to predict the temperature distribution and the thermal resistance, and the flow relations for the pressure drop and dryout limit prediction follow.

7.1.1 Heat transfer relations and prediction of thermal resistance

Heat transfer from the base surface occurs by conduction through the solid matrix, followed by volumetric evaporation occurring in the open pores within the domain. Kovalev *et al.* [80] followed the same approach to model the temperature distribution within porous coated surfaces in pool boiling. A control volume as shown in the side view schematic diagram of Figure 7.2 (a) is chosen to develop the governing heat transfer equations. It is assumed that the control volume consists of a representative elementary volume of particles and pores (as shown in Figure 7.2 (b)), in which volume-averaged quantities such as solid and liquid temperatures can be defined. The pore spaces between the particles are filled with liquid and vapor phases. An energy balance equation in the control volume can be written based on the conduction and evaporation fluxes:

$$
\begin{aligned}
&\frac{d\left(q_{cond}\right)}{dz}+\tilde{q}_{evap}=0\\
&\text{where}\\
&q_{cond}=-k_{eff}\frac{dT_s}{dz}\\
&\tilde{q}_{evap}=\tilde{h}_{evap}\left(T_s-T_{sat}\right)
\end{aligned}
\tag{7.1}
$$

In the above equation, q_{cond} is the conduction flux in the z-direction and $\tilde{q}_{evap}$ is the volumetric evaporation flux within the entire control volume. To estimate the volumetric heat transfer coefficient $\tilde{h}_{evap}$, a pore-scale evaporation model is developed, as described in APPENDIX F. The control volume is modeled as a collection of N pores; each pore is assumed to be cylindrical in shape with a nominal effective pore radius r_{eff}. The solid matrix in the pore is covered with an annular liquid film of thickness δ, and the vapor in the pore space occupies the cylindrical region of radius $r_{eff}-\delta$ (refer Figure F.1 in APPENDIX F).

This analysis provides an expression for the volumetric heat transfer coefficient:

$$
\tilde{h}_{evap}=\frac{2\left(r_{eff}-\delta\right)h_{lv}\varphi}{{r_{eff}}^{2}\left(1+\frac{h_{lv}}{k_l}\left(r_{eff}-\delta\right)\ln\left(\frac{r_{eff}}{r_{eff}-\delta}\right)\right)}
\tag{7.2}
$$

Introducing the solid matrix superheat $\theta = T_s - T_{sat}$, the governing energy equation in (1) becomes

$$
\frac{d^2\theta(z)}{dz}=\frac{\tilde{h}_{evap}}{k_{eff}}\theta(z)
\tag{7.3}
$$

The governing energy equation is solved with the boundary conditions,

$$
\begin{aligned}
&-k_{eff}\left.\frac{d\theta}{dz}\right|_{z=0}=q_w\\
&\left.\frac{d\theta}{dz}\right|_{z=t}=0
\end{aligned}
\tag{7.4}
$$

At the wall surface boundary ($z = 0$), the conduction flux is equal to the wall heat flux q_w because there is no volumetric evaporation at the surface of the wall. An adiabatic condition is assumed at the top surface of the wick ($z = t$), i.e., the conduction flux is zero at the surface (all the supplied heat input is removed through flow of the vapor out of the wick at $z = t$).

Using these boundary conditions, the solution for the temperature profile in the thickness direction can be obtained as

$$\theta(z)=\frac{q_w}{M_e k_{eff}\left(e^{2M_e t}-1\right)}\left(e^{M_e z}+e^{M_e(2t-z)}\right) \tag{7.5}$$

where $M_e=\sqrt{\tilde{h}_{evap}/k_{eff}}$. The capillary-fed boiling thermal resistance of the wick is obtained as

$$R_{th}=\frac{\theta|_{z=0}}{q_w}=\frac{1}{M_e k_{eff}}\frac{\left(e^{2M_e t}+1\right)}{\left(e^{2M_e t}-1\right)}=\frac{1}{M_e k_{eff}\tanh\left(M_e t\right)} \tag{7.6}$$

In the expression for h_{evap} in equation (7.2), the film thickness δ is the only unknown for a given wick geometry and working fluid combination. The parameter is found by calibrating the predicted thermal resistance to experimental data (for sintered particle wick structures in section 7.4.2 and with other porous evaporators from the literature in section 7.4.3.1).

7.1.2 Hydrodynamic relations and prediction of dryout

At steady state, the uniform heat input at the bottom of the evaporator Q_w is assumed to be completely utilized to change the phase of the saturated liquid that enters the domain. Accounting for the evaporated mass, the mass flow rate of liquid varies in the radial direction as,

$$\dot{m}_l(r)=\frac{Q_w}{h_{fg}}\frac{r^2}{r_e^{\,2}} \tag{7.7}$$

The liquid velocity in the radial direction is given by $u_l = \dot{m}_l/(2\pi rt)$. The Ergun equation for flow through porous media is used to obtain the liquid pressure drop in the radial direction,

$$\frac{dP_l(r)}{dr}=\frac{\mu_l}{KK_{rl}}u_l+\frac{\rho_l C_E}{K^{1/2}K_{rl}}u_l^{\,2} \tag{7.8}$$

where K is the intrinsic single-phase permeability and $C_E = 1.8\,(1-\varphi)\sqrt{K}/(D\,\varphi^2)$ is the Ergun coefficient. To account for the reduction in feeding area due to the presence of vapor in the pores, the single-phase permeability is reduced by a factor K_{rl} (the relative permeability of the liquid phase).

The vapor phase pressure gradient in the thickness direction of the wick (based on a purely viscous flow assumption) is,

$$\frac{dP_v}{dz}=\frac{\mu_v}{KK_{rv}}u_v \tag{7.9}$$

where K_{rv} represents the relative permeability of the vapor phase due to the presence of liquid in the pores. The vapor velocity for a given heat flux $u_v = q_w/\rho_v h_{fg}$ can be used to calculate the vapor pressure drop in the thickness direction, along with the boundary condition $P_v = P_{sat}$ at $z = t$, to obtain

$$P_v\left(z\right) = P_{sat} + \frac{\mu_v q_w}{K K_{rv} \rho_v h_{fg}}\left(t - z\right) \tag{7.10}$$

An average vapor pressure (averaged over the z-direction) is obtained as

$$P_{v,avg} = P_{sat} + \frac{\mu_v q_w t}{2 K K_{rv} \rho_v h_{fg}} \tag{7.11}$$

The relative permeability for a given fluid combination can be a function of the intrinsic properties of the two fluids (such as the viscosity, interfacial tension, and contact angle) [81]. The widely used correlations for relative permeability in a porous medium consider it to be a function of the local liquid saturation s, which is the fraction of the porous volume filled with liquid. The relative permeability correlations for various macroscale porous media are found using techniques such as X-ray computed tomography (e.g., see ref. [82]) to measure the liquid saturation directly during two-phase flow through the medium. For microscale porous media, relative permeability correlations are obtained using indirect methods, such as weighing the sample to find the liquid saturation after testing (e.g., see ref. [83] for porous media used in fuel cells). Due to a lack of experimental measurements of relative permeability for microscale porous evaporators, some prior works on capillary-fed boiling have used fitted expressions for relative permeability from experimental measurements of dryout heat flux. At the dryout heat flux, it is known that the pressure drop from liquid flow through the evaporator region equals the maximum (available) capillary pressure. Cai and Bhunia [84] fitted the relative areas available for liquid and vapor flows to match their experimental predictions. Zhang *et al*. [85] used a fit for the vapor relative permeability, which was taken as a fraction of the intrinsic permeability of the copper inverse opal (CIO) evaporator wick. In the absence of a universal correlation for relative permeability, we consider in this study the most general single-exponent power law expression for relative permeability [40,41], respectively given for the liquid and vapor as

$$\begin{aligned} K_{rl} &= s^n \\ K_{rv} &= \left(1 - s\right)^n \end{aligned} \tag{7.12}$$

The capillary pressure of the wick is the local difference between the average vapor and liquid pressures ($P_c = P_{v,avg} - P_l$). Similar to the relative permeability expression, the capillary pressure of a porous medium is modeled as a function of the local liquid saturation in multiphase flow as,

$$\begin{aligned} P_c(s) &= P_{c.\max} f(s) \\ &= \frac{2\sigma}{r_{eff}} f(s) \end{aligned} \tag{7.13}$$

where $P_{c,max}$ is the maximum capillary pressure of the porous medium, r_{eff} is the effective pore radius, σ is the surface tension of the fluid, and $f(s)$ characterizes the functional dependence on liquid saturation. When the porous medium is fully saturated, the capillary pressure is at its lowest. When liquid saturation decreases (i.e., as more vapor phase intrudes into the liquid saturated pore space), the capillary pressure increases. The capillary pressure function $f(s)$ for a given porous medium and fluid combination is typically found either by experimental measurements [86] or using pore-scale modeling and simulations [87]. Commonly used expressions for capillary-pressure saturation functions were tabulated by Kaviany [41]. In the absence of a universal capillary pressure-saturation relationship for microscale porous media, we consider a simple linear relationship $f(s) = 1 - s$ for the capillary pressure function.

Because the liquid and vapor pressures are functions of the radial coordinate, the capillary pressure ($P_c = P_{v,avg} - P_l$) and thereby the liquid saturation s, as well as relative permeabilities K_{rl} and K_{rv}, are all functions of the radial coordinate. The relative permeability of the liquid from equation (7.12) is substituted into equation (7.8) and using $P_c = P_{v,avg} - P_l$ gives,

$$\frac{dP_{v,avg}(s)}{dr} - \frac{dP_c(s)}{dr} = \frac{\mu_l}{K\left[s(r)\right]^n} G_w + \frac{\rho_l C_E}{K^{1/2}\left[s(r)\right]^n} G_w{}^2 \tag{7.14}$$

where $G_w = q_w r/(2 \rho_l h_{fg} t)$. Substituting the average vapor pressure from equation (7.11), the capillary pressure from equation (7.13), and rearranging the terms, we arrive at a differential equation for the liquid saturation (s) as a function of radial coordinate,

$$\frac{ds(r)}{dr} = \frac{\left[\dfrac{\mu_l}{K\left[s(r)\right]^n} G_w + \dfrac{\rho_l C_E}{K^{1/2}\left[s(r)\right]^n} G_w{}^2\right]}{\left[\dfrac{\mu_v q_w t}{2K\rho_v h_{fg}} \dfrac{n}{\left[1-s(r)\right]^{n+1}} + P_{c,\max}\right]} \tag{7.15}$$

The equation is solved using a numerical stepping procedure, where the gradient ds/dr is calculated from the edge of the solution domain, with a known boundary condition (s ($r = r_e$) = s_e). The boundary condition s_e is found from the average vapor pressure and the known value of liquid pressure at the boundary ($P_l = P_{sat}$) using $P_{v,avg}\big|_{r=r_e} - P_l\big|_{r=r_e} = P_c\big|_{r=r_e}$ as,

$$\frac{\mu_v q_w t}{2K\rho_v h_{fg}} \frac{1}{\left(1-s_e\right)^n} = P_{c,\max}\left(1-s_e\right) \tag{7.16}$$

which provides,

$$s_e = 1 - \left(\frac{\mu_v q_w t}{2K\rho_v h_{fg} P_{c,\max}}\right)^{\frac{1}{n+1}} \tag{7.17}$$

Once the saturation profile $s(r)$ is obtained, the relative permeabilities can be found. From the vapor pressure and the capillary pressures (equations (7.11) and (7.13)), the liquid pressure profile can be obtained as,

$$P_l\left(r\right) = P_{sat} + \frac{\mu_v q_w t}{2K\rho_v h_{fg}} \frac{1}{\left(1-s\left(r\right)\right)^n} - P_{c,\max}\left(1-s\left(r\right)\right) \tag{7.18}$$

Dryout is considered to occur when the liquid saturation falls to zero at the center of the evaporator ($s(r = 0) = 0$). To find the dryout heat flux, equation (7.15) is solved using a definite integral with two known boundary conditions (s ($r = r_e$) = s_e and $s(r = 0) = 0$). From equation (7.15), substituting $q_w = q_{dry}$ we obtain,

$$\int_{s_e}^{0} s^n \left[n\frac{Aq_{dry}}{\left[1-s\right]^{n+1}} + B \right] ds = \int_{r_e}^{0} \left[Cq_{dry} r + Dq_{dry}{}^2 r^2 \right] dr \tag{7.19}$$

where $A = \mu_v t/(2K\rho_v h_{fg})$, $B = P_{c,max}$, $C = \mu_l/(2K\rho_l h_{fg} t)$, $D = \rho_l C_E/(4K^{1/2}\rho_l^2 h_{fg}^2 t^2)$ are known constants for a given wick and working fluid combination. To obtain a solution, an initial guess value of q_{dry} for a given wick and working fluid is assumed, and then the boundary value of liquid saturation s_e is found using equation (7.17). The integral in equation (7.19) is solved using numerical integration in MATLAB. The process is repeated for different assumed values of q_{dry} to find the dryout heat flux when values of both sides in equation (7.19) are equal.

The only unknown in the expression to calculate the dryout heat flux (from equation (7.19)) is the saturation exponent n in the relative permeability relation. This exponent is obtained by calibrating the model-predicted dryout heat fluxes to experimentally measured values for sintered particle wick structures (in section 7.4.2) and for other common wick structures in the literature (in section 7.4.3.2).

7.2 Experimental Measurements of Dryout Heat Flux and Thermal Resistance

We characterize the dryout heat flux and boiling thermal resistance of sintered particle evaporator wicks with different particle sizes and heater sizes to collect data for model calibration. Deionized (DI) water is used as the working fluid. The experimental apparatus and data reduction procedures are detailed thoroughly in our prior work [65], and therefore are only briefly summarized here.

The capillary-fed boiling test setup allows the working fluid to be uniformly drawn into the evaporator from all directions and evaporate into the vapor space above that is maintained at saturation conditions (T_{sat} = 373 K, P_{sat} = 1 atm), as shown schematically in Figure 7.3. The heat input to the evaporator is provided using heater blocks (with embedded cartridge heaters) with two different contact areas of 5 mm × 5 mm and 10 mm × 10 mm. Copper particles of three different sizes (45 – 53 µm, 90 – 106 µm and 180 – 212 µm) and 1.5 mm thickness, are sintered onto solid copper substrates (38.1 mm × 38.1 mm dimension). The copper substrates with the evaporator wicks are then soldered to the copper block. The evaporator wicks are sealed using a novel dam structure to prevent liquid from flooding over the top. The open area for evaporation is 10 mm × 10 mm for both the heater sizes.

Prior to each test, the copper wick is functionalized to be hydrophilic by dipping in a solution of 2M NaOH and 0.1M $(NH_4)_2S_2O_8$, rinsed in DI water, dried thoroughly with compressed nitrogen, and sealed into the chamber. To obtain a boiling curve, heat input to the sample is turned on and increased in steps; the system is allowed to reach steady state at each step and thermocouple readings recorded. The heat flux into the wick (q_w) is calculated from a linear fit to a rake of thermocouple readings in the heater block; the wick base temperature is calculated by extrapolating from the thermocouple reading immediately below the substrate. The thermal resistance of the evaporator is then calculated as the ratio of the wick superheat to the heat input ($R_{th,wick} = (T_w - T_{sat})/(q_w A_{heater})$) where T_w is the wick base temperature and A_{heater} is the heater area. The heat flux is increased in steps until the occurrence of dryout is observed, signaled by a sudden and sharp increase in the wick base temperature.

7.3 Illustration of Model Predictions for an Example Case

This section utilizes an example case study to illustrate the key characteristics of the model predictions, as well as to explore the effect of the film thickness δ and saturation exponent n on the model predictions. Details of the porous evaporator wick and working fluid for this example simulation case are shown in Table 7.1. The working fluid is water (at 373 K saturation temperature). A 1 mm thick sintered particle wick of particle size D = 100 µm and porosity φ = 0.6 is used over a heated area of 1 cm^2. The permeability and effective pore radius of this sintered-particle wick can then be calculated using the standard expressions provided in the table.

Figure 7.4 (a) shows the model-predicted liquid saturation profiles along the radial direction (as calculated from equation (7.15)), for the example case at increasing values of heat flux. In this figure, the value of the saturation exponent is fixed at n = 3. At a heat flux of 25 W/cm^2, the liquid saturation does not vary much with the radial coordinate, and is nearly constant at its boundary value at $r = r_e$ (calculated from equation (7.17) as $s(r = r_e) = 0.71$). As the heat flux is increased, the magnitude of the liquid saturation decreases (due to the additional vapor generation in the evaporator). Further, the gradient along the radial direction increases, and the value of liquid saturation decreases from its boundary value toward the center of the domain (at r = 0). At q_w = 395 W/cm^2, the liquid saturation at the center of the domain reaches a value of zero, which signals the occurrence of dryout at this heat flux.

Figure 7.4 (b) plots the pressure profiles along the radial direction at the dryout heat flux value of q_w = 395 W/cm^2. The orange dash-dot curve shows the relative liquid pressure $P_l - P_{sat}$ as calculated from equation (7.18). The value reduces from zero at the outer edge of the evaporator to its minimum value at the center of the domain. The average excess vapor pressure $P_{v,avg} - P_{sat}$ reduces from the edge to the center, as shown by the blue curve. Since the liquid saturation reduces from the edge to the center, the relative permeability ($K_{rv} = (1 - s)^3$) and area available for vapor flow increases, and thus the average excess vapor pressure in the wick reduces (in the radially inward direction). Here, we note that the vapor temperature rise above saturation T_{sat} due to the excess vapor pressure would be negligible, thereby validating the assumptions made in the development of the thermal resistance model. Using the Clausius – Clapeyron relation ($dP/dT = h_{fg}P_{sat}/(R\ T_{sat}^2)$), the temperature rise for the maximum excess vapor pressure (~ 3200 Pa at the edge of the evaporator) is ~ 0.02 K. The capillary pressure of the wick (difference between the average vapor pressure and the liquid pressure) is lowest at the outer edge and highest at the center of the domain (at r = 0), where the liquid saturation is the lowest. At this dryout heat flux, the capillary pressure at the center of the domain becomes equal to the maximum available capillary pressure $P_{c,max}$ of the wick indicated by the dashed horizontal reference line in Figure 7.4 (b).

To illustrate the dependence of the dryout heat flux predicted by the model on the saturation exponent n, Figure 7.5 shows the liquid saturation at the center of the evaporator domain ($s(r = 0)$) as a function of the heat flux for different values of the saturation exponent. As seen in the plot, the saturation value decreases with increasing heat flux from s = 1 (at no heat input) to the dryout heat flux (q_w = 395 W/cm^2) at which $s(r = 0)=0$. The liquid saturation value, at any given value of n, exhibits a steep fall to zero as the heat fluxes approaches the dryout value. For example, in the yellow solid curve, the saturation value falls from $s \approx 0.3$ to $s = 0$ from q_w = 185 W/cm^2 to 196 W/cm^2. Since the liquid relative permeability scales as $K_l \sim s^n$, any reduction in the liquid saturation causes a much steeper reduction in the liquid permeability, which causes a higher drop in the liquid pressure and a subsequent rise in the capillary pressure. This further exacerbates the reduction in the liquid saturation, and hence causes this steep change close to the dryout heat flux. The dryout heat flux predicted by the model reduces from 395 W/cm^2 to 95 W/cm^2 as the exponent is increased from n = 3 to n = 5. This is primarily due to the decrease in the liquid relative permeability as the exponent value is increased, which contributes to a higher pressure drop and a steeper reduction in liquid saturation (with increasing heat fluxes), and thus a lower dryout heat flux.

Figure 7.6 shows the model-predicted solid superheat ($\theta_s = T_s - T_{sat}$) along the thickness of the wick (z direction), at an input heat flux of q_w = 100 W/cm^2, for different film thicknesses δ. The superheat is highest at the base of the wick and decreases to its minimum value at the top of the wick exposed to the saturated vapor. The boiling resistance predicted by the model is calculated using equation (7.6) based on the total temperature drop across the evaporator thickness. The plot also reveals the dependence of the wick superheat magnitude and profile on δ/r_{eff} (*i.e.,* the film thickness as a fraction of the effective pore radius of the wick). Following the pore-scale evaporation model outlined in APPENDIX F, at higher film thicknesses, the thermal resistance is dominated by conduction across the liquid film. This leads to a larger solid superheat and thus a larger boiling resistance for larger film thicknesses. The superheat profiles are analogous to 1D conduction heat transfer across a solid fin, with different effective thermal resistances to heat transfer from the surface of the fin. The maximum wick superheat ranges from θ_s = ~ 5 to 34 °C for film thickness ratio ranging from δ/r_{eff} = 0.1 to 0.95, which corresponds to a boiling resistance per unit area for this example case from R_{th} = 0.05 to 0.34 K cm^2/W. Note that for a given wick geometry and working fluid combination, and at a given film thickness, the model predicts that the boiling resistance per unit area (in K m^2/W) is a constant value, and not a function of the heat input.

As seen in Figure 7.5 and Figure 7.6, the model-predicted values of the dryout heat flux and thermal resistance are sensitive to the unknown parameters (namely, the saturation exponent n and the film thickness ratio δ/r_{eff}). This result signifies the importance of calibrating these unknown parameters with experimental data on different evaporator wick structures in order to adopt the model for more general use, as is explored next. We survey calibration against a broad set of data to evaluate if a single value of the parameters can be used against the whole set of data.

7.4 Model Calibration

The model developed in this work is calibrated against a wide range of data for different types of porous evaporators. The model unknowns, namely the film thickness δ and the saturation exponent n are fit to experimental measurements of thermal resistance and dryout heat flux, respectively. We focus on the most commonly used porous structures for loop heat pipes and vapor chambers, namely, sintered particle, sintered screen mesh, and micro-pillared structures. The inputs to the model are the effective properties of the evaporator wick structure (as will be described in the next subsection), and the thermophysical properties of the working fluid. The model calibration to experimental results for sintered particle wicks obtained in the current work is then presented, followed by calibration to data collected from the literature.

7.4.1 Evaluation of effective porous media properties

Table 7.2 lists expressions for the effective properties of the three different wick structures, namely sintered particles, sintered screen mesh, and micro-pillars.

For sintered copper particle wick structures, Bodla *et al.* [88] showed that the expression for effective thermal conductivity of the wick k_{eff} derived from effective medium theory (EMT) provided the best comparison to calculations from numerical simulations of heat conduction through geometrically faithful reconstructions of sintered particle wicks. The expression from EMT is:

$$k_{eff} = \frac{1}{4}\left[\left(3\varphi-1\right)k_l + \left[3\left(1-\varphi\right)-1\right]k_s + \sqrt{\left[\left(3\varphi-1\right)k_l + \left(3\left(1-\varphi\right)-1\right)k_s\right]^2 + 8k_l k_s}\right] \quad (7.20)$$

The expression can be simplified for a copper particle – water combination by enforcing $k_l << k_s$ to:

$$k_{eff} = \frac{\left(2-3\varphi\right)}{2}k_s \quad (7.21)$$

The effective pore radius of sintered particle wicks is recommended as $r_{eff} = 0.21\ D$ by Faghri [89] and is used in the current work. The intrinsic permeability of sintered particle structures is typically considered as $K = d^2\varphi^3/150(1-\varphi)^2$ [34]. However, Bodla *et al.* [88] found that the values calculated from single-phase flow simulations in sintered particle structures were 3 times lower than the ones calculated from this expression, and instead recommended $K = d^2\varphi^3/450(1-\varphi)^2$.

For sintered screen mesh wick structures, a number of studies proposed thermal conductivity correlations based on their own experiments, e.g., Refs. [90,91]. We use an expression provided by Li and Peterson [92] based on a correlation to experimental measurements obtained from staggered screen mesh wick structures of different mesh numbers and number of layers,

$$k_{eff} = 1.42\frac{k_s\left(M\times d\right)^2}{t}2n_{layer}d \quad (7.22)$$

where M is the mesh number and n_{layer} is the number of layers. The commonly recommended effective pore radius of screen mesh wicks is $r_{eff} = (W+d)/2$ [89] where d is the diameter of the screen mesh wire, and W is the width of the screen mesh pore. The intrinsic permeability is calculated as $K = d^2\varphi^3/122(1-\varphi)^2$ following Faghri [34].

Micro-pillared wick structures have been recently utilized in various thin-film evaporation applications [93]. They are best suited for usage in flexible polymer-based heat pipes [94] or titanium heat pipes [95]. We use the values of effective pore radius $r_{eff} = d/2(1-\varphi)$, effective thermal conductivity calculated from a parallel resistance network for thermal conduction through the micro-pillar structure $k_{eff} = k_s(1-\varphi)$ and intrinsic permeability $K = d^2\varphi^3/50\ (1-\varphi)^2$ as recommended by Cai and Bhunia [84].

7.4.2 Model calibration against sintered wick experimental results

Table 7.3 shows the measured dryout heat flux and the average boiling thermal resistance of the sintered particle evaporator wicks that were tested in the current work, at each heater size.

The dryout heat flux increases with particle size and is highest for the 180 – 212 µm wick structures, with a value of 191 W/cm^2 and 793 W/cm^2 for the 10 mm × 10 mm and 5 mm × 5 mm heater sizes, respectively. Furthermore, the dryout heat fluxes are higher for smaller heater areas; the significantly higher values for the 5 mm × 5 mm heater are due to the reduced flow length and pressure drop for liquid feeding over the smaller area. The reader is referred to APPENDIX G for the full boiling curve and thermal resistance curves plotted against the heat flux, and for the uncertainties in the measured values. In this section, the model is calibrated against the experiments by fitting for the film thickness ratio δ/r_{eff} and the saturation exponent n in the relative permeability expression.

Figure 7.7 shows a comparison of the predicted and experimental heat flux values for the three different particle sizes. The predicted heat flux q_{model} is calculated by dividing the measured wick superheat (at a measured heat flux) by the predicted boiling resistance (R_{th}, given by equation (7.6), as $q_{model} = \Delta T_{wick}/R_{th}$). The film thickness ratio δ/r_{eff} is assumed to be unique for a given wick particle size and therefore fitted separately for each particle size. Values of $\delta/r_{eff} = 0.76$ (for 45 – 53 µm particles), $\delta/r_{eff} = 0.48$ (for 90 – 106 µm), and $\delta/r_{eff} = 0.27$ (for 180 – 212 µm) provide the lowest least-squared error between the predicted and experimental heat fluxes. The experimental data are well-predicted within a spread of ±25% by the model across all particle sizes, heater areas, and superheats. Interestingly, the values of fitted film thickness ratio δ/r_{eff}, which reduce from 0.76 to 0.27 as the particle size increases, correspond to a relatively unchanged absolute value of film thickness (within a range between ~8-11 µm) across the different particle sizes.

Figure 7.8 shows a comparison of the predicted and experimentally measured dryout heat fluxes for all the test cases. The saturation exponent n in the relative permeability expression is again fitted uniquely for each evaporator wick particle size (but held constant across the different heater areas). A higher value of the relative permeability exponent means that the relative permeability of liquid is lower for the same value of liquid saturation, and suggests a higher liquid feeding pressure drop penalty imposed by boiling. Fitted values of $n = 3.9$ (for 45 – 53 µm particles), $n = 4.7$ (90 – 106 µm), and $n = 4.5$ (180 – 212 µm) provide the best fit. All the data are captured within a spread of ± 15%. The experimentally measured dryout heat flux values depend primarily on the particle size of the evaporator wick and the heater area. For larger particle sizes, the liquid feeding pressure drop from the sides of the evaporator will be lower due to a higher absolute permeability. Although the capillary pressure is lower for larger particle sizes ($P_{c,max}$ ~

1/*D*), the effect of the larger absolute permeability ($K \sim D^2$) outweighs the lower capillary pressure for this particle size range. The dryout heat fluxes are 3-4 times higher for the smaller heater size compared to the larger heater size, and this critical effect is well captured by the model for all the particle sizes as evidenced by Figure 7.8. Other prior works on capillary-fed boiling have also demonstrated the critical effect of heater size on the measured dryout heat fluxes [10,73]. The overall trends in particle size and heater size are predicted well by the model despite the small variation in the fitted exponent value ($n = 3.9 – 4.7$).

7.4.3 Model calibration against data from the literature

7.4.3.1 Thermal resistance calibration

Results from three studies in the literature for the three different wick structures are used in the calibration, all using water at 373 K saturation temperature (see Table 7.1 for properties) as the working fluid. The effective wick thermal conductivity and pore radius from Table 7.2 are used in the model.

Weibel *et al.* [96] characterized sintered particle evaporator wick structures (255 – 355 µm; $r_{eff} = 0.21$; $D = 63$ µm) of thicknesses ranging from 600 – 1200 µm. The measured substrate superheat is used to predict the heat flux q_{model} fitting the film thickness ratio ($\delta/r_{eff} = 0.1$) so that the RMS error between q_{exp} and q_{model} is the lowest. Li and Peterson [6] tested multiple layers of sintered screen mesh wick structures (mesh number $M = 5709$ m^{-1}, $d = 56$ µm, $W = 119$ µm, $r_{eff} =$ 87.5 µm), with the screen meshes placed in a staggered orientation. The boiling curve data for three different thicknesses $t = 370$, 570 and 740 µm ($n_{layer} = 4$, 6 and 8) are used here for model calibration by finding the best fit ($\delta/r_{eff} = 0.1$) to this group of experimental data. Cai and Bhunia [10] obtained boiling curves for monoporous silicon micro-pillar wicks of pillar diameter $d = 100$ µm, at two different thicknesses of 220 µm and 320 µm. The film thickness ratio obtained for these results is $\delta/r_{eff} = 0.01$.

Figure 7.9 shows the calibration data q_{exp} plotted against q_{model} for the three different sets of results [10,5,6]. The predicted values q_{model} are calculated from the measured superheat values, using the predicted thermal resistance (R_{th}), as $q_{model} = \Delta T_{wick}/R_{th}$. A majority of the predicted values >100 W/cm^2 fall within ±25% of the experimental data, for a wide range of heat fluxes from 100 – 1000 W/cm^2. This suggests a good correlation between the predicted and experimental values of thermal resistance, based on the different (fitted) film thickness ratios for different types of wicks. The deviation from the predicted values at heat fluxes less than 100 W/cm^2 is primarily due to evaporation-dominated heat transfer in the wick (prior to the onset of nucleate boiling) at lower heat fluxes. The absolute value of the fitted film thickness is on the same order of magnitude across the different wick structures (δ = 6.3 µm, 8.75 µm and 1.25 µm for the sintered particles, sintered screen mesh, and silicon micro-pillar structures, respectively).

7.4.3.2 Dryout heat flux model calibration

Dryout heat flux data from the literature on a wide variety of wick structures (water at 373 K saturation temperature is the working fluid), with different thickness, particle/pore sizes and heater areas are used in calibrating the model for dryout heat flux. The working fluid properties in Table 7.1 and the intrinsic wick permeability from Table 7.2 are inputs to the model in calculating the predicted dryout heat flux. Figure 7.10 shows a comparison between the model and the experimentally measured values. A single saturation coefficient (n = 4) is fit across all the predicted values, a majority of which fall within ± 25% of the experimental values across a wide variety of evaporator designs (with a mean absolute percentage error (MAPE) of 29%). This strong correlation between the model and experiment obtained using a single saturation coefficient demonstrates that the model captures well the widely accepted trends in the literature including the effects of wick thickness, pore size, and heater size. These key trends from the literature, and the corresponding model predictions are explained here.

The increase in dryout heat flux with increase in particle/pore size has been experimentally observed across all three wick structures. Li and Peterson [97] tested the effect of pore size on the dryout heat flux of screen mesh wicks using three different screen mesh openings (W = 119.3 µm, W = 139.7 µm, W = 232.8 µm) and found that the dryout heat flux increases with increase in mesh opening size. This was attributed to the increase in wick permeability. Cai and Bhunia [10] tested silicon micro-pillar wick structures of two different pillar diameters (30 µm and 100 µm) and found that the dryout heat flux increases with pillar diameter. In our recent work [73] and in the current work, this same trend is observed with increase in particle size (45 – 53 µm, 90 – 106 µm and 180 – 212 µm), due to the increased permeability offered by the larger particles. Similarly, Li and Peterson [6] concluded that increasing the wick thickness from 0.37 mm to 0.74 mm (by stacking multiple layers of sintered screens) improves the dryout heat flux by providing more cross-sectional area for liquid replenishment. Cai and Bhunia [84] found that increasing the pillar height from 220 µm to 320 µm enhances the dryout heat flux. Further, the critical effect of heater size on dryout heat flux was demonstrated by Weibel [98] and also in the current work (using 5 mm × 5 mm and 10 mm × 10 mm heaters) and by Cai and Bhunia [10] (using 2 mm × 2 mm and 10 mm × 10 mm heaters).

The model is able to capture the key trends of increasing dryout heat flux with increasing the characteristic particle/pore size, increasing wick thickness, and decreasing heater area, using a single saturation exponent value of $n = 4$ across the entire dataset ranging over nearly three orders of magnitude of dryout heat flux. This provides confidence that the capillary-fed boiling model developed here can be utilized to predict the dryout limit across a wide variety of evaporator wick geometries and properties.

7.5 Conclusions

This chapter developed a new thermofluidic model for the prediction of the dryout heat flux limit and thermal resistance during capillary-fed boiling in porous evaporators used in two-phase heat transport devices such as vapor chambers, loop heat pipes, and capillary pumped loops. The modeling of multi-phase flow within porous media relies on the availability of constitutive relationships for the relative permeability as a function of the liquid saturation. Hence, two-phase flow models typically utilize correlations based on experimental measurements of relative permeability that are only largely available for macroscale porous beds, and not for microscale capillary-fed porous evaporators in the flow configuration studied herein. The semi-empirical modeling framework presented here is developed for prediction of dryout heat flux and thermal resistance in these scenarios. In the model, conduction and evaporation heat transfer in the porous medium are solved for to obtain the boiling thermal resistance. Lateral liquid flow from the edge to the center of the evaporator and vapor flow across the thickness are modeled to obtain the local liquid and vapor pressures. The input heat flux at which the liquid saturation at the center of the evaporator falls to zero is defined as the dryout limit. Experiments were performed using sintered particle evaporators of different particle and heater sizes and the data was used for model calibration. The model is also calibrated against experimental data collected from the literature on sintered particles, sintered screen meshes, and micro-pillar structures. For the thermal resistance, the model is calibrated against individual sets of data with an accuracy of ± 25%. It was found that the calibrated values of film thickness ratios for the thermal resistance model depend on the specific wick structure. The model also predicts the dryout limit of a wide variety of porous evaporators ranging across nearly three orders of magnitude with a mean absolute percentage error of 29% and captures the trends in particle/pore size, evaporator wick thickness and heater size. From this universal calibration, a single saturation exponent value of $n = 4$ is recommended for use in boiling in capillary-fed porous evaporators as it provided the best fit across different evaporator wick geometries and effective properties.

Table 7.1. Properties of the working fluid and porous evaporator wick used in the example case simulation (properties are calculated at saturation temperature of 373 K).

Property	**Value**
Liquid density (ρ_l)	958.45 kg/m^3
Vapor density (ρ_v)	0.5952 kg/m^3
Liquid viscosity (μ_l)	2.82×10^{-4}
Vapor viscosity (μ_v)	1.22×10^{-5}
Latent heat of vaporization (h_{fg})	2.26×10^{6} J/Kg
Surface tension (σ)	5.88×10^{-2} N/m
Wick thickness (t)	1 mm
Wick particle size (D)	100 µm
Wick porosity (φ)	0.6
Heater radius (r_e)	5.6 mm
Solid thermal conductivity (k_s)	387.5 W/mK
Effective pore radius (r_{eff})	0.21 D
Wick permeability (K)	$D^2\varphi^3/450(1-\varphi)^2$
Effective thermal conductivity of wick (k_{eff})	$k_{eff} = (2-3\varphi)k_s/2$

Table 7.2. Relations for the intrinsic permeability (K), effective thermal conductivity (k_{eff}), and effective pore radius (r_{eff}) for three commonly used evaporator wick structures.

Wick Type	**Wick Permeability (K)**	**Effective thermal conductivity (k_{eff})**	**Effective pore radius (r_{eff})**
Sintered particles	$K = \frac{D^2\phi^3}{450\left(1-\phi\right)^2}$	$k_{eff} = \frac{\left(2-3\varphi\right)k_s}{2}$	$r_{eff} = 0.21\,D$
Sintered screen mesh	$K = \frac{d^2\phi^3}{122\left(1-\phi\right)^2}$	$k_{eff} = 1.42\frac{k_s\left(Md\right)^2}{t/2n_{layer}d}$	$r_{eff} = \frac{\left(W+d\right)}{2}$
Micro-pillars	$K = \frac{d^2\phi^3}{50\left(1-\phi\right)^2}$	$k_{eff} = k_s\left(1-\varphi\right)$	$r_{eff} = \frac{d}{2\left(1-\phi\right)}$

Table 7.3. Measured dryout heat flux and boiling thermal resistance of the wick structures at two different heater sizes.

Particle size (μm)	**Heater size (mm × mm)**	**Dryout heat flux (W/cm^2)**	**Average boiling resistance (K/W)**
45-53	5 × 5	247	0.111
	10 × 10	83	0.083
90-106	5 × 5	287	0.117
	10 × 10	104	0.106
180-212	5 × 5	793	0.110
	10 × 10	191	0.157

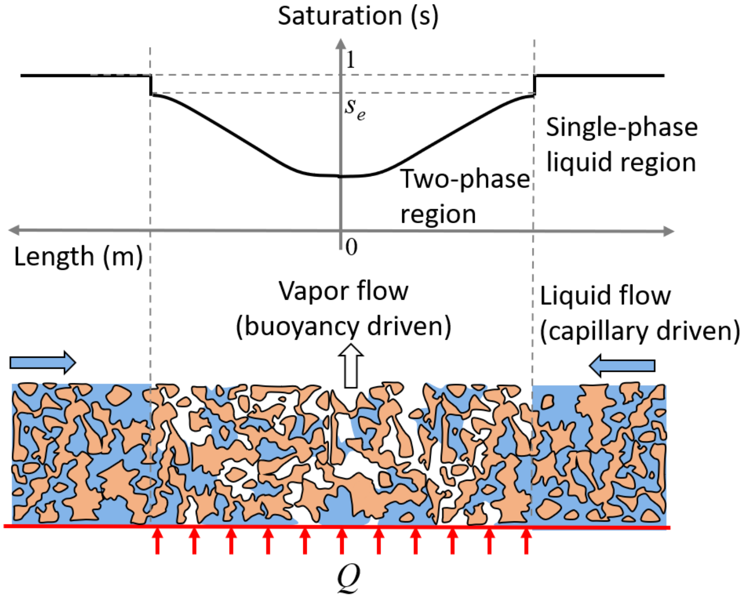
Saturation (s)
1
s_e
Single-phase
liquid region
Two-phase
region
Length (m)
0
Vapor flow
(buoyancy driven)
Liquid flow
(capillary driven)
Q

Figure 7.1. A schematic diagram of the two-phase flow configuration of interest in this work, and saturation profiles during boiling in capillary-fed porous evaporators.

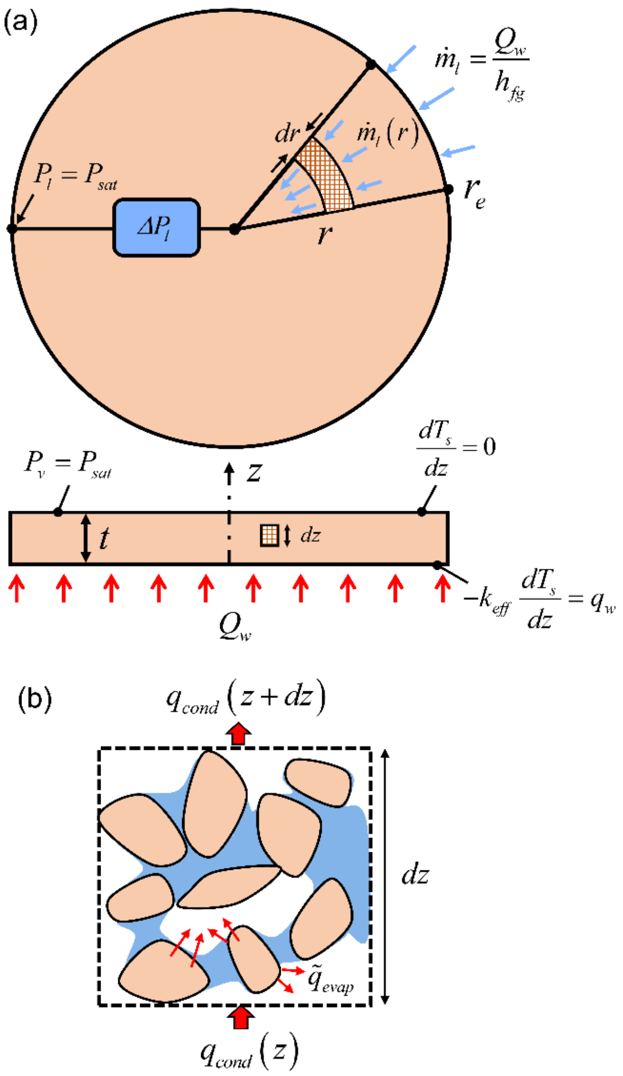
(a)
$\dot{m}_l = \frac{Q_w}{h_{fg}}$
dr
$\dot{m}_l(r)$
$P_l = P_{sat}$
ΔP_l
r_e
r
$\frac{dT_s}{dz} = 0$
$P_v = P_{sat}$
z
t
dz
$-k_{eff}\frac{dT_s}{dz} = q_w$
Q_w
(b)
$q_{cond}(z+dz)$
dz
$\tilde{q}_{evap}$
$q_{cond}(z)$

Figure 7.2. (a) Top-down view and cross-sectional side view schematic diagrams showing the geometry and boundary conditions for the cylindrical porous evaporator solution domain. The heat input is applied over a radius r_e over which boiling occurs. (b) A control volume considered in the thickness direction for the heat transfer model.

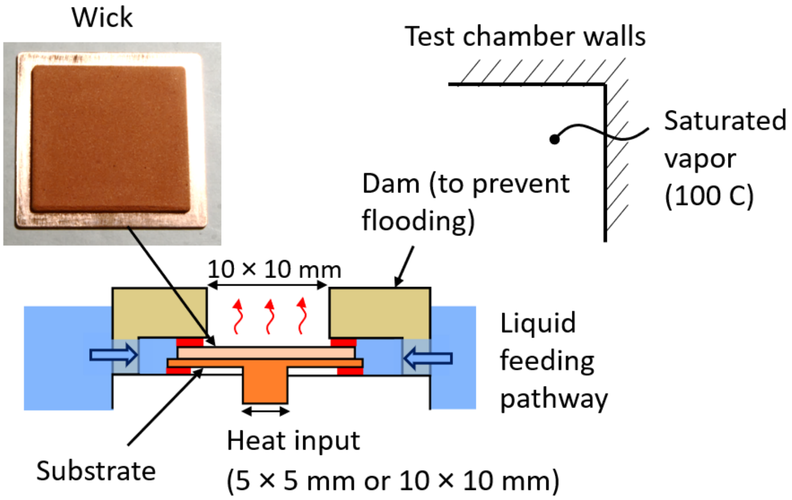
Wick
Test chamber walls
Saturated
vapor
(100 C)
Dam (to prevent
flooding)
10 × 10 mm
Liquid
feeding
pathway
Heat input
(5 × 5 mm or 10 × 10 mm)
Substrate

Figure 7.3. A schematic diagram illustrating the heating and liquid feeding mechanism for the evaporator wick, within the saturated test chamber. The inset image shows a photograph of a sample 90 – 106 µm particle wick structure.

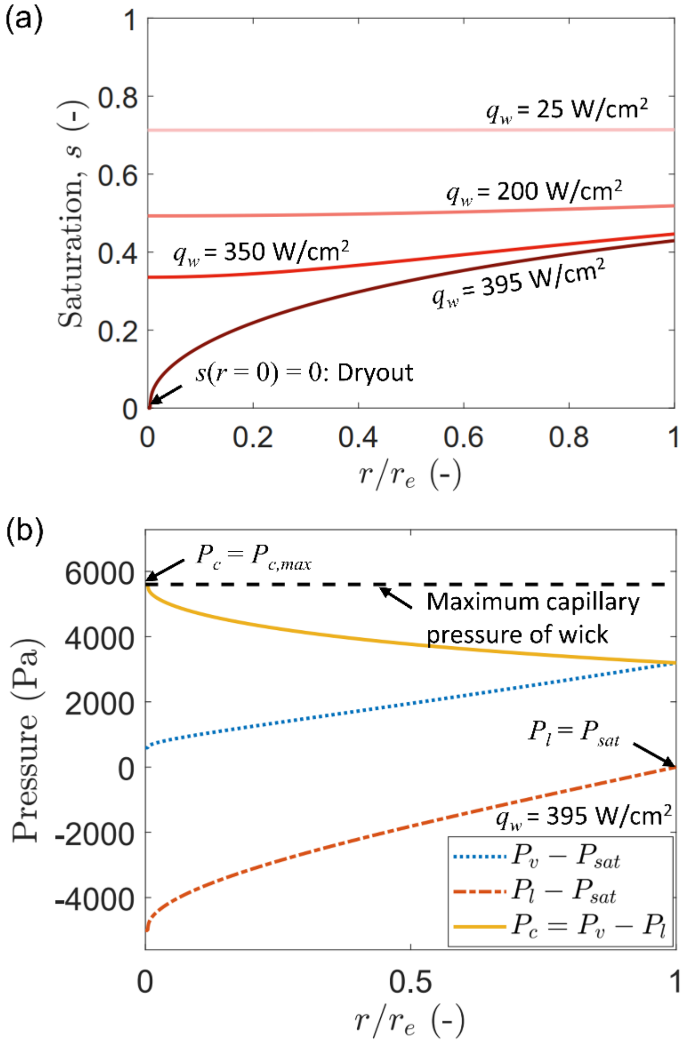

Figure 7.4. (a) A plot of the liquid saturation *s* as a function of the normalized radial coordinate r/r_e for the example case (refer Table 7.1 for properties) at different heat fluxes, calculated using the saturation exponent value n = 3. At q_w = 395 W/cm², dryout is indicated by the value of liquid saturation falling to zero at the center of the domain ($s(r = 0)=0$). (b) A plot of the liquid, average vapor, and capillary pressures as a function of the radial coordinate at the dryout heat flux (q_w = 395 W/cm²).

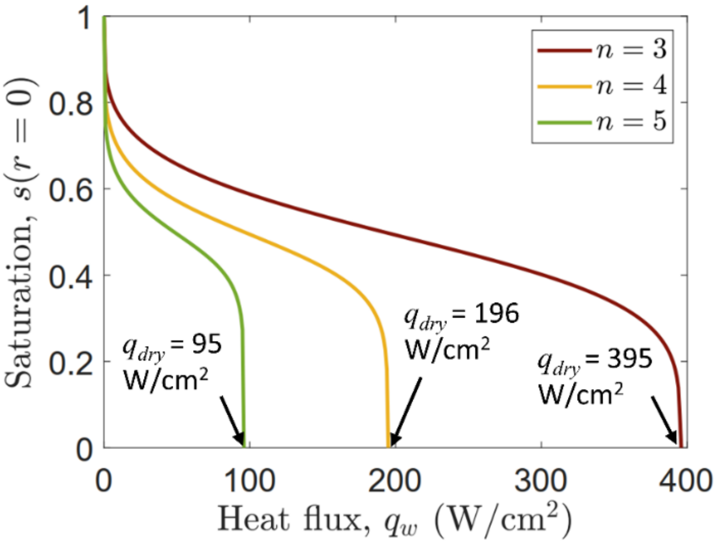

Figure 7.5. A plot of the liquid saturation at the center of the wick domain ($s(r = 0)=0$) as a function of the applied heat flux q_w for different values of the saturation exponent n for the example case (refer to Table 7.1 for properties). The values of the dryout heat flux at which ($s(r = 0)=0$) are labelled.

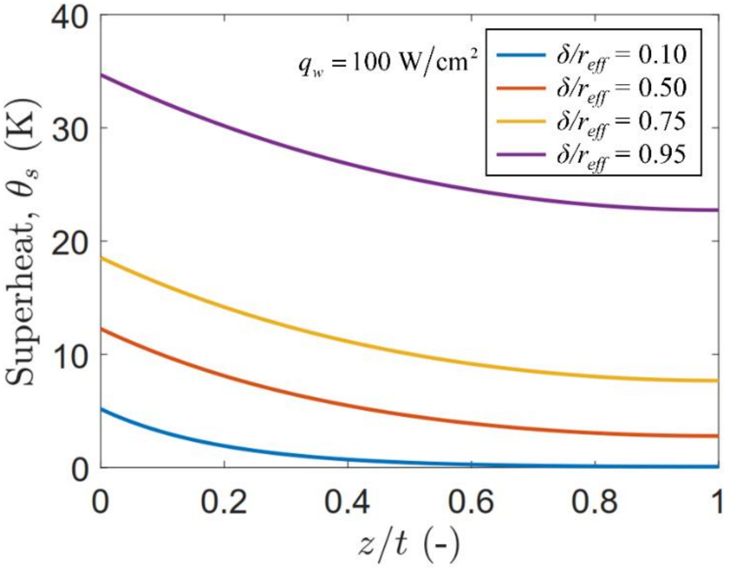

Figure 7.6. (a) A plot of the superheat of the solid matrix ($\theta_s = T_s - T_{sat}$) along the z-direction for different values of the film thickness ratio δ/r_{eff} for the example case (refer Table 7.1 for properties).

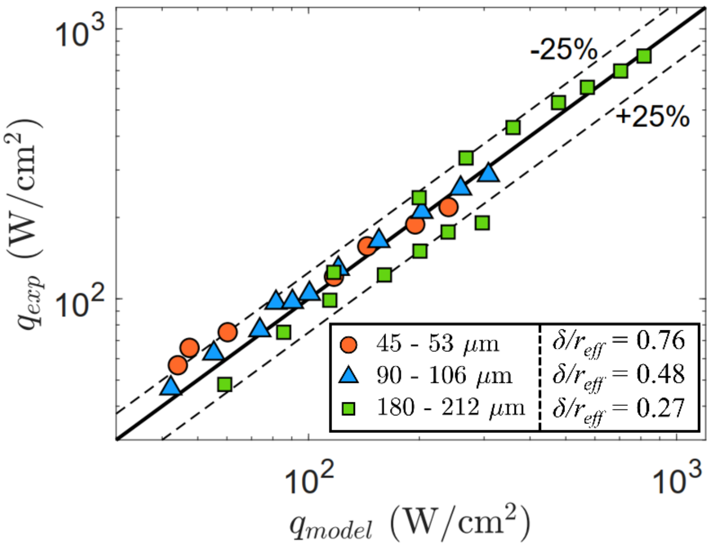

Figure 7.7. Comparison of the predicted and experimentally measured heat fluxes at a given superheat.

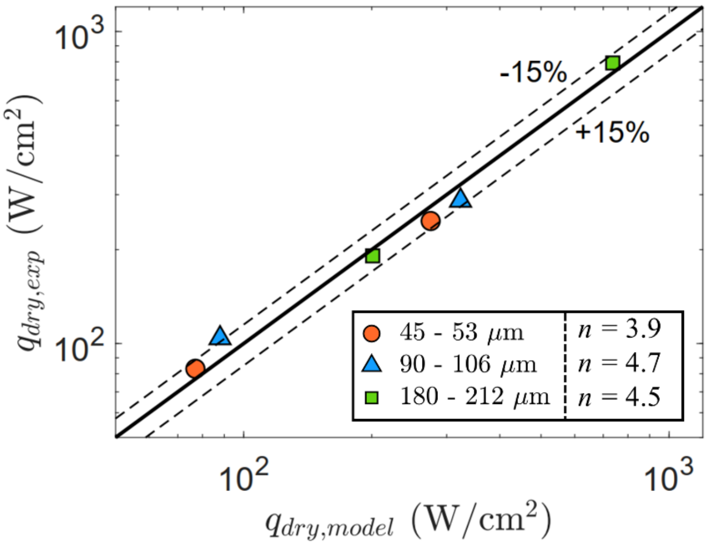

Figure 7.8. Comparison of the predicted and experimentally measured dryout heat fluxes (the two different values of dryout heat flux for each particle size correspond to the two different heater sizes).

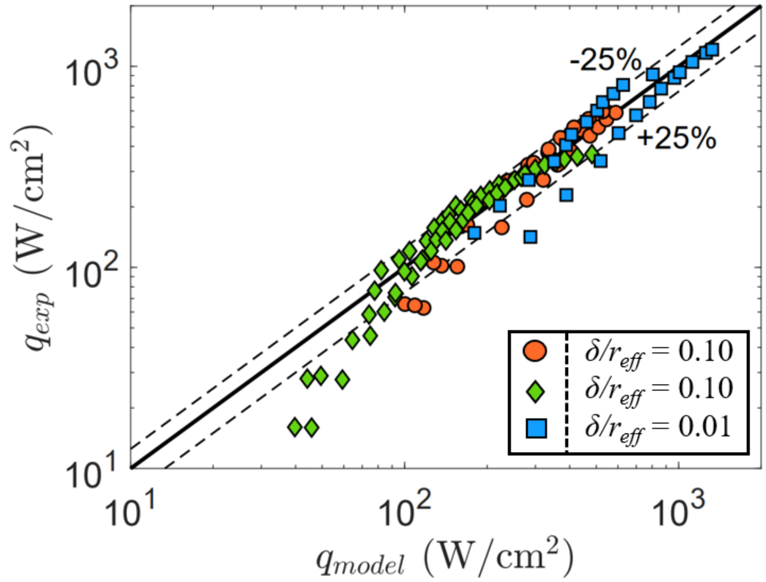

Figure 7.9. Comparison of the predicted and experimentally measured heat fluxes from three different evaporator wick structures in the literature: sintered particle [5] (circles), sintered screen mesh [6] (diamonds), and micro-pillar structures [84] (squares).

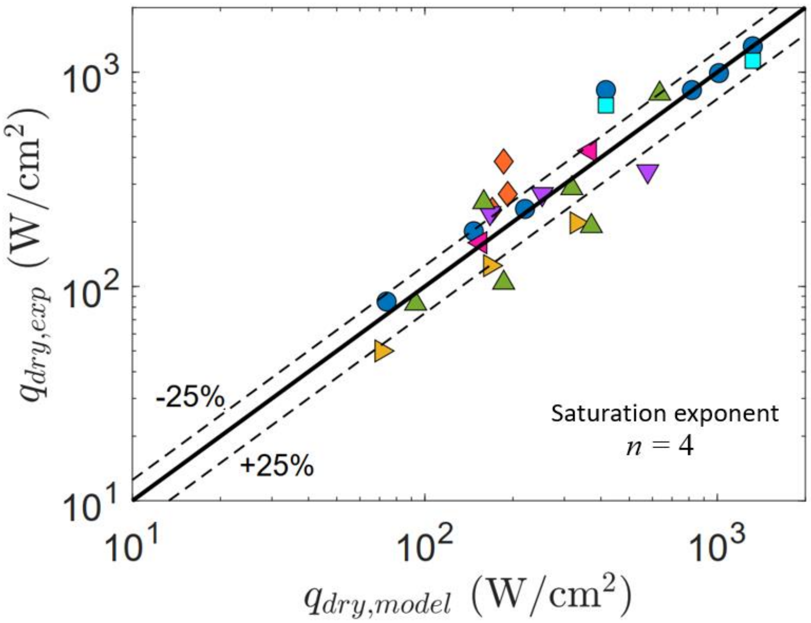

Figure 7.10. A comparison of the experimentally measured values of dryout heat flux from the literature and predicted values from the model developed in this study. The comparison includes data on sintered particle wicks from Weibel [98] and Sudhakar *et al.* [73], sintered screen mesh wick structures from Li and Peterson [6,97], and micro-pillar wick structures from Cai and Bhunia [10,84].

8. PREDICTION OF DRYOUT LIMITS OF HIGH-HEAT-FLUX VAPOR CHAMBERS CONSIDERING BOILING IN THE EVAPORATOR WICK

This chapter develops a vapor chamber model to account for boiling in the evaporator wick using the physics-based modeling approach derived in Chapter 7. The model formulation is divided into two major sections. The heat transfer equations discussed in Section 8.1 solves for the temperature fields in the substrate and vapor chamber, along with the vapor core pressure fields. Within this heat transfer model, the area of the wick undergoing boiling is found using a wall superheat threshold. After obtaining a solution for the temperature fields, the wick hydrodynamics are separately solved next using a numerical approach as described in Section 8.2.

8.1 Heat Transfer Model Formulation

The solution domain consists of a heat spreader, a vapor chamber and air-cooled fin array as shown in Figure 8.1 (a). A solid wall of thickness t_s serves as a heat spreader (and effectively the evaporator side wall of the vapor chamber) before interfacing to the vapor chamber. A single centrally placed heat input of area $l_x \times l_y$ is interfaced onto the bottom of the heat spreader. The vapor chamber is a rectangular device of lateral spreading area $L_x \times L_y$ with evaporator and condenser wick thicknesses $t_{wick,1,}$ and $t_{wick,2}$ and vapor core thickness t_{vap}. In the current approach, we do not model the condenser-side wall, since the thermal resistance offered by the wall on the condenser side is expected to be negligible (since the heat flux is a very low, uniform value over a large condenser area).

The overall framework and solution methodology of the analytical vapor chamber model developed by Patankar *et al.* [99] is used in the current work. The modeling framework described in ref. [99] neglects temperature drops along the thickness direction of the evaporator wall and wick. While this assumption is valid for ultra-thin devices used in low power density applications, the error due to the assumption increases with higher power and thicker walls [99]. To circumvent this assumption, the following heat transfer formulation solves 3D conduction in the solid wall to find the effective heat flux due to heat spreading q_w using a separate sub-model (by assuming a constant effective heat transfer coefficient h_w between the solid wall and the evaporator wick, and inputs it as a boundary condition into the vapor chamber sub-model (schematic in Figure 8.1 (b)).

An effective thermal resistance of the fin array is calculated assuming a uniform base temperature directly under the fins and a fully developed laminar air flow between the fins, as shown in APPENDIX H. An effective heat transfer coefficient $h_{eff} = 1/(R_{fin}L_xL_y)$ is calculated from this analysis and input as a boundary condition on the condenser side of the vapor chamber sub-model. Using these boundary conditions, the vapor chamber sub-model is solved to obtain the temperature fields. A new effective heat transfer coefficient $h_{w,new}$ is calculated and input into the conduction sub-model. The process is repeated until convergence of the effective heat transfer coefficient.

8.1.1 Effective heat flux from substrate conduction

The governing equations for the solid spreader at steady state is:

$$k_s\left(\frac{\partial^2 T}{\partial x^2}+\frac{\partial^2 T}{\partial y^2}+\frac{\partial^2 T}{\partial z^2}\right)=0 \tag{8.1}$$

with boundary conditions:

$$\begin{gathered}
-k_s\left.\frac{\partial T}{\partial z}\right|_{z=0}=\begin{cases}Q & \text{if } (x,y) \text{ inside heater}\\ 0 & \text{otherwise}\end{cases}\\
-k_s\left.\frac{\partial T}{\partial z}\right|_{z=t_s}=h_w\left(T-T_{sat}\right)\\
\text{at } x=0, L_x:\ \frac{\partial T}{\partial x}=0\\
\text{at } y=0, L_y:\ \frac{\partial T}{\partial y}=0
\end{gathered} \tag{8.2}$$

The governing equation along with the boundary condition is solved by assuming a constant heat transfer coefficient h_w on the spreader-wick boundary ($z = t_s$). The heat flux at the wall-wick boundary (q_w at $z = t_s$) can be analytically obtained by implementing an infinite series solution, following APPENDIX E as,

$$q_w\big|_{z=t_s} = \frac{Q}{l_x l_y}\left(\begin{array}{l} \dfrac{l_x l_y}{L_x L_y}\left(1+\mathrm{Bi}\right)+\dfrac{4\mathrm{Bi}}{\pi}\left(\dfrac{l_y}{L_y}\displaystyle\sum_{i=1}^{\infty}\dfrac{R_{i0}S_{i0}}{i}\cos(\alpha_i x)+\dfrac{l_x}{L_x}\displaystyle\sum_{j=1}^{\infty}\dfrac{R_{0j}S_{0j}}{j}\cos(\beta_j y)\right) \\ +16\dfrac{\mathrm{Bi}}{\pi^2}\displaystyle\sum_{i=1}^{\infty}\sum_{j=1}^{\infty}\dfrac{R_{ij}S_{ij}}{ij}\cos(\alpha_i x)\cos(\beta_j y) \end{array}\right)$$

where

$$\alpha_i = \frac{i\pi}{L_x}, \quad \beta_j = \frac{j\pi}{L_y}, \quad s_{ij} = \sqrt{\alpha_i^{\,2}+\beta_j^{\,2}}$$

$$R_{i0} = \sin\left(\frac{\alpha_i l_x}{2}\right)\cos\left(X_h\alpha_i\right) \quad \textit{and} \quad R_{0j} = \sin\left(\frac{\beta_j l_y}{2}\right)\cos\left(Y_h\beta_j\right)$$

$$R_{ij} = R_{i0}.R_{0j}$$

$$S_{ij} = \frac{1+\dfrac{\mathrm{Bi}}{s_{ij}t_s}\tanh\left(s_{ij}t_s\right)}{s_{ij}t_s\left[\tanh\left(s_{ij}t_s\right)+\dfrac{\mathrm{Bi}}{s_{ij}t_s}\right]} \qquad (8.3)$$

where Bi = $h_w t_s/k_s$ is the Biot number. The value of the heat transfer coefficient h_w is unknown and an initial value is assumed to start the solution. The effective heat flux q_w is input into the vapor chamber model to obtain the temperature fields as described below.

8.1.2 Evaluation of vapor chamber temperature fields

8.1.2.1 Evaporation based model of the evaporator wick

Patankar *et al.* [99] developed a validated low-cost analytical time-stepping model for vapor chamber transport. Following a scaling analysis, the following conclusions were made regarding the governing momentum and energy equations within the wick and vapor core of the vapor chamber at steady state, (the reader is referred to Ref. [99] for the complete scaling analysis and the derivation of the scaled equations),

1. Diffusion in *x* and *y* directions in the momentum and energy equations for the vapor core and wicks are negligible compared to the diffusion in the *z*-direction.
2. The convection terms in the momentum equation for the wicks and vapor core is negligible compared to the diffusion in the *z*-direction.
3. The convection terms in the energy equation for the wicks and the vapor core is negligible compared to the diffusion in the *z*-direction.

For the vapor core and the wicks, the governing equations at steady state reduce to:

$$k_{eff}\frac{\partial^2 T}{\partial z^2}=0 \tag{8.4}$$

The following boundary conditions are applied to the interfaces between the heat spreader and wick, and between the wicks and the vapor core,

$$\begin{gathered}
\text{at } z=t_s, \\
\left(-k_{eff}\frac{\partial T}{\partial z}\right)_{wick}=q_w \\
\text{at } z=t_s+t_{wick,1}, \\
\left(-k_{eff}\frac{\partial T}{\partial z}\right)_{wick}-\dot{m}_1''h_{fg}=\left(-k\frac{\partial T}{\partial z}\right)_{vap} \\
\text{at } z=t_s+t_{wick,2}+t_{vap}, \\
\left(k_{eff}\frac{\partial T}{\partial z}\right)_{wick}-\dot{m}_2''h_{fg}=\left(k\frac{\partial T}{\partial z}\right)_{vap} \\
\text{at } z=t_s+t_{wick,1}+t_{vap}+t_{wick,2}, \\
\left(-k_{eff}\frac{\partial T}{\partial z}\right)_{wick}=h_{air}\left(T_2-T_{air}\right)
\end{gathered} \tag{8.5}$$

In the above equation, T_2 is the temperature of the condenser-side wick. In addition, the sides of the vapor chamber are insulated,

$$\begin{gathered}
\text{at } x=0, L_x \quad \frac{\partial T}{\partial x}=0 \\
\text{at } y=0, L_y \quad \frac{\partial T}{\partial y}=0
\end{gathered} \tag{8.6}$$

The energy equations for the wick and vapor core are integrated along the z-direction over their respective thicknesses. Since information about the temperature variation along the z-direction is lost due to integration, profiles are assigned as described in ref [99]. The integrated equations and the boundary conditions are used to obtain solutions for the wick and vapor core temperatures in the vapor chamber.

The temperature gradient term $(k\ \partial T/\partial z)_{vap}$ is neglected from equation (8.5) for simplification. Removal of this term provides negligible difference in the temperature fields for large vapor core thicknesses. For the evaporator wick, the integrated governing equation along with the boundary condition yields,

$$-q_w+\dot{m}_1''h_{fg}=0 \tag{8.7}$$

For the condenser side wick, we obtain,

$$-h_{air}\left(T_2 - T_{air}\right) - \dot{m}_2'' h_{fg} = 0 \tag{8.8}$$

where the evaporation and condensation surface mass fluxes (across the wick – vapor core interface) can be written as,

$$\begin{aligned} &\dot{m}_1'' = \varphi\left(T_1 - T_{sat}\right) \\ &\dot{m}_2'' = \varphi\left(T_2 - T_{sat}\right) \\ &\text{where} \\ &\varphi = \frac{2\sigma}{2-\sigma}\frac{h_{fg}\rho_{vap}}{\left(T_{sat}^{\;1.5}\right)_{mean}}\left(\frac{1}{2\pi R}\right)^{0.5} \end{aligned} \tag{8.9}$$

In equation (8.9), T_1 and T_2 are the temperatures of the evaporator wick – vapor core and condenser wick – vapor core interfaces. The continuity and momentum equations in the vapor core are combined to obtain a single equation for the vapor core pressure field as,

$$\frac{\partial^2 P}{\partial x^2} + \frac{\partial^2 P}{\partial y^2} = -\frac{12\mu_{vap}}{\rho_{vap} t_{vap}^{\;3}}\left(\dot{m}_1'' + \dot{m}_2''\right) \tag{8.10}$$

The linearized Clausius-Clapeyron equation provides the relation between the saturation temperature and the vapor core pressure,

$$\frac{dP}{dT_{sat}} = \lambda = \frac{h_{fg} P_O}{R\left(T_{sat}^2\right)_{mean}} \tag{8.11}$$

which is used to obtain the equation for the saturation temperature in the vapor core,

$$\lambda\left(\frac{\partial^2 T_{sat}}{\partial x^2} + \frac{\partial^2 T_{sat}}{\partial y^2}\right) = -\frac{12\mu_{vap}}{\rho_{vap} t_{vap}^{\;3}}\left(\dot{m}_1'' + \dot{m}_2''\right) \tag{8.12}$$

The three relations for the evaporator wick interface temperature T_1, condenser wick interface temperature T_2 and vapor core saturation temperature T_{sat} given by eqns.(8.7), (8.8) and (8.12) are solved together. An appropriate Fourier series expansion for the temperatures that satisfies the boundary conditions is,

$$\begin{bmatrix} T_1 \\ T_2 \\ T_{sat} \end{bmatrix} = \sum_{l=0}^{\infty}\sum_{k=0}^{\infty}\left(\underline{a}_{lk}\cos\left(\frac{l\pi x}{L_x}\right)\cos\left(\frac{k\pi y}{L_y}\right)\right), \quad \text{where } \underline{a}_{lk} = \begin{bmatrix} a_1 \\ a_{sat} \\ a_2 \end{bmatrix}_{lk} \tag{8.13}$$

Substituting this in equations (8.21), (8.8) and (8.12), we obtain,

$$\begin{bmatrix} b_1 \\ b_2 \\ b_{sat} \end{bmatrix}_{lk} = \frac{\delta_{lk}}{L_x L_y}\int_0^{L_y}\int_0^{L_x}\begin{bmatrix} q_w \\ -hT_\infty \\ 0 \end{bmatrix}\cos\left(\frac{l\pi x}{L_x}\right)\cos\left(\frac{k\pi y}{L_y}\right)dxdy, \tag{8.14}$$

$$\begin{aligned} &\delta_{lk} = 4 \text{ for } l > 0 \text{ and } k > 0 \\ &\delta_{lk} = 2 \text{ for } l = 0 \text{ and } k > 0 \text{ or } l > 0 \text{ and } k = 0 \\ &\delta_{lk} = 1 \text{ for } l = 0 \text{ and } k = 0 \end{aligned}$$

where,

$$\underline{\underline{G}}\begin{bmatrix} a_1 \\ a_2 \\ a_{sat} \end{bmatrix}_{lk} = \begin{bmatrix} b_1 \\ b_2 \\ b_{sat} \end{bmatrix}_{lk}$$

where

$$\underline{\underline{G}} = \begin{pmatrix} \varphi h_{fg} & 0 & -\varphi h_{fg} \\ 0 & -h_{air} - \varphi h_{fg} & \varphi h_{fg} \\ \varphi h_{fg} & \varphi h_{fg} & -\lambda\left(\frac{\rho_{vap} t_{vap}{}^3}{12\mu_{vap}}\right) h_{fg}\pi^2\left(\frac{l^2}{L_x{}^2} + \frac{k^2}{L_y{}^2}\right) - 2\varphi h_{fg} \end{pmatrix} \tag{8.15}$$

8.1.2.2 Modeling boiling in the evaporator wick

The governing energy equation for the evaporator wick is modified to account for boiling. During boiling, heat transfer from the base of the evaporator wick occurs by conduction through the solid matrix, followed by volumetric evaporation in the pores, following Chapter 7. A representative elementary volume of particles and pores is considered in the wick; an energy balance equation in the control volume can be written based on the conduction and evaporation fluxes as,

$$-k_{eff}\frac{\partial^2 T}{\partial z^2} + \tilde{h}_{evap}\left(T - T_{sat}\right) = 0 \tag{8.16}$$

where the volumetric heat transfer coefficient ($\tilde{h}_{evap}$) is calculated using a pore-scale evaporation model, assuming a thin film of liquid (of thickness δ) sustained in the wick pore space during boiling, following the analysis in APPENDIX F,

$$\tilde{h}_{evap} = \frac{2\left(r_{eff} - \delta\right) h_{lv} \varphi}{r_{eff}^{\;2}\left(1 + \frac{h_{lv}}{k_l}\left(r_{eff} - \delta\right)\ln\left(\frac{r_{eff}}{r_{eff} - \delta}\right)\right)} \tag{8.17}$$

The boundary condition at the evaporator wick-vapor core interface ($z = t_s + t_{wick,1}$) is modified to:

$$-k_{eff}\left.\frac{\partial T}{\partial z}\right|_{z=t_s+t_{wick,1}} = 0 \tag{8.18}$$

(the surface mass flux term ($\dot{m}_1''$) and the vapor core temperature gradient in the z-direction ($\partial T/\partial z$) are excluded from equation (8.5)).

Integrating the governing equation for the evaporator wick,

$$-k_{eff}\left.\frac{\partial T}{\partial z}\right|_{t_s}^{t_s+t_{wick,1}} + \tilde{h}_{evap}\int_{t_s}^{t_s+t_{wick,1}}\left(T - T_{sat}\right)dz = 0 \tag{8.19}$$

And applying the boundary conditions from equation (8.18) yields,

$$-q_w + \tilde{h}_{evap}\int_{t_s}^{t_s+t_{wick,1}}\left(T - T_{sat}\right)dz = 0 \tag{8.20}$$

Defining an average evaporator wick temperature $\bar{T}_1 = \int_{t_s}^{t_s+t_{wick,1}}\left(T - T_{sat}\right)dz \Big/ t_{wick,1}$, we obtain,

$$-q_w + \tilde{h}_{evap} t_{wick,1}\left(\bar{T}_1 - T_{sat}\right) = 0 \tag{8.21}$$

An effective vapor mass flux transport from the evaporator wick to the vapor core ($\dot{m}_1''$) is defined as,

$$\dot{m}_1'' = \frac{q_w}{h_{fg}} = \frac{\tilde{h}_{evap} t_{wick,1}}{h_{fg}}\left(\bar{T}_1 - T_{sat}\right) \tag{8.22}$$

The solution to the temperature fields for the boiling model (average evaporator temperature $\bar{T}_1$, condenser temperature T_2 and vapor core saturation temperature T_{sat}) is obtained in the same way as explained in Section 8.1.2.1, by substituting appropriate Fourier series expansion terms for the temperature profiles, as shown in equations (8.13) and (8.14). In equation (8.15), the modifications described to account for boiling yields a modified matrix $\underline{\underline{G}}$ as,

$$\underline{\underline{G}} = \begin{pmatrix} \tilde{h}_{evap} t_{wick,1} & 0 & -\tilde{h}_{evap} t_{wick,1} \\ 0 & -h_{air} - \varphi h_{fg} & \varphi h_{fg} \\ \tilde{h}_{evap} t_{wick,1} & \varphi h_{fg} & -\lambda \left(\dfrac{\rho_{vap} t_{vap}{}^{3}}{12 \mu_{vap}} \right) h_{fg} \pi^2 \left(\dfrac{l^2}{L_x{}^2} + \dfrac{k^2}{L_y{}^2} \right) - \varphi h_{fg} - \tilde{h}_{evap} t_{wick,1} \end{pmatrix} \tag{8.23}$$

The only unknown in the boiling model is the film thickness δ; the value of this parameter (as a ratio of the effective pore radius of the wick, δ/r_{eff}) was found by fitting the model extensively to individual sets of experimental data on capillary-fed boiling in sintered particle, screen mesh and micro-pillar wick structures, with an accuracy of ± 25% (as was shown in Chapter 7). The current work utilizes this fitted value of the film thickness within the framework of the vapor chamber boiling model.

8.1.3 Coupling vapor chamber model with substrate conduction

The substrate conduction model is coupled with the vapor chamber model using an effective heat transfer coefficient on the substrate–evaporator wick boundary (h_w). An iterative process is followed as described by the steps below,

1. An initial assumption of the mean saturation temperature of the vapor core T_{sat} is taken as 300 K, to start the solution and obtain the thermophysical properties of the working fluid using the commercial software REFPROP [100].
2. An initial guess value of heat transfer coefficient h_w is used to solve the conduction model and obtain an effective heat flux q_w on the substrate-wick interface.
3. The evaporation model described in 8.1.2.1 is used to obtain temperature fields (T_1, T_2, T_{sat}) in the vapor chamber.
4. From the evaporation model, a new effective heat transfer coefficient and the temperature of the substrate wall interface can be obtained as,

$$h_{w,evap} = \frac{1}{\left(\frac{1}{\varphi h_{fg}} + \frac{t_{wick,1}}{k_{eff}} \right)}$$

$$T_w = T_{sat} + \frac{q_w}{h_{w,evap}} \tag{8.24}$$

5. A wall superheat criterion ($T_w - T_{sat} < T_{threshold}$) is used to find the boiling region of the wick.
    a. If no area of the wick satisfies the superheat threshold condition, the new effective heat transfer coefficient $h_{w,new} = h_{w,evap}$ is used and steps 2 – 5 are repeated until convergence of the heat transfer coefficient.
    b. If a region of the wick satisfies this superheat criterion, a new composite heat transfer coefficient is calculated as $h_{w,new} = (h_{w,boil} A_{boil} + h_{w,evap} A_{evap})/A_{total}$ where A_{boil} and A_{evap} are the boiling and evaporation areas of the wick. The new heat transfer coefficient is input into the substrate conduction model, to obtain q_w, following which the boiling model described in 8.1.2.2 is used henceforth to find the temperature fields. The wall temperature is calculated using the new composite heat transfer coefficient as,

$$T_w = T_{sat} + \frac{q_w}{\left(\frac{h_{w,boil} A_{boil} + h_{w,evap} A_{evap}}{A_{total}} \right)}$$

where

$$h_{w,boil} = M_e k_{eff} \tanh\left(M_e t\right)$$

$$M_e = \sqrt{\tilde{h}_{evap} / k_{eff}} \tag{8.25}$$

APPENDIX I provides a derivation of the heat transfer coefficients $h_{w,evap}$ and $h_{w,boil}$. The iterative process is repeated until convergence of the heat transfer coefficient. A suitable convergence criterion is selected as,

$$\left| \frac{h_{w,new} - h_w}{h_{w,new}} \right| < 10^{-4} \tag{8.26}$$

8.2 Wick hydrodynamic model formulation

To calculate the pressure fields in the evaporator wick, and subsequently the dryout heat flux of the vapor chamber, a hydrodynamic model is formulated. The evaporator mass flux ($\dot{m}_1''$) from the heat transfer model is used to obtain the pressure fields in the evaporator wick. In this study, the pressure fields/pressure drop for fluid return through the condenser wick is not modeled (since the condenser side wick contributes negligibly to the total pressure drop of the vapor chamber and does not influence the dryout heat flux prediction).

The governing equations (mass continuity and liquid momentum) for flow through the evaporator wick in a purely evaporation-based model is,

$$\begin{aligned} \nabla.\vec{U} &= \frac{\dot{m}_1''(x,y)}{\rho t_{wick,1}} \\ \nabla P_l &= \frac{\mu}{K}\overrightarrow{U_l} \end{aligned} \tag{8.27}$$

The liquid pressure fields are solved by combining the continuity and momentum equations in the wick,

$$\left(\frac{\partial^2 P_{wick,1}}{\partial x^2}+\frac{\partial^2 P_{wick,1}}{\partial y^2}\right)=\frac{\dot{m}_1''\mu}{\rho K_{wick,1} t_{wick,1}} \tag{8.28}$$

The equations are solved by substituting Fourier series expansions to the pressure fields as described by Patankar *et al.* [99].

When boiling is encountered in the wick as identified by the area of the evaporator wick with a wall superheat greater than the temperature threshold (Section 8.1.3), a new composite hydrodynamic model is formulated to find the pressure fields. A quarter geometry of the evaporator wick of the vapor chamber, as shown in Figure 8.2, is considered. The evaporator wick domain is split into a boiling region and an evaporative region outside, as shown in the figure.

The governing momentum in the evaporator wick is,

$$\begin{aligned} \nabla P_l &= \begin{cases} \dfrac{\mu}{K}\overrightarrow{U_l} & \text{outside boiling area} \\ \left(\dfrac{\mu}{KK_{rl}}+\dfrac{\rho_l C_E}{K^{1/2}K_{rl}}\left|\overrightarrow{U_l}\right|\right)\overrightarrow{U_l} & \text{inside boiling area} \end{cases} \\ \frac{dP_v}{dz} &= \frac{\mu_v}{KK_{rv}}\frac{\dot{m}_1''}{\rho_v} \quad \text{inside boiling area} \end{aligned} \tag{8.29}$$

with boundary conditions,

$$
\begin{aligned}
&P_l = P_{ref} \ \text{ at} \begin{cases} x = \dfrac{L_x}{2} \\ y = \dfrac{L_y}{2} \end{cases} \\
&\frac{\partial P_l}{\partial x} = 0 \ \text{ at } x = 0; \ \frac{\partial P_l}{\partial y} = 0 \ \text{ at } y = 0 \\
&P_v = P_{sat} \ \text{ at } z = t_s + t_{wick,1}
\end{aligned}
\tag{8.30}
$$

The saturation vapor pressure in the vapor core (P_{sat}) is taken as the reference pressure P_{ref} at the outer edges of the domain, and symmetry boundaries are considered on the symmetry planes $x = 0$ and $y = 0$. The Darcy equation for pressure drop through porous media is used in the single-phase region outside the boiling area, and the Darcy-Ergun equation corrected for two-phase relative permeability is used inside the boiling area, following Chapter 7. In equation (8.29), the absolute permeability K is reduced by a factor K_{rl}, (the relative liquid permeability). The viscous pressure drop due to vapor flow out of the wick is considered by the Darcy equation with the relative vapor permeability K_{rv} correction. The effective vapor mass flux $\dot{m}_1''$ is obtained from the heat transfer model, using equation (8.9). An average vapor pressure (averaged over the thickness of the wick is),

$$P_{v,avg} = P_{sat} + \frac{\mu_v q_w t_{wick,1}}{2KK_{rv}\rho_v h_{fg}} \tag{8.31}$$

The relative permeabilities are functions of the local liquid saturation s (fraction of the pore volume filled with liquid). The most widely used expressions for relative permeabilities consider them as power law functions of relative permeability, $K_{rl} = s^n$ and $K_{rv} = (1 - s)^n$. Chapter 7 detailed an approach for obtaining the saturation exponent n by model fitting to experimental data on dryout heat flux ranging three orders of magnitude collected across a wide variety of evaporator wicks (sintered particles, screen mesh, silicon micropillars). The dryout limit is defined as the input power at which the liquid saturation at the center of the domain ($x = y = 0$) falls to zero.

The capillary pressure of the wick (in the boiling region) is defined as the difference between the local average vapor pressure and liquid pressures, $P_c = P_{v,avg} - P_l$. Similar to the relative permeability, the capillary pressure is also a function of the local liquid saturation. When the porous medium is fully saturated, the capillary pressure is at its lowest. When liquid saturation decreases (i.e., as more vapor phase intrudes the saturated pore space), the capillary pressure increases. A simple linear relationship between the capillary pressure and liquid saturation $P_c = P_{c,max}\,(1 - s)$ is used in the current work, following Chapter 7.

The governing equation (8.29) is discretized using the finite volume method (on a rectangular grid), and the semi-implicit method for pressure linked equation (SIMPLE algorithm [101]) is used to solve for the evaporator wick pressure field. An iterative procedure is used with an initial guess of the liquid pressure and velocity magnitude (to avoid the non-linearity in the Darcy – Ergun equation) to start the solution. The discretized flow equations result in a system of linear equations which is solved by matrix inversion; the model is implemented in MATLAB. The solution algorithm is briefly discussed in APPENDIX J.

8.3 Results

8.3.1 Example case study simulation

To illustrate the working of the new vapor chamber model, an example case study is simulated. Figure 8.3 shows a plan and side view cross-sectional schematic diagram of the vapor chamber geometry simulated for the example case study. The geometry consists of a heat spreader of thickness t_s = 1 mm, evaporator and condenser wick thicknesses $t_{wick,1} = t_{wick,2}$ = 1.5 mm and vapor core thickness t_{vap} = 0.5 mm. The length and width of the vapor chamber are L_x = 50 mm and L_y = 50 mm; a centrally placed heat source has dimensions of $l_x = l_y$ = 10 mm. The fin geometry considered for this simulation is: fin thickness t_{fin} = 0.25 mm, fin spacing G_{fin} = 1 mm, and fin height H_{fin} = 20 mm. For these dimensions, and an air mass flow rate of 25 cfm yields an effective heat transfer coefficient on the condenser side as $h_{eff} = 1/(R_{fin}L_xL_y)$ = 1960 W/m^{2}K; a freestream air temperature of T_{air} = 300 K is considered. Table 8.1 shows the properties of the working fluid and the porous evaporator wick used in the example case simulation, at an initial temperature of T = 300 K. The wick is made of sintered copper particles of mean diameter D = 200 µm, with an effective pore radius of r_{eff} = 0.21 D. The wick permeability and effective thermal conductivity are calculated using expressions shown in Table 8.1.

The heat transfer simulation is conducted for a range of input powers Q = 25 W – 275 W. In the boiling model, a film thickness value of δ = 0.27 r_{eff} is used, following the capillary-fed boiling model calibration for 200 µm sintered particles detailed in Chapter 7; a temperature threshold of $T_{threshold}$ = 10 K is used. In the wick hydrodynamic model, a saturation exponent of n = 4 is used for the relative permeability expressions, following the universal model calibration. (Figure 7.10)

Figure 8.4 (a) shows a plan view of the quarter geometry of the evaporator wick domain (200 × 200 cells), with the region of the wick that satisfies the boiling temperature threshold criterion colored in red. Figure 8.4 illustrates the liquid saturation (in part (b)) and evaporator wick and vapor core pressure profiles (in part (c)) from the wick hydrodynamic model. At Q = 25 W, there is no portion of the wick that satisfies this criterion, hence the evaporation model is used to find the pressure profiles. The liquid saturation is not modeled here at Q = 25 W (s = 1 everywhere in the domain as shown in Figure 8.4 (b)), and the pressure drop in the evaporator wick is very small (as shown in Figure 8.4 (c)). At Q = 100 and 250 W, there is a portion of the wick that undergoes boiling, which expands as the heat flux increases, because more of the evaporator wick satisfies the superheat threshold criterion. The saturation value undergoes a step change from s =1 outside the boiling region to a value of s = ~ 0.5 immediately inside the boiling region. This step change occurs because of the vapor pressure excess $P_{v,avg}$ in the boiling region of the wick (given by equation (8.31)), as modeled by the capillary pressure saturation equation ($P_{v,avg} - P_l = P_{c,max}$ (1– s)). The pressure profile shown in part (c) exhibits an inflection point, liquid incurs a higher pressure drop in the boiling region of the wick, due to the reduction in the absolute permeability. As heat fluxes increase, the saturation gradient becomes steeper, as shown in Figure 8.4 (b), for the plot at Q = 250 W. The maximum heat dissipation is reached at Q = 275 W, where the saturation at the center of the wick reaches zero. At this heat flux, the liquid pressure at the center of the domain reaches the maximum capillary pressure (shown by the horizontal black line). We note that the pressure drop in the vapor core is negligible for the entire range of heat fluxes (< 100 Pa even for the highest heat flux of Q = 275 W) considered here, due to the large (500 μm) vapor core thickness.

Figure 8.5 (a) plots the temperature profiles along the centerline (dashed line in the plan view of the vapor chamber in Figure 8.3 (a)) for heat inputs ranging from Q = 25 W – 275 W. Four different temperatures are plotted: temperature along the source plane (z = 0), the spreader–evaporator wick interface ($z = t_s$, T_w), the saturation temperature of the vapor core, and the condenser temperature (T_2). It is seen that the saturation and condenser temperatures are almost similar, and spatially constant for all the heat inputs. The mean saturation temperature increases from ~ 305 K for Q = 25 W to ~ 355 K for Q = 275 W. The maximum temperature of the heat sink (at the middle of the heat source) ranges from ~ 314 K – 440 K, which corresponds to a total thermal resistance of the heat sink $R_{total} = (T_{max} - T_{air})/Q$ ranging from 0.56 K/W – 0.50 K/W. Figure 8.5 (b) plots the effective heat transfer coefficient h_w evolution (plotted against iteration number) while obtaining the steady state solution to the heat transfer model by coupling the substrate conduction and vapor chamber sub-models. Around ten iterations are sufficient to obtain convergence of the heat transfer coefficient per the criterion in equation (8.26). The converged value of heat transfer coefficient ranges from 1.20×10^4 W/m^{2}K – 3.53×10^4 W/m^{2}K for the range of heat inputs.

8.3.2 Comparison of evaporation and boiling models

To illustrate the difference between the dryout limit predicted by the boiling and evaporation models, a simulation is carried out (for the example case in Figure 8.3 and Table 8.1) comparing the capillary pressure ratio (at the center of the simulation domain, $P_c(0,0)/P_{c,max}$) predicted by the two models for a range of heat inputs from Q = 10 – 1300 W, as shown in Figure 8.6. For the evaporation model, the description provided in Section 8.1.2.1 is used without accounting for the occurrence of nucleate boiling in the wick. In this evaporation model, the capillary pressure at the center of the domain is calculated as the difference between the local saturation pressure in the vapor core and the local liquid pressure $P_c(0,0) = P_{sat}(0,0) - P_l(0,0)$. The pressure fields are calculated from the single-phase equation (8.28). For the boiling model, the capillary pressure is calculated as the difference between the local vapor and liquid pressures in the evaporator wick $P_c(0,0) = P_{v,avg}(0,0) - P_l(0,0)$. Dryout occurs in both the models when the capillary pressure ratio reaches unity at a given heat input. While the boiling model predicts a dryout limit of Q_{dry} = 275 W, the evaporation model does not reach dryout until an unrealistically high heat input of Q_{dry} ~ 1300 W since only single-phase flow is modeled in the wick. This comparison illustrates the large differences in model predicted values for high heat flux vapor chambers; the dryout prediction predicted based on a purely evaporation-based approach (using single-phase flow in the evaporator wick) is not practically achievable for the example case study parameters using an air-cooled finned heat sink. The wall temperature of the vapor chamber predicted by the evaporation-based modeling approach at the dryout heat flux of 1300 W is an extremely high value of ~680 K. It is clear from this analysis that incipience would indeed occur in vapor chambers at high heat fluxes and in such cases, the inclusion of a boiling model for calculation of pressure fields provides a more realistic dryout limit prediction.

8.4 Conclusions

This chapter presents a new modeling framework for dryout limit and thermal performance prediction of high-heat-flux vapor chambers used as embedded heat spreaders in the base of air-cooled heat sinks. Models that consider boiling in the evaporator wick is critical for understanding the design tradeoffs in such heat sink architectures. In the present study, the occurrence of nucleate boiling in the evaporator wick is modeled using a physics-based approach. The heat transfer model formulation considers a conduction sub-model (for 3D conduction in the heat spreader) and an analytical vapor chamber sub-model; these sub-models are coupled iteratively using an average heat transfer coefficient between the spreader–evaporator wick interface. Within the heat transfer model, a wall superheat criterion is used to find the region of the wick undergoing boiling. While a single value of this wall superheat threshold is used in the present case study, the modeling framework allows for the user to input a value based on a specific case, which could be experimentally obtained. The wick hydrodynamic model leverages concepts of relative permeability and capillary pressure as functions of local liquid saturation and uses a numerical finite volume-based approach for calculation of pressure fields within a quarter geometry of the evaporator wick. An example case is simulated, with heat fluxes ranging from 25 W – 275 W, to illustrate the working of the heat transfer and hydrodynamic models, while identifying the boiling region of the wick. Dryout in the wick is detected by the liquid saturation falling to zero in the center of the domain. An evaluation of the dryout limit predicted by the evaporation model that considers only single-phase fluid flow (~ 1300 W) illustrates the need for incorporating the effect of boiling in the evaporator wick. The inclusion of boiling in the evaporator wick leads to a more realistic prediction of dryout heat flux of 275 W.

Table 8.1. Properties of the working fluid and porous evaporator wick used in the vapor chamber simulation (properties are calculated at a temperature of 300 K).

Property	**Value**
Liquid density (ρ_l)	998.2 kg/m^3
Vapor density (ρ_v)	0.02 kg/m^3
Liquid viscosity (μ_l)	1.79×10^{-5}
Vapor viscosity (μ_v)	1×10^{-3}
Latent heat of vaporization (h_{fg})	2.45×10^{6} J/Kg
Surface tension (σ)	7.17×10^{-2} N/m
Wick particle size (D)	200 µm
Wick porosity (φ)	0.6
Solid thermal conductivity (k_s)	387.5 W/mK
Effective pore radius (r_{eff})	0.21 D
Wick permeability (K)	$D^2\varphi^3/450(1-\varphi)^2$
Effective thermal conductivity of wick (k_{eff})	$k_{eff} = (2 - 3\varphi)k_s/2$

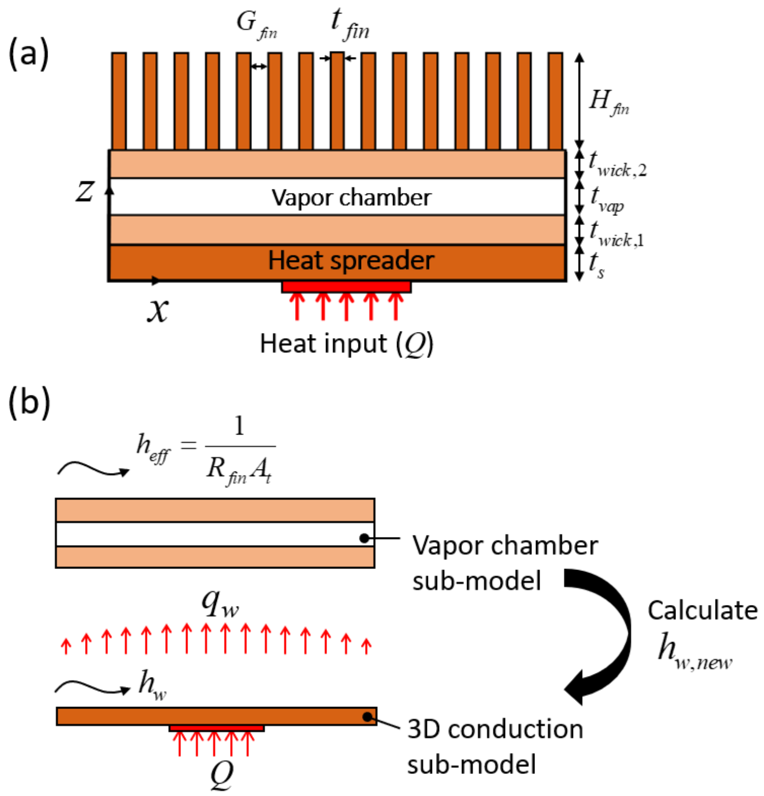
(a)
G_{fin}
t_{fin}
H_{fin}
$t_{wick,2}$
t_{vap}
$t_{wick,1}$
t_s
z
Vapor chamber
Heat spreader
x
Heat input (Q)
(b)
$h_{eff} = \frac{1}{R_{fin} A_t}$
Vapor chamber sub-model
q_w
Calculate $h_{w,new}$
h_w
3D conduction sub-model
Q

Figure 8.1. (a) A schematic diagram of the heat transfer solution domain consisting of a solid heat spreader (thickness t_s), vapor chamber (evaporator and condenser wick thicknesses $t_{wick,1}$ and $t_{wick,2}$; vapor core thickness t_{vap}), and an air-cooled fin array (height H_{fin}, thickness t_{fin}, spacing G_{fin}). (b) A diagram illustrating the heat transfer solution method consisting of solving separate conduction and vapor chamber sub-models, and coupling them using an iterative process.

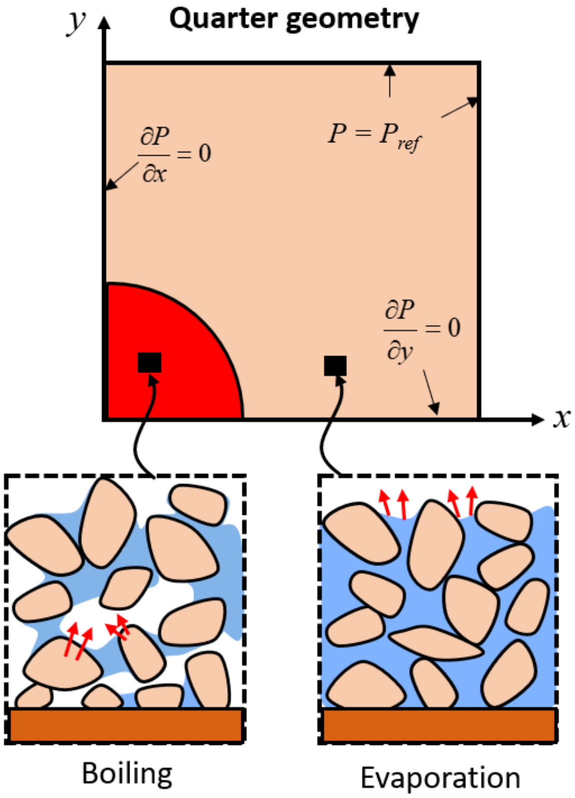
y
Quarter geometry
$\frac{\partial P}{\partial x} = 0$
$P = P_{ref}$
$\frac{\partial P}{\partial y} = 0$
x
Boiling
Evaporation

Figure 8.2. A schematic diagram of the solution domain (quarter geometry of the evaporator wick) and boundary conditions used in the wick hydrodynamics (numerical) model. The domain consists of a boiling region (shown in red) and an evaporation region outside. Inset diagrams show sketches of a control volume spanning the wick thickness in the boiling and evaporation region.

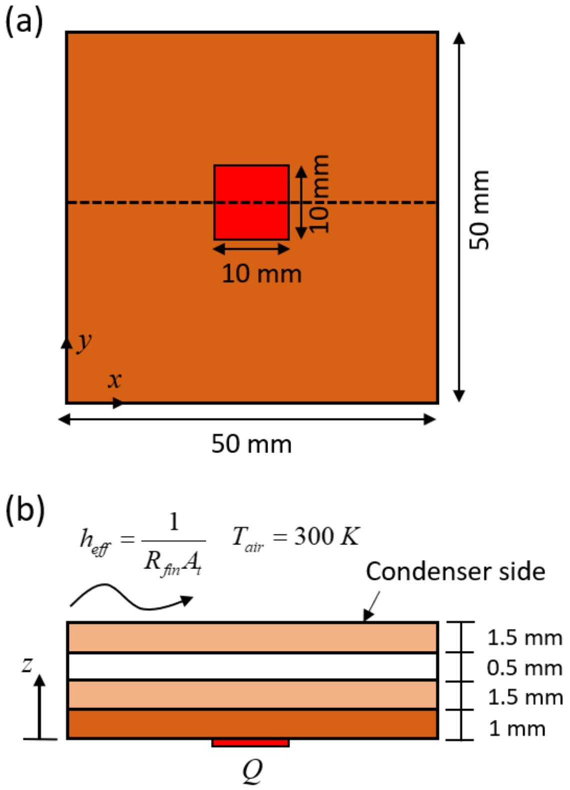
(a)
10 mm
10 mm
50 mm
50 mm
y
x
(b)
$h_{eff} = \frac{1}{R_{fin}A_t}$
$T_{air} = 300\ K$
Condenser side
z
1.5 mm
0.5 mm
1.5 mm
1 mm
Q

Figure 8.3. (a) Plan view and (b) cross-sectional view schematic diagram of the simulated geometry and boundary conditions for the example case illustration. The plan view is drawn to scale; the cross-sectional view is not-to-scale. The dashed line in the plan view denotes the line across which the temperature profiles are plotted.

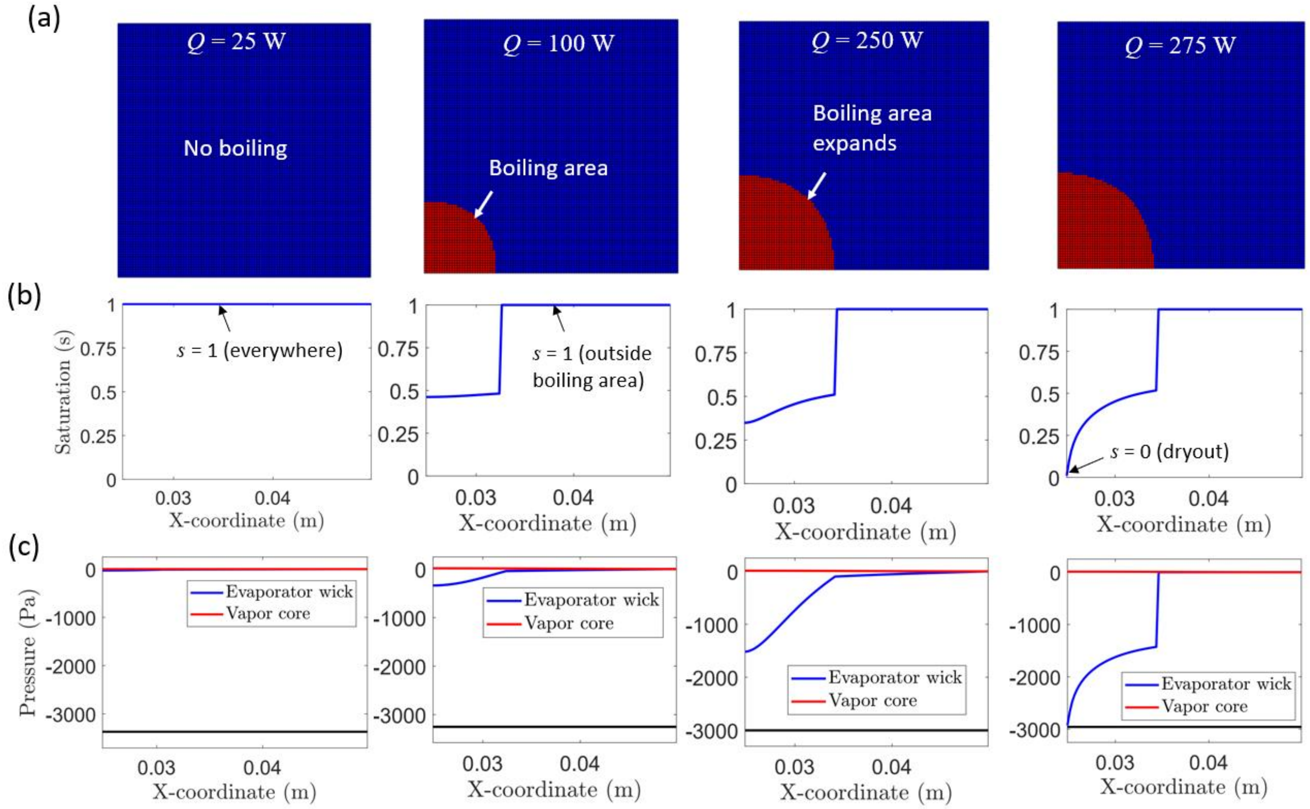

Figure 8.4. (a) Footprint area of the quarter geometry of the wick used in the wick hydrodynamics simulation (200 × 200 cells), that shows the boiling area found from the temperature threshold (cells in red). A plot of the (b) saturation profiles and (c) pressure profiles along the evaporator wick and the vapor core along the diagonal of the quarter geometry. The results are shown at four discrete heat fluxes ranging from Q = 25 W (no occurrence of boiling) to Q = 275W (dryout occurs).

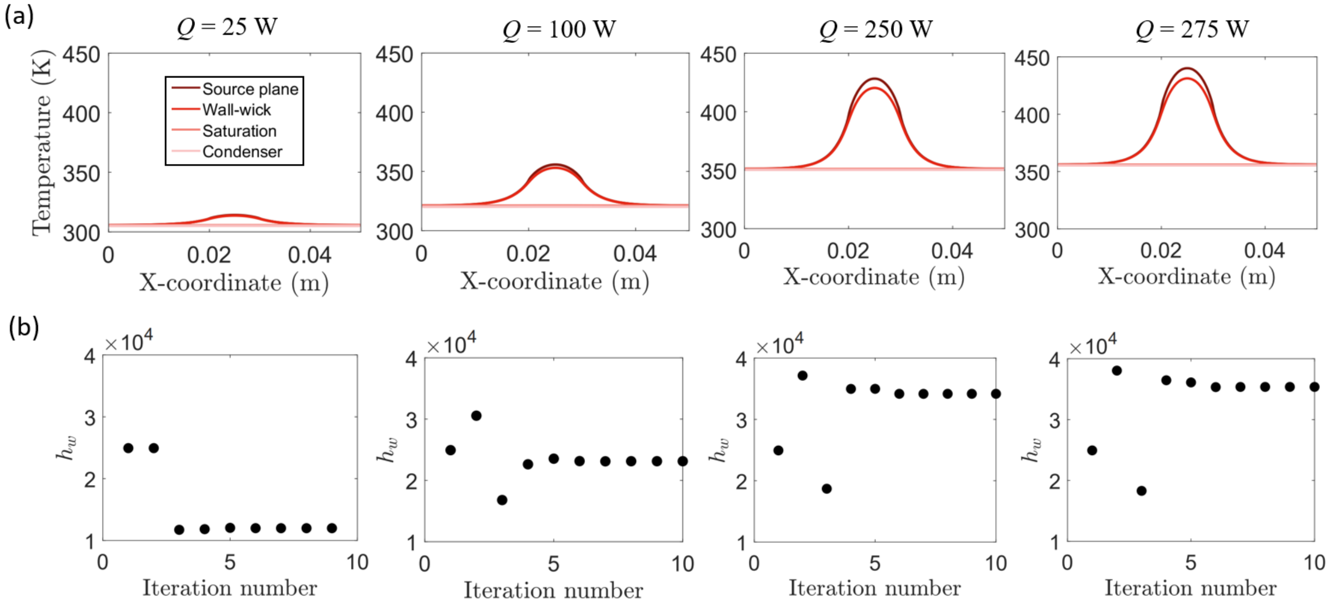

Figure 8.5. (a) Plots of steady state temperature profiles (along the dashed line in Figure 8.3 (a)) at four different planes (source, wall-wick, vapor core saturation and condenser side) for different input powers ranging from Q = 25 W – 275 W. (b) Evolution of the effective heat transfer coefficient h_w with iteration number, showing convergence of the value, which is used to obtain the steady state temperature profiles.

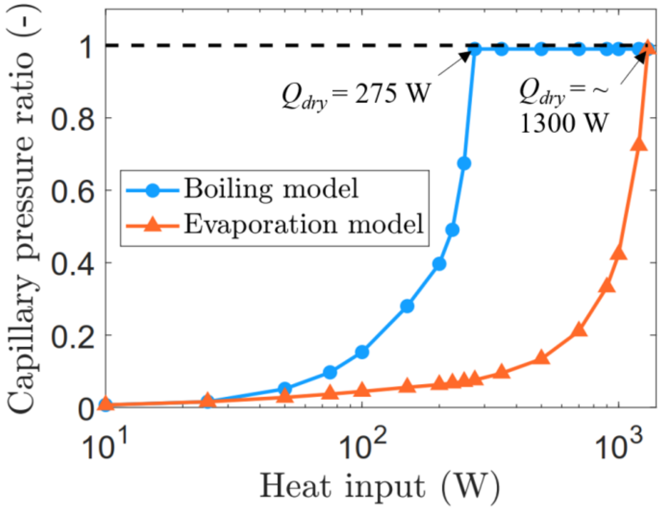

Figure 8.6. A plot of the capillary pressure ratio ($P_c(0,0)/P_{c,max}$) of the vapor chamber as a function of heat input Q for the boiling and evaporation models. The model predicted dryout heat flux values are 275 W for the boiling model and ~1300 W for the evaporation model.

9. CONCLUSIONS AND FUTURE WORK

The main objective of this thesis was to advance the state of the art in vapor chamber technology and understanding of operation at high heat fluxes. The heat input to the vapor chamber dictates the phase-change behavior in the evaporator wick; at high heat fluxes, the performance is governed by boiling and the resulting two-phase flow and heat transfer in the porous wick. This thesis introduced the concept of a new two-layer evaporator wick structure, followed by the design, fabrication, experimental characterization and demonstration of high heat flux dissipation using this design. In addition, a new mechanistic modeling framework was developed to estimate the dryout heat flux and thermal resistance during boiling in capillary fed wicks. This mechanistic framework was incorporated into a vapor chamber model to predict the power dissipation limits of air-cooled heat sinks with embedded vapor chambers. The major conclusions from this thesis and suitable directions for future research are discussed in this chapter.

9.1 Summary of conclusions

In Chapter 3, the concept of the two-layer vapor chamber evaporator wick structure was introduced and evaluated. This novel design leveraged a thin base wick for low thermal resistance during capillary-fed boiling; a thick cap layer and liquid-feeding posts are responsible for providing uniform liquid supply over the entire evaporator area. A reduced-order model was developed to model the thermal and hydraulic resistances in the new design when incorporated within a vapor chamber heat spreader. Parametric studies were used to identify the critical effect of number and size of liquid-feeding posts; denser arrays with smaller diameter posts could reduce the total pressure drop while maintaining the same footprint area of liquid feeding compared to sparse arrays of larger diameter posts. The reduced-order model predicted that heat fluxes on the order of ~1 kW/cm^2 could be dissipated over areas as large as 1 cm^2 without the occurrence of dryout by utilizing a sufficiently large number of liquid-feeding posts. The model provided useful insights into the design of the proposed two-layer evaporator wick structure.

Chapter 4 experimentally studied capillary-fed boiling in the new two-layer wick design and compared its performance to a conventional single-layer design. A novel capillary-fed boiling experimental setup was developed that simulates the saturation and liquid feeding conditions within a vapor chamber. Three designs of evaporator wicks were tested: a single-layer wick and two designs of the two-layer evaporator wick. The single-layer wicks exhibit partial dryout that increased the measured thermal resistance after a certain heat flux is reached, while the two-layer wick avoided this mechanism due to the distributed feeding by the posts. The two-layer wicks also extended the dryout heat flux of the single-layer wick, from ~ 50 W/cm^2 to 151 W/cm^2 (for the 5 × 5 two-layer wick) and up to 198 W/cm^2 (for the 10 × 10 two-layer wick). High-speed visualization aided the identification of different boiling regimes in the wicks; the two-layer wick was observed to operate in a separated flow regime during high heat flux dissipation where the liquid feeding and vapor venting mechanisms are separated, offering unimpeded flow pathways for liquid and vapor.

Chapters 5 and 6 showcased the development of high heat flux dissipation using the two-layer wick. The fabrication of the structure was achieved using a combination of sintering and laser machining processes. SEM images and μ-CT scans were used to characterize the internal structure of the wick. An optimal particle size range was identified from the boiling tests on single-layer wicks of different particle sizes; the 180–212 μm size range provided the highest dryout heat flux which was attributed to the higher intrinsic permeability of the wick. A two-layer wick with 15 × 15 array of liquid-feeding posts, sintered using the 180–212 μm particles dissipated a maximum of 485 W/cm^2 over 1 cm^2 at a thermal resistance of 0.052 K/W. The two-layer wick was shown to provide an unprecedented combination of high total heat dissipation at low thermal resistance, when compared to various other investigations in the literature.

Parametric effects of vapor venting and liquid feeding areas were also experimentally studied to enhance the power dissipation limits of the two-layer wick. Increasing the fraction of vapor venting area (relative to the heater area) from 7% to 16% improved the dryout limit from 315 W/cm^2 to 405 W/cm^2. High-speed visualizations showed that the lower vapor venting area caused vapor to bubble through the cap layer, obstructing the liquid replenishment pathway and reducing the maximum heat flux. An optimized performance was measured for a 10 × 10 array of 650 μm diameter posts with an offset 9 × 9 array of 500 μm vents. Among all the designs, this wick reached the highest dryout limit of ~ 512 W/cm^2 over a 1 cm^2 heated area at the lowest thermal resistance of 0.08 K/W.

Chapter 7 introduced a mechanistic model framework for the prediction of dryout heat flux and thermal resistance during boiling in capillary-fed porous evaporators. Conduction and evaporation heat transfer, and the two-phase Darcy-Ergun equation were solved. The input heat flux at which the liquid saturation at the center of the evaporator falls to zero was defined as the dryout limit. The model was calibrated against a variety of experiments, performed using sintered particle evaporators of different particle and heater sizes, and data collected from the literature on sintered particles, sintered screen meshes, and micro-pillar structures. For the thermal resistance, the model was calibrated against individual sets of data with an accuracy of ± 25%; the calibrated film thickness values depended on the specific wick structure. The model predicted dryout limit agreed well with a wide variety of porous evaporators, with a mean absolute percentage error of 29%; the model captured the trends in particle/pore size, evaporator wick thickness and heater size. A single (fitted) saturation exponent value of $n = 4$ was recommended for use in boiling in capillary-fed porous evaporators from a universal model calibration.

The modeling framework introduced in Chapter 7 was implemented into a vapor chamber model in Chapter 8. This model could be used for the prediction of thermal performance limits of air-cooled heat sinks with embedded vapor chambers, specifically for high power density applications. The heat transfer model considered 3D conduction in the solid wall and was coupled iteratively to the vapor chamber model using an average heat transfer coefficient between the wall–evaporator wick interface. A wall superheat criterion was used to find the region of the wick undergoing boiling. A numerical finite volume-based approach was used for the calculation of pressure fields within a quarter geometry of the evaporator wick. The simulation of an example case with heat fluxes ranging from 25 W – 275 W illustrated the working of the new vapor chamber model. The dryout limit predicted using a single-phase flow model in the wick provided unreasonably high values, reinforcing the need to account for boiling in the wick for high heat flux vapor chambers.

9.2 Future Work

Avenues for future research related to the ideas introduced in this thesis are discussed below:

- The semi-empirical model formulation discussed in Chapter 7 requires a knowledge of the capillary pressure–saturation relationships during imbibition and drainage processes in porous media. These constitutive relationships are dependent on the surface wetting properties and the specific working fluid pair of interest; they can either be obtained from pore-scale simulations (using pore network or other advanced models), or from microfluidic experiments on the corresponding porous media. APPENDIX K discusses an experimental methodology for measuring the capillary pressure saturation relationship for microscale porous media, following the literature on similar experiments in the fuel cell community [137-141] for characterization of air -water two-phase flows in gas diffusion layers (GDLs). Future work in this field can be aimed at leveraging these techniques to obtain functional relationships for different types of porous media and fluid combinations of interest for the heat pipe/vapor chamber community.

- Similarly, the relative permeability–saturation relationship for the specific porous media and fluids pairs of interest in vapor chambers can be experimentally obtained. Earlier works on in-plane relative permeability measurements in large scale porous media, as described in refs. [102, 103], typically allow pre-mixing of the two phases before measurements. In addition, the pressure drop in each phase must be separately found (to use the Darcy equation for each phase). For this purpose, separate probes (with hydrophilic and hydrophobic tips) attached to pressure sensors are used to obtain pressure measurements. For relative permeability measurements in microscale porous media, careful design of the test setup is necessary to incorporate these considerations. A recent work by Hussaini and Wang [104] describes a method for such measurements in thin gas diffusion layers (GDLs). Similar approaches can be explored for in-plane relative permeability measurements as a function of liquid saturation in metallic sintered porous samples.

- The two-layer evaporator wick technology introduced in this work can be incorporated into vapor chamber devices. Our past work in collaboration with Toyota [105] explored a methodology to embed two-layer wicks as evaporators into a vapor chamber with the help of an external vendor. The performance of a 50 mm × 50 mm × 5.5 mm vapor chamber with an embedded two-layer evaporator wick (with a 5 × 5 array of posts; 4 × 4 array of vents) was tested as the heat spreader under a straight pin fin heat sink cooled via air jet impingement for a 1cm^2 area heat source. It was observed that a power dissipation of ~500 W, the air-cooled two-layer wick vapor chamber provides a 12% reduction in the thermal resistance compared to a conventional monolayer wick vapor chamber assembly. Further work in this field can explore different variations of two-layer evaporators, with different particle sizes, post and vent diameters to improve the heat dissipation limits. In addition, area enhancement techniques can be employed to increase the effective boiling area from 1 cm^2 (heater size) to a higher value by utilizing topologically optimized design of heat spreaders (substrate), on which the evaporator wicks can be fabricated.

- Other techniques for enhancing the maximum heat transfer capabilities can be explored to reach the performance targets of 1 kW/cm^2 of heat dissipation. Pump assisted capillary loops have shown promise in improving the maximum power dissipation limits of capillary limited evaporators [106, 107, 108], using an active mechanical element to pump fluid through the system. Future work can involve designing suitable systems to leverage pump assistance.

- While the approaches developed in Chapter 8 modeled the physics of capillary-fed boiling in the evaporator wick of a vapor chamber, a specific superheat threshold was used to define boiling incipience. The conditions that trigger initiation of nucleate boiling in capillary-fed evaporators are still not well understood and the process is considered probabilistic. Prior studies [109] have found that incipience superheats for capillary-fed boiling have a wide range (from 20 – 75 C above the saturation temperature), which is very high compared to pool boiling over porous structures (where incipient superheats can be as low as 1.5 C). Additional experiments with controlled liquid feeding, saturation conditions and enhanced visualization techniques are necessary to understand the effect of operating conditions (such as system pressure) on incipience during capillary-fed conditions, and to devise mechanisms for the observed suppression of bubble nucleation under such conditions.

- The boiling model developed in this work can be extended to consider the behavior after the occurrence of dryout, and include the effects of partial/local dryout in capillary-fed systems, similar to the observations made in Chapter 4, Section 4.3.1 for the single-layer evaporator wick. While the present model defines dryout when the liquid saturation falls to zero at the center of the wick, the framework can be advanced to include the effect of a ‘dry front’ at steady state, and model the stability of such fronts similar to the attempts made to model intermittent dry and wet areas in porous beds as described in refs. [38, 41]. In addition, capillary-fed boiling systems typically observe temperature hysteresis after dryout, during powering down (for example, as seen in ref. [72]). This mechanism is believed to be due to the differences in de-wetting (before dryout) and rewetting behavior (after dryout) in porous media. Based on the understanding developed using imbibition/drainage experiments in APPENDIX K, capillary hysteresis (which is the difference in observed behavior between imbibition and drainage) could be posed as a potential cause of this observed temperature hysteresis. Future work can explore the development of advanced models that incorporate the effect of capillary hysteresis on the thermal performance of capillary-fed boiling systems.

APPENDIX A. LIST OF EXPERIMENTAL EQUIPMENT

Table A.1. Equipment used in the capillary-fed boiling test facility

Part Name	**Vendor/ Manufacturer**	**Part Number**	**Description**
100 V power supply	Sorensen	XG-100-8.5	Power supply for cartridge heaters in heater block
60 V power supply	Sorensen	DLM 60-50 E	Power supply for immersion heaters
Data acquisition (with input module)	Fluke	2640A	Data acquisition (all thermocouple voltage signals)
Thermocouples	Omega	TMTSS-062U-6	T-Type thermocouples for heater block
RTD	Omega	P-M-1/10-1/4-6-0-P-3	Reference temperature sensor
Ice point cell	Omega	TRCIII	Ice point reference for calibration
4- wire pressure transducer	Omega	PX302	Sensor used to measure pressure in test chamber
Graham condensers	Ace Glass	5977-14	Graham condensers used to condense vapor during degassing
Chiller	Coherent	T255P	Chiller for coolant during degassing
Chiller	ThermoFlex	ThermoFlex 900	Chiller for condenser coil within test chamber

APPENDIX B. TECHNICAL DRAWINGS OF CUSTOM FABRICATED COMPONENTS

This section details the fabrication of custom components for the capillary-fed boiling test facility, shown in Figure 4.2. The test facility consists of a sealed test chamber, the heater block assembly and the coolant flow lines. The technical drawings for each fabricated component is included.

Table B.1. Description of components used in the capillary-fed boiling test facility

Component	Drawing	Description
Chamber walls	Figure B.1 Figure B.2 Figure B.3 Figure B.4	Machined polycarbonate and PEEK walls for the test chamber
Insulation assembly	Figure B.8 Figure B.9	PEEK supports for the heater block insulation assembly
Heater block	Figure B.7	Copper heater block that supplies heat input to the wicks
Glass cover	Figure B.6	PEEK glass cover on chamber top wall to enable high-speed visualization
Dam	Figure B.5	Machined PEEK dam to seal and avoid flooding over the wick
Fixture	Figure B.10	Machined PEEK to assemble insulation assembly to the test chamber

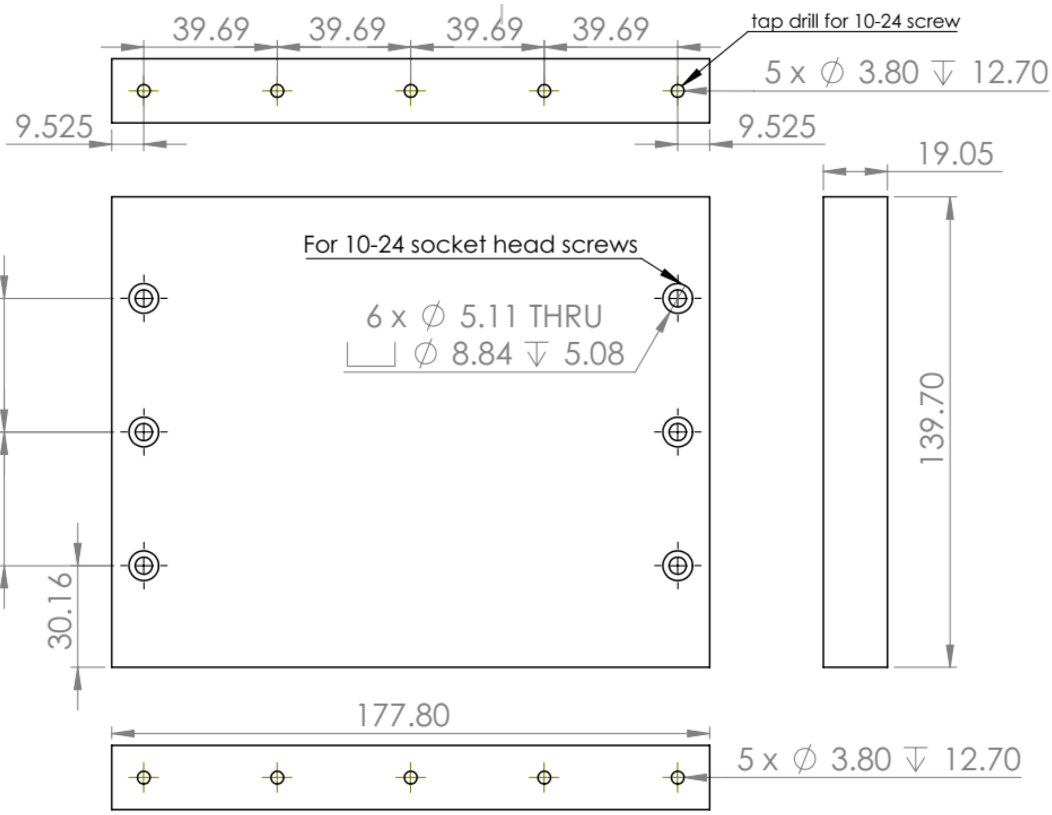
39.69
39.69
39.69
39.69
tap drill for 10-24 screw
5 x ∅ 3.80 ↧ 12.70
9.525
9.525
19.05
For 10-24 socket head screws
6 x ∅ 5.11 THRU
⌴ ∅ 8.84 ↧ 5.08
39.69
39.69
30.16
139.70
177.80
5 x ∅ 3.80 ↧ 12.70

Figure B.1. Technical drawing of the chamber front wall, made from polycarbonate. All the dimensions are in millimeters.

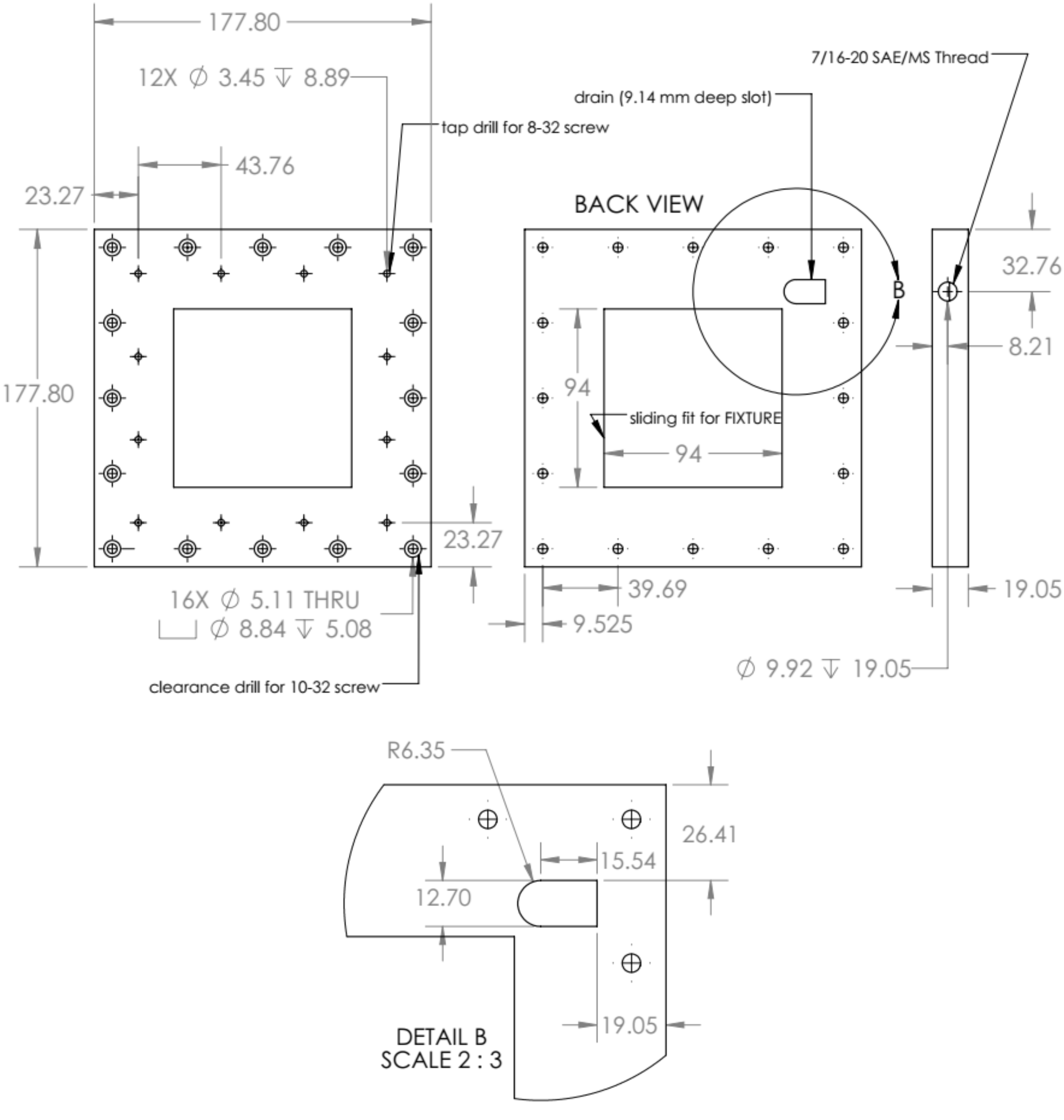
177.80
12X ∅ 3.45 ↧ 8.89
tap drill for 8-32 screw
43.76
23.27
177.80
23.27
16X ∅ 5.11 THRU
⌴ ∅ 8.84 ↧ 5.08
clearance drill for 10-32 screw
BACK VIEW
drain (9.14 mm deep slot)
7/16-20 SAE/MS Thread
B
94
sliding fit for FIXTURE
94
39.69
9.525
32.76
8.21
19.05
∅ 9.92 ↧ 19.05
R6.35
26.41
15.54
12.70
19.05
DETAIL B
SCALE 2 : 3

Figure B.2. Technical drawing of the chamber bottom wall, made from PEEK. All the dimensions are in millimeters.

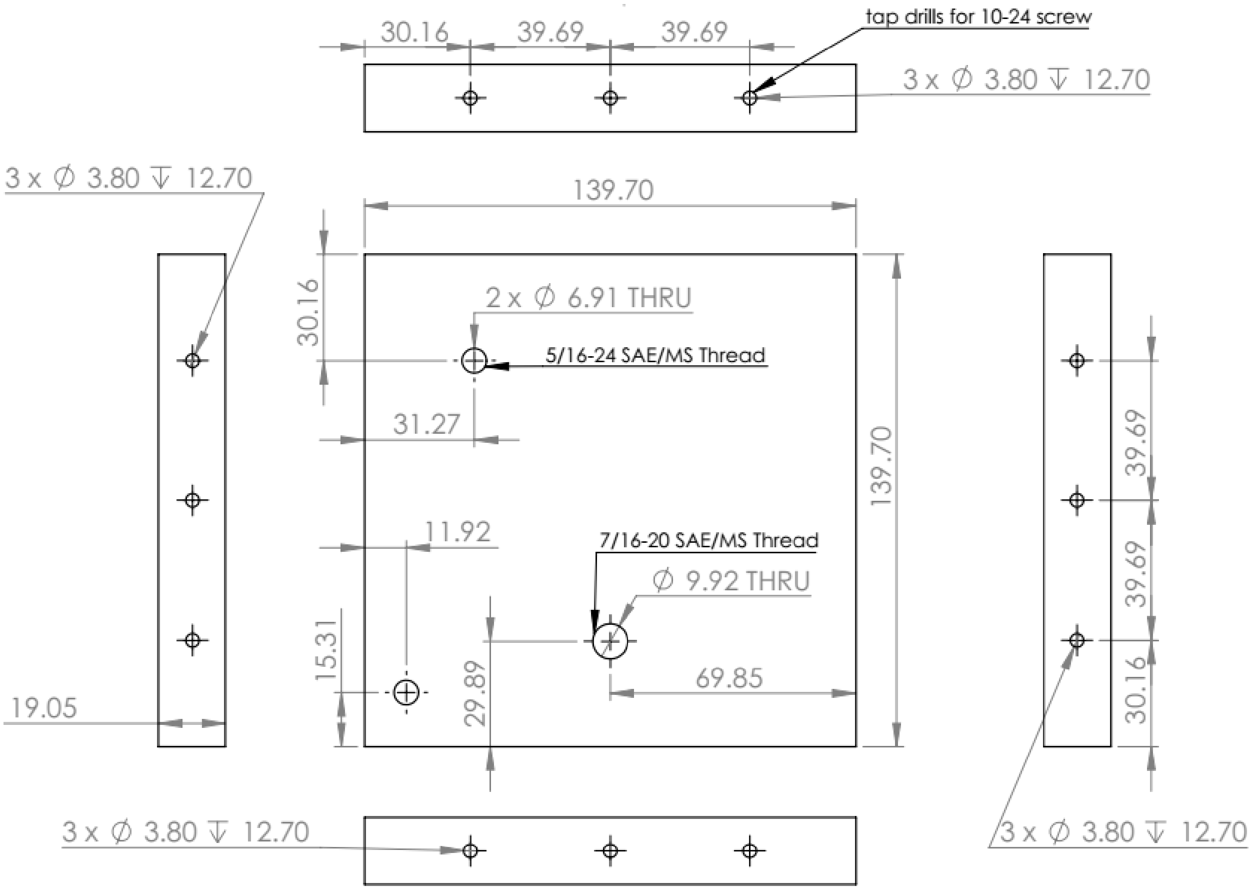
30.16
39.69
39.69
tap drills for 10-24 screw
3 x ∅ 3.80 ↧ 12.70
3 x ∅ 3.80 ↧ 12.70
139.70
30.16
2 x ∅ 6.91 THRU
5/16-24 SAE/MS Thread
31.27
139.70
39.69
39.69
30.16
11.92
7/16-20 SAE/MS Thread
∅ 9.92 THRU
15.31
29.89
69.85
19.05
3 x ∅ 3.80 ↧ 12.70
3 x ∅ 3.80 ↧ 12.70

Figure B.3. Technical drawing of the chamber side wall, made from PEEK. All the dimensions are in millimeters.

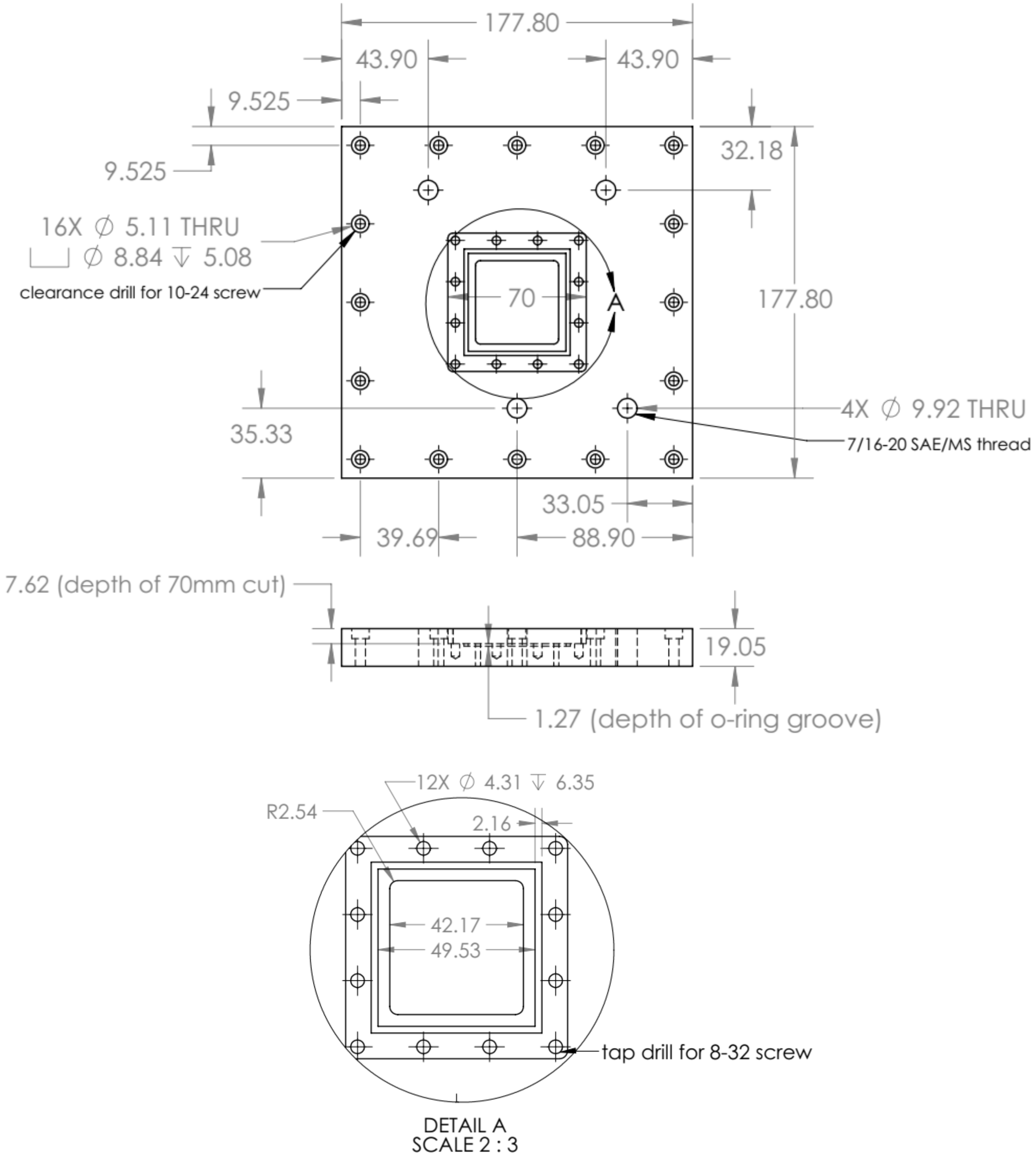
177.80
43.90
43.90
9.525
9.525
32.18
16X ∅ 5.11 THRU
⌴ ∅ 8.84 ↧ 5.08
clearance drill for 10-24 screw
70
A
177.80
35.33
4X ∅ 9.92 THRU
7/16-20 SAE/MS thread
33.05
39.69
88.90
7.62 (depth of 70mm cut)
19.05
1.27 (depth of o-ring groove)
12X ∅ 4.31 ↧ 6.35
R2.54
2.16
42.17
49.53
tap drill for 8-32 screw
DETAIL A
SCALE 2 : 3

Figure B.4. Technical drawing of the top wall of the test chamber, made from PEEK. All the dimensions are in millimeters.

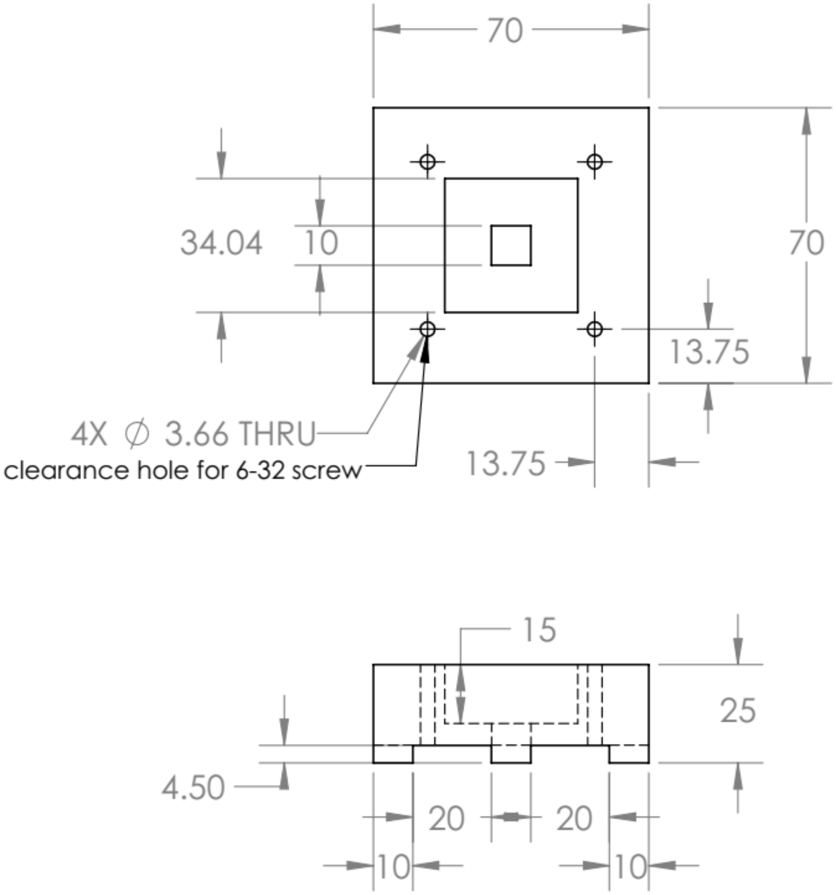
70
70
34.04
10
13.75
13.75
4X ∅ 3.66 THRU
clearance hole for 6-32 screw
15
25
4.50
20
20
10
10

Figure B.5. Technical drawing of the dam structure used to seal and avoid flooding over the top of the wick. All the dimensions are in millimeters.

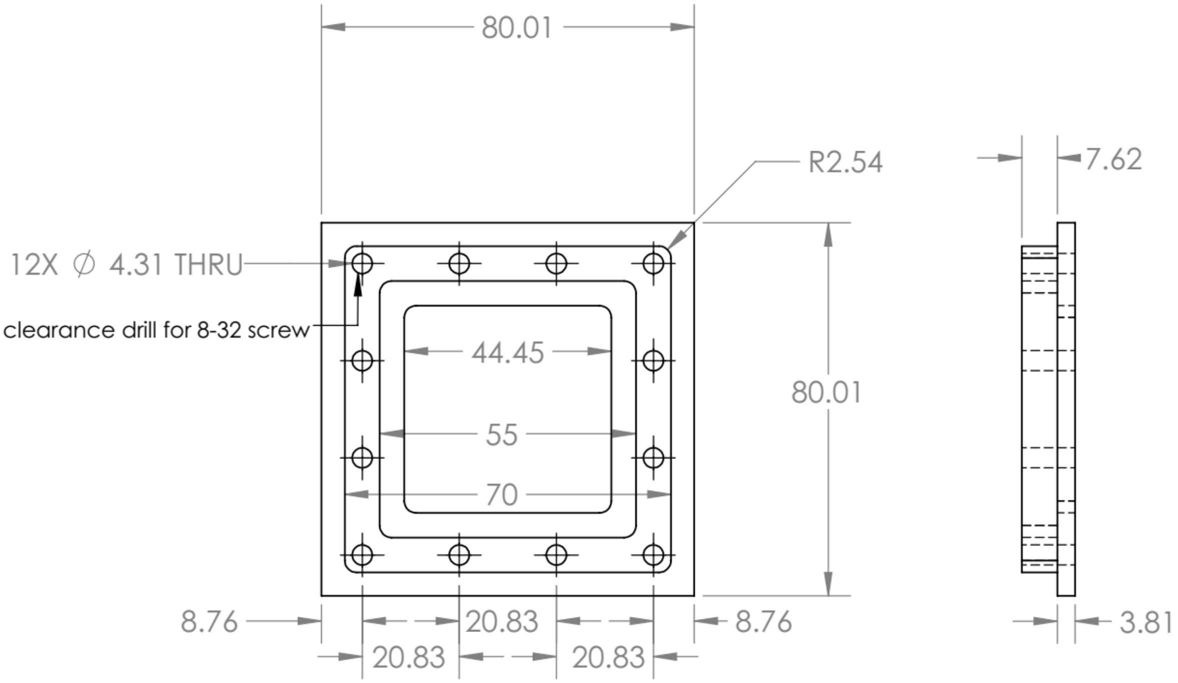
80.01
R2.54
7.62
12X ∅ 4.31 THRU
clearance drill for 8-32 screw
44.45
80.01
55
70
8.76
20.83
8.76
3.81
20.83
20.83

Figure B.6. Technical drawing of the glass cover on the top chamber wall, made from PEEK. All the dimensions are in millimeters.

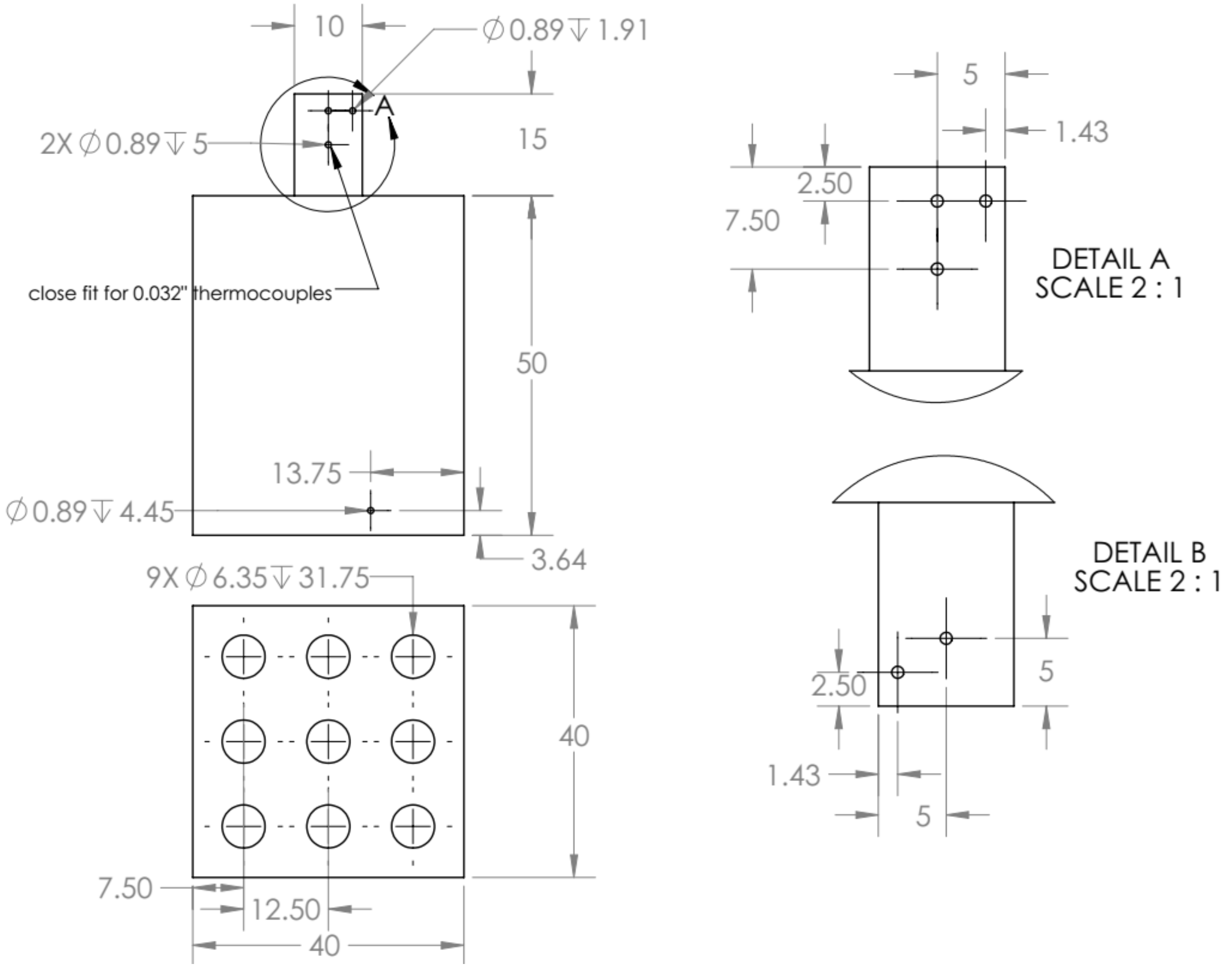
10
∅0.89↧1.91
A
2X∅0.89↧5
15
close fit for 0.032" thermocouples
50
13.75
∅0.89↧4.45
3.64
9X∅6.35↧31.75
40
7.50
12.50
40
5
1.43
2.50
7.50
DETAIL A
SCALE 2 : 1
DETAIL B
SCALE 2 : 1
5
2.50
1.43
5

Figure B.7. Technical drawing of the copper heater block. All dimensions are in millimeters.

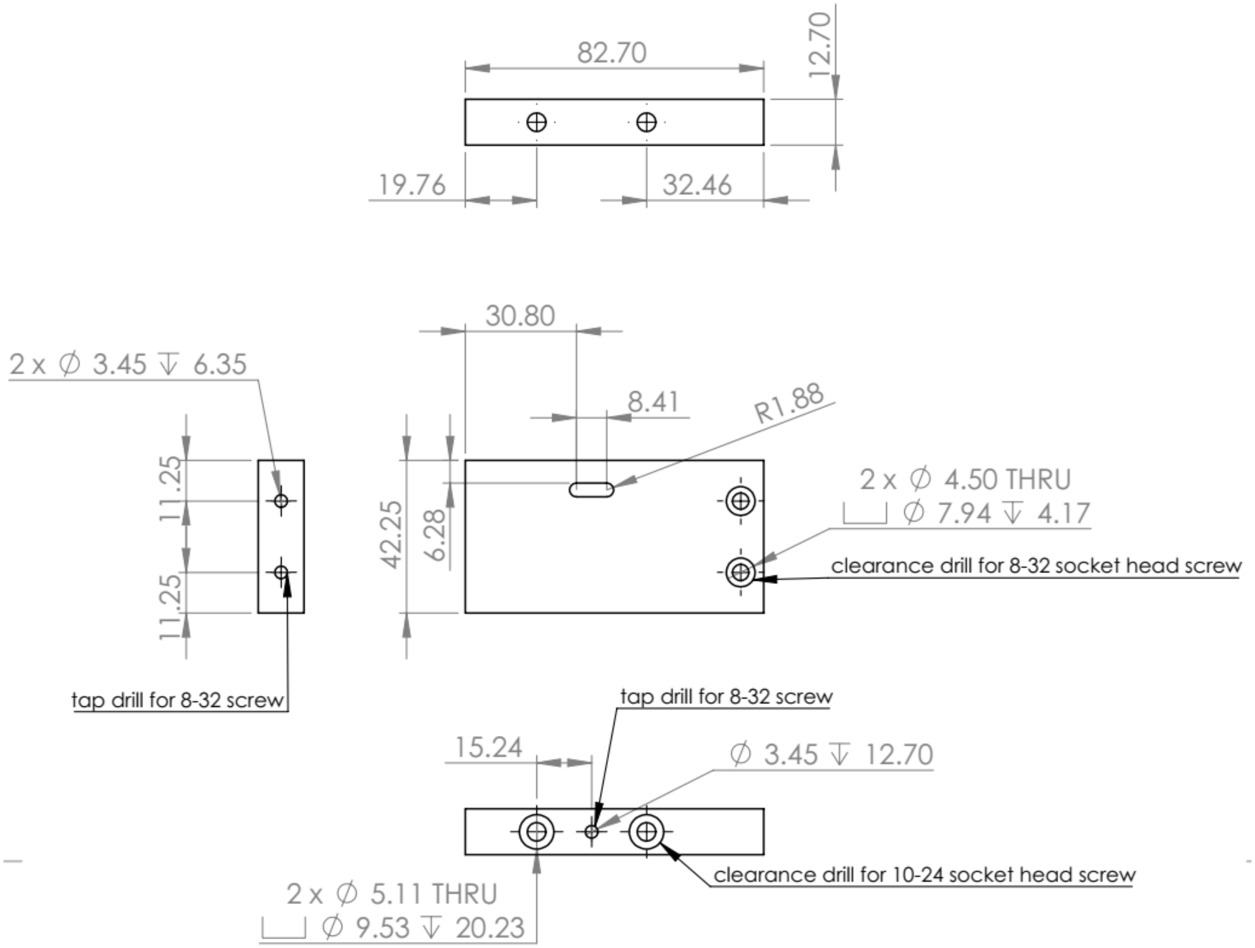
82.70
12.70
19.76
32.46
30.80
8.41
R1.88
2 x ∅ 3.45 ↧ 6.35
11.25
11.25
42.25
6.28
2 x ∅ 4.50 THRU
⌴ ∅ 7.94 ↧ 4.17
clearance drill for 8-32 socket head screw
tap drill for 8-32 screw
tap drill for 8-32 screw
15.24
∅ 3.45 ↧ 12.70
clearance drill for 10-24 socket head screw
2 x ∅ 5.11 THRU
⌴ ∅ 9.53 ↧ 20.23

Figure B.8. Technical drawings of the PEEK insulation used around the copper heater block. All dimensions are in millimeters.

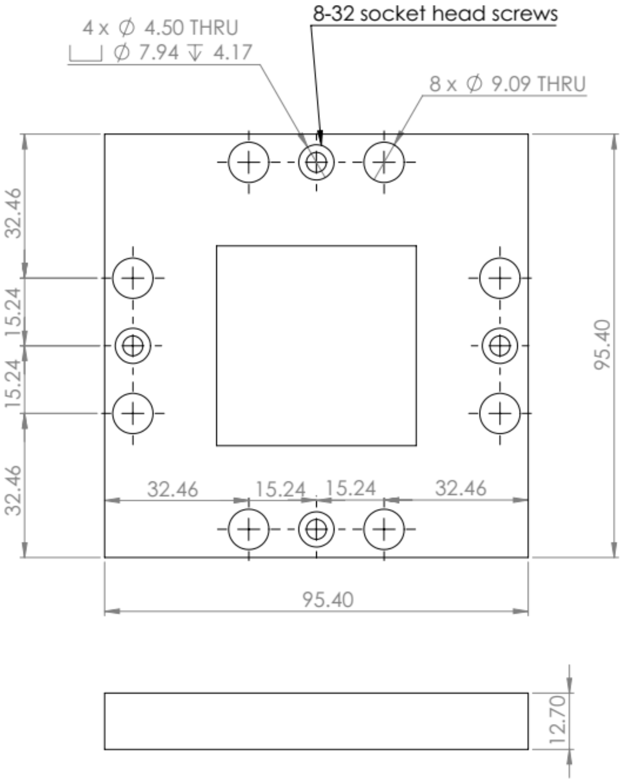
4 x ∅ 4.50 THRU
⌴ ∅ 7.94 ↧ 4.17
8-32 socket head screws
8 x ∅ 9.09 THRU
32.46
15.24
15.24
32.46
95.40
32.46
15.24
15.24
32.46
95.40
12.70

Figure B.9. Technical drawings of the PEEK insulation used around the copper heater block. All dimensions are in millimeters.

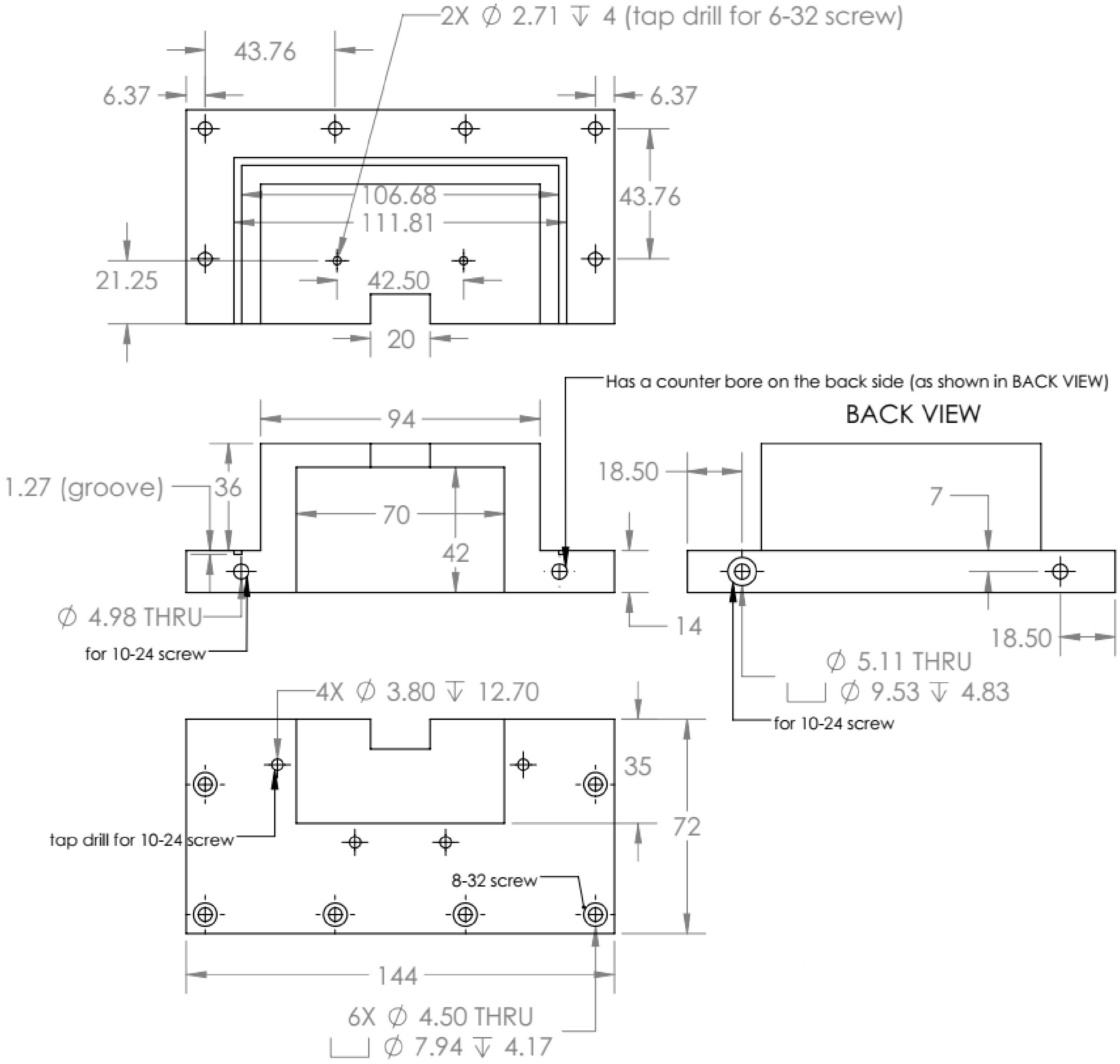
2X ∅ 2.71 ↧ 4 (tap drill for 6-32 screw)
43.76
6.37
6.37
106.68
111.81
43.76
21.25
42.50
20
Has a counter bore on the back side (as shown in BACK VIEW)
BACK VIEW
94
1.27 (groove)
36
70
42
18.50
7
∅ 4.98 THRU
for 10-24 screw
14
18.50
∅ 5.11 THRU
⌴ ∅ 9.53 ↧ 4.83
for 10-24 screw
4X ∅ 3.80 ↧ 12.70
35
72
tap drill for 10-24 screw
8-32 screw
144
6X ∅ 4.50 THRU
⌴ ∅ 7.94 ↧ 4.17

Figure B.10. Technical drawings of the fixture that is used to seal the heater block/wick assembly into the test facility. All dimensions are in millimeters.

APPENDIX C. REDUCED ORDER MODEL OF HOMOGENEOUS AND GRID-PATTERNED EVAPORATOR WICK STRUCTURES

Figure C.1 (a) and (b) show the pressure and temperature drops along the primary fluid flow path in the homogeneous and grid-patterned wick structures. Similar to the two-layer wick reduced-order model, a representative radial flow domain is considered in each case for the calculation of the pressure drop. The effective radius of the evaporator (r_{evap}) is calculated based on the footprint area given by the square edge length (l_{evap}). The liquid returning from the periphery of the vapor chamber incurs the same bulk liquid pressure drop, $\Delta P_{l,bulk}$, as was given for the two-layer wick in equation (3.6)

For the homogeneous wick, the liquid pressure drop through the evaporator wick of thickness t_{base} ($\Delta P_{l,h}$) is calculated by integrating the governing momentum equation from the limit of $r=r_{evap}$ to $r=0$, using the reduced porosity (ϕ_{eff}) and permeability (K_{eff}) for the liquid flow through the base wick layer. This yields:

$$\Delta P_{l,h} = \rho_l \left[\frac{c_6^{\ 2}}{\phi_{eff}^{\ 2}} + \frac{\nu_l c_6}{K_{eff}} \right] \frac{r_{evap}^{\ 2}}{2};\ c_6 = \frac{\dot{m}_{total}}{2\pi \rho_l r_{evap}^{\ 2}\ t_{base}} \tag{C.1}$$

The vapor pressure drop is assumed to be negligible because of the wide area available for vapor flow out of the homogeneous evaporator wick and through the vapor core. The total pressure drop for the homogeneous wick is the sum of the bulk wick and the base wick layer pressure drops, *i.e.*, $\Delta P_{total,h} = \Delta P_{l,bulk} + \Delta P_{l,h}$.

For the grid-patterned evaporator wick, liquid from the bulk wick flows through the grid-patterned area to the center of the evaporator. The evaporator region can be split into a ‘grid layer’, which is the thickness of the wick that contains the square liquid feeding structures (the grids), and a ‘base’ layer wick underneath the grids. Liquid pressure drop through the grid layer is calculated assuming a uniform extraction of liquid to the base layer below. The mass flow rate of liquid is a function of radial position and decreases from $\dot{m}_{total}$ at the evaporator periphery (r_{evap}) to zero at the center:

$$\dot{m}_{l,grid}\left(r\right) = \dot{m}_{total}\left(r^2 / r^2_{\ evap}\right) \tag{C.2}$$

A grid layer liquid flow velocity is calculated as

$$u_{l,grid}\left(r\right)=\dot{m}_{l,grid}\Big/\left(\rho_l 2\pi r t_{grid,eff}\right) \tag{C.3}$$

where, to account for the reduced area available for flow due to the openings in the grid, a reduced effective thickness of the layer $t_{grid,eff}$ is calculated based on the equivalent volume. Integrating equation (3.3) from $r = r_{evap}$ to $r = 0$, the grid layer pressure drop is,

$$\Delta P_{l,grid}=\rho_l\left[\frac{c_7{}^2}{\phi^2}+\frac{\nu_l c_7}{K}\right]\frac{r_{evap}{}^2}{2};\ c_7=\frac{\dot{m}_{total}}{2\pi\rho_l r_{evap}{}^2\, t_{grid,eff}} \tag{C.4}$$

In the base layer, liquid is assumed to flow inward in a unit cell around each grid. This unit cell spans a circular area of radius $r_{eff,grid}$ around each grid (radius r_{grid}), as shown in Figure C.2. The total mass flow rate is equally divided among the unit cells ($\dot{m}_{l,grid} = \dot{m}_{total}/N_{grid}$) and remains constant from $r=r_{eff,grid}$ to $r=r_{grid}$, while it reduces to zero at $r=0$

$$\dot{m}_{l,base,grid}\left(r\right)=\begin{cases}\dot{m}_{l,grid} & r_{grid}\le r\le r_{eff,grid}\\ \dot{m}_{l,grid}\left[\dfrac{r^2}{r_{grid}{}^2}\right] & 0\le r\le r_{grid}\end{cases} \tag{C.5}$$

Integrating the governing momentum equation using the mass flow rate and velocity $u_{l,base} = \dot{m}_{l,base,grid}/(2\pi\rho_l r t_{base})$, the pressure drop is

$$\begin{aligned}\Delta P_{l,base,grid} &= \frac{\rho_l c_8{}^2}{2\phi^2}\left(\frac{1}{r_{eff,grid}{}^2}-\frac{1}{r_{grid}{}^2}\right)+\frac{\mu_l c_8}{K}\ln\left(\frac{r_{eff,grid}}{r_{grid}}\right)\\ &+\frac{\rho_l r_{grid}{}^2}{2}\left(\frac{c_9{}^2}{\phi_{eff}{}^2}+\frac{\nu_l c_9}{K_{eff}}\right)\end{aligned} \tag{C.6}$$

where,

$$c_8=\frac{\dot{m}_{l,grid}}{2\pi\rho_l t_{base}};\ c_9=\frac{\dot{m}_{l,grid}}{2\pi\rho_l t_{base} r_{grid}{}^2}$$

The vapor pressure drop through the grids in the grid-patterned wick and through the vapor core is assumed to be negligible. Hence, the total fluid pressure drop of the grid-patterned wick is given by

$$\Delta P_{total,grid}=\Delta P_{l,bulk}+\Delta P_{l,grid}+\Delta P_{l,base,grid} \tag{C.7}$$

The thermal resistances for the vapor chamber with the homogeneous and the grid-patterned evaporator wick are calculated as done for the two-layer wick. The conduction resistances in the walls of the vapor chamber and the boiling resistance are given by equations (3.23) and (3.21) respectively. Note that in the calculation of the boiling resistance, a reduced evaporator area (area covered by the grids, where boiling occurs) is used for the grid-patterned wick while the complete evaporator area is used for the homogeneous wick. The thermal resistance due to the saturation temperature change is assumed to be negligible. The total thermal resistance in both cases is given by $\Delta T_{total,h} = \Delta T_{condn} + \Delta T_{boil}$.

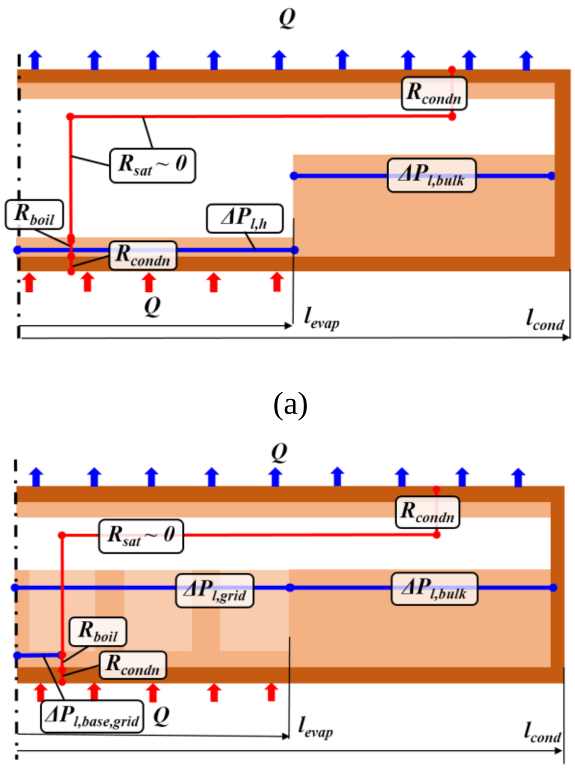
Q
R_condn
R_sat ~ 0
ΔP_l,bulk
R_boil
ΔP_l,h
R_condn
Q
l_evap
l_cond
Q
R_condn
R_sat ~ 0
ΔP_l,grid
ΔP_l,bulk
R_boil
R_condn
ΔP_l,base,grid
Q
l_evap
l_cond

(a)

(b)

Figure C.1. Schematic drawings of cross-sections of a vapor chamber incorporating a (a) homogeneous and (b) grid-patterned wick. The pressure drops (*ΔP*) and thermal resistances (*R*) along the primary fluid flow path are shown for both cases.

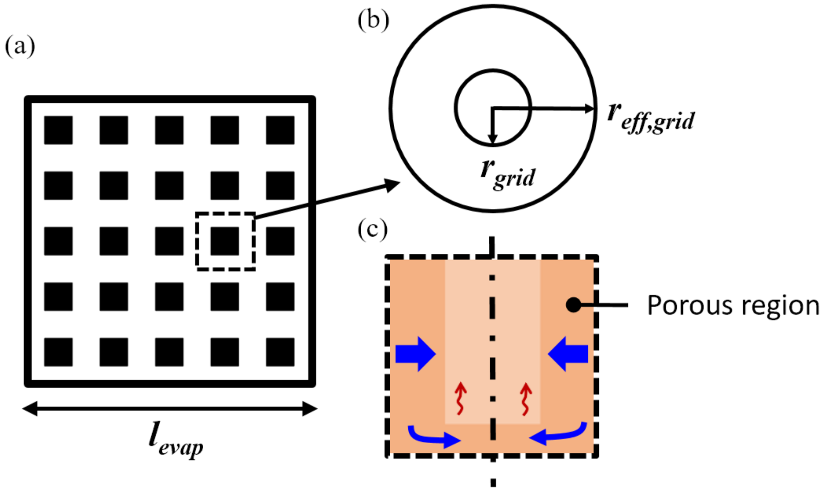
(a)
(b)
(c)
l_{evap}
$r_{eff,grid}$
r_{grid}
Porous region

Figure C.2. Plan view diagram of the grid patterned wick over the evaporator area for an example 5-by-5 grid pattern (filled squares). A square unit cell around a grid is outlined, which is approximated by an axisymmetric radial unit cell with (b) plan and (c) side views shown.

APPENDIX D. SUBSTRATE HEAT SPREADING ANALYSIS

The two-layer wick is fabricated on a copper substrate that is 1 mm thick (t) and square dimensions of 38.1 mm × 38.1 mm (A_b). The heat input (active) region is the center 10 mm × 10 mm area (A_s). At very high heat fluxes, it is expected that boiling can occur over a wick area larger than the heated area, due to heat spreading in the substrate. To calculate the effective spreading area, a conduction domain as shown in Figure D.1 (a) was considered. A heat input (Q) of 500 W was applied as a boundary condition on the heater side, and a convective heat transfer coefficient (h) imposed on the boiling (wick) side of the substrate, along with a reference temperature (T_∞) equal to the saturation temperature. The value of the heat transfer coefficient ($h = 1.78 \times 10^5$ W/m^{2}K) was obtained from experimental data on capillary-fed boiling on two-layer wicks from Section 4.3.2. The sides of the substrate were assumed to be insulated. An analytical 3D conduction model [110] was used to solve for the temperature map on the wick side (shown in Figure D.1 (b)). From this model, it was seen that a 15 mm × 15 mm area of the substrate on the wick side had temperatures exceeding the saturation temperature, and this is identified as the heat spreading area. Informed by this heat spreading analysis, the two-layer wick features were fabricated on this 15 mm × 15 mm area.

To estimate the reduction of the thermal resistance due to heat spreading, the following analysis is performed. Figure D.2 (a) and (b) show schematic diagrams of two different testing configurations, with and without heat spreading. Consider a case where the total evaporating area of the wick is the same as the heat input area (as shown in Figure D.2 (a)). In this case, the dam that seals the wick has the same 10 mm × 10 mm opening for evaporation directly above the heated area, and heat spreading is not expected to have an impact on the thermal resistance. The total thermal resistance that is measured in the experimental characterization of the wicks is thus a sum of the 1D conduction resistance and a boiling resistance.

$$\begin{aligned} R_{total} &= R_{cond,1D} + R_{boil} \\ &= \frac{t}{k_{Cu} A_s} + \frac{1}{h A_s} \end{aligned} \tag{D.1}$$

where k_{Cu} is the thermal conductivity of copper. For the case of heat spreading to a larger evaporating area, the total resistance is a sum of a 1D conduction resistance, a spreading resistance in the substrate ($R_{cond,sp}$) and the boiling resistance of the wick (R_{boil}).

$$\begin{aligned} R_{total} &= R_{cond,1D} + R_{cond,sp} + R_{boil} \\ &= \frac{t}{k_{Cu} A_{sp}} + R_{cond,sp} + \frac{1}{h A_{sp}} \end{aligned} \tag{D.2}$$

where A_{sp} is the spreading area (15 mm × 15 mm). The expression for $R_{cond,sp}$ was taken from a correlation for spreading resistance [111],

$$R_{cond,sp} = \frac{1}{2} \frac{(1-\varepsilon)^{3/2}}{k_{Cu}\sqrt{A_s}} \frac{\left[\tanh(\lambda\tau) + \lambda/Bi\right]}{\left[1 + \lambda/Bi \tanh(\lambda\tau)\right]}$$

where (D.3)

$$\varepsilon = \sqrt{\frac{A_s}{A_{sp}}};\; \tau = \frac{t}{\sqrt{A_{sp}}};\; \lambda = \pi + \frac{1}{\sqrt{\pi\varepsilon}};\; Bi = \frac{h\sqrt{A_{sp}}}{k_{Cu}}$$

Considering the same heat transfer coefficient (h), the values of the individual resistances and the total resistance for the two cases are tabulated in Table D.1. The total thermal resistance is reduced by ~35% in the case with heat spreading. It is concluded from this analysis that, for the current experimental facility, fabricating the two-layer wick features over a larger 15 mm × 15 mm area and allowing for evaporation over this area enables a significant reduction in the thermal resistance due to heat spreading.

Table D.1. Values of individual resistances in the two test cases, with and without heat spreading.

Case	**Resistances (K/W)**			
	1D conduction ($R_{cond,1D}$)	**Spreading ($R_{cond,sp}$)**	**Boiling (R_{boil})**	**Total resistance (R_{total})**
No spreading	0.025	-	0.056	0.081
Spreading	0.011	0.022	0.019	0.052

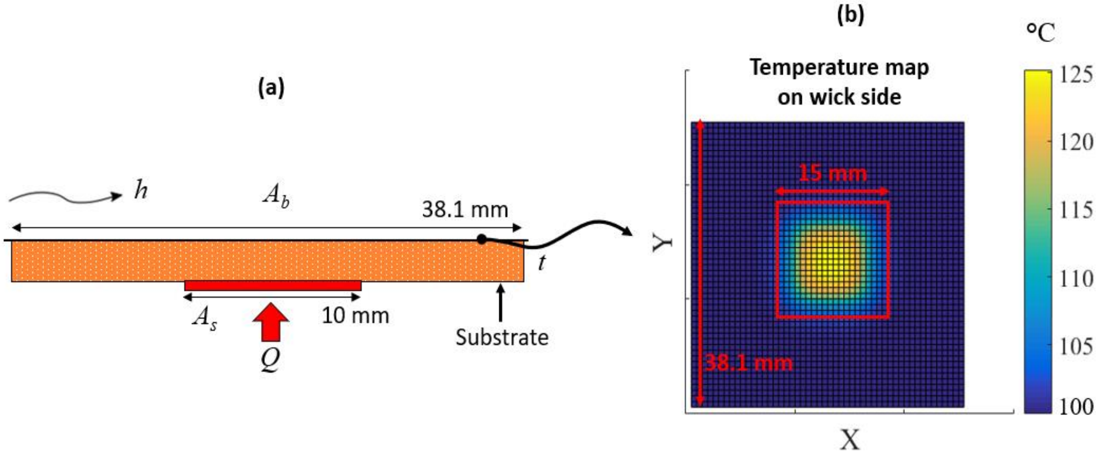
(a)
h
A_b
38.1 mm
t
A_s
10 mm
Q
Substrate
(b)
Temperature map on wick side
°C
15 mm
38.1 mm
Y
X
125
120
115
110
105
100

Figure D.1. (a) Domain and boundary conditions for calculating the spreading area in the substrate. (b) Temperature map on the wick side from the conduction solution.

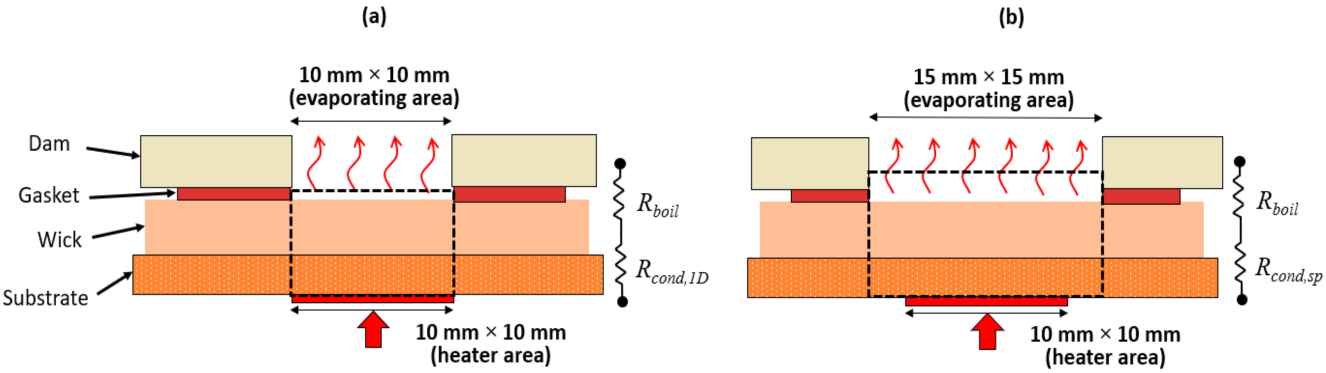
(a)
10 mm × 10 mm
(evaporating area)
Dam
Gasket
Wick
Substrate
R_{boil}
$R_{cond,1D}$
10 mm × 10 mm
(heater area)
(b)
15 mm × 15 mm
(evaporating area)
R_{boil}
$R_{cond,sp}$
10 mm × 10 mm
(heater area)

Figure D.2. Schematic diagram of two configurations (a) with and (b) without heat spreading.

APPENDIX E. TRANSIENT ANALYSIS OF NON-UNIFORM HEAT INPUT PROPAGATION THROUGH A HEAT SINK BASE

This appendix presents the development of a transient model for three-dimensional heat spreading in a Cartesian chip-on-substrate geometry. This geometry is used to calculate coolant-side temperature responses in the presence of transient heat inputs on the chip-side. The degree of spatial and temporal non-uniformity in these responses is quantitatively assessed. The material presented in this appendix was published in the *Journal of Electronic Packaging* [110].

E.1. Introduction

For thermal packaging architectures that rely on thick heat spreaders to dissipate time-varying heat loads generated from multiple discrete components, the heat sink generally does not encounter temperature non-uniformity. This has permitted the use of steady-state or reduced-order transient models for thermal management design. However, packages comprising multiple heat spreading and interfacial layers impose high thermal resistance, rendering them unsuitable for high-heat-flux dissipation within next-generation radar, high-performance computing, and other electronics systems. The emerging need for cooling of high-power-density components has established a new embedded cooling paradigm in which microfluidic heat sinks are directly integrated close to the heat source [112,113]. In this scenario, the heat sink experiences temporally and spatially varying heat loads due to the inherent heat generation non-uniformities and the duty cycle of operation. Suitable transient models should be developed to account for dynamic non-uniformities in the heat sink base.

The high-performance two-phase microchannel heat sinks proposed for embedded cooling architectures are susceptible to flow instabilities and coolant maldistribution [114,115,116,117], which depend on the boundary condition of the heat sink and can affect performance prediction even under uniform heating conditions. The dependence of two-phase microchannel heat sink performance on the heat input boundary conditions and flow distribution has been reported in the literature, *viz.*, investigation of the effects of non-uniform spatial heating on the performance characteristics and maximum heat fluxes dissipated [118,119,120].

A chip-on-substrate geometry is typically considered to represent an architecture wherein a heat source is directly interfaced with the coolant through a heat sink base. This geometry has been widely investigated for different boundary conditions using *steady state* models based on analytical series solutions or numerical methods. Hingorani *et al.* [121] briefly reviewed these methods and used axisymmetric and three-dimensional series solutions to find optimal substrate thicknesses that minimized chip temperature rise. These multi-dimensional solutions are commonly reduced to area-averaged and centroid-based spreading resistance models. Lee *et al.* [111] proposed simplified correlations for spreading resistances in an axisymmetric chip-on-substrate geometry. Muzychka *et al.* [122] developed expressions for the spreading resistance in a three-dimensional Cartesian domain for any eccentrically placed heat source.

Models for *transient* thermal conduction in chip-on-substrate geometries have also been investigated in the literature. Specific chip architectures can leverage lumped resistor–capacitor (RC) network models wherein the chip and package are divided into multiple functional blocks each representing a node in the RC circuit [123]. Owing to the large thermal time constants of the heat sink compared to the corresponding values for the functional blocks on the chip, Skadron *et al.* [123] assumed that the average heat sink temperatures were constant at short time scales. For a more general chip-on-substrate geometry, Yovanovich [124] derived transient spreading resistances for half-space propagations under different isoflux contact area shapes. Yazawa and Ishizuka [125] developed a reduced-order model by extending this transient one-dimensional model [124] to a three-dimensional Cartesian domain. Radial and axial heat conduction were assumed to be independent, superposed phenomena; each corresponding resistance was summed to obtain the total transient thermal resistance. These transient thermal resistance models only yield chip temperatures or area-averaged, coolant-side temperatures.

A transient multi-dimensional conduction model is required to obtain spatially and temporally varying coolant-side temperature responses. Fisher *et al.* [126] calculated the transient chip temperature rise for an axisymmetric chip-on-substrate geometry. The maximum chip temperatures were plotted as a function of various geometric parameters and boundary conditions. Axisymmetric approximation of a three-dimensional domain is valid only at certain heat source placement eccentricities and aspect ratios with respect to the substrate footprint, as shown by Kadambi and Abuaf [127].

While transient models characterizing the chip temperature response for an axisymmetric chip-on-substrate geometry are readily found in the literature, multi-dimensional models that solve for (and describe) the coolant-side temperature and heat flux responses are not reported.

E.2. Transient Modeling Approach

The chip-on-substrate domain, described schematically in Figure E.1, consists of a square heat source of side length *a* placed eccentrically on a larger square substrate of side length *b*. The location of the center of the heat source is (x_c, y_c). The time-varying input heat flux $q(t)$ is uniform over the heat source area. The area surrounding the heat source (and the side surface) is insulated; a convective boundary condition with a constant, uniform heat transfer coefficient *h* is assumed on the opposite coolant-side surface. The problem is non-dimensionalized using the characteristic source length *a*, resulting in the nondimensional variables as follows:

$$\begin{aligned} &x^* = \frac{x}{a};\quad y^* = \frac{y}{a};\quad z^* = \frac{z}{a} \\ &d^* = \frac{d}{a};\quad b^* = \frac{b}{a};\quad t^* = \frac{\alpha t}{a^2} \\ &Bi = \frac{ha}{k};\quad \theta^* = \frac{h\theta}{q_{\max}} \end{aligned} \tag{E.1}$$

where *Bi* is the Biot number, $\theta^*(x^*,y^*,z^*,t^*)$ is the nondimensional temperature rise above the ambient, and $q_{\max}$ is the maximum value of the time-varying input heat flux. The nondimensional governing heat equation in the domain is:

$$\frac{\partial^2\theta^*}{\partial x^{*2}} + \frac{\partial^2\theta^*}{\partial y^{*2}} + \frac{\partial^2\theta^*}{\partial z^{*2}} = \frac{\partial\theta^*}{\partial t^*} \tag{E.2}$$

subject to the boundary and initial conditions:

$$\begin{aligned} &\left.\frac{\partial\theta^*}{\partial x^*}\right|_{x^*=0,\,b^*} = \left.\frac{\partial\theta^*}{\partial y^*}\right|_{y^*=0,\,b^*} = 0;\qquad \left.\frac{\partial\theta^*}{\partial z^*}\right|_{z^*=0} = Bi\,\theta^*\big|_{z^*=0} \\ &\left.\frac{\partial\theta^*}{\partial z^*}\right|_{z^*=d^*} = \begin{cases} Bi\,\dfrac{q\left(t^*\right)}{q_{\max}} & \text{if} \begin{cases} x_c^* - \dfrac{1}{2} \le x^* \le x_c^* + \dfrac{1}{2} \\ y_c^* - \dfrac{1}{2} \le y^* \le y_c^* + \dfrac{1}{2} \end{cases} \\ 0 & \text{otherwise} \end{cases} \\ &\theta^*\big|_{t^*=0} = 0 \end{aligned} \tag{E.3}$$

E.2.1. Unit Step Heat Input Response

Kadambi and Abuaf [128] derived a series solution for the unit step response ($q(t)/q_{\max} = 1$) for a Cartesian chip-on-substrate problem. Briefly, to obtain the unit step response of the system, the solution is split into a steady part and a transient part.

$$\theta_u^*\left(x^*, y^*, z^*, t^*\right) = \theta_s^*\left(x^*, y^*, z^*\right) + \theta_{tr}^*\left(x^*, y^*, z^*, t^*\right) \tag{E.4}$$

Henceforth, the spatial dependency is not shown in the nondimensional temperature expressions and only the temporal dependency is indicated. The steady solution θ_s^* satisfies the governing equation given by Eq. (E.2) with the time rate of change term removed, and the boundary conditions in Eq. (E.3). The non-homogeneity in space is accounted for by expanding the localized heat input into a double Fourier series and applying separation of variables to obtain the steady solution. The unit step response is subsequently obtained by solving Eq. (E.2) for the unknown transient term $\theta_{tr}^*(t^*)$ using separation of variables following Ref. [128]:

$$\begin{aligned}\theta_u^*\left(t^*\right) = \theta_s^* - 2Bi\sum_{k=1}^{\infty}\frac{\left(\cos(\gamma_k z^*) + \dfrac{Bi}{\gamma_k}\sin(\gamma_k z^*)\right)e^{-\gamma_k^2 t^*}}{\cos\left(\gamma_k d^*\right)\left[\gamma_k^2 d^* + Bi(1+Bid^*)\right]}\\ \left[\begin{array}{l}\left(\dfrac{1}{b^*}\right)^2 + \dfrac{4}{\pi b^*}\displaystyle\sum_{l=1}^{\infty}\frac{A_{l0}\gamma_k^2}{l\left(\gamma_k^2+\lambda_l^2\right)}\cos(\lambda_l x^*)e^{-\lambda_l^2 t^*} + \\ \dfrac{4}{\pi b^*}\displaystyle\sum_{m=1}^{\infty}\frac{A_{0m}\gamma_k^2}{m\left(\gamma_k^2+\mu_m^2\right)}\cos(\mu_m y^*)e^{-\mu_m^2 t^*} + \\ \dfrac{16}{\pi^2}\displaystyle\sum_{l=1}^{\infty}\sum_{m=1}^{\infty}\frac{A_{lm}\gamma_k^2}{lm(\gamma_k^2+\nu_{lm}^2)}\cos(\lambda_l x^*)\cos(\mu_m y^*)e^{-\nu_{lm}^2 t^*}\end{array}\right]\end{aligned} \tag{E.5}$$

where

$$\theta_s^*\left(x^*,y^*,z^*\right)=\left(\frac{1}{b^{*2}}\right)\left(1+z^*Bi\right)+4\frac{Bi}{\pi b^*}\left[\begin{array}{l}\displaystyle\sum_{l=1}^{\infty}\frac{A_{l0}B_{l0}}{l}\cos\left(\lambda_l x^*\right)+\\ \displaystyle\sum_{m=1}^{\infty}\frac{A_{0m}B_{0m}}{m}\cos\left(\mu_m y^*\right)\end{array}\right]+$$

$$16\frac{Bi}{\pi^2}\sum_{l=1}^{\infty}\sum_{m=1}^{\infty}\frac{A_{lm}B_{lm}}{lm}\cos\left(\lambda_l x^*\right)\cos\left(\mu_m y^*\right)$$

$$\nu_{lm}=\sqrt{\lambda_l^{\,2}+\mu_m^{\,2}};\ A_{l0}=\sin\left(\frac{\lambda_l}{2}\right)\cos\left(x_c^{\,*}\lambda_l\right);$$

$$A_{0m}=\sin\left(\frac{\mu_m}{2}\right)\cos\left(y_c^{\,*}\mu_m\right);\ A_{lm}=A_{l0}A_{0m};$$

$$B_{lm}=\frac{\cosh\left(\nu_{lm}z^*\right)+\dfrac{Bi}{\nu_{lm}}\sinh\left(\nu_{lm}z^*\right)}{\nu_{lm}\left[\sinh\left(\nu_{lm}d^*\right)+\dfrac{Bi}{\nu_{lm}}\cosh\left(\nu_{lm}d^*\right)\right]}$$

In Eq.(E.5), $\lambda_l = l\pi/b^*$ and $\mu_m = m\pi/b^*$ are the respective eigenvalues in x and y; γ_k are the roots of the characteristic equation $\gamma_k \tan(\gamma_k d^*) = Bi$.

E.2.2. Arbitrary Transient Heat Input Response

The unit step response can be used to obtain the response to any arbitrary time-varying input heat flux using Duhamel's method [129].

$$\theta_D^*\left(t^*\right)=f\left(0\right)\theta_u^*\left(t^*\right)+\int_{\tau=0}^{t}\left[\theta_u^*\left(t^*-\tau\right)\frac{df\left(\tau\right)}{d\tau}\right]d\tau \qquad \text{(E.6)}$$

where $f(\tau)$ is the time-varying input heat flux and θ_D^* is the solution obtained by Duhamel's method.

E.2.3. Time-Periodic Heat Input Response

If the heat input is time-periodic, the temperature profile at any location in the domain will eventually reach a steady-periodic oscillation around a constant mean. The method of complex temperature [130] can be used to estimate the steady-periodic response. The Fourier series expansion of a time-periodic heat input is

$$\frac{q(t^*)}{q_{\max}} = \frac{a_0}{2} + \sum_{n=1}^{\infty} a_n \cos\left(\frac{2\pi n t^*}{Fo}\right) + \sum_{n=1}^{\infty} b_n \sin\left(\frac{2\pi n t^*}{Fo}\right) \tag{E.7}$$

where $Fo = \alpha p/a^2$ is the Fourier number based on the period, p, and a_0, a_n, and b_n are the coefficients in the Fourier series expansion. The steady-periodic solution is split into a steady part and a periodic oscillating transient part.

$$\theta_{sp}^{\ *}\left(t^*\right) = \theta_s^{\ *} + \theta_{tr}^{\ *}\left(t^*\right) \tag{E.8}$$

The steady solution solves the system considering the first term in the Fourier series expansion as the heat input; the solution is given by the same expression for θ_s^* in Eq. (E.5), multiplied by the factor $a_0/2$. The transient solution considers the second and third terms of the Fourier series expansion and is obtained by the method of complex temperature. According to the method, the transient solution is divided into a real and imaginary component, both satisfying the governing equation and the boundary conditions given in Eqs. (E.2) and (E.3), respectively.

$$\theta_{tr}^{\ *}\left(t^*\right) = \sum_{n=1}^{\infty}\left\{\mathrm{Re}\left[\sigma_n\, e^{\frac{i2\pi n t^*}{Fo}}\right] + \mathrm{Im}\left[\psi_n\, e^{\frac{i2\pi n t^*}{Fo}}\right]\right\} \tag{E.9}$$

Using separation of variables, we obtain σ_n as

$$\sigma_n^{\ *} = a_n \begin{bmatrix} \left(\frac{1}{b^{*2}}\right)\left(\cosh\left(\delta_n z^*\right) + \frac{Bi}{\delta_n}\sinh\left(\delta_n z^*\right)\right) \\ +4\frac{Bi}{\pi b^*}\begin{bmatrix} \sum_{l=1}^{\infty}\frac{A_{l0}B_{l0n}}{l}\cos(\lambda_l x^*) + \\ \sum_{m=1}^{\infty}\frac{A_{0m}B_{0mn}}{m}\cos(\mu_m y^*) \end{bmatrix} \\ +16\frac{Bi}{\pi^2}\sum_{l=1}^{\infty}\sum_{m=1}^{\infty}\frac{A_{lm}B_{lmn}}{lm}\cos(\lambda_l x^*)\cos(\mu_m y^*) \end{bmatrix} \tag{E.10}$$

where

$$\delta_n = \sqrt{i2\pi n/\mathrm{Fo}}\,;\;\; \nu_{lmn} = \sqrt{\lambda_l^{\,2} + \mu_m^{\,2} + \delta_n^{\,2}}$$

$$B_{lmn} = \frac{\cosh\left(\nu_{lmn} z^*\right) + \dfrac{Bi}{\nu_{lmn}} \sinh\left(\nu_{lmn} z^*\right)}{\nu_{lmn}\left[\sinh\left(\nu_{lmn} d^*\right) + \dfrac{Bi}{\nu_{lmn}} \cosh\left(\nu_{lmn} d^*\right)\right]}$$

The expression for ψ_n is identical in form to σ_n, but with a_n replaced by b_n in Eq. (E.10). These expressions for σ_n and ψ_n are substituted into Eq. (E.9) to solve for the steady-periodic response.

E.3. Results

E.3.1. Response to Multiple Transient Heat Inputs

To demonstrate solution of the temperature response in the heat sink base for multiple heat inputs with differing transient heat flux profiles, we consider a chip-on-substrate geometry with nondimensional parameters $b^* = 5$, $d^* = 0.5$, and $Bi = 0.1$. A plan view of the three heat inputs is shown in Figure E.2 (a); the size of each heat input is identical with respective (x_c,y_c) center locations of (1.25,2.5), (3.75,3.75), and (3.5,1.25). Each heat source has a different time-varying heat input profile (Figure E.2 (b); $Fo = 1.26$).

For heat sources #1 and #2, Duhamel's method is used; for heat source #3, the unit step solution given by Eq. (E.5) is used. The final solution is obtained by superposition of the three individual heat input solutions. The integral term in Eq. (E.6) is approximated by a summation; each of the transient inputs was discretized into 100 divisions per period of oscillation. Further increasing the number of divisions yielded less than 2% change in the nondimensional temperature solution. The terms in each of the infinite series expansions are summed until an absolute error of 10^{-6} is reached. This criterion was observed to provide sufficiently accurate results for the nondimensional temperatures over the wide variety of cases presented in this work.

The coolant-side nondimensional temperature profiles ($z^* = 0$) at select time instants are shown in Figure E.2 (c). The temperature rise is initially localized to the regions close to the sources. As time proceeds, the peak temperature at the constant heat input source #3 increases and heat spreading expands the size of this temperature signature to the surrounding region. The temperature responses at the locations of sources #1 and #2 oscillate in time in accordance with the transient heat inputs.

E.3.2. Single Centrally Placed Heat Source

A simplified scenario is posed to investigate the effects of heating characteristics, geometry, and boundary conditions on the spatial and temporal non-uniformity at the coolant side. For conditions under which the effect of thermal spreading from a heat source is localized, the problem can be reduced to a single square heat source placed at the center of the domain. To assess the frequency dependence of the temperature response, we consider on-off operation of the chip (*viz.*, a square wave heat input with a prescribed duty cycle). Duhamel's method is applied for the square wave heat input to obtain the complete transient response:

$$\theta_D^*\left(t^*\right) = \theta_u^*\left(t^*\right) + \sum_{n=1}^{N} (-1)^n \ \theta_u^*\left(t^* - \tau_n\right)$$

$$\tau_n = \begin{Bmatrix} \left(\omega + \dfrac{n-1}{2}\right) Fo & n \text{ is odd} \\ \dfrac{n}{2} Fo & n \text{ is even} \end{Bmatrix} \qquad \text{(E.11)}$$

where ω is the duty cycle of the input.

The steady-periodic response of the system is calculated by the method of complex temperature using the corresponding Fourier coefficients for the square wave heat input.

$$a_0 = 2\omega; \ a_n = \frac{\sin\left(2\pi n\omega\right)}{n\pi}; \ b_n = \frac{1 - \cos\left(2\pi n\omega\right)}{n\pi} \qquad \text{(E.12)}$$

An example case is demonstrated for the nondimensional parameters: $Bi = 0.1$; $d^* = 0.5$; $1/b^* = 0.5$; $Fo = 0.5$; and $\omega = 0.5$. Figure E.3 (a) shows the time-evolution of the nondimensional temperature at the center point on the coolant side, obtained using Duhamel's method. This location experiences the maximum temperature fluctuation on the surface. The solution reaches a steady-periodic regime after sufficient time (Figure E.3 (a) inset). Figure E.3 (b) shows the mean steady nondimensional temperature profile on the coolant-side surface. Henceforth, steady-periodic solutions will be evaluated for this single heat source problem to quantify the amount of spatial and temporal non-uniformity at the coolant side.

E.3.3. Spatial Non-Uniformity

To quantify the spatial temperature non-uniformity on the coolant-side surface, the steady-periodic solution is obtained at a grid of discrete points on the $z^* = 0$ plane. A suitable metric is chosen that represents the extent of spatial non-uniformity.

$$RMS\left\{\theta_s^* \big/ \overline{\theta_s^*} - 1\right\} \qquad \text{(E.13)}$$

where $\overline{\theta_s^*}$ is mean of the $z^* = 0$ plane. For the range of cases presented herein, a grid of 100×100 points in *x* and *y* was sufficient to attain converged results for the *RMS* evaluation.

The spatial non-uniformity is a function of only nondimensional thickness d^*, Biot number Bi, and the nondimensional substrate side length b^*. Figure E.4 (a) plots spatial non-uniformity against the nondimensional thickness for different Biot numbers. In all cases, the temperatures become more smeared as thickness increases and consequently, the non-uniformity decreases. At very low Biot numbers, the convective resistance is dominant over the conductive resistance; the coolant side assumes near-uniform temperature profiles. As the Biot number increases, and the relative effectiveness of conductive heat spreading is reduced, the non-uniformity increases. Figure E.4 (b) shows the dependence of spatial non-uniformity on the inverse of nondimensional substrate length $1/b^*$. The limiting case of $1/b^* = 1$ (*i.e.*, the heat source covers the entire substrate footprint area) corresponds to one-dimensional conduction and spatial non-uniformity is zero. Smaller heat sources relative to the substrate always produce more non-uniformity per the chosen metric.

Figure E.5 (a) plots isolines on a map of spatial non-uniformity for Biot number versus nondimensional thickness. Such a map can be used to rapidly determine the conditions under which the coolant-side spatial non-uniformity reaches a prescribed value (*e.g.*, to assess whether a particular case approaches some limit of non-uniformity at which coolant behavior will be significantly impacted).

To demonstrate the utility of such maps for design purposes, case studies representing three different thermal packaging architectures are presented:

- Case #1 represents an air-cooled device with a finned copper heat sink;

- Case #2 represents a high-power device on a silicon substrate with microchannels directly etched into the back side; and
- Case #3 represents a low-power device that dissipates heat through a low-conductivity printed circuit board substrate.

The schematic diagrams of these cases are displayed in Figure E.6 lists the values of the geometric and thermophysical parameters chosen for these cases, as well as an effective convective resistance $R_{conv} = 1/hb^2$ imposed on the base area.

The coolant-side temperature profiles are evaluated for each of the cases and the calculated values of spatial non-uniformity are shown as dots in Figure E.5 (a). Figure E.5 (b) and (c) show mean steady temperature profiles for Case #1 and Case #2. These cases illustrate extremes of spatial non-uniformity in temperature for the coolant side under practical conditions. While Case #1 produces a fairly uniform temperature profile owing to the thick heat-spreading base, Case #2 yields high non-uniformity on the coolant-side surface, with the temperature rise concentrated to the region directly aligned with the heat source footprint area.

E.3.4. Temporal Non-Uniformity

To characterize the temporal non-uniformity, the steady-periodic solution of nondimensional temperature is monitored at the center point on the coolant side. The extent of the temporal non-uniformity is quantified as the RMS value over one time period at this center point.

$$RMS\left\{\theta_{sp}^{*}\left(t^{*}\right)\Big/\overline{\theta_{sp}^{*}}-1\right\} \tag{E.14}$$

where $\overline{\theta_{sp}^{*}}$ refers the time-averaged, steady-periodic temperature at the center point. A time-discretization of 50 points per period was sufficient to obtain converged results for the *RMS* evaluation.

For a fixed geometry and convective boundary conditions, the temporal non-uniformity is a function of Fourier number *Fo* and duty cycle ω of the prescribed square wave heat input. Figure E.7 plots the temporal non-uniformity against the Fourier number for varying duty cycle. High-frequency oscillations in the heat input (*i.e.*, low Fourier numbers) produce little temporal non-uniformity. In the limit of $\omega = 1$, a constant heat input in time, the non-uniformity is zero. A smaller duty cycle results in higher temporal non-uniformity.

Temporal non-uniformity is mapped as a function of the Fourier number and duty cycle, with isolines of this map shown in Figure E.8 (a). Figure E.8 (b) and (c) display the nondimensional center point temperature on the coolant side for one time period in the steady-periodic regime. These represent two extreme Cases A and B of low and high temporal non-uniformity (0.0085 and 0.2376, respectively) in the coolant-side temperature for comparatively high- and low-frequency heat input profiles.

E.4. Conclusions

A three-dimensional transient model for a chip-on-substrate geometry is used to predict the extent of spatial and temporal temperature non-uniformity that propagates through the heat sink base from the heat source to the coolant side. The model can readily accommodate any transient heat input from multiple heat sources by superposition. The extent of non-uniformity was mapped as a function of the geometric parameters and boundary conditions.

The analysis developed in this work is useful in quantifying the conditions under which non-uniform heat loads are not completely smeared, but instead propagate though a heat sink base to the coolant side. For a range of cases representing practical thermal management architectures, the coolant side can assume widely differing temporal and spatial temperature profiles. Commonly used steady state and reduced-order transient models may not be capable of capturing such temporal and spatial non-uniformity characteristics that the coolant side assumes. Mapping of these non-uniformities, as presented herein, provides a means to screen for the conditions under which higher-fidelity modeling approaches may be required to satisfactorily resolve the coolant-side temperature response.

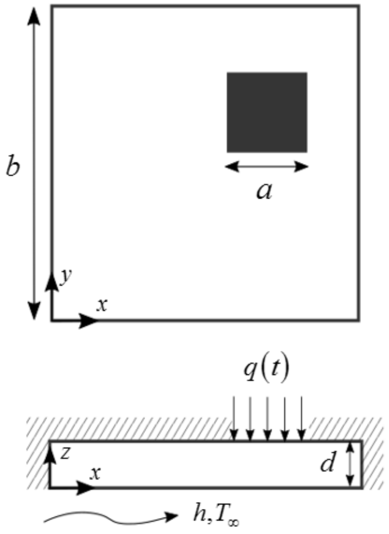
b
a
y
x
q(t)
z
x
d
h, T∞

Figure E.1. Schematic diagram of the chip-on-substrate domain.

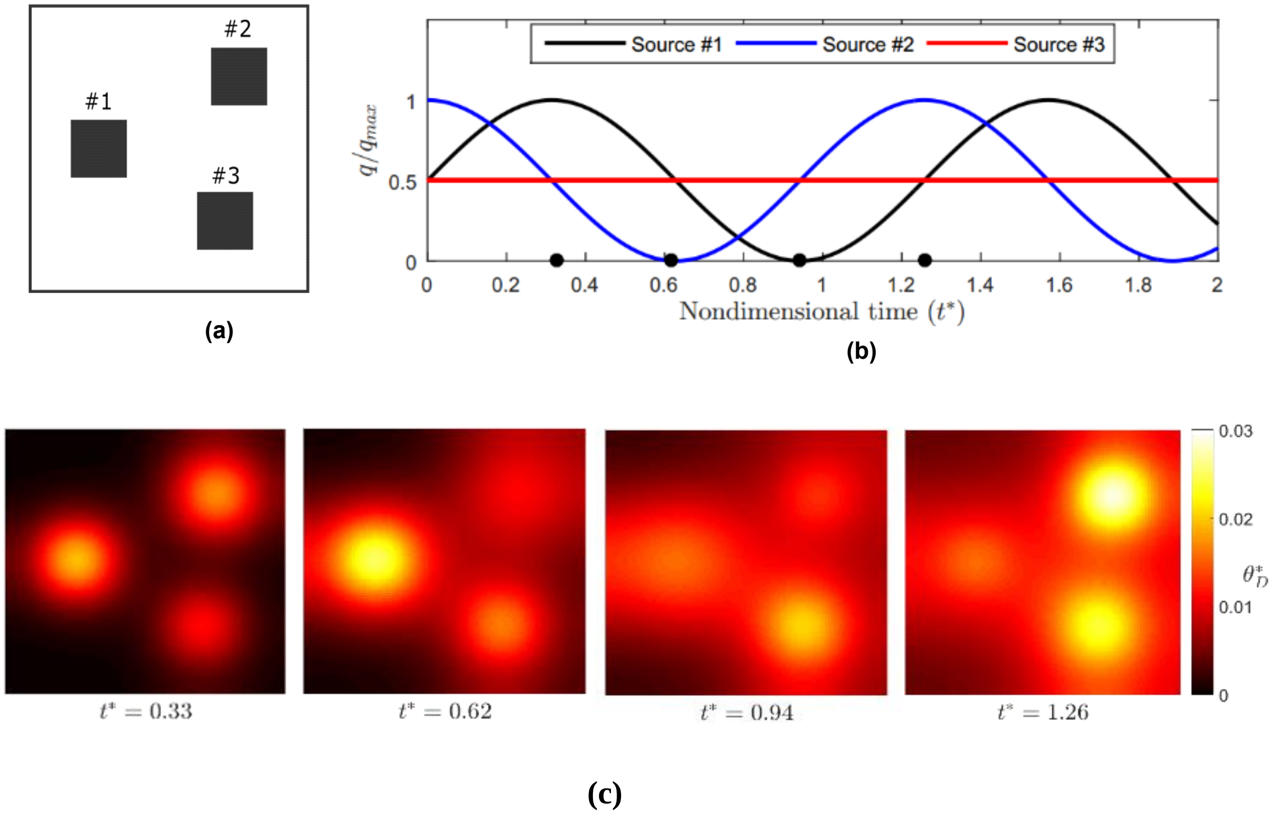

(a)

(b)

(c)

Figure E.2. (a) Plan-view locations and (b) transient heat input profiles for multiple heat sources on a single substrate. (c) The nondimensional temperature profile is shown for the coolant side at selected nondimensional time instants (indicated by the dots on the axis in (b)).

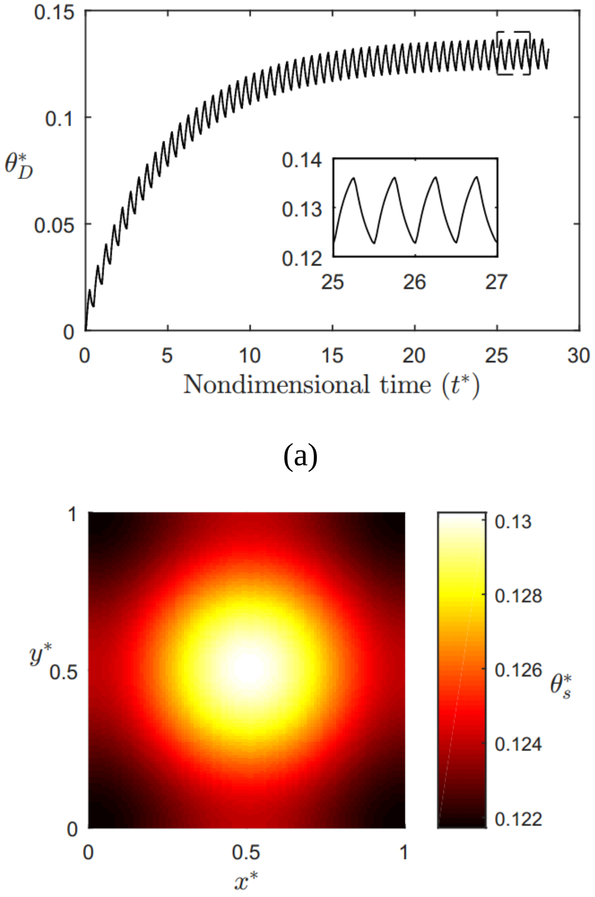

(a)

(b)

Figure E.3. (a) Nondimensional temperature-time plot at the center of the coolant-side surface and (b) mean steady temperature profile.

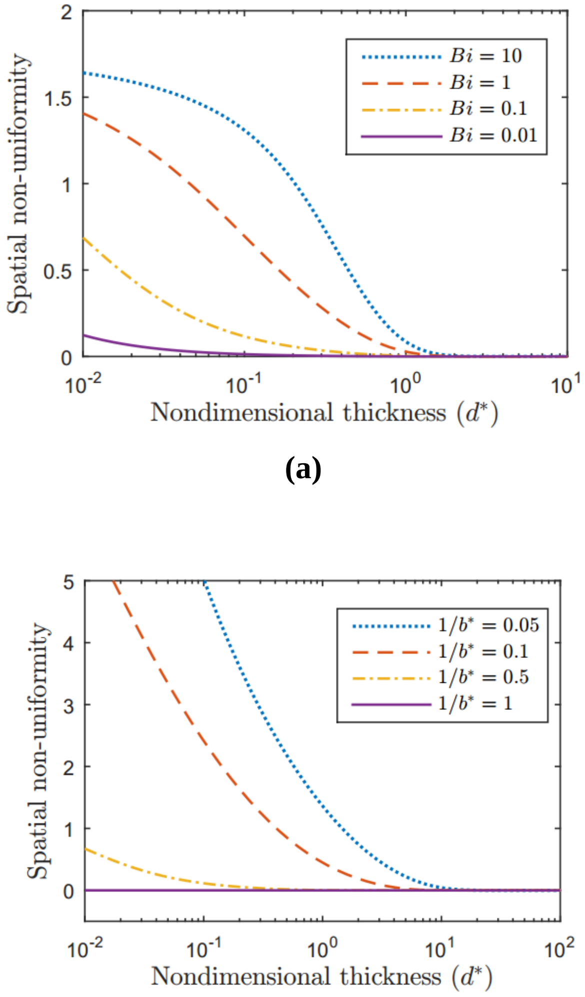

(a)

(b)

Figure E.4. Variation of spatial non-uniformity with non-dimensional thickness d^* for different (a) *Bi* (at $1/b^* = 0.5$) and (b) $1/b^*$ (at $Bi = 0.1$).

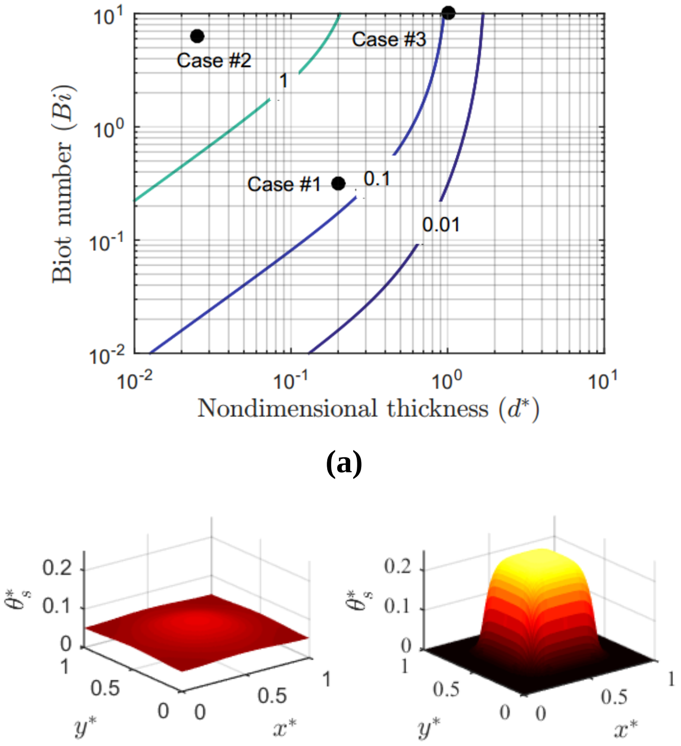

(a)

(b) **(c)**

Figure E.5. (a) Isolines of spatial non-uniformity map for *Bi* versus d^* (at $1/b^* = 0.5$); case studies are indicated on the map with a dot. Nondimensional temperature profiles on the coolant side are shown for (b) Case #1 and (c) Case #2.

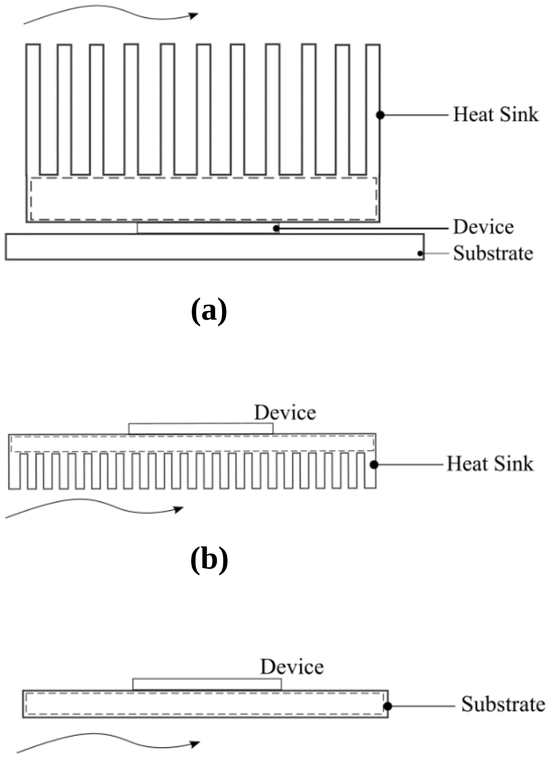
Heat Sink
Device
Substrate
(a)
Device
Heat Sink
(b)
Device
Substrate

(c)

Figure E.6. Schematic drawings of: (a) Case #1 (air-cooled device); (b) Case #2 (embedded microchannel cooling); and (c) Case #3 (low-power device); the solution domain is outlined with a dotted line.

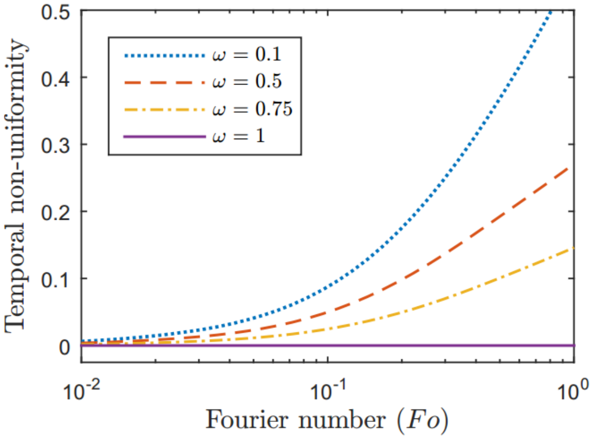

Figure E.7. Variation of temporal non-uniformity with *Fo* for different ω ($d^* = 0.1$, $1/b^* = 0.5$, $Bi = 0.1$).

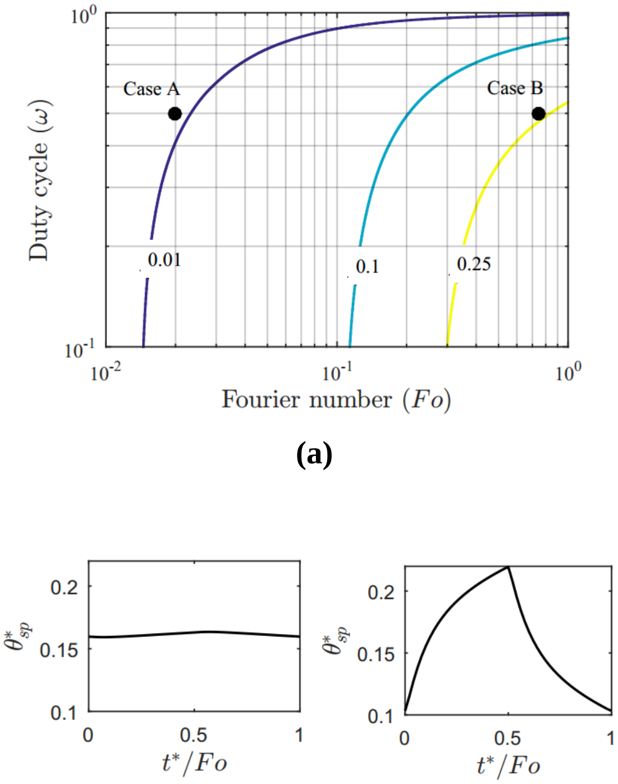

(a)

(b) **(c)**

Figure E.8. (a) Isolines of temporal non-uniformity map for ω versus Fo ($d^* = 0.1$, $1/b^* = 0.5$, $Bi = 0.1$); dots on the map indicate representative cases with high (Case A; $\omega = 0.5$ and $Fo = 0.02$) and low (Case B; $\omega = 0.5$ and $Fo = 0.75$) frequency heat inputs. The evolution of the non-dimensional center point temperature over one time period in the steady-periodic regime is shown for (b) Case A and (c) Case B.

Table E.1. Values of the dimensional parameters chosen for the case studies.

Parameter	Case #1	Case #2	Case #3
a (cm)	1	1	0.1
b (cm)	2	2	0.2
d (mm)	2	0.25	1
k (W/mK)	400	200	1
R_{conv} (K/W)	0.2	0.02	25
Spatial non-uniformity	0.17	1.52	0.09

APPENDIX F. PORE-SCALE EVAPORATION MODEL

To obtain a volumetric heat transfer coefficient, a pore-scale evaporation model is developed as detailed below. The heat transfer in each pore (from the solid porous matrix to the vapor in the pore, as shown in Figure 7.2 (b) in the main text) occurs by conduction across the annular liquid film and evaporation from the liquid-vapor interface, as shown schematically in Figure F.1. The vapor phase in the pore is at T_{sat} and the liquid-vapor interface is at a constant temperature T_{lv}. The conduction flux across the annular liquid film is obtained as

$$q_{cond,l} = -k_l \frac{\left(T_s - T_{lv}\right)}{\left(r_{eff} - \delta\right) \ln\left(\frac{r_{eff} - \delta}{r_{eff}}\right)} \tag{F.1}$$

The pore-scale evaporation flux is

$$q_{evap,p} = h_{lv}\left(T_{lv} - T_{sat}\right) \tag{F.2}$$

where h_{lv} is the heat transfer coefficient for evaporation of liquid to vapor at a saturation temperature T_{sat} and pressure P_{sat} obtained from kinetic theory [131]

$$h_{lv} = \frac{2\sigma}{\left(2-\sigma\right)} \frac{h_{fg}{}^2}{T_{sat} v_{fg}} \left(\frac{1}{2\pi R T_{sat}}\right)^{1/2} \left(1 - \frac{P_{sat}}{2 v_{fg} h_{fg}}\right) \tag{F.3}$$

In the above expression, an accommodation coefficient of $\sigma = 0.03$ is used. The total heat transfer rate from each pore is obtained by integrating the evaporation flux over the open pore area,

$$Q_{pore} = 2\pi\left(r_{eff} - \delta\right) h_{lv}\left(T_{lv} - T_{sat}\right) t_{pore} \tag{F.4}$$

Equating the expressions in equations (F.1) and (F.2), and eliminating the liquid-vapor interface temperature variable T_{lv}, we obtain the expression for the total heat transfer from each pore,

$$Q_{pore} = 2\pi\left(r_{eff} - \delta\right) h_{lv} \frac{\left(T_s - T_{sat}\right) t_{pore}}{\left(1 + \frac{h_{lv}}{k_l}\left(r_{eff} - \delta\right) \ln\left(\frac{r_{eff}}{r_{eff} - \delta}\right)\right)} \tag{F.5}$$

The volumetric evaporation heat transfer rate in the control volume is calculated by summing the heat transfer across all the pores in the control volume per unit volume as

$$\tilde{q}_{evap} = \frac{Q_{pore}N}{V_{CV}} = \frac{2\left(r_{eff} - \delta\right)h_{lv}\varphi}{r_{eff}^{\ 2}\left(1 + \frac{h_{lv}}{k_l}\left(r_{eff} - \delta\right)\ln\left(\frac{r_{eff}}{r_{eff} - \delta}\right)\right)}\left(T_s - T_{sat}\right) \tag{F.6}$$

In the above equation, $V_{CV} = N.V_{pore}/\varphi$ where φ is the porosity of the wick and $V_{pore} = \pi r_{eff}^{2} t_{pore}$ were utilized. Equating (F.6) to the expression for $\tilde{q}_{evap}$ from equation (7.1) in the main text, the volumetric heat transfer coefficient is obtained as,

$$\tilde{h}_{evap} = \frac{2\left(r_{eff} - \delta\right)h_{lv}\varphi}{r_{eff}^{\ 2}\left(1 + \frac{h_{lv}}{k_l}\left(r_{eff} - \delta\right)\ln\left(\frac{r_{eff}}{r_{eff} - \delta}\right)\right)} \tag{F.7}$$

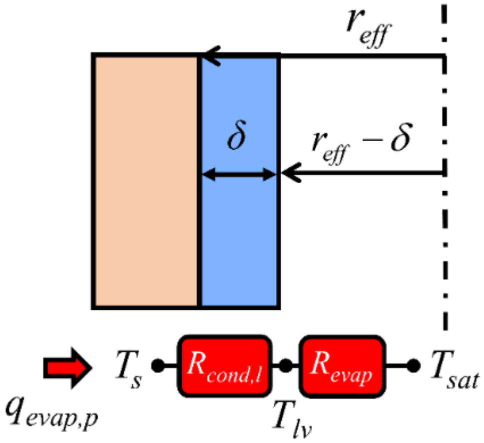
r_{eff}
δ
$r_{eff} - \delta$
T_s
$R_{cond,l}$
R_{evap}
T_{sat}
T_{lv}
$q_{evap,p}$

Figure F.1. A schematic diagram illustrating the pore-scale evaporation model, including the resistances for heat transfer by conduction across a thin liquid film and evaporation from the liquid-vapor interface.

APPENDIX G. BOILING CURVES FOR SINTERED PARTICLE WICKS

Figure G.1 and Figure G.2 show the (a) boiling curve, *i.e.*, the input heat flux q_w plotted against the substrate superheat ΔT_{sub} and (b) thermal resistance ($R_{th,meas} = \Delta T_{sub} / (q_w A_{heater})$) plotted against the input heat flux, for the three different particle size evaporator wicks with the 10 mm × 10 mm and 5 mm × 5 mm heater sizes, respectively. The highest heat flux value shown in the plots is the maximum heat flux sustained by the evaporator at steady state prior to dryout, which is the measured dryout heat flux of the sample. The complete data reduction and uncertainty calculation procedures are detailed in our prior work in Ref. [65].

To obtain the wick superheat, the temperature drop due to conduction resistance across the substrate is deduced from the measured substrate superheat as,

$$\Delta T_{wick} = \Delta T_{sub} - \frac{t_{sub}}{k_{Cu} A_{boil}} Q_w \tag{G.1}$$

where t_{sub} is the substrate thickness, k_{Cu} is the thermal conductivity of the copper substrate, A_{boil} is the boiling area (10 mm × 10 mm open area) and Q_w is the heat input. The average boiling resistance quoted in Table 7.3 is calculated by subtracting the 1D substrate conduction resistance from the measured thermal resistance, as shown below, and averaging over the measured values once the thermal resistance reaches a nearly constant value as a function of heat flux,

$$R_{th,wick} = R_{th,meas} - \frac{t_{sub}}{k_{Cu} A_{boil}} \tag{G.2}$$

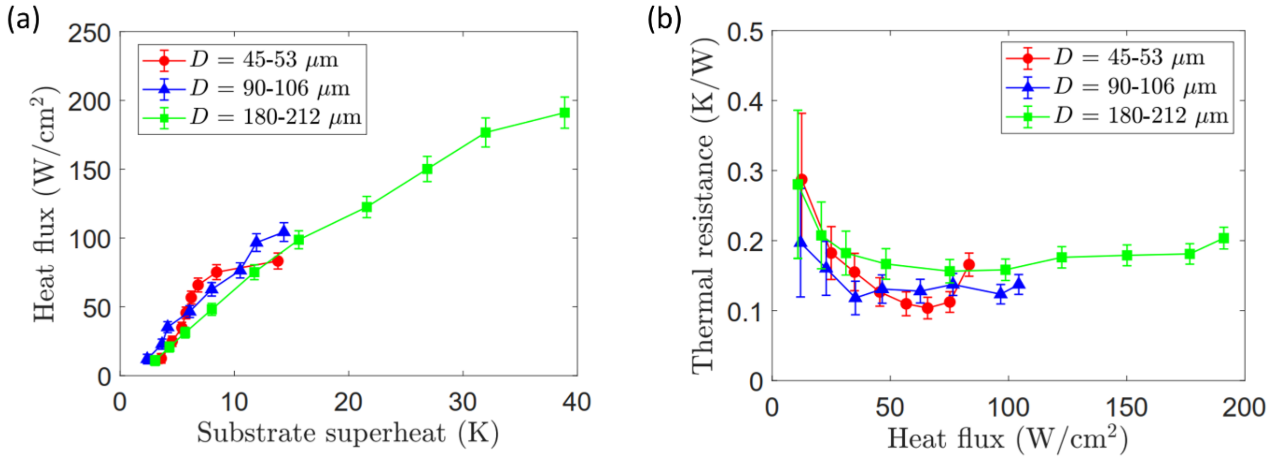

Figure G.1. (a) The input heat flux (q_w) plotted against the measured substrate superheat (ΔT_{sub}) and (b) the thermal resistance plotted against the input heat flux, for the three particle size evaporator wicks, for a heater size of 10 mm × 10 mm. Error bars in part (a) and (b) show the uncertainty in the measured heat flux and the thermal resistance, respectively

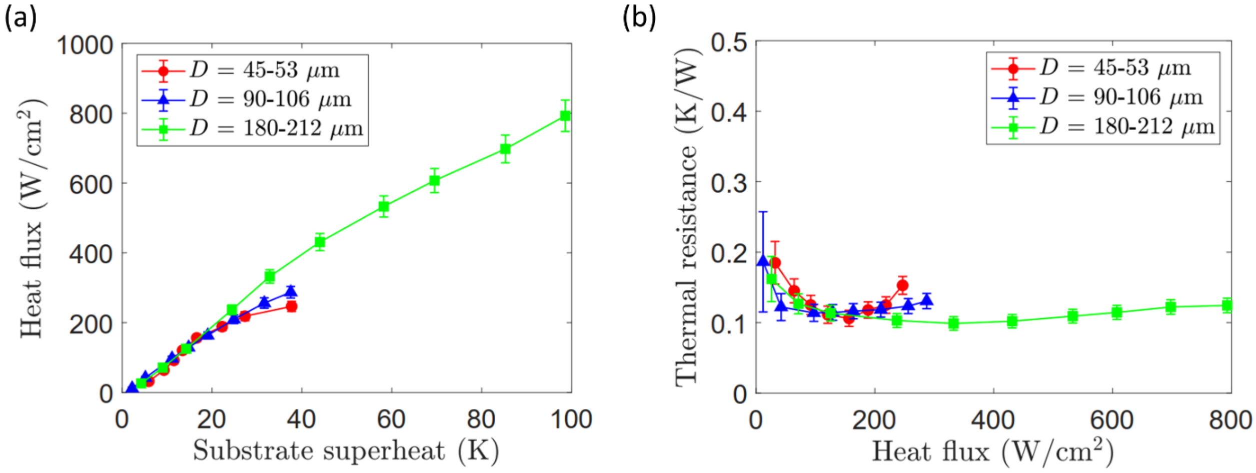

Figure G.2. (a) The input heat flux (q_w) plotted against the measured substrate superheat (ΔT_{sub}) and (b) the thermal resistance plotted against the input heat flux, for the three particle size evaporator wicks, for a heater size of 5 mm × 5 mm. Error bars in part (a) and (b) show the uncertainty in the measured heat flux and the thermal resistance, respectively

APPENDIX H. EFFECTIVE THERMAL RESISTANCE OF THE HEAT SINK FIN ARRAY

This analysis calculates the effective thermal resistance of a parallel plate-fin array for a given set of design and boundary conditions. The model assumes a uniform base temperature directly under the fins, and a fully developed laminar air flow between the fins.

The design consists of an array of N parallel fins of length L_x, height H_{fin}, thickness, t_{fin} and width, G_{fin} as shown in Figure 8.1. The temperature of the air flowing into the fin array is $T_{a,in}$ and the temperature of air leaving the array is $T_{a,out}$. The hydraulic diameter for the flow between two fins is $D_h = 2G_{fin} H_{fin}/(G_{fin}+H_{fin})$, and the aspect ratio of the fins is $AR = H_{fin}/G_{fin}$. The effective heat transfer coefficient for air flow through the fins is calculated from the Nusselt number correlation for flow in isothermal ducts as,

$$\begin{aligned} Nu_{D,h} &= 7.541\left(1-\frac{2.610}{AR}+\frac{4.970}{AR^2}-\frac{5.119}{AR^3}+\frac{2.702}{AR^4}-\frac{0.548}{AR^5}\right) \\ h_{fin} &= \frac{Nu_{D,h}k_{air}}{D_h} \end{aligned} \tag{H.1}$$

Fin analysis is then performed to calculate the fin efficiency for a single fin as,

$$\eta_{fin} = \frac{\tanh\left(mH_{fin}\right)}{mH_{fin}} \tag{H.2}$$

where $m = \sqrt{}(h_{fin}P/k_{fin}A_c)$, P and A_c are the perimeter and cross-sectional area of the wick, k_{fin} is the thermal conductivity of the material of the fin. The fin efficiency for an array of fins is,

$$\eta_0 = 1-\frac{NA_f}{\left(NA_f + A_b\right)}\left(1-\eta_{fin}\right) \tag{H.3}$$

where N is the number of fins, and A_f and A_b are the fin area and the base area respectively. Considering the temperature rise of the air within the heat sink and modeling the heat sink as an effective heat exchanger, the effective thermal resistance of the fin array is,

$$R_{fin} = \frac{T_{base}-T_{a,in}}{\dot{m}c_p\left(T_{a,out}-T_{a,in}\right)} = \frac{1}{\dot{m}c_p\left(1-\exp\left(-\frac{\eta_0 hA_t}{\dot{m}c_p}\right)\right)}$$

where (H.4)

$$A_t = A_b + N_{fin}\left(A_f - Lt_{fin}\right)$$

APPENDIX I. EVALUATION OF EVAPORATION AND BOILING HEAT TRANSFER COEFFICIENTS

The effective heat transfer coefficients described in Chapter 8 (in the model coupling in Section 8.1.3) $h_{w,evap}$ and $h_{w,boil}$ can be found from the evaporator wick temperature profiles as described below.

For the evaporation model, the governing equation and boundary conditions for the evaporator wick, as described in Section 8.1.2.1 is,

$$\begin{aligned} & k_{eff}\frac{\partial^2 T}{\partial z^2}=0 \\ & \text{with} \\ & \left(-k_{eff}\frac{\partial T}{\partial z}\right)_{z=t_s}=q_w \\ & \left(-k_{eff}\frac{\partial T}{\partial z}\right)_{z=t_s+t_{wick,1}}-\dot{m}_1''h_{fg}=0 \end{aligned} \tag{I.1}$$

The z-direction temperature profile for the evaporator wick is linear. Using the mass flux equation $\dot{m}_1''h_{fg}=\varphi h_{fg}\left(T_1-T_{sat}\right)$, the wall superheat $T_w - T_{sat}$ is obtained as,

$$T_w-T_{sat}=q_w\left(\frac{t_{wick,1}}{k_{eff}}+\frac{1}{\varphi h_{fg}}\right) \tag{I.2}$$

which provides the heat transfer coefficient,

$$h_{w,evap}=\frac{q_w}{T_w-T_{sat}}=\frac{1}{\left(\dfrac{t_{wick,1}}{k_{eff}}+\dfrac{1}{\varphi h_{fg}}\right)} \tag{I.3}$$

The boiling heat transfer coefficient $h_{w,boil}$ is derived from the solution to the temperature profile in the z-direction of the evaporator wick for the boiling model described in Section 8.1.2.2. The governing equation and boundary conditions for the evaporator wick are,

$$\begin{aligned} -k_{eff}\,\frac{\partial^2 T}{\partial z^2}+\tilde{h}_{evap}\left(T-T_{sat}\right)&=0 \\ -k_{eff}\,\frac{\partial T}{\partial z}\bigg|_{z=t_s}&=q_w \\ -k_{eff}\,\frac{\partial T}{\partial z}\bigg|_{z=t_s+t_{wick,1}}&=0 \end{aligned} \tag{I.4}$$

The temperature profile is obtained as,

$$T\left(z\right)=T_{sat}+\frac{q_w}{M_e k_{eff}\left(e^{2M_e t}-1\right)}\left(e^{M_e z}+e^{M_e\left(2t-z\right)}\right) \tag{I.5}$$

where $M_e=\sqrt{\tilde{h}_{evap}\big/k_{eff}}$. The effective heat transfer coefficient can then be calculated as

$$h_{w,boil}=\frac{q_w}{T_w-T_{sat}}=M_e k_{eff}\,\frac{\left(e^{2M_e t_{wick,1}}-1\right)}{\left(e^{2M_e t_{wick,1}}+1\right)}=M_e k_{eff}\,\tanh\left(M_e t_{wick,1}\right) \tag{I.6}$$

APPENDIX J. ALGORITHM FOR SOVING WICK HYDRODYNAMICS

When boiling occurs in the evaporator wick as found from the temperature threshold criterion, the wick hydrodynamics model described in Chapter 8 uses a numerical solution procedure, by discretizing the governing equations using the finite volume method (on a rectangular grid). The solution domain is split into a boiling and an evaporation region. The SIMPLE algorithm [132] is used for finding the evaporator wick pressure fields. The numerical procedure follows as:

An initial guess of the pressure and velocity (magnitude) field is considered,

$$\begin{aligned} &P_l^*\left(x,y\right)=P_{ref} \\ &\left|\vec{U}_l\right|\left(x,y\right)=\frac{\dot{m}_1''}{\left(2\rho_l t_{wick,1}\right)}\sqrt{\left(x^2+y^2\right)} \end{aligned} \tag{J.1}$$

To start the solution, the reference pressure is taken as the saturation pressure of the vapor core (P_{ref} = P_{sat} (x,y) obtained from the heat transfer model). An initial guess for the saturation field in the wick (based on the capillary pressure saturation equation $P_{v,avg} - P_l = P_{c,max}$ (1− s) and using the average vapor pressure from equation (8.31) in Chapter 8) is,

$$s\left(x,y\right)=\begin{cases}1 & \text{evaporation region}\\ 1-\left(\dfrac{\mu_v \dot{m}_1'' t_{wick,1}}{2K\rho_v P_{c,\max}}\right)^{1/\left(n+1\right)} & \text{boiling region}\end{cases} \tag{J.2}$$

The discretized x-momentum equation (on a staggered grid) is:

$$\frac{P_E-P_P}{\Delta x}=\begin{cases}\dfrac{\mu_l}{K}u_e & \text{evaporation region}\\ \left(\dfrac{\mu_l}{K}+\dfrac{\rho_l C_E}{K^{1/2}}\left|\vec{U}_l\right|\right)\dfrac{u_e}{{s_e}^n} & \text{boiling region}\end{cases} \tag{J.3}$$

The velocity corrections are obtained by subtracting a starred equation from the original equation to obtain,

$$u_e{}' = a_e\left(P_E' - P_P'\right)$$
$$where\ a_e = \begin{cases} \dfrac{1}{\left(\dfrac{\mu_l}{K}\right)\Delta x} & \text{evaporation region} \\ \dfrac{s_e{}^n}{\left(\dfrac{\mu_l}{K} + \dfrac{\rho_l C_E}{K^{1/2}}\left|\vec{U}_l\right|\right)\Delta x} & \text{boiling region} \end{cases} \tag{J.4}$$

Similarly, we can obtain expressions for the corrected velocities u_w, v_n and v_s. The discretized continuity equation (on the main grid) is:

$$\left(u_e - u_w\right)\Delta y + \left(v_n - v_s\right)\Delta x = \frac{\dot{m}_1''}{\left(2\rho_l t_{wick,1}\right)}$$
$$\underbrace{\left(u_e{}^* - u_w{}^*\right)\Delta y + \left(v_n{}^* - v_s{}^*\right)\Delta x}_{b_u} + \left(u_e' - u_w'\right)\Delta y + \left(v_n' - v_s'\right)\Delta x = \underbrace{\frac{\dot{m}_1''}{\left(2\rho_l t_{wick,1}\right)}}_{b_m} \tag{J.5}$$
$$\left(u_e' - u_w'\right)\Delta y + \left(v_n' - v_s'\right)\Delta x = b_m - b_u$$

Substituting for the corrected velocities and regrouping, we obtain

$$P_P'\left(a_e\Delta y + a_w\Delta y + a_n\Delta x + a_s\Delta x\right) \quad = \quad \left(a_e\Delta y P_E' + a_w\Delta y P_W' + a_n\Delta x P_N' + a_s\Delta x P_S'\right) + b_u - b_m$$

(J.6)

From here, we get the pressure correction equation for a given cell center in the main grid, which can be written in terms of the pressure correction of the neighboring cells,

$$a_P P_P' = \sum_{nb} a_{nb} P_{nb}' + \left(b_u - b_m\right) \tag{J.7}$$

The pressure correction equation for all the cells in the domain can be written as a linear system of equations, which can be solved by matrix inversion,

$$\underline{\underline{A}} P' = \underline{b} \tag{J.8}$$

After solving this by matrix inversion, the new velocity and pressure fields can be obtained.

$$\begin{aligned} u_{e,new} &= u_e{}^* + \alpha a_e\left(P_E' - P_P'\right) \\ P_{P,new} &= P_P{}^* + \alpha P_P' \end{aligned} \tag{J.9}$$

where α is a relaxation parameter.

The liquid saturation field within the boiling region is obtained from the capillary pressure equation $P_c = P_{v,avg} - P_l = P_{c,max}\,(1 - s)$. Substituting for $P_{v,avg}$ from equation (31) in the main text, we obtain,

$$P_{sat} + \frac{\mu_v \dot{m}_1'' t_{wick,1}}{2K\rho_v \left(1 - s_{new}\right)^n} - P_{l,new} = P_{c,\max}\left(1 - s_{new}\right) \tag{J.10}$$

This non-linear equation is solved using a Newton-Raphson method (with an initial guess given by equation (J.2)) to find the new liquid saturation field ($s_{new}\,(x,y)$). The new velocity magnitudes are then found at each cell centers,

$$\left|\overrightarrow{U}\right|_{new} = \sqrt{\left(u_{e,new}{}^2 + v_{n,new}{}^2\right)} \tag{J.11}$$

The new velocity and pressure corrections are then found, and the process is repeated until convergence. Convergence is attained when the sum of mass residuals (residual error) falls below a preset value,

$$\sum_{all\ cells}\left(\left(u_e - u_w\right)\Delta y + \left(v_n - v_s\right)\Delta x - \frac{\dot{m}_1''}{\rho h_{wick,1}}\right) < 10^{-5} \tag{J.12}$$

APPENDIX K. MEASUREMENT OF CAPILLARY PRESSURE – SATURATION RELATIONSHIP IN SINTERED POROUS MEDIA

The modeling framework for dryout prediction in capillary-fed porous evaporators described in Chapter 7 relies on the constitutive relationship between capillary pressure and liquid saturation for the specific porous media of interest. In Chapters 7 and 8, a simple linear relationship $P_c = P_{c,max}\,(1 - s)$ was used. This appendix presents an approach to experimentally measure this relationship for microscale sintered porous media, made from different particle sizes.

K.1. Introduction

Two-phase flow through microscale metallic porous media is of interest in evaporators within wicked heat pipes and vapor chambers, capillary pumped loops [133], loop heat pipes [134], gas diffusion membranes in fuel cells [137], pore-scale drying in thin porous media [135], among other applications. Many prior studies have utilized continuum methods for modeling two-phase flow in macroscopic porous media as described in the literature review in section 2.5, these models require the knowledge of the capillary pressure -saturation relation during imbibition and drainage processes in porous media. Imbibition is the process by which a wetting fluid displaces a non-wetting fluid in a porous media initially saturated with the non-wetting fluid; the displacement of a wetting fluid by a non-wetting fluid is termed drainage.

To characterize the relationship between capillary pressure and liquid saturation, various studies in the past have utilized experimental measurement techniques, derived from the classical porous diaphragm method [136]. To analyze both the sides of the capillary pressure curve, *i.e.*, imbibition and drainage, the general theme in these experiments is to sandwich the porous sample between two semi-permeable membranes, each permitting only one phase to pass through. The wetting fluid (liquid) and the non-wetting fluid (gas) are introduced on two sides of the porous medium. To obtain a drainage curve, the sample is completed saturated with the wetting fluid (liquid), and the capillary pressure (defined as the difference between the gas and liquid pressures $P_c = P_g - P_l$) is increased in steps and capillary equilibrium is achieved in each step. At capillary equilibrium (steady state), there is no flow across the porous media, and stable menisci are formed within the porous domain. When the capillary pressure rises, the liquid from the porous media is displaced by the gas; the displaced volume/mass is measured to obtain the liquid saturation. A similar process is carried out to obtain the imbibition curve, where the sample is initially dry and the capillary pressure is decreased in steps to allow the liquid to displace the gas in the pore volume. The capillary pressure – saturation relationship can be expressed as,

$$\frac{P_c(s)}{\sigma\cos(\theta)\sqrt{\frac{\varepsilon}{K}}} = f(s) \tag{K.1}$$

The nature of the curves depend on the surface tension σ, contact angles (θ) of the two-phases in contact with the porous media [137, 141], and the pore structure of the porous media itself. Normalizing the capillary pressure P_c measured in different porous media and fluid pairs by the expression shown in equation (K.1) causes the measured data to collapse into a single curve which is a function of the liquid saturation only. The resulting capillary pressure – saturation relationship is not the same for imbibition and drainage processes; hysteresis is generally observed because capillary equilibrium depends on the history of saturation change [136], and advancing and receding contact angles.

Various experimental works from the fuel cell literature have characterized the capillary pressure saturation relation for gas diffusion media [138-141]. Here, we follow a procedure similar to the one developed by Gostick *et al.* [141] and Fairweather *et al.* [138] to measure the drainage curves for sintered copper powder wick structures with water and air as the working fluid pair.

K.2. Experimental methods

K.2.1. Experimental setup and design of sample holder

The experimental setup used in this work is detailed in Figure K.1 (a). The setup consists of a sample holder (with a gas port and a liquid port on either side) that houses the sintered porous sample. A syringe pump is connected to the gas port of the sample holder, and the liquid port is connected to a beaker placed on a digital mass balance. The height between the bottom of the sample and the surface of liquid in the beaker (H) is measured during the experiment. The beaker is open to atmosphere, so the liquid pressure directly below the sample is a fixed value ($P_l = P_{atm} - \rho g H$). The syringe pump is controlled manually to set value of gas pressure P_g, which is measured using a pressure transducer. Similarly, the atmospheric pressure is measured using a separate transducer. A Sartorius BCE224I1S mass balance (220g, 0.1 mg resolution, with internal calibration) is used to measure the differences in liquid saturation. An exploded view of the sample holder is shown in Figure K.1 (b). The sample holder consists of a machined polycarbonate bottom plate, a middle and top plate fabricated from acrylic, and two distributor plates also made of acrylic. When assembled, the sample is tightly sandwiched between a hydrophilic membrane below the sample (polyethersulfone (PES) membrane filter, 0.1 µm pore size, Sterlitech) and a hydrophobic membrane above (PTFE membrane filter, 5 µm pore size, Sterlitech).

The assembly and sealing procedure is performed as follows: The liquid distributor plate is placed within a recess in the bottom plate (after assembly, it is flush with the top surface of the bottom plate). The hydrophilic membrane is placed on the distributor plate and is firmly secured by bolting the middle plate to the bottom plate. The dry sample is then loaded above the hydrophilic membrane, along with the sample gasket. The hydrophobic membrane is then placed on top of the sample, followed by the gas distributor plate. The distributor plates provide support to the membranes and keep them from bending under the application of a pressure. The distributor plates have small holes (of 1 mm diameter), for even distribution of liquid and gas to the sample. The top gasket is then laid on top of the middle plate, followed by securing the top plate with bolts running through the assembly.

Sintered samples of three different particle sizes (45 – 53 µm, 90 – 106 µm and 180 – 212 µm) are used for characterization of the capillary pressure saturation curves. The samples are sintered using the same procedure outlined in Chapter 4, Section 4.1. The samples are sintered using a circular mold; the final dimensions are shown in Table K.1.

K.2.2. Experimental procedure

Figure K.2 shows a typical plot of the gas pressure against time for the duration of the test. After mounting the sample, a high positive gas pressure of 20,000 Pa is applied on the gas port (using the syringe pump), to initially drain any water that may have been imbibed by the sample during the assembly process. The high pressure of 20,000 Pa is well below the bubble point of the hydrophilic membrane (~ 3×10^6 Pa for the 0.1 µm pore size). To start the test, the mass balance is tared to zero. A negative gas pressure is applied on the gas port (by setting the syringe pump in the opposite direction) in steps. The syringe pump is stopped after each step, and water is allowed to imbibe into the sample. This is shown in Figure K.2 by the decreasing gas pressure (and eventual steady states after each step) during the imbibition process. The gas pressure is reduced in steps until no further imbibition occurs in the sample at high negative pressures. The sample is fully saturated if no further imbibition occurs and then the total imbibed mass is noted from the mass balance. To obtain the drainage curve, the direction of the syringe pump is changed, and a positive gas pressure is applied in steps (see drainage part of Figure K.2), and the system is held at a constant gas pressure at each step until the mass balance reading reaches a stable value at each step. The air slowly displaces the liquid, and the capillary pressure is increased until no further drainage occurs from the sample.

K.2.3. Data reduction and uncertainty calculation

The capillary pressure is controlled by changing the gas pressure on the gas port, and is calculated as,

$$P_c = P_l - P_g = P_{atm} - \rho_l g H - P_g \tag{K.2}$$

The water saturation is calculated as the ratio of the volume of water lost by the beaker, to the total volume of liquid imbibed by the sample at a large negative pressure (when no further imbibition occurs).

$$s = \frac{V_{lost}}{V_{total}} = \frac{\Delta m_{liq}}{\Delta m_{total}} \tag{K.3}$$

where Δm_{liq} is the change in mass recorded from the mass balance. The total pore volume of the sample is calculated theoretically using the porosity of the sample as,

$$\begin{aligned} &V_{total,pore} = \rho_l V_{porous} = \rho_l \left(V_{sample} \phi_{sample} \right) \\ &\text{where} \\ &V_{sample} = \frac{\pi d_{sample}{}^2}{4} t_{sample} \\ &\phi_{sample} = 1 - \frac{m_{sample}}{\rho_{Cu} V_{sample}} \end{aligned} \tag{K.4}$$

A check is made by comparing the total volume of liquid imbibed by the sample (V_{total}) to the total pore volume calculated theoretically from equation (K.4); it was found that the values are within 10% of each other for the sintered samples tested in this work.

The uncertainty in capillary pressure is calculated as,

$$\Delta P_c = \sqrt{\left(\Delta P_g\right)^2 + \left(\Delta P_{atm}\right)^2 + \left(\rho g \Delta H\right)^2} \tag{K.5}$$

The uncertainty in the gas pressure and atmospheric pressure measurement is taken as twice the standard deviation of the steady state measurements from the pressure transducers. The uncertainty in the height measurements is twice the least count of the ruler used to measure the height difference between the sample and the surface of liquid in the beaker. The uncertainty in saturation measurements is,

$$\frac{\Delta s}{s} = \sqrt{\left(\frac{\Delta m_{liq}}{m_{liq}}\right)^2 + \left(\frac{\Delta m_{total}}{m_{total}}\right)^2} \tag{K.6}$$

The uncertainty in mass measurements from the balance is twice the resolution of the balance (0.1 mg).

K.2.4. Results

Figure K.3 shows the imbibed mass from the mass balance plotted against the capillary pressure during the drainage process for the 180 – 212 µm sample. The plot compares two curves one for a sample obtained directly from sintering, and the other for a sample that was cleaned in a dilute piranha solution prior to testing, following the same method discussed in Section 5.2.1. For the as-sintered sample, the total imbibed mass during the imbibition process is ~ 140 mg. During drainage, any small value of positive capillary pressure results in a drop in the imbibed mass, and the value keeps decreasing as capillary pressure increases. This suggests that the sample is hydrophobic since a small positive gas pressure caused intrusion of air into the sample. In contrast, the drainage curve for the sample cleaned with dilute piranha exhibits resistance to intrusion up to a positive value of capillary pressure of ~2000 Pa; the sample sustained this capillary pressure before the maximum pore radius of the sample was breached by air. After the first intrusion, further increases in capillary pressure causes slow decreases in the imbibed mass until a high capillary pressure. It is noted that for both the samples, the imbibed mass does not fall back to zero and there is some mass remaining (around 20 – 25 mg) within the sample even at high capillary pressures. The liquid mass that does not have any connected pathway to the liquid port remains within the sample, and this irreducible mass can only be removed by evaporation, as is typically mentioned in the literature.

Figure K.4 shows the capillary pressure – saturation curves, with error bars for the three sintered samples, the nature of the curves of these samples are very similar; the saturation value remains constant up to a positive capillary pressure illustrating that the sample holds capillary pressure corresponding to its maximum pore radius. The 180 – 212 µm exhibits first intrusion pressure of ~ 1500 Pa, followed by the 45 – 53 µm sample at 2300 Pa, and the 90 – 106 µm sample at 3700 Pa. The maximum capillary pressure $P_{c,max}$ of the samples (pressure at which the saturation does not decrease any further; irreducible saturation) increases with decreasing particle size. The 180 – 212 µm sample exhibits a minimum saturation of 0.16 at a capillary pressure of 7300 Pa, while for the 90 – 106 µm sample, the minimum value is ~ 0.09 at the maximum capillary pressure of 12000 Pa. Among the samples tested, the 45 – 53 sample exhibits the highest $P_{c,max}$ of 17500 Pa at a minimum saturation of 0.12. The maximum uncertainty in the capillary pressure measurement (among the entire range) is ± 305 Pa. The maximum uncertainty in the saturation measurements is a low value of ± 0.003.

K.3. Conclusions and future work

This chapter presented an experimental methodology, and results for capillary pressure – saturation relationship of sintered particle samples of three different particle sizes (45 – 53 µm, 90 – 106 µm and 180 – 212 µm). The maximum capillary pressure increased with decreasing particle size, as expected. The linear relationship $P_c = P_{c,max} (1 - s)$ assumed in Chapters 7 and 8 for the semi-empirical modeling can be revisited by taking into account the first intrusion pressure and the nature of the curve obtained here. In this regard, future work can explore obtaining functional relationships by curve fitting to well-known curves, as described in refs. [142,143]. To verify and validate the accurate working of the experimental setup described here, standard samples of known wettability and capillary pressure curves can be tested.

Table K.1. The measured diameter, thickness and mass of the three different samples used in the experimental measurements

Sample	Diameter (mm)	Thickness (mm)	Mass (mg)
45 – 53 µm	13.83	1.00	594.8
90 – 106 µm	13.96	0.95	511.8
180 – 212 µm	14.94	1.20	739.1

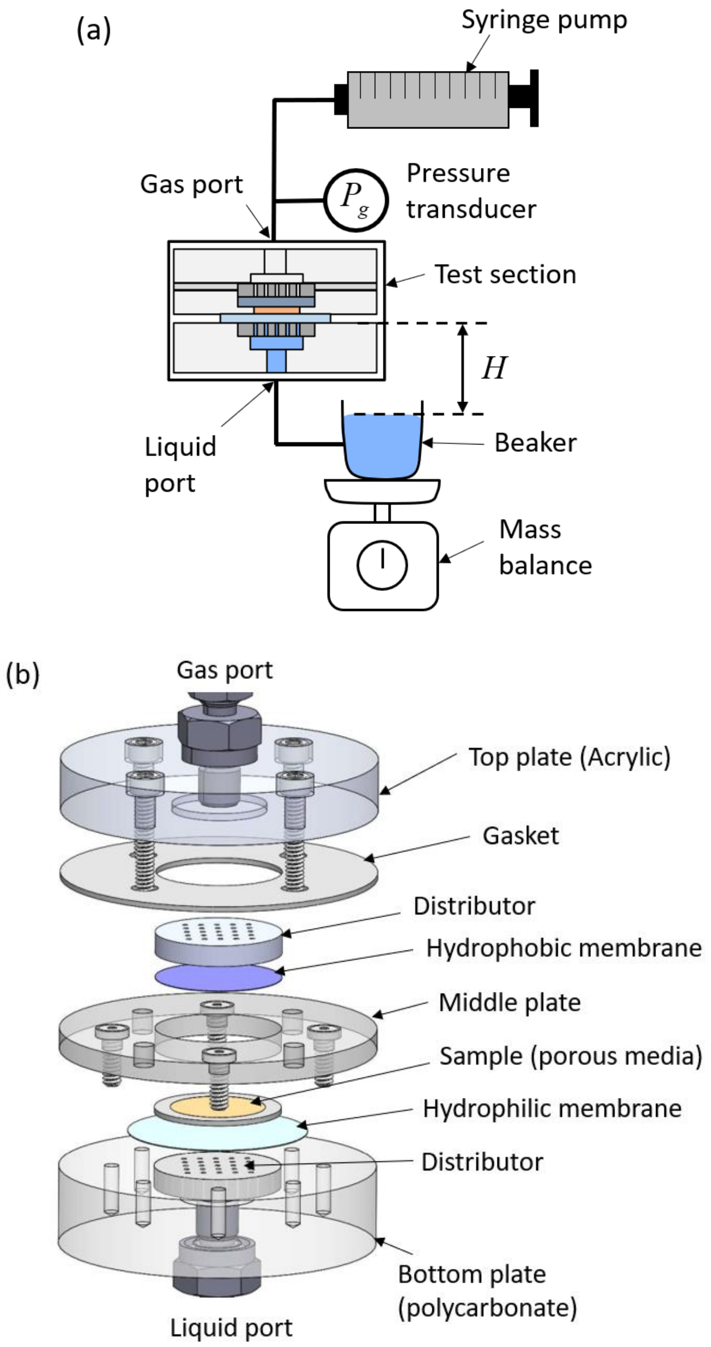
(a)
Syringe pump
Pressure transducer
P_g
Gas port
Test section
H
Liquid port
Beaker
Mass balance
(b)
Gas port
Top plate (Acrylic)
Gasket
Distributor
Hydrophobic membrane
Middle plate
Sample (porous media)
Hydrophilic membrane
Distributor
Bottom plate (polycarbonate)
Liquid port

Figure K.1. (a) A schematic diagram of the experimental setup used to measure capillary pressure – saturation relationship in porous media. (b) An exploded view of the test section showing internal parts.

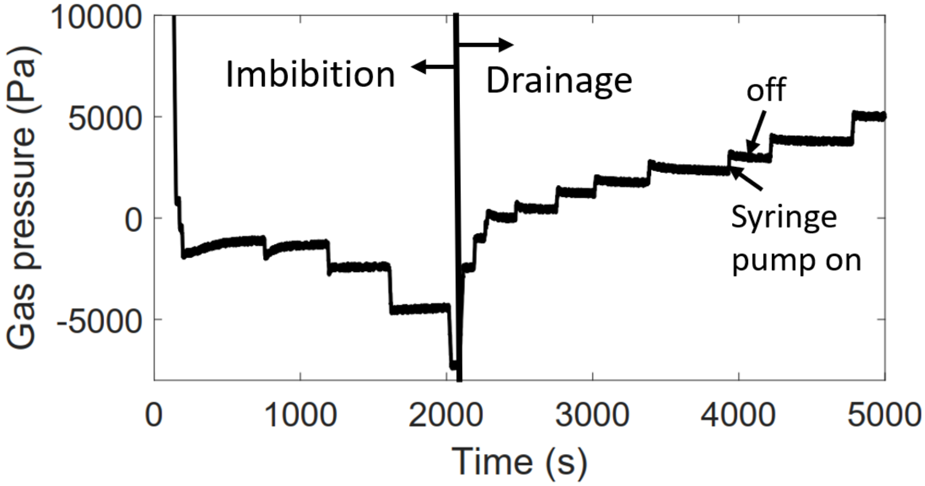

Figure K.2. A plot of the air pressure against time during the duration of the test. At the start of the test, gas pressure is reduced successively (negative values) to allow imbibition into the sample. To obtain the drainage curve, the gas pressure is increased in steps until the sample is completely drained.

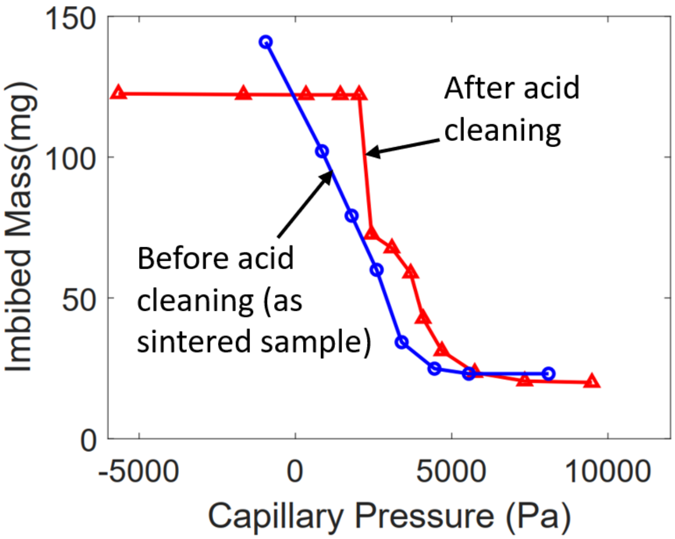

Figure K.3. A plot of the imbibed mass plotted against the capillary pressure (at steady state) for the 180 – 212 µm sample. The blue and the red curves are obtained for samples before and after acid cleaning, respectively.

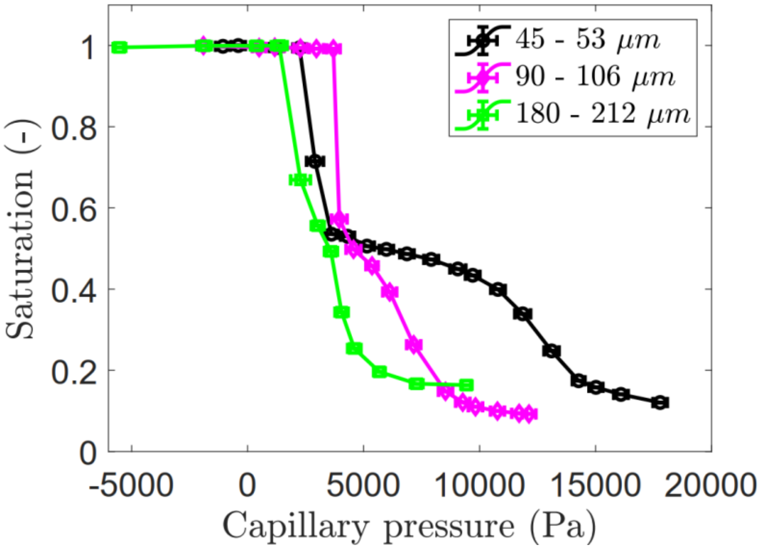

Figure K.4. The capillary pressure – saturation plot for the three samples (45 – 53 µm, 90 – 106 µm and 180 – 212 µm)

REFERENCES

[1] A. Faghri, “Steady Hydrodynamic and Thermal Characteristics”, in *Heat Pipe Science and Technology*, Washington, DC, USA: Taylor & Francis, pp. 115-220, 1995.

[2] R. R. Williams, and D. K. Harris, “A device and technique to measure the heat transfer limit of a planar heat pipe wick,” *Experimental Thermal and Fluid Science*, vol. 30, pp. 277–284, 2006.

[3] M. P. Mughal, and O. A. Plumb, “An experimental study of boiling on a wicked surface,” *International Journal of Heat and Mass Transfer*, vol. 39, pp. 771–777, 1996.

[4] A. Brautsch, and P. A. Kew, “Examination and visualisation of heat transfer processes during evaporation in capillary porous structures,” *Applied Thermal Engineering*, vol. 22, pp. 815–824, 2002.

[5] J. A. Weibel, S. V. Garimella, and M. T. North, “Characterization of evaporation and boiling from sintered powder wicks fed by capillary action,” *International Journal of Heat and Mass Transfer*, vol. 53, pp. 4204–4215, 2010.

[6] C. Li, G. P. Peterson, and Y. Wang, “Evaporation/Boiling in thin capillary wicks (l) – Wick thickness effects,” *Journal of Heat Transfer*, vol. 128, pp. 1312–1319, 2006.

[7] T. Semenic, and I. Catton, “Experimental study of biporous wicks for high heat flux applications,” *International Journal of Heat and Mass Transfer*, vol. 52, pp. 5113–5121, 2009.

[8] J. A. Weibel, A. S. Kousalya, T. S. Fisher and S. V. Garimella, “Characterization and nanostructured enhancement of boiling incipience in capillary-fed, ultra-thin sintered powder wicks,” *13th IEEE Intersociety Conference on Thermal and Thermomechanical Phenomena in Electronic Systems (ITherm)*, San Diego, CA, pp. 119–129, 2012.

[9] A. Bar-Cohen, “Gen-3 Thermal Management Technology: Role of Microchannels and Nanostructures in an Embedded Cooling Paradigm.” *Journal of Nanotechnology in Engineering and Medicine* vol. 4, p. 20907, 2013.

[10] S. Q. Cai., and A. Bhunia, “Characterization of phase change heat and mass transfers in monoporous silicon wick structures,” *Journal of Heat Transfer*, vol. 136, p. 072001, 2014.

[11] D. Ćoso, V. Srinivasan, M. C. Lu, J. Y. Chang, and A. Majumdar, “Enhanced heat transfer in biporous wicks in the thin liquid film evaporation and boiling regimes,” *Journal of Heat Transfer*, vol. 134, p. 101501, 2012.

[12] J. W. Palko., C. Zhang, J. D. Wilbur, T. J. Dusseault., M. Asheghi, K. E. Goodson, and J. G. Santiago, "Approaching the limits of two-phase boiling heat transfer: High heat flux and low superheat," *Applied Physics Letters*, vol. 107, p. 253903, 2015.

[13] Y. S. Ju, M. Kaviany, Y. Nam, S. Sharratt, G. S. Hwang, I. Catton, E. Fleming, and P. Dussinger "Planar vapor chamber with hybrid evaporator wicks for the thermal management of high-heat-flux and high-power optoelectronic devices," *International Journal of Heat and Mass Transfer*, vol. 60, pp. 163–169, 2013.

[14] J. A. Weibel, S. S. Kim, T. S. Fisher, and S. V. Garimella, "Carbon nanotube coatings for enhanced capillary-fed boiling from porous microstructures," *Nanoscale and Microscale Thermophysical Engineering*, vol. 16, pp. 1–17, 2012.

[15] Y. Zhao., and C. L. Chen, "An investigation of evaporation heat transfer in sintered copper wicks with microgrooves," *Proceedings of the ASME International Mechanical Engineering Congress and Exposition (IMECE)*, Chicago, IL, pp. 177–181, 2006.

[16] S. Ryu, J. Han, J. Kim, C. Lee, and Y. Nam, "Enhanced heat transfer using metal foam liquid supply layers for micro heat spreaders," *International Journal of Heat and Mass Transfer*, vol. 108, Part B, pp. 2338–2345, 2017.

[17] B. Weisenseel, P. Greil, and T. Fey, "Biomorphous Silicon Carbide as Novel Loop Heat Pipe Wicks," *Advanced Engineering Materials*, vol. 19, p. 1600379, 2016.

[18] J. A. Weibel and S. V. Garimella, "Visualization of vapor formation regimes during capillary-fed boiling in sintered-powder heat pipe wicks," *International Journal of Heat and Mass Transfer*, vol. 55, pp. 3498–3510, 2012.

[19] J. A. Weibel and S. V. Garimella, "Chapter Four - Recent Advances in Vapor Chamber Transport Characterization for High-Heat-Flux Applications," in *Advances in Heat Transfer*, vol. 45, Ed. Elsevier, pp. 209–301, 2013.

[20] Y. Nam, S. Sharratt, G. Cha, and Y. S. Ju, "Characterization and modeling of the heat transfer performance of nanostructured Cu micropost wicks," *Journal of Heat Transfer*, vol. 133, p. 101502, 2011.

[21] P. Xu and Q. Li, "Visualization study on the enhancement of heat transfer for the groove flat-plate heat pipe with nanoflower coated CuO layer," *Applied Physics Letters.*, vol. 111, p. 141609, 2017.

[22] X. Dai, F. Yang, R. Yang, Y. C. Lee, and C. Li, "Micromembrane-enhanced capillary evaporation," *International Journal of Heat and Mass Transfer*, vol. 64, pp. 1101–1108. 2013.

[23] G. S. Hwang, Y. Nam, E. Fleming, P. Dussinger, Y. S. Ju, and M. Kaviany, "Multi-artery heat pipe spreader: Experiment," *International Journal of Heat and Mass Transfer*, vol. 53, pp. 2662–2669, 2010.

[24] G. S. Hwang, E. Fleming, B. Carne, S. Sharratt, Y. Nam, P. Dussinger, Y. S. Ju and M. Kaviany, "Multi-artery heat-pipe spreader: Lateral liquid supply," *International Journal of Heat and Mass Transfer*, vol. 54, pp. 2334–2340, 2011.

[25] C. Byon and S. J. Kim, "Effects of geometrical parameters on the boiling limit of bi-porous wicks," *International Journal of Heat and Mass Transfer*, vol. 55, pp. 7884–7891, 2012.

[26] T. W. Davis and S. V. Garimella, "Thermal Resistance Measurement across a Wick Structure Using a Novel Thermosyphon Test Chamber," *Experimental Heat Transfer*, vol. 21, pp. 143–154, 2008.

[27] M. R. S. Shirazy, S. Blais, and L. G. Fréchette, "Mechanism of wettability transition in copper metal foams: From superhydrophilic to hydrophobic," *Applied Surface Science*, vol. 258, pp. 6416–6424, 2012.

[28] S. C. Wong and Y. C. Lin, "Effect of copper surface wettability on the evaporation performance: Tests in a flat-plate heat pipe with visualization," *International Journal of Heat and Mass Transfer*, vol. 54, pp. 3921–3926, 2011.

[29] Y. Nam, S. Sharratt, C. Byon, S. J. Kim, and Y. S. Ju, "Fabrication and Characterization of the Capillary Performance of Superhydrophilic Cu Micropost Arrays," *Journal of Microelectromechanical Systems*, vol. 19, pp. 581–588, 2010.

[30] B.D. Iverson and S.V. Garimella, "Experimental measurements of heat and mass transport in heat pipe wicks," in: *Proceedings of the ASME Heat Transfer/Fluids Engineering Summer Conference*, Charlotte, NC, 2004, pp. 209–217.

[31] S. G. Liter and M. Kaviany, "Pool-boiling CHF enhancement by modulated porous-layer coating: theory and experiment," *International Journal of Heat and Mass Transfer*, vol. 44, pp. 4287–4311, 2001.

[32] R. L. Webb, "Nucleate Boiling on Porous Coated Surfaces," *Heat Transfer Engineering*, vol. 4, pp. 71–82, 1983.

[33] S. M. Rao and A. R. Balakrishnan, "Analysis of pool boiling heat transfer over porous surfaces," *Heat and Mass Transfer*, vol. 32, pp. 463–469, 1997.

[34] J. Y. Chang and S. M. You, "Boiling heat transfer phenomena from microporous and porous surfaces in saturated FC-72," *International Journal of Heat and Mass Transfer*, vol. 40, pp. 4437–4447, 1997.

[35] N. Zuber, "Hydrodynamic aspects of boiling heat transfer," PhD Thesis, University of California, Los Angeles, 1959.

[36] S. Sudhakar, J. A. Weibel, F. Zhou, E. M. Dede, and S. V. Garimella, “Area-scalable high-heat-flux dissipation at low thermal resistance using a capillary-fed two-layer evaporator wick,” *International Journal of Heat and Mass Transfer*, vol. 135, pp. 1346–1356, Jun. 2019.

[37] K. S. Udell, “Heat transfer in porous media considering phase change and capillarity—the heat pipe effect,” *International Journal of Heat and Mass Transfer*, vol. 28, pp. 485–495, 1985.

[38] H. H. Bau, and K. E. Torrance. "Boiling in low-permeability porous materials," *International Journal of Heat and Mass Transfer,* vol. 251, pp. 45-55, 1982.

[39] V. X. Tung and V. K. Dhir, “A hydrodynamic model for two-phase flow through porous media,” *International Journal of Multiphase Flow*, vol. 14, pp. 47–65, 1988.

[40] A. E. Scheidegger, “The physics of flow through porous media,” Third edition, *University of Toronto Press*, 1974.

[41] M. Kaviany, “Principles of heat transfer in porous media,” Second edition, Springer Science & Business Media, New York, NY, USA, 1995.

[42] R. Ranjan, J.Y. Murthy, S.V. Garimella, U. Vadakkan, “A numerical model for transport in flat heat pipes considering wick microstructure effects,” *International Journal of Heat and Mass Transfer,* vol. 54, pp. 153–168, 2010.

[43] R. Ranjan, J.Y. Murthy, S.V. Garimella, D.H. Altman, M.T. North, “Modeling and design optimization of ultrathin vapor chambers for high heat flux applications,” *IEEE Transactions on Components, Packaging and Manufacturing Technology,* vol. 2, pp. 1465–1479, 2012.

[44] S. Harmand, R. Sonan, M. Fakès, H. Hassan, “Transient cooling of electronic components by flat heat pipes,” *Applied Thermal Engineering* vol. 31, pp. 1877– 1885, 2011.

[45] R. S. Prasher, “A simplified conduction based modeling scheme for design sensitivity study of thermal solution utilizing heat pipe and vapor chamber technology,” *Journal of Electronic Packaging*, vol. 125, pp. 378–385, 2003.

[46] K. Baraya, J. A. Weibel, and S. V. Garimella, “Simultaneous wick and fluid selection for the design of minimized-thermal-resistance vapor chambers under different operating conditions,” *International Journal of Heat and Mass Transfer,* vol. 136, pp. 842–850, 2019.

[47] M. Aghvami, A. Faghri, “Analysis of flat heat pipes with various heating and cooling configurations,” *Applied Thermal Engineering*, vol. 31, pp. 2645–2655, 2011.

[48] F. Lefèvre, M. Lallemand, “Coupled thermal and hydrodynamic models of flat micro heat pipes for the cooling of multiple electronic components,” *International Journal of Heat and Mass Transfer* vol. 49, pp. 1375–1383, 2006.

[49] G. Patankar, J. A. Weibel, and S. V. Garimella, “A validated time-stepping analytical model for 3D transient vapor chamber transport,” *International Journal of Heat and Mass Transfer*, vol. 119, pp. 867–879, Apr. 2018.

[50] L. Lv and J. Li, “Managing high heat flux up to 500W/cm 2 through an ultra-thin flat heat pipe with superhydrophilic wick,” *Applied Thermal Engineering*, vol. 122, pp. 593 – 660, 2017.

[51] Y. Koito, H. Imura, M. Mochizuki, Y. Saito, and S. Torii, “Numerical analysis and experimental verification on thermal fluid phenomena in a vapor chamber,” *Applied Thermal Engineering*, vol. 26, pp. 1669–1676, 2006.

[52] H.-Y. Li, M.-H. Chiang, C.-I. Lee, and W.-J. Yang, “Thermal performance of plate-fin vapor chamber heat sinks,” *International Communications in Heat and Mass Transfer*, vol. 37, pp. 731–738, 2010.

[53] J.-Y. Chang, R. S. Prasher, S. Prstic, P. Cheng, and H. B. Ma, “Evaporative Thermal Performance of Vapor Chambers Under Nonuniform Heating Conditions,” *Journal of Heat Transfer*, vol. 130, pp. 121501–9, 2008.

[54] S.-C. Wong, S.-F. Huang, and K.-C. Hsieh, “Performance tests on a novel vapor chamber,” *Applied Thermal Engineering*, vol. 31, pp. 1757–1762 2011.

[55] H. Peng, J. Li, and X. Ling, “Study on heat transfer performance of an aluminum flat plate heat pipe with fins in vapor chamber,” *Energy Conversion and Management*, vol. 74, pp. 44–50, 2013.

[56] R. S. Prasher, “A Simplified Conduction Based Modeling Scheme for Design Sensitivity Study of Thermal Solution Utilizing Heat Pipe and Vapor Chamber Technology,” *Journal of Electronic Packaging*, vol. 125, pp. 378–385, 2003.

[57] S. Sudhakar, J. A. Weibel, and S. V. Garimella, “Design of an Area-Scalable Two-Layer Evaporator Wick for High-Heat-Flux Vapor Chambers,” *IEEE Transactions on Components, Packaging and Manufacturing Technology*, vol. 9, pp. 458–472, 2019.

[58] J. A. Weibel, S. V. Garimella, J. Y. Murthy and D. H. Altman, “Design of integrated nanostructured wicks for high-performance vapor chambers,” *IEEE Transactions on Components, Packaging and Manufacturing Technology*, vol. 1, pp. 859–867, 2011.

[59] D. H. Min, G. S. Hwang, and M. Kaviany, “Multi-artery, heat-pipe spreader,” *International Journal of Heat and Mass Transfer*, vol. 52, pp. 629–635, 2009.

[60] R. S. Prasher, “A Simplified Conduction Based Modeling Scheme for Design Sensitivity Study of Thermal Solution Utilizing Heat Pipe and Vapor Chamber Technology.” *Journal of Electronic Packaging*, vol. 125, pp. 378–385, 2003.

[61] Smirnov, “Approximate theory of heat transfer in porous structures.” *Thermal Engineering (Teploenergetika)*, vol. 24, pp. 55-58, 1977.

[62] R. D. Blevins, "Applied fluid dynamics handbook" *New York, Van Nostrand Reinhold Co.*,568 p, 1984.

[63] ANSYS® FLUENT, Academic Research, Release 17.1.

[64] “Porous media conditions”, Section 7.2.3, ANSYS FLUENT 12.0 User’s Guide. [Online]. Available: http://www.afs.enea.it/project/neptunius/docs/fluent/html/ug/node233.htm

[65] S. Sudhakar, J. A. Weibel, and S. V. Garimella, “Experimental investigation of boiling regimes in a capillary-fed two-layer evaporator wick,” *International Journal of Heat and Mass Transfer*, vol. 135, pp. 1335–1345, Jun. 2019.

[66] S. Sarangi, J. A. Weibel, and S. V. Garimella, “Effect of particle size on surface-coating enhancement of pool boiling heat transfer,” *International Journal of Heat and Mass Transfer*, vol. 81, pp. 103–113, 2015.

[67] Y. Nasersharifi, M. Kaviany, and G. Hwang, “Pool-boiling enhancement using multilevel modulated wick,” *Applied Thermal Engineering*, vol. 137, pp. 268–276, 2018.

[68] User Guide for ANSYS FLUENT 12.0, Fluent Inc., 2009.

[69] X. Chen, J. A. Weibel, and S. V. Garimella, “Exploiting Microscale Roughness on Hierarchical Superhydrophobic Copper Surfaces for Enhanced Dropwise Condensation,” *Advanced Materials Interfaces*, vol. 2, p. 1400480, 2015.

[70] K. Brown, H. Coleman, and W. Steele, “Estimating uncertainty intervals for linear regression,” *Proceedings of the 33rd Aerospace Sciences Meeting and Exhibit*, Reno, NV, p. 796, 1995.

[71] Y. Nam, S. Sharratt, G. Cha, and Y. S. Ju, “Characterization and Modeling of the Heat Transfer Performance of Nanostructured Cu Micropost Wicks,” *Journal of Heat Transfer*, vol. 133, p. 101502, 2011.

[72] Q. Cai and Y. C. Chen, “Investigations of Biporous Wick Structure Dryout,” *Journal of Heat Transfer*, vol. 134, p. 021503, 2011.

[73] S. Sudhakar, J. A. Weibel, F. Zhou, E. M. Dede, and S. V. Garimella, “Area-scalable high-heat-flux dissipation at low thermal resistance using a capillary-fed two-layer evaporator wick,” *International Journal of Heat and Mass Transfer*, vol. 135, pp. 1346–1356, 2019.

[74] C. Li and G. P. Peterson, “Parametric study of pool boiling on horizontal highly conductive microporous coated surfaces,” *J. Heat Transfer*, vol. 129, pp. 1465–1475, 2007.

[75] K. K. Bodla, J. Y. Murthy, and S. V. Garimella, “Direct simulation of thermal transport through sintered wick microstructures,” *Journal of heat transfer*, vol. 134, p. 012602, 2012.

[76] S. Sarangi, J. A. Weibel, and S. V. Garimella, “Quantitative Evaluation of the Dependence of Pool Boiling Heat Transfer Enhancement on Sintered Particle Coating Characteristics,” *Journal of Heat Transfer*, vol. 139, pp. 021502–13, 2016.

[77] J. W. Palko, C. Zhang, J. D. Wilbur, T. J. Dusseault, M. Asheghi, K. E. Goodson and J. G. Santiago, “Approaching the limits of two-phase boiling heat transfer: High heat flux and low superheat,” *Applied Physics Letters*, vol. 107, p. 253903, 2015.

[78] Q. Cai and A. Bhunia, “High heat flux phase change on porous carbon nanotube structures,” *International Journal of Heat and Mass Transfer*, vol. 55, pp. 5544–5551, 2012.

[79] S. Sudhakar, J. A. Weibel, F. Zhou, E. M. Dede, and S. V. Garimella, “The role of vapor venting and liquid feeding on the dryout limit of two-layer evaporator wicks,” *International Journal of Heat and Mass Transfer*, vol. 148, p. 119063, 2020.

[80] S. A. Kovalev, S. L. Solov'yev, and O. A. Ovodkov, “Liquid boiling on porous surfaces,” *Heat transfer Soviet research*, vol. 19, pp.109-120, 1987.

[81] D. G. Avraam and A. C. Payatakes, “Flow regimes and relative permeabilities during steady-state two-phase flow in porous media,” *Journal of Fluid Mechanics*, vol. 293, pp. 207–236. 1995.

[82] J. M. Schembre and A. R. Kovscek, “A technique for measuring two-phase relative permeability in porous media via X-ray CT measurements,” *Journal of Petroleum Science and Engineering*, vol. 39, pp. 159–174, 2003.

[83] I. S. Hussaini and C. Y. Wang, “Measurement of relative permeability of fuel cell diffusion media,” *Journal of Power Sources*, vol. 195, pp. 3830–3840, 2010.

[84] S. Q. Cai and A. Bhunia, “Geometrical effects of wick structures on the maximum phase change capability,” *International Journal of Heat and Mass Transfer*, vol. 79, pp. 981–988, 2014.

[85] C. Zhang, J. W. Palko, M. T. Barako, M. Asheghi, J. G. Santiago, and K. E. Goodson, “Enhanced capillary-fed boiling in copper inverse opals via template sintering,” *Advanced Functional Materials*, vol. 28, p. 1803689, 2018.

[86] J. T. Gostick, M. A. Ioannidis, M. W. Fowler, and M. D. Pritzker, “Direct measurement of the capillary pressure characteristics of water–air–gas diffusion layer systems for PEM fuel cells,” *Electrochemistry Communications*, vol. 10, pp. 1520–1523, 2008.

[87] V. Joekar-Niasar, S. M. Hassanizadeh, and A. Leijnse, "Insights into the relationships among capillary pressure, saturation, interfacial area and relative permeability using pore-network modeling," *Transp Porous Med*, vol. 74, pp. 201–219, 2008.

[88] K. K. Bodla, J. Y. Murthy, and S. V. Garimella, "Direct simulation of thermal transport through sintered wick microstructures," *Journal of Heat Transfer*, vol. 134, p. 012602, 2012.

[89] A. Faghri, "Heat pipe science and technology," *Taylor & Francis*, Washington, DC, 1995.

[90] W. S. Chang, "Porosity and effective thermal conductivity of wire screens," *Journal of Heat Transfer*, vol. 112, pp. 5–9, 1990.

[91] B. S. Singh, A. Dybbs, and F. A. Lyman, "Experimental study of the effective thermal conductivity of liquid saturated sintered fiber metal wicks," *International Journal of Heat and Mass Transfer*, vol. 16, pp. 145–155, 1973.

[92] C. Li and G. P. Peterson, "The effective thermal conductivity of wire screen," *International Journal of Heat and Mass Transfer*, vol. 49, pp. 4095–4105, 2006.

[93] S. Adera, D. Antao, R. Raj and E. N. Wang, "Design of micropillar wicks for thin-film evaporation," *International Journal of Heat and Mass Transfer*, vol. 101, pp.280-294, 2016.

[94] R. Lewis, L.A. Liew, S. Xu, Y.C. Lee and R. Yang, "Microfabricated ultra-thin all-polymer thermal ground planes," *Science Bulletin*, vol. 60, pp.701-706, 2015.

[95] C. Ding, G. Soni, P. Bozorgi, B. D. Piorek, C. D. Meinhart and N. C. MacDonald, "A flat heat pipe architecture based on nanostructured titania," *Journal of Microelectromechanical Systems*, vol. 19, pp.878-884, 2010.

[96] J. A. Weibel, S. V. Garimella, and M. T. North, "Characterization of evaporation and boiling from sintered powder wicks fed by capillary action," *International Journal of Heat and Mass Transfer*, vol. 53, pp. 4204–4215. 2010.

[97] C. Li and G. P. Peterson, "Evaporation/Boiling in thin capillary wicks (II)—Effects of volumetric porosity and mesh size," *Journal of Heat Transfer*, vol. 128, pp. 1320–1328, 2006.

[98] J. A. Weibel, "Characterization of fluid-thermal transport and boiling in micro/nano-engineered porous structures," Ph.D. thesis, Purdue University, Indiana, USA, 2012.

[99] G. Patankar, J. A. Weibel, and S. V. Garimella, "A validated time-stepping analytical model for 3D transient vapor chamber transport," *International Journal of Heat and Mass Transfer*, vol. 119, pp. 867–879, Apr. 2018.

[100] E.W. Lemmon, M.L. Huber, M.O. McLinden, NIST Standard Reference Database 23: Reference Fluid Thermodynamic and Transport Properties-REFPROP, Version 9.1, National Institute of Standards and Technology, Standard Reference Data Program. Gaithersburg, 2013.

[101] S. V. Patankar, "Numerical Heat Transfer and Fluid Flow," First Edition, CRC Press, 1980.

[102] D. G. Avraam and A. C. Payatakes, "Flow regimes and relative permeabilities during steady-state two-phase flow in porous media," *Journal of Fluid Mechanics*, vol. 293, pp. 207–236, Jun. 1995.

[103] A. H. Demond and P. V. Roberts, "Estimation of two-phase relative permeability relationships for organic liquid contaminants," *Water Resources Research*, vol. 29, no. 4, pp. 1081–1090, 1993.

[104] Hussaini, I. and C. Wang. "Measurement of relative permeability of fuel cell diffusion media." *Journal of Power Sources*, vol. 195, pp. 3830 – 3840, 2010.

[105] S. N. Joshi, F. Zhou, E. M. Dede, D. J. Lohan, S. Sudhakar, and J. A. Weibel, "Thermal Performance Evaluation of a Two-Layer Wick Vapor Chamber for High Heat Flux Dissipation by Air Cooling," in 2020 19th *IEEE Intersociety Conference on Thermal and Thermomechanical Phenomena in Electronic Systems* (ITherm), Jul. 2020, pp. 91–96.

[106] C. Jiang, W. Liu, H. C. Wang, D. D. Wang, J. G. Yang, J. Y. Li and Z. C. Liu, "Experimental investigation of pump-assisted capillary phase change loop," *Applied Thermal Engineering*, vol. 71, pp. 581–588, 2014.

[107] I. Setyawan, N. Putra, and I. I. Hakim, "Experimental investigation of the operating characteristics of a hybrid loop heat pipe using pump assistance," *Applied Thermal Engineering*, vol. 130, pp. 10–16, 2018.

[108] M. Crepinsek and C. Park, "Effect of Operational Conditions on Cooling Performance of Pump-Assisted and Capillary-Driven Two-Phase Loop," *Journal of Thermophysics and Heat Transfer*, vol. 25, pp. 572–580, 2011.

[109] D. H. Altman, J. R. Wasniewski, M. T. North, S. S. Kim, and T. S. Fisher, "Development of micro/nano engineered wick-based passive heat spreaders for thermal management of high power electronic devices," *ASME 2011 Pacific Rim Technical Conference and Exhibition on Packaging and Integration of Electronic and Photonic Systems (InterPACK)*, Portland, OR, USA, pp. 213–220, 2011.

[110] S. Sudhakar and J. A. Weibel, "Transient Analysis of Nonuniform Heat Input Propagation Through a Heat Sink Base," *Journal of Electronic Packaging*, vol. 139, pp. 021001–7, 2017.

[111] Lee, S., Song, S., Au, V., and Moran, K. P., "Constriction/Spreading Resistance Model for Electronics Packaging," *4th ASME/JSME Thermal Engineering Joint Conference*, Lahaina, HI, Mar. 19–24, pp. 199–206, 1995.

[112] Bar-Cohen, A., "Gen-3 thermal management technology: role of microchannels and nanostructures in an embedded cooling paradigm," *Journal of Nanotechnology in Engineering and Medicine*, vol. 4, p. 020907, 2013.

[113] Drummond, K. P., Weibel, J. A., Garimella, S. V., Back, D., Janes, D. B., Sinanis, M. D., and Peroulis, D., "Evaporative intrachip hotspot cooling with a hierarchical manifold microchannel heat sink array," *IEEE Intersociety Conference on Thermal and Thermomechanical Phenomena in Electronic Systems* (*ITherm*), Las Vegas, NV, May 31-June 3, 2016.

[114] Hetsroni, G., Mosyak, A., Segal, Z., and Pogrebnyak, E., "Two-phase flow patterns in parallel micro-channels," *International Journal of Multiphase Flow*, vol. 29, pp. 341–360, 2003.

[115] Szczukiewicz, S., Borhani, N., and Thome, J. R., "Two-phase flow operational maps for multi-microchannel evaporators," *International Journal of Heat and Fluid Flow*, vol. 42, pp. 176–189, 2013.

[116] Wu, H. Y., Cheng, P., and Wang, H., "Pressure drop and flow boiling instabilities in silicon microchannel heat sinks," *Journal of Micromechanics and Microengineering*, vol. 16, p. 2138, 2006.

[117] Kandlikar, S. G., "Fundamental issues related to flow boiling in minichannels and microchannels," *Experimental Thermal and Fluid Science*, vol. 26, pp. 389–407, 2002.

[118] Bogojevic, D., Sefiane, K., Walton, A. J., Lin, H., Cummins, G., Kenning, D. B. R., and Karayiannis, T. G., "Experimental investigation of non-uniform heating effect on flow boiling instabilities in a microchannel-based heat sink," *International Journal of Thermal Sciences*, vol. 50, pp. 309–324, 2011.

[119] Ritchey, S. N., Weibel, J. A., and Garimella, S. V., "Local measurement of flow boiling heat transfer in an array of non-uniformly heated microchannels," *International Journal of Heat and Mass Transfer*, vol. 71, pp. 206–216, 2014.

[120] Ritchey, S., Weibel, J., and Garimella, S., "Effects of non-uniform heating on the location and magnitude of critical heat flux in a microchannel heat sink," *International Journal of Micro-Nano Scale Transport*, vol. 5, pp. 95–108, 2014.

[121] Hingorani, S., Fahrner, C. J., Mackowski, D. W., Gooding, J. S., and Jaeger, R. C., "Optimal sizing of planar thermal spreaders," *Journal of Heat Transfer*, vol. 116, pp. 296–301, 1994.

[122] Muzychka, Y. S., Culham, J. R., and Yovanovich, M. M., “Thermal spreading resistance of eccentric heat sources on rectangular flux channels,” *Journal of Electronic Packaging*, vol. 125, pp. 178–185, 2003.

[123] Skadron, K., Abdelzaher, T., and Stan, M. R., “Control-theoretic techniques and thermal-RC modeling for accurate and localized dynamic thermal management,” *Proceeding of the Eighth International Symposium on High-Performance Computer Architecture*, pp. 17–28, Cambridge, MA, Feb 2-6, 2002.

[124] Yovanovich, M. M., “Transient spreading resistance of arbitrary isoflux contact areas - Development of a universal time function,” *Proceedings of the 32nd Thermophysics Conference, AIAA-97-2458,* Atlanta, GA, June 23-25, 1997.

[125] Yazawa, K., and Ishizuka, M., “Optimization of heat sink design with focus on transient thermal response,” *Proceedings of the ASME International Mechanical Engineering Congress* (*IMECE*), *IMECE2004-60513,* Anaheim, CA, Nov.13-19, 2004.

[126] Fisher, T. S., Avedisian, C. T., and Krusius, J. P., “Transient thermal response due to periodic heating on a convectively cooled substrate,” *IEEE Transactions on Components, Packaging, and Manufacturing Technology, Part B: Advanced Packaging,* vol. 19, pp. 255–262, 1996.

[127] Kadambi, V., and Abuaf, N., “Axisymmetric and three-dimensional chip-spreader calculations”, *AlChE Symposium Series*, vol. 79**,** pp. 130–139, 1983.

[128] Kadambi, V., and Abuaf, N., “An analysis of the thermal response of power chip packages,” *IEEE Transactions on Electron Devices*, vol. 32, pp. 1024–1033, 1985.

[129] Hahn, D. W., and Özişik, M. N., “Use of Duhamel’s theorem,” Heat Conduction, John Wiley & Sons, Inc., pp. 273–299, 2012.

[130] Arpaci, V., 1966, “Conduction Heat Transfer”, Addison-Wesley, New York, NY.

[131] V. P. Carey, “Liquid-vapor phase-change phenomena: An introduction to the thermophysics of vaporization and condensation processes in heat transfer equipment,” Third edition, *CRC Press, Taylor and Francis Group*, 2020.

[132] S. V. Patankar, “Numerical Heat Transfer and Fluid Flow,” First Edition, CRC Press, 1980.

[133] M. R. Shaeri, R. W. Bonner, and M. C. Ellis, “Thin hybrid capillary two-phase cooling system,” *International Communications in Heat and Mass Transfer*, vol. 112, p. 104490, 2020.

[134] C. Figus, Y. L. Bray, S. Bories, and M. Prat, “Heat and mass transfer with phase change in a porous structure partially heated: continuum model and pore network simulations,” *International Journal of Heat and Mass Transfer*, vol. 42, pp. 2557–2569, 1999.

[135] M. Prat, “Recent advances in pore-scale models for drying of porous media,” *Chemical Engineering Journal*, vol. 86, pp. 153–164, 2002.

[136] F. A. L. Dullien, “2 - Capillarity in Porous Media,” in *Porous Media*, Ed. Academic Press, pp. 5–74, 1979.

[137] J. T. Gostick, M. A. Ioannidis, M. W. Fowler, and M. D. Pritzker, “Characterization of the Capillary Properties of Gas Diffusion Media,” in Modeling and Diagnostics of Polymer Electrolyte Fuel Cells, Springer New York, pp. 225–254, 2009.

[138] J. D. Fairweather, P. Cheung, J. St-Pierre, and D. T. Schwartz, “A microfluidic approach for measuring capillary pressure in PEMFC gas diffusion layers,” *Electrochemistry Communications*, vol. 9, pp. 2340–2345, 2007.

[139] I. R. Harkness, N. Hussain, L. Smith, and J. D. B. Sharman, “The use of a novel water porosimeter to predict the water handling behaviour of gas diffusion media used in polymer electrolyte fuel cells,” *Journal of Power Sources*, vol. 193, pp. 122–129, 2009.

[140] T. V. Nguyen, G. Lin, H. Ohn, and X. Wang, “Measurement of Capillary Pressure Property of Gas Diffusion Media Used in Proton Exchange Membrane Fuel Cells,” *Electrochemical and Solid-State Letters*, vol. 11, p. B127, 2008.

[141] J. T. Gostick, M. A. Ioannidis, M. W. Fowler, and M. D. Pritzker, “Direct measurement of the capillary pressure characteristics of water–air–gas diffusion layer systems for PEM fuel cells,” *Electrochemistry Communications*, vol. 10, pp. 1520–1523, 2008.

[142] J. I. Gerhard and B. H. Kueper, “Capillary pressure characteristics necessary for simulating DNAPL infiltration, redistribution, and immobilization in saturated porous media,” *Water Resources Research*, vol. 39, p.1212, 2003.

[143] K. Li and R. N. Horne, “Comparison of methods to calculate relative permeability from capillary pressure in consolidated water-wet porous media,” *Water Resources Research*, vol. 42, w06405, 2006.

VITA

Srivathsan Sudhakar received his Bachelor of Technology in Mechanical Engineering from Indian Institute of Technology Hyderabad in 2015. He is currently pursuing his Ph.D. in Mechanical Engineering at Purdue University under the advisement of Dr. Justin A. Weibel and Dr. Suresh V. Garimella. His research interests include design and experimental characterization of porous wick structures and vapor chambers for high-heat-flux applications. He is also the recipient of the Bilsland Dissertation Fellowship 2020-21 from the College of Engineering at Purdue University.

PUBLICATIONS

[1] S. Sudhakar, J.A. Weibel, F. Zhou, E.M. Dede, S.V. Garimella, “The role of vapor venting and liquid feeding on the dryout limit of two-layer evaporator wicks,” *International Journal of Heat and Mass Transfer*, vol.148, p. 119063, 2020.

[2] S. Sudhakar, J. A. Weibel, F. Zhou, E. M. Dede, and S. V. Garimella, “Area-scalable high-heat-flux dissipation at low thermal resistance using a capillary-fed two-layer evaporator wick,” *International Journal of Heat and Mass Transfer*, vol. 135, pp. 1346–1356, Jun. 2019.

[3] S. Sudhakar, J. A. Weibel, and S. V. Garimella, “Experimental investigation of boiling regimes in a capillary-fed two-layer evaporator wick,” *International Journal of Heat and Mass Transfer*, vol. 135, pp. 1335–1345, Jun. 2019.

[4] S. Sudhakar, J. A. Weibel, and S. V. Garimella, “Design of an Area-Scalable Two-Layer Evaporator Wick for High-Heat-Flux Vapor Chambers,” *IEEE Transactions on Components, Packaging and Manufacturing Technology*, vol. 9, pp. 458–472, Mar. 2019.

[5] S. Sudhakar and J. A. Weibel, “Transient Analysis of Nonuniform Heat Input Propagation Through a Heat Sink Base,” *Journal of Electronic Packaging*, vol. 139, pp. 021001-021001–7, Apr. 2017.

[6] S. Sudhakar, J. A. Weibel, and S. V. Garimella, “An area-scalable two-layer evaporator wick concept for high-heat-flux vapor chambers,” in *2017 16th IEEE Intersociety Conference on Thermal and Thermomechanical Phenomena in Electronic Systems (ITherm)*, 2017, pp. 537–546.

[7] S. Sudhakar, J.A. Weibel, S.V. Garimella, “A Semi-empirical model for thermal resistance and dryout during boiling in thin porous wicks fed by capillary action,” *Submitted for publication*, 2021.

[8] S. Sudhakar, J.A. Weibel, S.V. Garimella, “Modeling the power dissipation limits of high heat flux vapor chambers considering boiling in the evaporator wick,” *In preparation*, 2021.

[9] S. Sudhakar, S.N. Joshi and J.A. Weibel, “Observation of boiling behaviors in vapor chambers in response to transient heat input profiles”, *Submitted for publication in Applied Thermal Engineering*, 2021.

[10] S. N. Joshi, F. Zhou, E. M. Dede, D. J. Lohan, S. Sudhakar, and J. A. Weibel, “Thermal Performance Evaluation of a Two-Layer Wick Vapor Chamber for High Heat Flux Dissipation by Air Cooling,” in *2020 19th IEEE Intersociety Conference on Thermal and Thermomechanical Phenomena in Electronic Systems* (*ITherm*), pp. 91–96, Jul. 2020.